

**Titre:** Influence of Mg Content on the Mechanical Properties of Cast  
Title: Hypereutectic Al-Si Alloys

**Auteur:** Xichun Liu  
Author:

**Date:** 2009

**Type:** Mémoire ou thèse / Dissertation or Thesis

**Référence:** Liu, X. (2009). Influence of Mg Content on the Mechanical Properties of Cast  
Citation: Hypereutectic Al-Si Alloys [Mémoire de maîtrise, École Polytechnique de  
Montréal]. PolyPublie. <https://publications.polymtl.ca/160/>

 **Document en libre accès dans PolyPublie**  
Open Access document in PolyPublie

**URL de PolyPublie:** <https://publications.polymtl.ca/160/>  
PolyPublie URL:

**Directeurs de  
recherche:** Frank Ajersch  
Advisors:

**Programme:** Génie métallurgique  
Program:

**UNIVERSITÉ DE MONTRÉAL**

**INFLUENCE OF MG CONTENT ON THE MECHANICAL PROPERTIES OF  
CAST HYPEREUTECTIC AL-SI ALLOYS**

**XICHUN LIU**

**DÉPARTEMENT DE GÉNIE CHIMIQUE  
ÉCOLE POLYTECHNIQUE DE MONTRÉAL**

**MÉMOIRE PRÉSENTÉ EN VUE DE L'OBTENTION  
DU DIPLÔME DE MAÎTRISE ÈS SCIENCES APPLIQUÉES  
(GÉNIE MÉTALLURGIQUE)**

**SEPTEMBRE 2009**

**UNIVERSITÉ DE MONTRÉAL**  
**ÉCOLE POLYTECHNIQUE DE MONTRÉAL**

Ce mémoire intitulé:

**INFLUENCE OF MG CONTENT ON THE MECHANICAL PROPERTIES OF  
CAST HYPEREUTECTIC AL-SI ALLOYS**

présenté par: LIU XiChun

en vue de l'obtention du diplôme de: Maîtrise ès sciences appliqués

a été dûment accepté par le jury d'examen constitué de:

M. BALE Christopher W., Ph.D., président

M. AJERSCH Frank, Ph.D., membre et directeur de recherche

M. MEDRAJ Mamoun, Ph.D., P.Eng., membre

## Dedication

To the memory of my father, ChengXue

To my mother, YuXiang

To my wife, YuKun

To my daughter, QingXian

To my brother, XiDong

In every word and every page of this work,  
exists a bit of you because of your encouragements  
and your infinite support to accomplish my project



## Acknowledgement

“One flower makes no garland”. This thesis would not have been completed without all those who gave me the possibility to approach my goals, little by little. I am deeply indebted to my supervisor, Prof. Frank Ajersch for his valuable advice, patience, encouragements, and his professional guidance throughout my studies and research works. It is he who brought me into this science world where I found my interests and my abilities. I want to thank my colleague, Alireza Hekmat Ardakan, the former Ph.D. student, who helped me to understand the new alloy systems what he invented. Also, I thank to Prof. Christopher Bale who helped me to understand and perform all thermodynamic calculations using the software FactSage<sup>TM</sup>, and to Mr. Adarsh Shukla and Madam Liling Jin, Ph.D. students in CRCT (Centre de Recherche en Calcul Thermochimique) in clarifying some concepts of thermodynamic problems involved in this study. I would like to express my specific gratitude to Myriam Brochu, the current Ph.D. student, who gave me extensive assistance to complete all the tensile tests with great detail and for her translation of the “Résumé” and “Condensé en français” in my thesis, sacrificing her valuable time to help me whenever I asked. In addition, I am grateful to Carole Massicotte, the technician of the chemical engineering department, who aided me a lot in preparing the raw materials and assisting me without any hesitates in using the lab resources, as well Josée Laviolette, the technician of the mechanical

engineering department, who helped me in producing numerous microstructure photos in addition to offering explanations I did not understand in the lab. Likewise, I also want to thank Éric Duchesne and Philippe Beaulieu, the experts of the cm<sup>2</sup> laboratory, for all their assistances to train me on the SEM/ EDS operations.

The work was carried out in accordance with the “University Research Center on Aluminum (CURAL) of Chicoutimi” and the “Mining, Metals, and Materials Engineering Metals Processing Centre at McGill University” by providing their facilities to produce the permanent mould tensile bar castings. I want to thank prof. X. Grant Chen and his teams in UQAC and prof. Mihriban Pekguleryuz and the lab technician Pierre Vermette in McGill, especially the latter one who made his great efforts in scheduling my experiments among his many tasks.

Additionally, I would like to thank the jury members, prof. Christopher Bale, prof. Frank Ajersch, and prof. Mamoun Medraj, for their valuable contributions to my final version of the thesis. And I will also acknowledge NSERC (Natural Science and Engineering Research Council of Canada), REGAL-FQRNT (Fonds Québécois de Recherche sur la Nature et Technologies), and Rio Tinto Alcan for their financial supports. Finally, I will express my special gratitude to my wife YuKun for her patient love and infinite patience, allowing me to complete my work without any burdens.

## Résumé

L'objectif de ce travail est d'étudier l'influence de la teneur en magnésium (Mg) sur la microstructure et les propriétés mécaniques d'un alliage d'aluminium (Al) – silicium (Si) hypereutectique. Un nouvel alliage hypereutectique à forte teneur en magnésium a été développé en ajoutant 6% et 10% massique de magnésium. Les résultats obtenus montrent qu'en augmentant la teneur en Mg, la phase intermétallique  $Mg_2Si$  se substitue progressivement à la phase primaire Si. Des calculs thermodynamiques réalisés à l'aide du logiciel FactSage<sup>TM</sup> ont servi à prévoir la séquence de précipitation des phases au sein des alliages étudiés. Ces calculs ont été réalisés pour des systèmes binaires, ternaires et quaternaires. Pour les alliages auxquels ont été ajoutés de 6% de 10% de Mg, il y a corrélation entre les prédictions thermodynamiques et les séquences de solidification observées, particulièrement pour les deux régions de transition. Dans ces régions de transition, les deux phases primaires Si et  $Mg_2Si$  précipitent dans un ordre précis, mais différent pour chaque alliage. Pour l'alliage à faible teneur en Mg (6%), le silicium précipite d'abord tandis que pour l'alliage à forte teneur en Mg (10%) l'ordre de précipitation est inversé. Pour les deux alliages, la fraction massique de  $Mg_2Si$  dans la microstructure est significative.

À partir de ces deux alliages modifiés, des pièces ont été coulées par gravité

dans des moules métalliques. Les propriétés mécaniques et la dureté des pièces produites ont été mesurées et comparées à celles de l'alliage conventionnel A390. Les résultats préliminaires montrent que la dureté augmente avec l'ajout de Mg, car il y a durcissement par solution solide. En ce qui concerne la limite d'élasticité et le module d'Young des alliages à forte teneur en Mg, ces propriétés sont légèrement différentes de celles mesurées pour l'alliage A390. En contre partie, la résistance mécanique des alliages modifiés est plus faible que celle de l'alliage conventionnel.

L'ajout de bismuth (Bi) ainsi que l'effet d'un durcissement structural T6 ont aussi été investigués. L'ajout du Bi (0,6 à 0,8% massique), modificateur de structure, à l'alliage contenant 6% Mg a eu pour effet d'augmenter toutes les propriétés mécaniques. La phase riche en Bi, qui a une forme dendritique, précipite sur le front de solidification du  $Mg_2Si$  ce qui a pour effet d'en affiner la taille. Quant au durcissement structural, ce traitement thermique a aussi eu pour effet d'augmenter les propriétés des alliages modifiés, mais de façon moins significative que lorsque réalisé sur l'alliage A390. Le traitement thermique et la présence de défauts de fonderie pourraient expliquer cette différence d'efficacité. En effet, des porosités et des films d'oxyde se sont formés lors de la mise en forme des pièces. Une étude détaillée de la microstructure des pièces a montré qu'en augmentant la teneur en Mg, la coulabilité de l'alliage est réduite ce qui favorise la formation de défauts. D'ailleurs, l'examen fractographique des

éprouvettes de traction a mis en évidence que les bris s'initient de porosités et de films d'oxyde et se produisent de façon fragile. Il faut donc conclure que la présence de défauts limite l'utilisation du moulage permanent pour mettre en forme ces alliages modifiés, même si ceux-ci permettent de réduire la masse des pièces de 2,6% et 4,9% pour un ajout de 6% et 10% Mg respectivement. Néanmoins, la qualité métallurgique des pièces pourrait être améliorée en utilisant d'autres procédés de mise en forme tels le moulage sous pression ou le moulage semi-solide.

## Abstract

The current study focuses on the influence of the Mg content on the mechanical properties of cast hypereutectic Al-Si alloys. With increasing the Mg content, the formation of the primary  $\text{Mg}_2\text{Si}$  tends to substitute for the primary Si progressively in the modified castings with the properties close to the Si crystals, both of which are believed to be important in Al alloys. Other than the Al-Si alloy system has been fully developed, the Al- $\text{Mg}_2\text{Si}$  composites however just start to be concerned recently. A new alloy system is thus established based on the conventional cast hypereutectic Al-Si A390 alloy with increasing Mg content. The formation of the primary  $\text{Mg}_2\text{Si}$  is the main characteristic of adding Mg into the alloy A390, tending to substitute for the primary Si progressively. Equilibrium calculations and binary/ ternary/ quaternary phase diagram plots were carried out using the FactSage<sup>TM</sup> software, predicting the Al-Si alloy system alternatives with the Mg additions. The 6 and 10 wt% Mg alloys were found to be representative of the different decomposition behaviours in two transition regions where both primary phases can be precipitated in a particular order of Si to  $\text{Mg}_2\text{Si}$  for the alloy with lower magnesium content and  $\text{Mg}_2\text{Si}$  to Si for the second composition. For both alloys, the  $\text{Mg}_2\text{Si}$  phase is significant in the aluminum matrix.

Permanent mould castings were produced of these two alloy compositions, and

further tested for their hardness and tensile properties in comparison with the conventional A390 alloy. T6 heat treatment and Bi modifications of these two alloy compositions were also tested. The preliminary results denote that their hardness was increased somewhat with Mg additions due to the solid solution strengthening mechanism, while the yield strength and elastic modulus exhibited only a slight difference with respect to A390, whereas ultimate tensile strength was lower for the new alloys. The structure modifications due to Bi additions (0.6~0.8 wt%) to the 6 wt% Mg alloy show an overall improvement of the mechanical properties. It was observed that the snowflake-shaped Bi-bearing phases segregating at the primary  $Mg_2Si$  solidifying fronts, thus refining  $Mg_2Si$  crystals.

The T6 heat treatments of these new alloys increased the mechanical properties with respect to their as cast condition but smaller than the increment measured from the alloy A390. One of reasons might be relates to the heat treatments while another could be associated with the high level casting flaws, including the porosities and oxidation products that were encountered when casting these alloys. Further investigation of the microstructures showed that increased Mg additions favour the defect formation and reduce the castability. The tensile fracture analysis indicates most cracks were initiated by these porosities or oxidation products in the castings resulting in brittle fracture. This limits the application of the permanent mould castings for these new alloys even though

weight reductions can be achieved 2.6% for the 6 wt% alloy and 4.9% for the 10 wt% alloy when compared to the conventional A390 alloy. However, this further can be improved by introducing die casting or semi-solid forming.



## Condensé en français

### Contexte

L'influence des teneurs en magnésium (Mg) élevées (6 et 10% massique) sur les propriétés mécaniques d'un alliage d'aluminium (Al) – silicium (Si) hypereutectique moulé en coquille a été étudiée en utilisant des éprouvettes de traction. Les résultats ont été comparés à ceux d'un alliage Al-Si hypereutectique conventionnel, le A390 (Al-17%Si, 4.5%Cu, 0.5%Mg). Lorsque du Mg est ajouté au A390, des précipités de phase primaire  $Mg_2Si$  sont formés, ce qui a un effet déterminant sur les propriétés mécaniques en traction ainsi que sur la dureté de l'alliage. L'ajout de magnésium produit aussi, au sein de l'alliage, des changements microstructuraux significatifs.

L'alliage d'aluminium A390 a d'abord été utilisé pour fabriquer des blocs moteurs sans chemise. L'usage de cet alliage s'est maintenant élargi aux blocs moteurs avec chemises des voitures de pointe Audi et Volvo et aux applications maritimes. Plus léger que les blocs moteurs conventionnels en fonte, la technologie des moteurs sans chemise augmente le débit d'énergie et réduit l'usure de la surface interne des cylindres où de dures particules de silicium sont présentes. Le faible coefficient de dilatation thermique du silicium contribue aussi à la stabilité dimensionnelle de ces composantes, même à de hautes

températures. L'objectif de cette recherche est d'évaluer l'effet d'un ajout de Mg sur les propriétés mécaniques et la microstructure de ces alliages.

La séquence de solidification hors équilibre des alliages Al-Si hypereutectiques est différente de celle prédite par le logiciel FactSage. Des essais de solidification ont démontré l'existence d'une microstructure dans laquelle une phase primaire riche en Al (phase alpha) est présente en plus de la phase primaire riche en silicium et du constituant eutectique typiquement observés. Cela s'explique du fait que, lors de la solidification du silicium primaire, la composition chimique locale du liquide peut s'enrichir en aluminium. La transformation eutectique du système binaire Al-Si a alors lieu à plus basse température.

Les éléments d'alliage peuvent modifier les propriétés de l'alliage. La présence de 4.0% à 5.0% massique de cuivre (Cu) dans l'alliage A390 permet d'obtenir le durcissement structural le plus efficace. Quant au fer (Fe), il maximise la résistance aux criques à chaud et il réduit la tendance au collage avec le moule métallique. L'ajout de seulement 0.65% mass. de Mg empêche la formation du  $\text{Al}_5\text{FeSi}$  de forme aciculaire. La modification de la microstructure est aussi nécessaire pour améliorer les propriétés des pièces coulées en Al-Si. Un affinage des grains peut être réalisé en utilisant un agent affineur de grains efficace comme le  $\text{TiAl}_3$  et le  $\text{TiB}_2$  pour modifier l'aluminium de la matrice dans

les alliages Al-Si ce qui réduit la propension de former des criques à chaud lorsque l'espace entre de larges dendrites ne peut pas être efficacement alimenté en métal liquide. La morphologie des phases peut aussi être contrôlée en ajoutant des modificateurs de silicium comme le strontium (Sr), le sodium (Na), l'antimoine (Sb) qui transforment le silicium aciculaire de l'eutectique en une morphologie fibreuse composée de branches maclées. L'ajout de phosphore (P), sous forme de Cu-P, peut aussi affiner les particules de silicium primaire.

L'ajout de particules, comme le  $\text{Al}_2\text{O}_3$  ou le SiC, à la matrice d'aluminium permet d'obtenir des composites renforcis d'une phase secondaire ce qui augmente les propriétés mécaniques des pièces. Ces particules cohérentes durcissent la matrice d'aluminium puisque leur paramètre de maille est comparable, ce qui génère une déformation élastique au sein de la matrice d'aluminium ayant pour effet d'augmenter la résistance au mouvement des dislocations. Les précipités de  $\text{Mg}_2\text{Si}$  qui se forment au sein des alliages hypereutectiques enrichis de Mg peuvent aussi être considérés comme des renforts in-situ formant un composite.

En pratique, le contrôle précis de la composition du métal et de l'affinement des phases sont nécessaires pour réussir à produire, par moulage par gravité, des pièces saines en alliages Al-Si hypereutectiques. Les porosités gazeuses formées d'hydrogène et les inclusions d'oxydes sont considérées comme les

défauts les plus nuisibles pour la qualité métallurgique des pièces. Le bullage de gaz inertes ( $N_2$  ou Ar) est communément utilisé pour éliminer l'hydrogène en excès qui se dissout dans l'aluminium liquide. En plus, la teneur en inclusions de laitier doit être minimisée en utilisant des techniques de séparation comme l'écémage du laitier et la filtration.

La fluidité, propriété déterminante de la coulabilité de l'alliage, est fonction de la composition de l'alliage, de sa chaleur latente de fusion, de sa surfusion, de la morphologie et de la taille des phases qui se solidifient, du matériau, des revêtements et de la température du moule et, de la propreté et de la viscosité du métal liquide. L'alliage A390 a une teneur en silicium optimale pour obtenir la meilleure fluidité de tous les alliages du système Al-Si. De plus, le traitement thermique de type T6 est très efficace pour l'alliage A390 puisque la phase  $\theta$ - $Al_2Cu$  précipite en une fine structure qui durcit la matrice Al par le mécanisme d'ancrage d'Orowen.

## **Calculs thermodynamiques**

Tous les calculs thermodynamiques ont été réalisés à l'aide du logiciel de modélisation thermodynamique FactSage pour le système Al-Si-Cu-Mg à forte teneur en Mg. En utilisant la base de données pour métaux légers FACTSage FSLite, un composé stœchiométrique ( $Mg_2Si$ ) et quatre autres phases composent le diagramme de phases d'équilibre. Le diagramme de phases

quasi-binaire Al-Mg calculé montre la séquence de solidification et la microstructure de trois alliages typiques soient le A390 et les alliages contenant 6% et le 10% massique de Mg. Pour l'alliage A390, la première phase solidifiée est le silicium primaire, suivie par la transformation eutectique binaire  $L \rightarrow \alpha + \text{Si}$ , suivie par une décomposition ternaire où le  $\text{Mg}_2\text{Si}$  apparaît, avant de se terminer par une réaction quaternaire qui forme de la phase  $\theta\text{-Al}_2\text{Cu}$ . Pour l'alliage contenant 6% de Mg, la phase primaire Si sera toujours le premier solide à se former à partir du liquide avec le  $\text{Mg}_2\text{Si}$  comme deuxième phase primaire avant que le reste des réactions eutectiques aient lieu. Cependant, pour l'alliage contenant 10% de Mg, la solidification des phases primaires débute par la formation de  $\text{Mg}_2\text{Si}$  suivi par le Si. Après cette étape, la décomposition procède comme pour l'alliage précédent.

Dans le système ternaire Al-Mg-Si, des projections des surfaces du liquidus ont été produites avec une série de lignes invariantes où le liquide est en équilibre avec deux phases solides. La solidification est complète au point invariant pour une température et une composition donnée, où il existe un équilibre entre quatre phases. La séquence de solidification des alliages enrichis de Mg est en accord avec les résultats obtenus pour le système quasi-binaire Al-Si.

Les trois diagrammes d'équilibre calculés ont montré l'effet de la teneur en Mg sur la précipitation du  $\text{Mg}_2\text{Si}$ . La phase primaire Si est graduellement remplacée

par la phase primaire  $\text{Mg}_2\text{Si}$  lorsque la teneur en Mg augmente. La température de la réaction eutectique du diagramme binaire Al-Si a aussi diminué. La température de la décomposition quaternaire ( $496.94^\circ\text{C}$ ) où le dernier liquide se solidifie n'a cependant pas été modifiée par l'ajout de Mg.

Les calculs thermodynamiques montrent qu'une phase liquide apparaît à  $640^\circ\text{C}$  dans les trois alliages. L'alliage A390 contient du silicium primaire à cette température mais, l'alliage 10%Mg contient plutôt comme phase primaire du  $\text{Mg}_2\text{Si}$ . Toutefois, l'alliage 6%Mg, est entièrement liquide puisque la température de son liquidus est  $613^\circ\text{C}$ . En diminuant la température, du silicium primaire précipite au sein de l'alliage 6%Mg à  $590^\circ\text{C}$  tandis que l'alliage 10%Mg est à la frontière où les deux phases primaires Si et  $\text{Mg}_2\text{Si}$  sont présentes. La réaction eutectique binaire ( $\text{L} \rightarrow \alpha\text{-Al} + \text{Si}$ ) se produit à  $540^\circ\text{C}$  pour l'alliage A390 tandis que les réactions eutectiques ternaires ( $\text{L} \rightarrow \alpha\text{-Al} + \text{Si} + \text{Mg}_2\text{Si}$ ), pour les alliages 6% massique Mg et 10% massique Mg, se produisent à la même température. Tout le liquide restant disparaît à  $490^\circ\text{C}$  pour atteindre un équilibre solide quaternaire entre les phases  $\alpha\text{-Al}$ , Si,  $\theta\text{-Al}_2\text{Cu}$  et  $\text{Mg}_2\text{Si}$ , le point invariant.

Les calculs d'équilibre des phases ont été réalisés pour déterminer la séquence de solidification de l'alliage et pour calculer la fraction solide de chacune des phases à leur température de transition pour des conditions d'équilibre et des conditions de refroidissement Scheil. Les résultats peuvent être utilisés pour

contrôler les procédés de mise en forme à l'état semi-solide des alliages enrichis de Mg. Les courbes d'enthalpie (H) et de chaleur spécifique ( $C_p$ ) des trois alliages indiquent que la plupart des échanges d'énergie ont lieu à une température unique où la réaction eutectique binaire se produit.

## **Résultats expérimentaux et discussion**

Des éprouvettes de traction ont été fabriquées par moulage en coquille pour mesurer les propriétés mécaniques de l'alliage A390 ainsi que celles des alliages enrichis de Mg. Deux types d'éprouvettes ont été moulés, des éprouvettes de forme cylindrique et des éprouvettes de forme rectangulaire. Les éprouvettes cylindriques ont été fabriquées à partir des alliages de 6% et 10% de Mg et de l'alliage A390. Ces éprouvettes ont aussi été traitées thermiquement à l'état T6 afin de comparer leurs propriétés avec celles à l'état brut de coulée. Les éprouvettes rectangulaires ont été fabriquées des mêmes trois alliages auxquels un modificateur d'eutectique (du bismuth ou du phosphore) a été ajouté pour modifier la phase primaire. La densité des alliages a été mesurée par la méthode d'Archimède où la poussée d'Archimède correspond à la masse du liquide (l'eau) déplacée par l'objet submergé. Les propriétés mécaniques ainsi que la dureté des éprouvettes de traction ont aussi été mesurées. Des examens de la microstructure ont été réalisés sur des échantillons polis par microscopie optique et à l'aide de l'analyseur d'images

Clemex et les surfaces de rupture des éprouvettes de traction ont été observées au microscope électronique à balayage (MEB).

Il a été observé qu'une forte teneur en Mg peut modifier la microstructure de l'alliage significativement ainsi que sa coulabilité. Différent du film d'oxyde de structure spinelle ( $\text{Al}_2\text{MgO}_4$ ) observé au sein de l'alliage A390, un épais film de magnésie ( $\text{MgO}$ ) a été observé dans les alliages contenant 6% et 10% de Mg. Ce film est collant et a une structure plissée provoquant de la striation en surface des pièces solidifiées. Ce type de film de surface a contribué à diminuer la fluidité des alliages enrichis en Mg. De plus, avec ce film de surface, des inclusions sont facilement entraînées dans le métal liquide ce qui produit des reprises au sein des pièces coulées.

Les porosités gazeuses et les criques de retrait sont aussi des défauts importants retrouvés au sein des alliages enrichis de Mg, qui sont créés par la vaporisation continue du Mg liquide. Une fraction volumique de 2.28% et 2.52% a été mesurée pour les porosités des alliages à 6% et 10% Mg respectivement comparée à 0.88% pour l'alliage A390. Des images en électrons secondaires (SEI) ont montré des protubérances de cristaux de  $\text{Mg}_2\text{Si}$  à l'intérieur de plusieurs porosités gazeuses ce qui indique que, pour ces alliages, la formation des pores est tributaire à la teneur en magnésium. Cela peut être expliqué de deux façons. La vapeur de Mg peut être emprisonnée ce qui forme un vide



entouré par des cristaux de  $\text{Mg}_2\text{Si}$  à cause de la solidification rapide qui a lieu lors de la réaction eutectique. De plus, l'hydrogène en solution est relâché lorsque la température du métal liquide diminue et contribue à la formation des porosités. Il a été observé que les cavités de retrait se forment suite à une alimentation insuffisante en métal liquide dans les dernières régions à se solidifier provoquant des porosités de formes irrégulières. À la surface intérieure de ces porosités, on retrouve des phases intermétalliques comme des dendrites de  $\alpha\text{-Al}$ , du  $\theta\text{-Al}_2\text{Cu}$  et/ou des amas de  $\text{Q-Al}_5\text{Cu}_2\text{Mg}_8\text{Si}_6$ , des protubérances de cristaux de  $\text{Mg}_2\text{Si}$  et des inclusions.

La fluidité à l'état liquide de ces alliages enrichis de Mg est plus faible que celle de l'alliage A390, pour un moulage par gravité dans une coquille préchauffée à  $400^\circ\text{C}$ . La chaleur latente de fusion plus faible du  $\text{Mg}_2\text{Si}$ , lorsque comparé à celle du Si, la densité du matériau et le taux de perte de chaleur sont les principales causes de cette fluidité relativement faible.

Les images SEI ainsi que les analyses EDX ont permis d'identifier les caractéristiques microstructurales des constituants solidifiés et observés sur les faciès de rupture de ces alliages. Les images montrent la croissance sans facettes du  $\alpha\text{-Al}$  (tige unique  $\rightarrow$  branches 2D  $\rightarrow$  dendrites 3D), les amas de  $\text{Q-Al}_5\text{Cu}_2\text{Mg}_8\text{Si}_6$  (aciculaires), la phase  $\text{Mg}_2\text{Si}$  et les précipités de  $\theta\text{-Al}_2\text{Cu}$ .

Les densités de ces nouveaux alliages, corrigées pour tenir compte de la teneur en porosités, sont 2.714, 2.640 et 2.580 ( $\text{g/cm}^3$ ), ce qui représente un allègement d'environ 2.6% et 4.9% pour les alliages contenant respectivement 6% et 10% de Mg. La dureté des éprouvettes et les propriétés mécaniques ont aussi été mesurées mais elles étaient fortement influencées par la qualité métallurgique des éprouvettes coulées. Néanmoins, certaines tendances ont été déduites des résultats obtenus. D'abord, à l'état brut de coulée, les alliages enrichis de Mg ont une dureté plus élevée comparée à celle de l'alliage A390 et cette augmentation de dureté est grossièrement proportionnelle à la concentration en Mg. Il y avait une exception pour les éprouvettes de l'alliage 10%Mg pour lesquelles la dureté est inférieure à celle des éprouvettes en alliage 6%Mg. Ce résultat est expliqué par la présence de plusieurs microporosités, observées sur la surface éprouvée, qui influencent les mesures. La fraction solide plus élevée de  $\text{Mg}_2\text{Si}$  peut augmenter la dureté des ces nouveaux alliages enrichis de Mg.

Les propriétés mécaniques en traction des éprouvettes à l'état brut de fonderie montrent que l'ajout de magnésium a peu d'effet sur la limite d'élasticité des alliages (~50 à 66 MPa) lorsque comparée à celle de l'alliage de référence, le A390. Les valeurs du module d'Young (~72 à 82 GPa) sont presque les mêmes pour les trois alliages. Toutefois, la résistance à la traction des alliages enrichis

de Mg est plus faible que celle de l'alliage A390, possiblement à cause des défauts.

Néanmoins, le traitement thermique T6 montre une augmentation globale des propriétés mécaniques en traction et de la dureté pour les trois alliages, et la plus forte augmentation a été mesurée pour l'alliage A390. Les mêmes conditions de traitement thermique ont été utilisées pour chacun des alliages, selon les recommandations de l'ASTM pour l'alliage A390. Les conditions n'ont pas été optimisées pour les alliages enrichis de Mg et des recherches supplémentaires seront nécessaires pour étudier leurs effets sur ces alliages.

Les microstructures des surfaces de rupture ont montré qu'en plus du principal précipité durcissant le  $\theta$ -Al<sub>2</sub>Cu retrouvé dans la matrice, le silicium eutectique et les phases Q contribuent au durcissement par précipitation. Les modifications de structure ont eu des influences positives sur les propriétés de l'alliage. L'alliage conventionnel A390 a aussi été modifié en ajoutant 100 ppm de phosphore. Bien que les tailles des particules de silicium aient été réduites, les propriétés de l'alliage A390 n'ont pas été améliorées. Cela peut aussi être dû à la présence de défauts de fonderie.

D'un autre côté, l'ajout de Bi (0.6-0.8% en référence à l'annexe 9.1) à l'alliage contenant 6% de Mg a permis d'augmenter les propriétés mécaniques en

traction, probablement à cause de la légère diminution de la taille des particules de phase primaire  $Mg_2Si$ . Cette diminution de taille est probablement causée par la ségrégation, sur les cristaux en solidification, des précipités composés de Bi ce qui retarde leur croissance. Ces particules distribuées dans la matrice durciront probablement l'alliage avec leur morphologie dendritique (en flocon). L'alliage 10% Mg devrait réagir de façon similaire à des modifications au bismuth. Cela n'a pu être déterminé au cours des présentes expériences parce que ces alliages étaient très difficiles à couler et contenaient conséquemment plusieurs défauts de fonderie.

Les analyses fractographiques ont montré que les alliages enrichis de Mg sont sujets à des ruptures fragiles. Les fissures s'amorcent en apparence de défauts de fonderie comme des porosités et des films d'oxyde. La taille, la morphologie et la distribution des précipités primaires ont une influence sur la propension au clivage. De façon générale, il peut être proposé qu'une microstructure fine et globulaire et une faible teneur en défauts améliorent la résistance aux ruptures fragiles.

## **Conclusion**

Bien que l'ajout de Mg aux alliages Al-Si hypereutectiques puisse modifier de façon significative leurs séquences de solidification et leurs microstructures, le  $Mg_2Si$  a une plus faible stabilité thermique et une plus faible chaleur latente de

fusion que le Si. Il a été démontré que l'addition de Mg facilite la formation de gros défauts de fonderie. Le traitement thermique T6 et la modification au bismuth peuvent grandement accroître les propriétés mécaniques des alliages coulés. Toutefois, les nouveaux alliages enrichis de Mg sont difficiles à couler en coquille par gravité. Pour obtenir des pièces coulées plus saines, il sera nécessaire d'utiliser des procédés de coulée sous pression. Le clivage est le mécanisme de rupture observé pour les trois alliages sollicités en traction produisant des caractéristiques fractographiques d'une rupture fragile qui s'amorce généralement à des défauts de fonderie.

## Table of Contents

<b>DEDICATION .....</b>	<b>III</b>
<b>ACKNOWLEDGEMENT .....</b>	<b>IV</b>
<b>RÉSUMÉ .....</b>	<b>VI</b>
<b>ABSTRACT .....</b>	<b>IX</b>
<b>CONDENSÉ EN FRANÇAIS .....</b>	<b>XII</b>
<b>TABLE OF CONTENTS .....</b>	<b>XXV</b>
<b>LIST OF FIGURES .....</b>	<b>XXVII</b>
<b>LIST OF TABLES .....</b>	<b>XXXVI</b>
<b>CHAPTER 1. INTRODUCTION .....</b>	<b>1</b>
1.1. PROJECT OVERVIEW .....	1
1.2. OBJECTIVES .....	2
<b>CHAPTER 2. LITERATURE REVIEWS .....</b>	<b>4</b>
2.1. HISTORICAL PERSPECTIVE OF A390 ALLOY .....	4
2.2. SOLIDIFICATION BEHAVIOUR OF HYPEREUTECTIC AL-SI ALLOYS .....	8
2.2.1. <i>General solidification characteristics</i> .....	8
2.2.1.1. Chemical thermodynamics and kinetics .....	9
2.2.1.2. Nucleation mechanisms .....	11
2.2.1.3. Growth and crystal morphologies .....	14
2.2.2. <i>Solidification behaviour of hypereutectic Al-Si alloys</i> .....	17
2.3. CONTROL OF ALLOY QUALITIES .....	20
2.3.1. <i>Effect of alloying elements</i> .....	21
2.3.2. <i>Cast structure refining</i> .....	22
2.3.3. <i>Reinforced composites</i> .....	28
2.3.4. <i>Liquid metal treatments</i> .....	30
2.3.5. <i>Alloy fluidity</i> .....	35
2.3.6. <i>Heat treatment</i> .....	36
<b>CHAPTER 3. METHODOLOGY .....</b>	<b>40</b>
3.1. THERMODYNAMIC CALCULATIONS .....	40
3.2. EXPERIMENTAL METHODOLOGY .....	41
3.2.1. <i>Overall experiment description</i> .....	41
3.2.2. <i>Material preparation</i> .....	42
3.2.3. <i>Castings</i> .....	43
3.2.4. <i>Heat treatment (T6)</i> .....	47
3.2.5. <i>Density determination</i> .....	48

3.2.6.	<i>Tensile tests</i> .....	49
3.2.7.	<i>Hardness tests</i> .....	51
3.2.8.	<i>Microstructural examination</i> .....	53
<b>CHAPTER 4. THERMODYNAMIC CALCULATIONS</b> .....		<b>55</b>
4.1.	PRIMARY $Mg_2Si$ VERSUS $Si$ .....	55
4.2.	PHASE DIAGRAMS .....	56
4.2.1.	<i>Isopleth binary Al-Mg phase diagram</i> .....	62
4.2.2.	<i>Ternary polythermal projection of liquidus surfaces</i> .....	63
4.2.3.	<i>Isopleth binary Al-Si phase diagrams</i> .....	66
4.2.4.	<i>Isothermal quasi-binary Si-Mg phase diagrams</i> .....	68
4.3.	EQUILIBRIUM CALCULATIONS – ALLOY DECOMPOSITION BEHAVIOURS .....	71
4.4.	ENTHALPY (H) AND HEAT CAPACITY ( $C_p$ ) .....	80
<b>CHAPTER 5. RESULTS AND DISCUSSION</b> .....		<b>85</b>
5.1.	CASTING PRACTICE .....	85
5.1.1.	<i>Surface films</i> .....	85
5.1.2.	<i>Porosities</i> .....	92
5.1.3.	<i>Flow behaviour</i> .....	100
5.2.	CHARACTERISTICS OF SOLIDIFICATION PRODUCTS .....	107
5.3.	DENSITY .....	115
5.4.	HARDNESS .....	117
5.5.	TENSILE PROPERTIES .....	125
5.6.	MICROSTRUCTURES .....	136
5.6.1.	<i>Effects of T6 heat treatment</i> .....	136
5.6.2.	<i>Effect of structure modifiers</i> .....	142
5.6.3.	<i>Tensile fractography</i> .....	154
<b>CHAPTER 6. GENERAL DISCUSSION</b> .....		<b>167</b>
<b>CHAPTER 7. CONCLUSION AND FUTURE STUDIES</b> .....		<b>177</b>
7.1.	CONCLUSION .....	177
7.2.	FUTURE STUDIES .....	179
<b>REFERENCES</b> .....		<b>180</b>
<b>APPENDIX: CASTING CHEMICAL COMPOSITIONS</b> .....		<b>184</b>

## List of Figures

Figure 1.1 Typical applications of hypereutectic Al-Si alloys.....	2
Figure 2.1 Fatigue property comparison between cast iron and aluminum engines .....	4
Figure 2.2 a) Alusil® low pressure die casting (LPDC) for new Audi V6 and V8 Si linerless engine with only 5.5 mm land width; b) The surface bare-bore technology to expose Si phases; c) Sikasil® high pressure die casting (HPDC) with cast in BMI grey iron liners for Volvo in-line 5 cyl. diesel block.....	7
Figure 2.3 Gibbs free energy curves v.s. T under equilibrium cooling process for pure Aluminum calculated by the FactSage™ .....	11
Figure 2.4 a) The plot of free energy change $\Delta G$ v.s. nuclei size $r$ ; b) The homogeneous nucleation; c) The heterogeneous nucleation.....	12
Figure 2.5 Wetting effects on varying barrier interfacial energies illustrated for heterogeneous nucleation mechanisms.....	13
Figure 2.6 Growth morphologies during solidification process relates to varying heat flow gradients .....	14
Figure 2.7 a) Free movement of dendrites at beginning of solidification via the Mass feeding mode; and developing to a solid network where only the Interdendritic feeding can take place .....	16
Figure 2.8 a) FactSage™ calculated binary Al-Si phase diagram under an equilibrium condition (solid lines), with a demonstration of a Scheil cooling characters.....	17
Figure 2.9 a) Coupled growth of eutectic Si + $\alpha$ - Al; b) Metallic non-faceted growth mode; c) Non-metallic faceted growth mode; d) Twin formation of eutectic Si growth....	18
Figure 2.10 Three typical primary Si morphologies: (a) Star-shaped; (b) Polyhedral; and (c) Dendrites.....	19
Figure 2.11 Schematics of a) Three essential elements (grains, Al dendrites – DAS, and eutectic Si) in a basic hypoeutectic Al-Si microstructure; b) Perfect grain refiner particles .....	23



Figure 2.12 The binary Al-Si phase diagram illustrates the precipitation of $AlB_2$ is prior to the primary Si liquidus as 0.02 wt% B is added into the A390 alloy.....	24
Figure 2.13 Schematics of a) Diamond Si in its standard step-growing mode.....	25
Figure 2.14 Most effective eutectic Si modifiers having an atomic radii ratio of the impurity induced elements to Si in optimum.....	26
Figure 2.15 Illustrations of (A) Coherent precipitation particles strengthening the Al matrix; (B) Non-coherent structure between precipitates and Al atoms .....	29
Figure 2.16 Plots of a) Hydrogen solubility in aluminum at $PH_2 = 1atm$ ; b) Equilibrium gas removal ratio at $760^\circ C$ .....	30
Figure 2.17 Schematics of a) The inert gas flushing .....	32
Figure 2.18 Schematic of forming the shrinkage porosities during the solidification process.....	33
Figure 2.19 Schematics of void nucleation at particles initiated by a) The particle-matrix de-cohesion; b) The particle fracture .....	34
Figure 2.20 Effects of Si and Cu compositions on the fluidity of a) Al-Si and b) Al-Cu alloys respectively, tested at a constant pouring temperature .....	35
Figure 2.21 a) Binary Al- $Al_2Cu$ phase diagram calculated by the FactSage <sup>TM</sup> ; b) TTT curve for Al-Cu alloys; c) As cast microstructures of coarse $\theta$ - $Al_2Cu$ precipitating on grain boundaries; d) Fine $\theta$ - $Al_2Cu$ particles distributing in the Al matrix after ageing treatment; and e) The Orowan's bowing strengthening effect.....	37
Figure 2.22 The yield strength - microstructure relationships during the ageing heat treatment process for an Al-3.5~5.5 wt% Cu alloy .....	39
Figure 3.1 The species to be used in the FactSage <sup>TM</sup> calculations consisting of 4 solutions (FSlite-Liquid, FSlite- $AlCu_6$ < $\theta$ - $Al_2Cu$ >, FSlite-DIAM <Si>, and FSlite-FCC <Al>) and 1 compound ( $Mg_2Si(s)$ ) for the Al-Si-Cu-Mg alloy system in weight basis. ....	41
Figure 3.2 a) Melting unit: Pyradia stationary electric resistance furnace in CURAL of Chicoutimi; b) The circular tensile bar assembly before de-moulding from a refractory coated permanent metallic mould sitting on the top of a metallic plate in CURAL. ....	43

Figure 3.3 The detailed drawing of the circular tensile bar assembly .....	44
Figure 3.4 a) Induction furnace set-up (20kw/ 5khz); b) Graphite crucible with one charge of bulk A390 alloy to be melted by the magnetic field; c) Permanent Metallic mould and the rectangular cast assembly.....	46
Figure 3.5 Schematic of Archimedes' principle for the density measurement.....	48
Figure 3.6 Two types of tensile specimens used in the study. ....	49
Figure 3.7 Tensile test set-up in two types of equipments: Left – Instron 1362 for round tensile bars; Right – Instron 1333 for flat tensile bars. ....	50
Figure 3.8 Hardness test set-up in two types of equipments: Left – Clemex MT-2001 for micro-hardness tests; Right – Mitutoyo ATK-600 for RockWell bulk hardness tests.....	52
Figure 3.9 Devices for the microstructure analysis: a) Clemex® image processing set; and b) SEM equipment – type JOEL 840. ....	53
Figure 4.1 Binary a) Al-Si, b) Al-Mg phase diagrams from Al, Si, Cu, and Mg elements.....	59
Figure 4.1 (Continued) Binary c) Mg-Si, d) Al-Cu phase diagrams from Al, Si, Cu, and Mg elements.....	60
Figure 4.1 (Continued) Binary e) Cu-Si, and f) Cu-Mg phase diagrams from Al, Si, Cu, and Mg elements .....	61
Figure 4.2 The quasi-binary Al-Mg phase diagram is plotted by fixing Cu at 4.5wt% and Si at 17wt% and the typical microstructures are illustrated for primary phases in each alloy (FactSage, phase diagram).....	62
Figure 4.3 Liquidus projection of ternary Al-Mg-Si phase diagram with Cu fixed at 4.5wt% (FactSage, phase diagram). ....	64
Figure 4.4 Detailed view of the Al corner where the new alloy system attains at point 1 of the 4-phase interaction with liquid (FactSage, phase diagram). ....	65
Figure 4.5 The plots of quasi-binary Al-Si phase diagrams fixed Cu at 4.5wt% and Mg at a) 0.5wt%; b) 6wt% (FactSage, phase diagram).....	67

Figure 4.6 Isothermal Si-Mg phase diagrams in weight basis at a) 640°C; b) 590°C (FactSage, phase diagram).....	69
Figure 4.6 (Continued) Isothermal Si-Mg phase diagrams in weight basis at c) 540°C; b) 490°C (FactSage, phase diagram). ....	70
Figure 4.7 a) Solid fraction (wt%) plot for the alloy A390 as a function of solidification temperature under both b) equilibrium and c) scheil cooling conditions with detailed quantitative descriptions (FactSage, Equilibrium). In addition, a group of experimental data is also presented in three different cooling rates as a comparison....	74
Figure 4.8 a) Solid fraction (wt%) plot for the alloy A390-6Mg as a function of solidification temperature under both b) equilibrium and c) scheil cooling conditions with detailed quantitative descriptions (FactSage, Equilibrium). ....	75
Figure 4.9 a) Solid fraction (wt%) plot for the alloy A390 + 10Mg as a function of solidification temperature under both b) equilibrium and c) scheil cooling conditions with detailed quantitative descriptions (FactSage, Equilibrium). ....	76
Figure 4.10 Solid fraction (wt%) plot for alloy A356 as a function of solidification T (°C) under both equilibrium and scheil cooling conditions (FactSage, Equilibrium).....	78
Figure 4.11 The weight fraction of poly-isothermal Si and Mg <sub>2</sub> Si phases dynamically changing with Mg addition in A390 alloys (FactSage, Equilibrium).....	79
Figure 4.12 Plots of a) enthalpy and b) heat capacity as a function of solidification T (°C) for alloy A390 under both equilibrium and scheil cooling conditions (FactSage, Euqilib-XML).....	81
Figure 4.12 (Continued) Plots of c) enthalpy and d) heat capacity as a function of solidification T (°C) for alloy A390+6wt% Mg under both equilibrium and scheil cooling conditions (FactSage, Euqilib-XML).....	82
Figure 4.12 (Continued) Plots of e) enthalpy and f) heat capacity as a function of solidification T (°C) for alloy A390+10wt% Mg under both equilibrium and scheil cooling conditions (FactSage, Euqilib-XML).....	83
Figure 5.1 Types of oxide film on the Mg added A390 casting surface from: melt over flow collected in a metallic basin and cast flat tensile bars for alloy a),b) A390; c),d) A390-0.01P; and e),f) A390-6Mg-1.2Bi respectively.....	87

Figure 5.2 Molten liquid with the turbulent front illustrating the mechanism of the bi-film formation and surface entrainment.....	88
Figure 5.3 Magnesia oxide films appeared in a tensile fracture surface of the 10 wt% Mg added A390 alloy: a) Cold shut trapped in an area near to the wall (20x); b) Films covering the entrapment (cold shut) with apparent folds (500x).....	90
Figure 5.3 (Continued) Magnesia oxide films appeared in a tensile fracture surface of the 10 wt% alloy: c) Interface of the cold shut and Al matrix (250x); and d) Fold structure on the cold shut surface (2000x). ....	91
Figure 5.4 Clemex® image analysis examples of gas and shrinkage porosities for alloy a) A390 (0.88 vol.%), b) 6wt% Mg (2.28 vol.%), c) 10Mwt% Mg (2.52 vol.%), and d) The average porosity for each alloy. ....	93
Figure 5.5 Gas porosities displaying $Mg_2Si$ crystal protrusions from their smooth cavities observed in 10wt% Mg alloy fracture surfaces for both a) and b). ....	94
Figure 5.5 (Continued) Gas porosities displaying $Mg_2Si$ crystal protrusions from their smooth cavities observed in the alloy c) 10wt% Mg and d) 6wt% Mg - 0.6Bi fracture surfaces.....	95
Figure 5.6 Vapour pressure for the elements in aluminum melts.....	96
Figure 5.7 Shrinkage porosities illustrating as a) $\alpha$ -Al dendrites in an 6wt% Mg alloy, b) Cold shut interacting with the 10wt% Mg base alloy. ....	98
Figure 5.7 (Continued) Shrinkage porosities illustrating c) A void containing complex constituents in an A390 alloy after T6 heat treatment, and d) A cavity surrounded with significant $Mg_2Si$ formation in the 10wt% Mg alloy.....	99
Figure 5.8 The comparison of latent heat of the fusion for Al, Si, and $Mg_2Si$ phases (FactSage, Reaction). ....	101
Figure 5.9 a) A failed mould filling case in a 10 wt% Mg alloy (pouring at 750°C); b) and c) Showing many oxidation defects at the fracture surfaces caused by the de-molding process. ....	103
Figure 5.10 Oxides on the fracture surface of the A390-10Mg tensile bar shown in Figure 5.9 b) and EDS analysis.....	105

Figure 5.11 Oxides on the fracture surface of the A390-10Mg tensile bar shown in Figure 5.9 c) and EDS analysis.....	106
Figure 5.12 The overall morphologies of the permanent mould casting A390, A390-6Mg and A390-10Mg at a), b), c) 50X and d), e), f) 200X magnification respectively observed by OM images. ....	108
Figure 5.13 Non-faceted $\alpha$ -Al growing evolution in the 6wt% Mg alloy: a) Single stem-shaped growth; b) Branching in one side; c) 2-D structure in a flat bar fracture (A390-6Mg-0.6Bi); and d) 3-D morphologies in a round bar fracture (A390); e) The EDS analysis of dendrites. ....	109
Figure 5.14 $Q$ - $Al_5Cu_2Mg_8Si_6$ phase growing in a), b) A390-6Mg; and c), d) A390-10Mg alloys found at the rectangular tensile bar fracture surfaces; e) The EDS analysis of the $Q$ phase “needles”.....	110
Figure 5.15 Faceted $Mg_2Si$ crystals growing in a) A390-6Mg; and b), c), d) Photographs of fracture surface of A390-10Mg alloys from rectangular tensile bar; e) The EDS analysis of the $Mg_2Si$ . ....	111
Figure 5.16 $\theta$ - $Al_2Cu$ phases with two morphologies: a) Dendrites in a flat tensile bar fracture of alloy A390-0.01P; b) Irregular shape in a circular tensile bar fracture of alloy A390 under T6 condition; c) The EDS analysis of the $\theta$ phase. ....	112
Figure 5.17 Comparison of the calculated densities using equilibrium and Scheil cooling of the alloys with the measured values for increasing Mg content.....	116
Figure 5.18 A micro-hardness (GPa) comparison between the measurements and reported data (Table 3.1) for the phase primary Si and $Mg_2Si$ . ....	118
Figure 5.19 Hardness measurements of circular tensile bars under both as cast (F) and T6 condition: a) $\alpha$ -Al matrix (Vicker’s scale); b) Bulk material (RockWell B scale).....	119
Figure 5.19 (continued) Hardness measurements of circular tensile bars under both as cast (F) and T6 condition: c) Their comparison. ....	120
Figure 5.20 RockWell hardness measurements from as cast A390 tensile bars with and without bismuth modifications: a) A390-xMg and A390-0.01P; b) A390-6Mg-xBi..	123

Figure 5.20 (Continued) RockWell hardness measurements from as cast rectangular tensile bars with and without bismuth modifications: c) A390-10Mg-xBi; and d) Their overall comparison.....	124
Figure 5.21 Bulk material hardness comparisons between two types of castings. ....	125
Figure 5.22 Tensile curves for A390+0.01%P specimen. ....	126
Figure 5.23 Tensile properties of the circular Mg tensile bars under both as cast and T6 conditions: a) Yield strength; b) Ultimate tensile strength (UTS). ....	128
Figure 5.23 (Continued) Tensile properties of the circular Mg tensile bars under both as cast and T6 conditions: c) Elastic modulus, d) Elongations. ....	129
Figure 5.24 Tensile properties of Mg alloys with and without Bi modifications: a) Yield strength and UTS; b) Elastic modulus.....	132
Figure 5.24 (Continued) Tensile properties of Mg alloys with and without Bi modifications: c) Fracture elongations.....	133
Figure 5.25 Tensile property comparison of Mg alloys for two types of as cast tensile bars: a) Yield strength (0% offset); b) Tensile strength (UTS). ....	134
Figure 5.25 (Continued) Tensile property comparison of Mg alloys for two types of tensile bars: c) Elastic modulus; d) Elongation.....	135
Figure 5.26 Optical images of the A390 before and after T6 at 200X. ....	137
Figure 5.26 (Continued) Optical images of the 6Mg before and after T6 at 200X.....	138
Figure 5.26 (Continued) Optical images of the 10Mg before and after T6 at 200X.....	139
Figure 5.27 Optical images of Mg alloys before and after T6 at 500X. ....	140
Figure 5.28 Optical images (50X) of the a) Alloy A390 comparing to b) Alloy A390-0.01P. ....	143
Figure 5.28 (Continued) Optical images (200X) of the c) Alloy A390 comparing to d) Alloy A390-0.01P.....	144
Figure 5.29 Optical images of the alloy A390-6Mg with Bi modifications at a) 0 wt%; b) 0.6 wt% (targets). ....	146

Figure 5.29 (Continued) Optical images of the 6Mg alloy with Bi modifications at c) 0.9 wt%; d) 1.2 wt% (targets). .....	147
Figure 5.30 Optical images of the 10Mg alloy with Bi modifications at a) 0 wt%; b) 0.7 wt% (targets). Black holes are porosities. ....	148
Figure 5.30 (Continued) Optical images of the 10Mg alloy with Bi modifications at c) 1.0 wt%; d) 1.3 wt% (targets). Black holes are porosities. ....	149
Figure 5.31 Two Bi-bearing phase morphologies (SEM – BSE) observed from the polished sections: a) Rod-shaped (6Mg-0.6Bi) and b) Snowflake-shape (10Mg-1.3Bi). ....	150
Figure 5.32 SEM Linescan (~25.1 $\mu$ m) determining the bismuth-bearing phases in a gap between two growing branches of one Mg <sub>2</sub> Si crystal (10Mg-1.3Bi). ....	151
Figure 5.33 Bismuth-bearing flakes segregating on the Mg <sub>2</sub> Si crystal surfaces observed at a tensile fracture site of 6Mg-0.6Bi. ....	153
Figure 5.34 Examples of the low magnification fracture surface for a) Circular tensile specimen (10Mg-T6); and for b) Rectangular tensile specimen (6Mg-1.2Bi); and for c) Rectangular tensile specimen A390. Crack initiations in samples are indicated by arrows.....	155
Figure 5.35 Defects often occurring in fracture surfaces as: a) Porosities; b) Porosity-related secondary crack in 10Mg alloy of a rectangular section sample. ....	157
Figure 5.35 (Continued) Defects occurring in fracture surfaces as: c) $\alpha$ -Al dendrite-related shrinkage cavity (circular specimen, A390); d) Impurity or oxidation particles distributing in an area where an intergranular fracture took place (rectangular specimen, 6Mg-0.6Bi). ....	158
Figure 5.36 a) Multiple cleavages in one primary Si phase for circular A390 tensile fractures after T6 heat treatment; b) Schematic of cleavage modes and cleavage plane; c) Tearing interface (Brookes & Choudhury, 1993). ....	159
Figure 5.37 Primary Si cleavages of circular A390 (T6) test specimens: a) A typical grain boundary slowing down the crack propagation. ....	161

Figure 5.37 (Continued) Primary Si cleavages of b) circular A390-T6 test specimens: A block-like cracks; and of c) circular A390 test specimens: A spiral crack propagation in a single Si crystal.....	162
Figure 5.37 (Continued) Primary Si cleavages of d) Circular A390 test specimens: Herringbone structure from plane cleavage; and of e) Circular 6Mg test specimens: A cascading pattern fracture. ....	163
Figure 5.38 Primary $Mg_2Si$ cleavages observed at as cast circular tensile specimen fracture surface: both a) and b) 6Mg alloys.....	164
Figure 5.38 (Continued) Primary $Mg_2Si$ cleavages observed at the rectangular tensile specimen fracture surfaces: c) 10Mg-1.3Bi; and d) 6Mg-0.6Bi.....	165
Figure 6.1 Primary Si cleavages in circular tensile specimens of A390: a) Massive Si crack; and b) traceable cleavage origin. ....	168
Figure 6.1 (Continued) Primary Si cleavages in circular tensile specimens of A390-T6: c) Star-shaped Si crystal cracking; and d) Lamellar illustration. ....	169
Figure 6.2 Primary $Mg_2Si$ related faceted cleavage fractures in rectangular tensile bars: a) Similar fracture surfaces (6Mg) to Si; b) Cleavage along dendrites (10Mg). ...	170
Figure 6.2 (Continued) Primary $Mg_2Si$ related faceted cleavage fractures of alloy 6Mg-0.6Bi from rectangular tensile bars: both c) and d) Radial marks. ....	171
Figure 6.3 SEM mapping of the primary $Mg_2Si$ (dendrites) related faceted cleavage fractures associating with the image Figure 5.40 b).....	172



## List of Tables

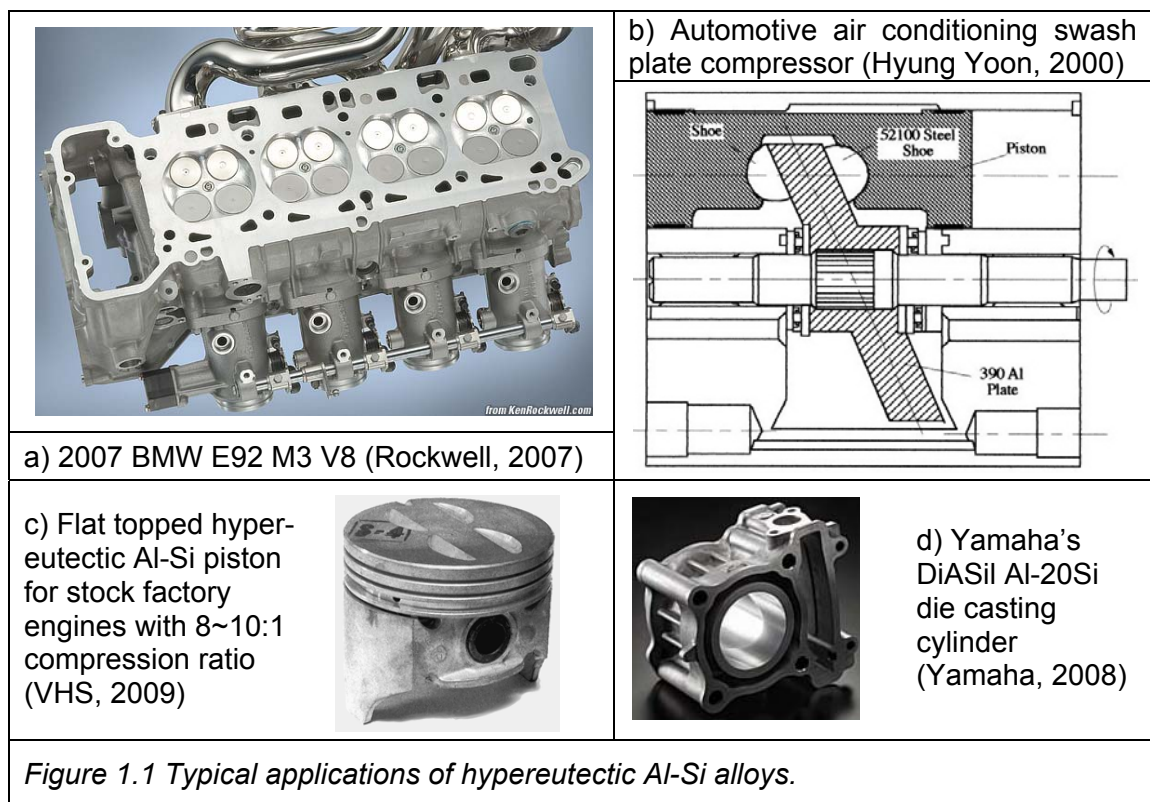
Table 2.1 AA-standard A390 alloy composition .....	8
Table 3.1 A390 ingot composition (source: UQAC) .....	42
Table 4.1 The comparison of crystal structure and properties between Si and Mg <sub>2</sub> Si ....	55
Table 4.2 The summary of phase equilibrium decompositions in all transition points for Mg added A390 alloys (FactSage, Equilibrium). ....	72
Table 4.3 The summary of equilibrium phase fraction solids in all transition points for Mg added A390 alloys (FactSage, Equilibrium). ....	72
Table 4.4 The summary of phase scheil cooling decompositions in all transition points for Mg added A390 alloys (FactSage, Equilibrium). ....	73
Table 4.5 The summary of scheil cooling phase fraction solids in all transition points for Mg added A390 alloys (FactSage, Equilibrium). ....	73
Table 5.1 A summary of the melt oxide film forming along with Mg addition in an Al-Mg alloy system.....	85
Table 5.2 An estimation of the density, porosity, and weight reduction for Mg added A390 alloys.....	115
Table 5.3 An estimation of the micro-hardness for $\alpha$ -Al matrix and the RockWell B hardness for bulk material of Mg added A390 alloys under as cast and T6 conditions. ....	118
Table 5.4 RockWell B hardness measurements of the rectangular Mg added A390 tensile bars with and without modifications. ....	121
Table 5.5 Tensile properties of the circular Mg tensile bars for both as cast and T6 conditions. ....	127
Table 5.6 Tensile properties of the rectangular Mg added tensile bars with and without structure modification additions. ....	130
Table 9.1 The casting chemical compositions reported by the LAB ÉLITE LTÉE.....	184

## CHAPTER 1. Introduction

### 1.1. Project overview

The typical hypereutectic Al-Si alloy is A390 (Al-17Si-4.5Cu-0.5Mg) which usually serves where the high wear properties are required, especially in the automobile industry, such as for engine blocks, air compressors (swash plate), rotary engine side housing, master brake cylinders, pistons, auto transmission pump bodies. Figure 1.1 lists some typical applications of this type of alloy. Due to the hard primary Si phase in the aluminum matrix and its low thermal expansion coefficient (T.E.C.), the alloy A390 has excellent wear resistance, a high Young's modulus for combined high strength and hardness for varying temperature conditions, and also good castability (Jorstad, 1996). In a new series of high Mg content alloys (Al-17Si-4.5Cu-xMg), the  $Mg_2Si$  precipitate becomes predominant during the solidification and replaces the primary Si phase, which also results in excellent wear properties. By comparing with silicon crystals, magnesium silicide ( $Mg_2Si$ ) is found to have a similar crystal structure (FCC cubic) and physical/ mechanical properties but, of a lower density, which contributes to weight reduction for automobile applications (up to 4.9 wt% saving with 10 wt% Mg addition). It was also observed that the common acicular Al-Si eutectic morphology is considerably modified to form finer and more skeleton fibre structures due to the pronounced  $Mg_2Si$  crystals appearing in the alloy matrix. Consequently, these new alloys have demonstrated more interesting

features in both weight saving and the enhancement of mechanical properties. More research to overcome casting difficulties relating to porosity, inclusions etc. needs to be addressed in order to determine the optimal casting conditions before introducing these alloys to present production.



## 1.2. Objectives

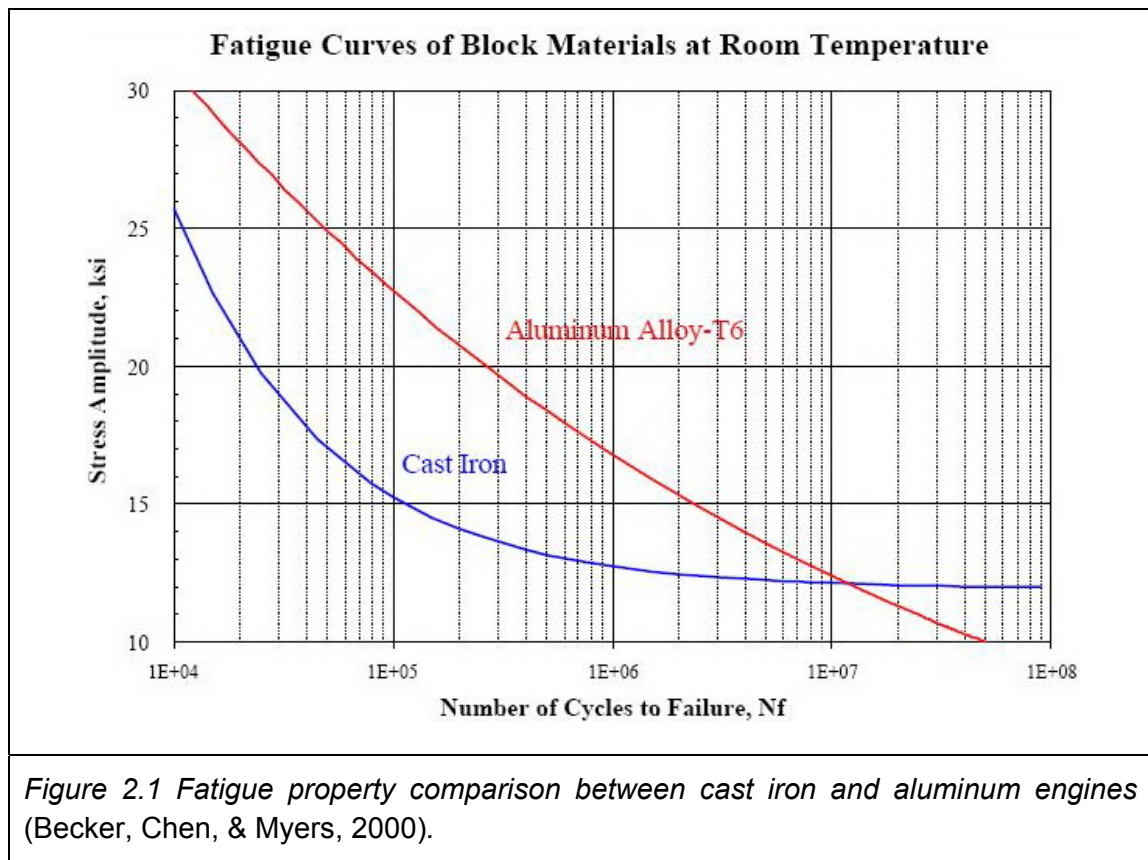
The scope of this study consists of the determination of the alloy castability, mechanical properties, microstructural modifications, and fracture analysis that result from introducing the Mg content to the conventional hypereutectic Al-Si alloy. In order to achieve these objectives, the experimental work is thus carried

out by a complete thermodynamic investigation, casting practice and property measurement, as well as a detailed analysis of the microstructural features of the fracture surface.

## CHAPTER 2. Literature reviews

### 2.1. Historical perspective of A390 alloy

Alloy A390 (Al-17Si-4.5Cu-0.5Mg, weight basis), is the first of hypereutectic Al-Si alloys (Jorstad, 1996), and features exceptional performance characteristics including the excellent wear resistance, the low thermal expansion coefficient, and the melt good fluidity due to excessive Si presence. This alloy was not exploited before the 1970's because the hard primary Si phase considerably reduces tool life during machining.



General Motors Corporation first introduced this alloy in producing the linerless Chevrolet Vega engine block using the bare-bore technology in 1971. Since then, the conventional iron-liner cylinders were progressively redesigned to adopt this new alloy development in the high-end linerless blocks for greater performances. Weight saving, outstanding sealing, better dimensional stability, enhanced thermal dispersion, lower friction, durability, and easier recyclability were achieved when compared to the original iron-liner engines (Meara, 2008). Figure 2.1 indicates that the fatigue results from the Al-Si diesel engine block are quite comparable to the cast iron block, but with a weight saving up to 25 wt% (Becker, Chen, & Myers, 2000). In addition, the machining problems were solved by introducing polycrystalline diamond cutting which have a prolonged tool life (Hatch, 1984). Machining A390 alloy results in short chips and produces a high-quality surface finish (MAC, 2005).

Research and development for the production of A390 alloy engines by KS Aluminum-Technologie AG has produced the Alusil® and Lokasil® for Audi and Volvo's engines. DaimlerChrysler AG developed its Silitec® cast-in aluminum liners based on powder metallurgy (KS Aluminum-Technologie AG, 2007) and Mahle GmbH has applied its trademark ALBOND® for the cylinder liner compound with a rough exterior surface (MAHLE, 2007). Brunswick Corporation uses its Mercosil® technology in the Mercury Marine applications (Donahue & Fabiyi, 2000) and Yamaha has developed DiASil® for the new 150cc YZF-R15

by using the Yamaha CF<sup>a</sup> Aluminum Die-cast Technology (Rearset). Without any exception, all these high end engines require both lighter weight and the closer land width<sup>b</sup> between the cylinder bore, thus generating higher horsepower. The land width for the cast-in iron liner engines of the Volvo® in-line 5 cylinder diesel block shown in the Figure 2.2-c). However, most manufacturers prefer to fabricate the integral linerless engine blocks using only A390 alloy via the LPDC<sup>c</sup> process, further reducing the weight and improving the recyclability. The land width of A390 alloy cylinder as low as 5.5 mm is achieved for the Audi® linerless cylinder blocks for its V6 and V8 engine generations as illustrated in Figure 2.2-a). Moreover, the cylinder bore surface has excellent wear characteristics due to the extremely hard Si phase particles in A390 alloys, compared to the cast iron liners. The bare bore technology enables the primary silicon particles to protrude ever-so-slightly from the surface (Jorstad, 1996) by removing the soft aluminum matrix around it by chemical etching or by mechanical elastomer-bond exposure in order to maintain 0.5~1  $\mu\text{m}$  protrusion of the Si crystal above the matrix phase (Figure 2.2-b) (Meara, 2008). The working pistons, therefore, are in contact with the silicon surfaces, resulting in the super oil lubrication due to the available spaces among silicon crystals.

Hypereutectic Al-Si alloy pistons are one of these developments, offering an incredible piston-to-wall clearance with a typical value of one thousandth inch

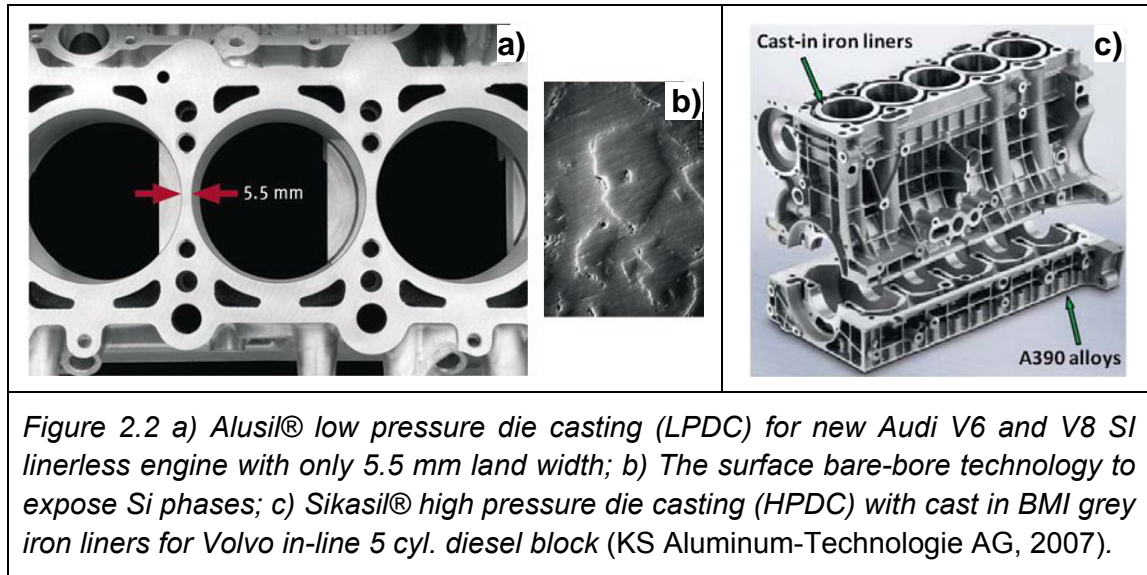
---

<sup>a</sup> CF – Abbreviation of Controlled Filling.

<sup>b</sup> Land width: The cylinder wall thickness between neighbouring bores.

<sup>c</sup> LPDC: Abbreviation of Low Pressure Die Casting

due to the silicon's low thermal expansion property. There is no doubt that the unburned hydrocarbons above the top ring, the emissions, and the noise level can be minimized by employing this type of piston.



In addition, A390 alloy has many other applications including housings for chain saws for small engines, computer disc spacers, air conditioning compressor related components (i.e. bodies, swash plates etc.), pump covers and center supports, master break cylinders, auto transmission parts, rotary engine side housings, and clutch input housings etc. (Jorstad, 1996) (Hatch, 1984). These components can be typically formed by both permanent mould casting and high or low pressure die casting. Standards suggest the alloy A390 with a composition specified in the Table 2.1. The excellent mechanical properties can be traced to the alloying elements (copper and magnesium) corresponding to the intermetallic binary phase  $\theta$ -Al<sub>2</sub>Cu and quaternary compound Q-



$\text{Al}_5\text{Cu}_2\text{Mg}_8\text{Si}_6$  (Backerud, Chai, & Tamminen, 1990) which can strengthen the alloy after heat treatment due to their precipitation hardening effects. A small amount of iron addition enables an easier demoulding of die castings. However, the detrimental acicular  $\beta$ - $\text{Al}_5\text{FeSi}$  phase, readily formed, can degrade alloy properties, must also be minimized.

*Table 2.1 AA-standardd A390 alloy composition* (Backerud, Chai, & Tamminen, 1990)

Alloy	Al	Si	Fe	Cu	Mn	Mg	Zn	Ti
A390.1 <sup>e</sup>	Bal.	16.0-18.0	0.40	4.0-5.0	0.10	0.50-0.65	0.10	0.20

## 2.2. Solidification behaviour of hypereutectic Al-Si alloys

### 2.2.1. General solidification characteristics

Final components, made either by the conventional casting process, i.e. as cast, or by the mechanical forming technique such as forging, rely mainly on the solidification structures of its original materials to achieve satisfactory properties. Both the alloy composition and the heat flow conditions need to be carefully controlled (Stefanescu, 1988). Efforts to achieve this goal become quite necessary throughout the solidification process of an alloy by contributing to the reduction of the casting defects (i.e. porosities, shrinkage etc.).

<sup>d</sup> AA standards – Aluminum Association casting alloy designation system.

<sup>e</sup> A390.1 – Under AA standards, “A” means the first variation in the composition limits comparing to the first version of alloy 390”; “3xx.1” indicates standard ingots (John Gilbert Kaufman, 2004).

#### 2.2.1.1. Chemical thermodynamics and kinetics

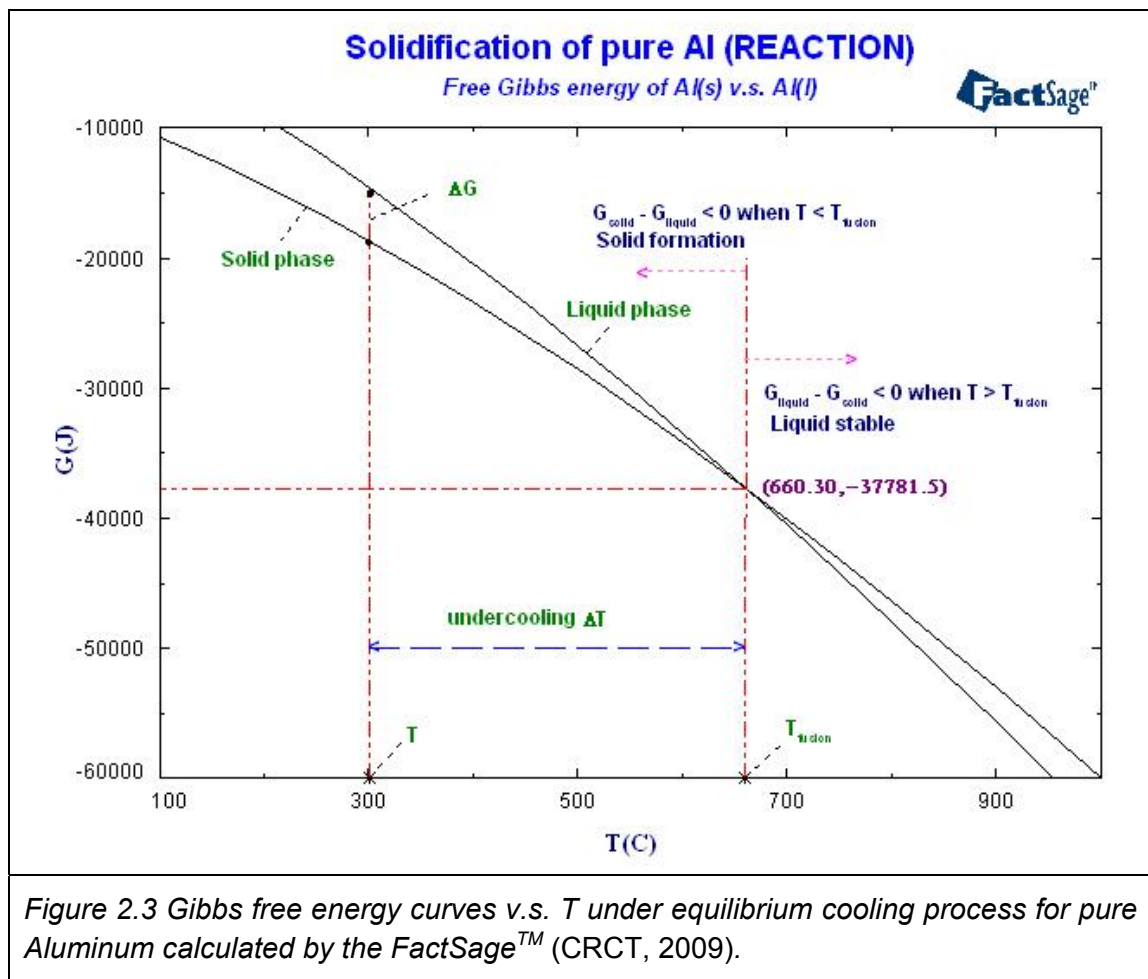
During the solidification from a melt, chemical thermodynamics and kinetics are generally considered in terms of the enthalpy and Gibbs free energy changes, the solidification path, composition changes, and phase transformations etc.. Chemical thermodynamics describes the most stable phases at equilibrium conditions (i.e. temperature, pressure, compositions etc.) relating to only the initial and final states of a system. Accordingly, the solidification rate in a metallurgical system can be estimated by the enthalpy ( $H$ ) and heat capacity ( $C_p$ ), and how these thermodynamic properties reflect the system thermal state and heat energy requirements. Chemical equilibrium is controlled by the Gibbs free energy ( $G$ ) of the system which is minimized for equilibrium conditions. In contrast, the dynamic system transformation between initial and final states controlled by chemical kinetics, indicates the path and phase changes of a chemical reaction in a system when the limited atomic movement (i.e. in solids, low temperatures, etc.) becomes dominant in a short process time. Hence the solidification rate under a real time condition will be greatly influenced by the nucleation efficiency and the atom diffusion between phases (Stefanescu, 1988).

For any pure substance (i.e. pure Al in this case), the Gibbs free energy ( $G$ ) is a function of temperature ( $T$ ) instead of other two parameters (composition and pressure). The plot of Gibbs free energy curve for the pure aluminum is

illustrated in the Figure 2.3. The solid phase attains below the fusion point ( $T_f = 660.30^\circ\text{C}$ ) and the liquid phase is above the melting temperature since the most stable phase occurs at a temperature with the lowest Gibbs free energy. Meanwhile, the equilibrium state of the solid and the liquid is achieved at the temperature  $T_f$  where two curves intersect. Consequently, the Gibbs free energy change  $\Delta G_f$  of a pure metal (Al in this case) can be described as  $\Delta G_f = \Delta H_f - T\Delta S_f = 0 \therefore \Delta H_f = T\Delta S_f$  where  $\Delta H_f$  is the enthalpy change between the solid and liquid and  $\Delta S_f$  is the entropy changes between the solid and liquid. Any temperature  $T$  other than  $T_f$ ,  $\Delta G_f \neq 0$ , and thus the combination of above two equations can be described as  $\Delta G_f = \frac{\Delta H_f(T_f - T)}{T_f} = \frac{\Delta H_f \Delta T}{T_f}$  (George F., 2004). When the free energy decreases where  $T < T_f$  (see Fig.2.3), the driving force of the solidification is proportional to the undercooling  $\Delta T$ , forming the stable solid from an undercooled liquid in a metastable state.

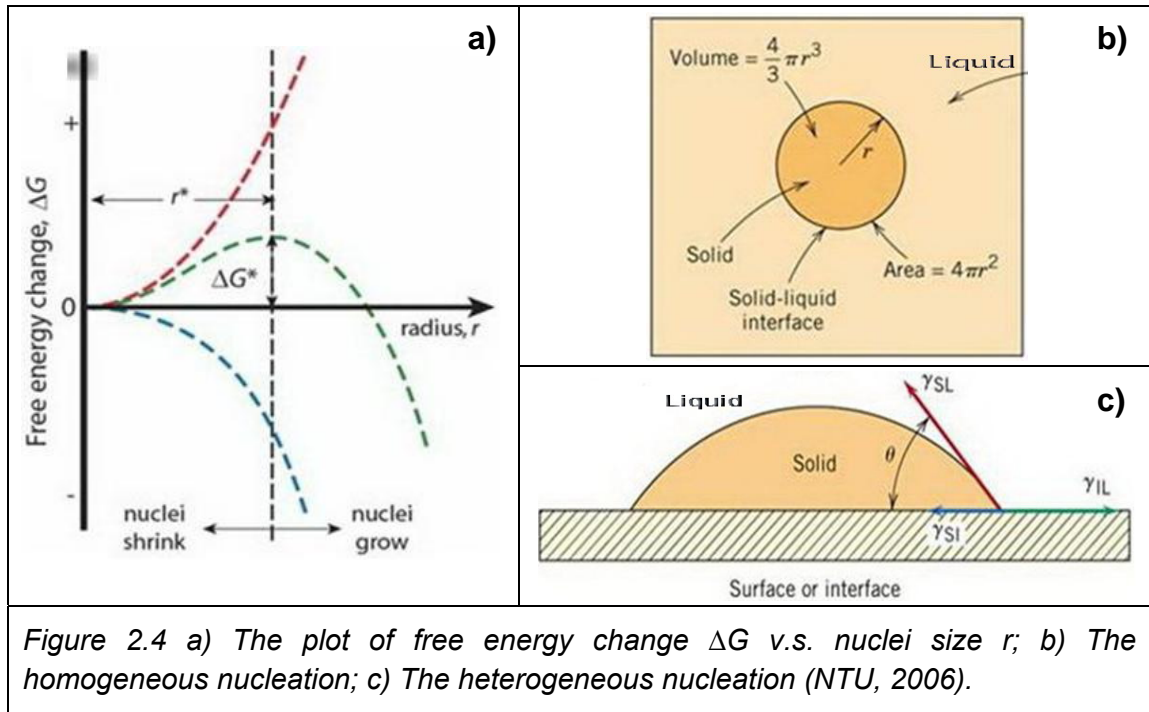
However for an alloy, the determination of the Gibbs free energy for a phase becomes more complex since the composition factor must be considered in addition to the temperature. Consequently, a thermodynamic solution model is used to represent the molar free energy change  $\Delta G_m$  for the case of an alloy with variable compositions. At a given composition, the molar free energy is established as a function of the chemical potential  $\mu_i$ , which strongly depends on the range of composition and temperature in all phases of an alloy. Moreover, “when two or more phases are in equilibrium, the chemical potential of any

component is the same in all phases (Pelton, 2001).” This implies the basic principle for all phase equilibrium.



#### 2.2.1.2. Nucleation mechanisms

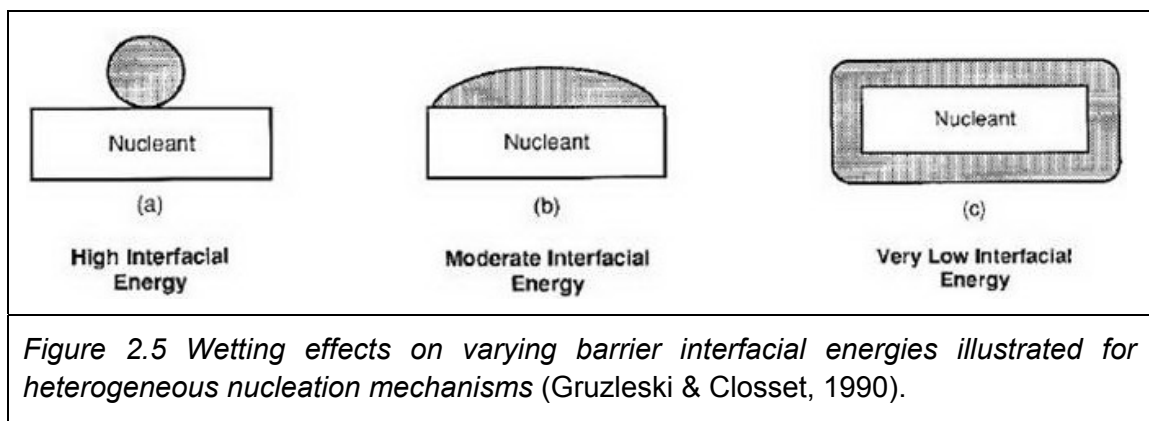
Nucleation, an important term for the solidification process, is thermodynamically initiated by forming stable atom clusters from the surrounding undercooled liquid. In general, a nucleus interfacial energy offers an activation energy  $W$  to stabilize the nucleation either homogeneously or heterogeneously (Figure 2.4-b, c).



In fact, the activation energy of spontaneous nucleation can be considered as a function of the surface and volume energy changes:  $W = \Delta G_S + \Delta G_V = 4\pi r^2 \gamma_{SL} - \frac{4}{3}\pi r^3 \Delta H_f \frac{\Delta T}{T_m}$  where  $\Delta G_S, \Delta G_V$  are the surface and volume free energy,  $\gamma_{SL}$  is the unit solid-liquid interface energy,  $\Delta H_f$  is the change of latent heat of fusion,  $r$  is the nuclei size,  $\Delta T$  is the undercooling and  $T_m$  is the fusion point. To increase the undercooling  $\Delta T$  is the more direct means to minimize the total Gibbs free energy for homogeneous nucleation.

At the very beginning of the nucleation, the precipitated phase attains its size at only an atomic scale, which represents an extremely high activity in terms of the chemical potential. Furthermore, the spontaneous nucleation takes place once

the high enough supersaturation for the nuclei formation is generated from the homogeneous melt (Stefanescu, 1988). A large undercooling ( $\sim 100\text{K}$ ), which provides the driving force for the nucleation, is thus required to achieve the critical nuclei size  $r^*$  (Figure 2.4–a). The nucleus shrinks (melting) if its size is under the critical value, whereas it grows if the size is larger than  $r^*$  since the lower free Gibbs energy is also met (Pekguleryuz, 2007).

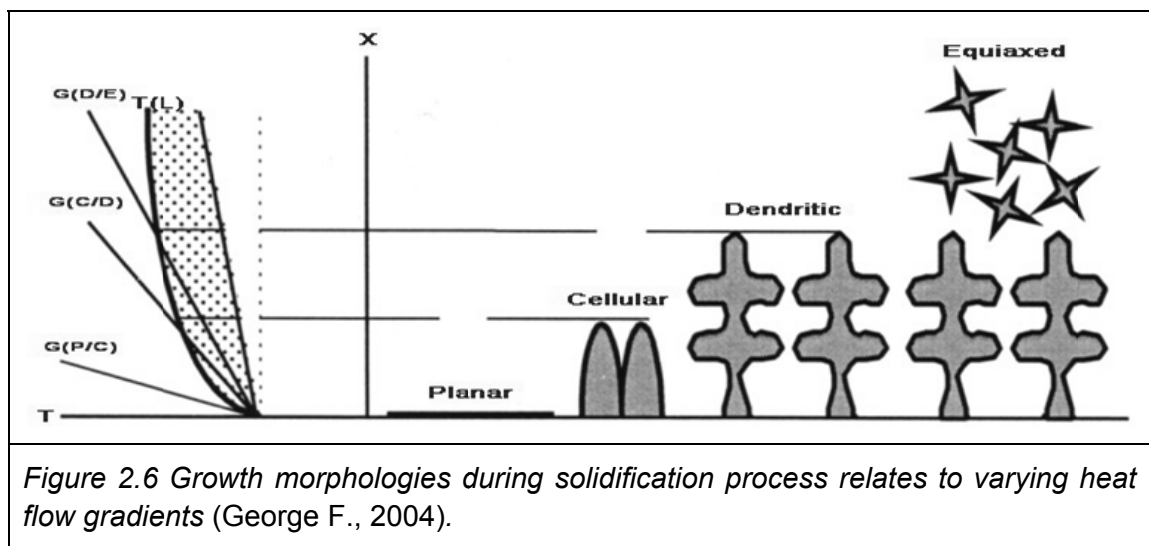


Nevertheless, the interfacial energy can also be reduced during heterogeneous nucleation (Figure 2.4–c) and Figure 2.5) in the presence of catalytic surfaces, i.e. mould walls, and/or inclusions, as well as grain refiners such as  $\text{AlB}_2$ ,  $\text{TiB}_2$ ,  $\text{AlP}$  in  $\text{Al-Si}$  alloy system etc., or other existing non-equilibrium defects (i.e. grain boundaries, dislocations, free surfaces, etc.) which are introduced to a melt before the solidification. The heterogeneous mechanism alters interfacial energy via the introduced nuclei which requires only  $\sim 5\text{K}$  undercooling, resulting in a great potential to save foundry cost (Pekguleryuz, 2007). Obviously, the grain refiner provides the most effective wetting condition (i.e. Figure 2.5 - b) or c) in

the solidifying melt by depressing the solid-liquid interfacial energy  $\gamma_{SL}$ , leading to a lowest free energy state. This wetting effect is mainly caused by the atomic mismatch between the solid and liquid interfaces such as  $\text{Al}_3\text{Ti}$  (peritectic reaction related) or  $\text{AlB}_2$  (stable particles) used for aluminum casting alloys, to achieve a finer structure. Consequently, the heterogeneous nucleation is readily achievable in practice (Gruzleski & Closset, 1990).

### 2.2.1.3. Growth and crystal morphologies

As soon as the nucleation is stable, the growth takes place on further cooling during the solidification process depending on the alloy composition and the heat flow condition. When there are more atoms joining the solid nuclei than leaving the solid-liquid interface, the phase transformation of liquid to solid can occur for either positive or negative temperature gradients in the liquid. This phenomenon can be explained by constitutional undercooling.



In general, phase growth occurs at the solid/ liquid interface where the varying morphologies are formed in the direction of heat flow, depending on the cooling rate (Figure 2.6). Planar growth results for near equilibrium conditions (low growth rate or high temperature gradient), when the interface grows at a constant rate. Cellular and dendritic growth occurs if the growth rate for planar is exceeded. Solute segregation then takes place in the solid phase, where the temperature of the leading edge is higher than its root. Dendrite formation cannot be avoided when the growth rate of interface is higher than that of the cellular mode. Dendrites are a common morphology present in the cast alloys and have a great influencing on the material properties such as toughness, strength, corrosion resistance. Dendritic structures are subsequently produced when accumulated heat and solute gradients build up in the front of interface along the heat flow direction, forming a supercooled zone to change the unstable cells from circular cross section to become maltese serrations as the secondary arms (Figure 2.7-b). The growth of secondary branches of dendrites causes dendrite coalescence, leading to the grain formation where the high solute content is trapped in the interdendritic space (Figure 2.7-a). As well, the equiaxed structure can be obtained for a supercooled solidification condition resulting from any perturbation in which the melt closest to the dendrite growing front could form a undercooled region, combining with the nuclei present (Stefanescu, 1988).



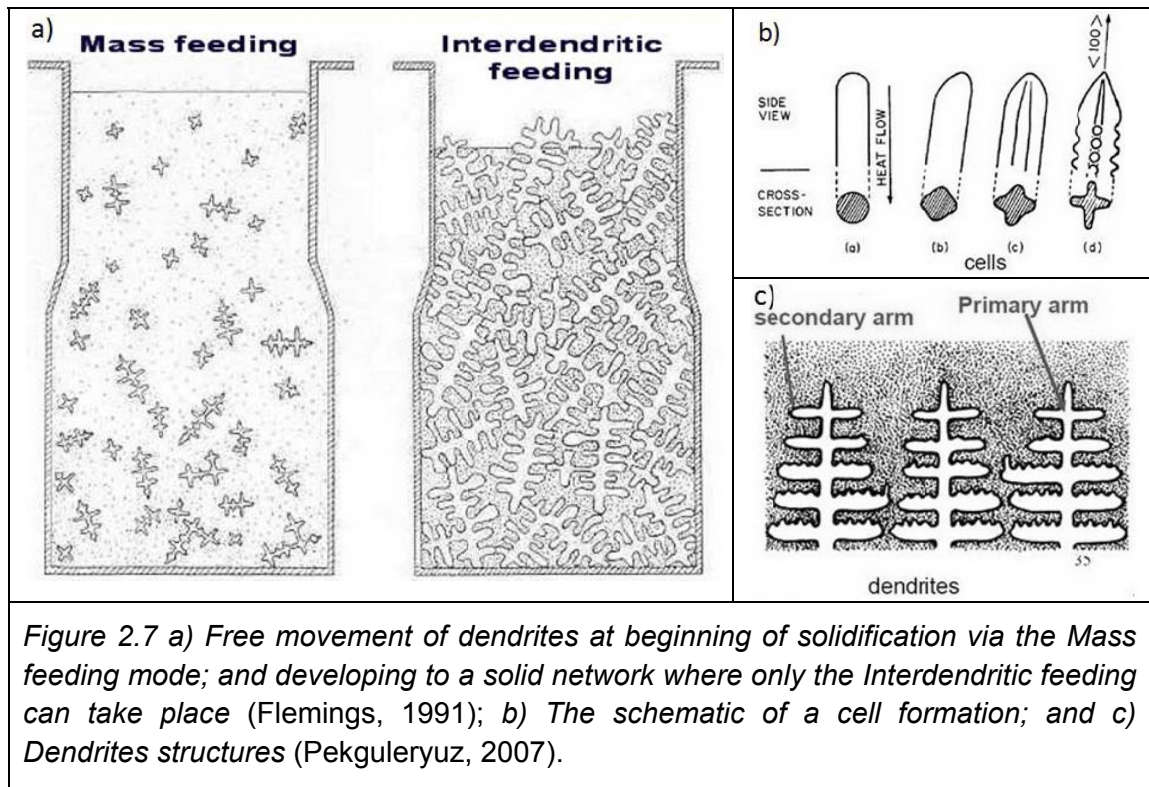


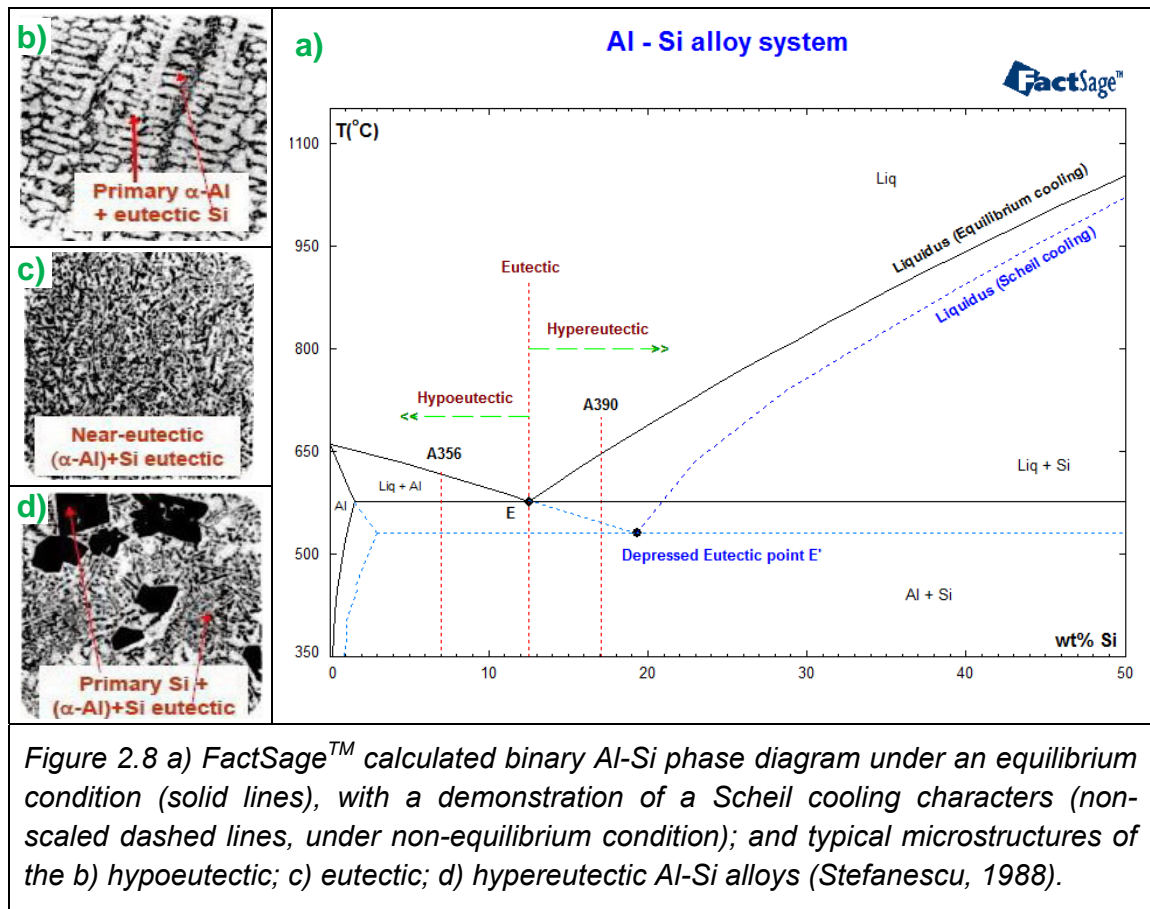
Figure 2.7 a) Free movement of dendrites at beginning of solidification via the Mass feeding mode; and developing to a solid network where only the Interdendritic feeding can take place (Flemings, 1991); b) The schematic of a cell formation; and c) Dendrites structures (Pekguleryuz, 2007).

Dendrite arms with smaller radius may remelt into the molten liquid along with the decreasing total interfacial energy. The Ostwald–ripening effect on the formation of Dendrite Arm Spacing (DAS, Figure 2.7-c) is determined by local solidification time, allowing smaller particles to grow and merge into the larger ones due to the reduced total surface energy in the system. Dendrite Arm Spacing (DAS), which is proportional to  $(AverageCoolingRate)^{-n}$  where  $n = 1/2$  and  $1/3$  for the primary and secondary dendrites respectively, generally ranging from 10 to 150 mm and which are controlled mainly by the solidification rate (Pekguleryuz, 2007). These dendrites can be cracked by introducing mechanical or magnetic stirring or ultrasound vibration in the semi-solid state. To gain an

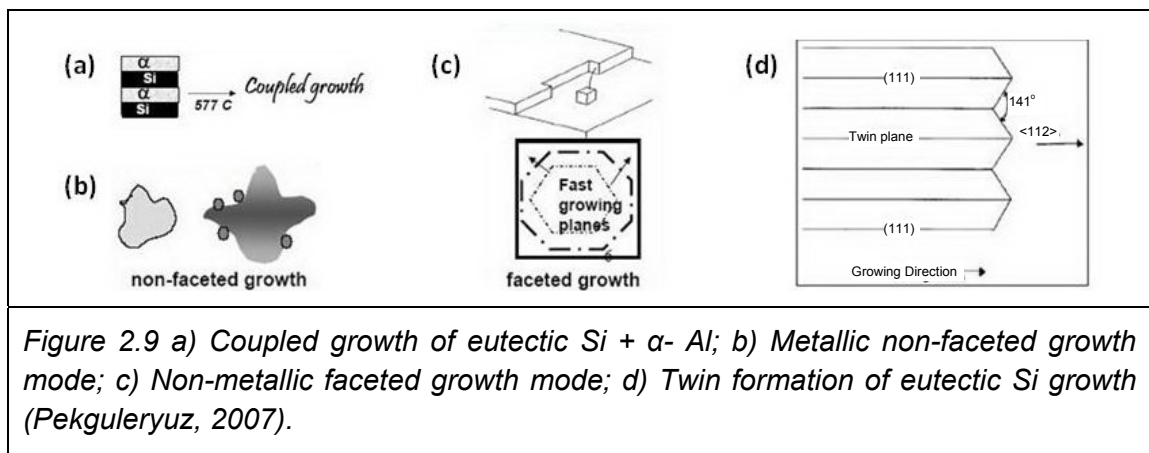
optimum property of an alloy, the DAS therefore must be minimized and distributed homogeneously.

### 2.2.2. Solidification behaviour of hypereutectic Al-Si alloys

The equilibrium binary Al-Si phase diagram is shown in Figure 2.8-a) where all thermodynamic calculations in an Al-17Si-4.5Cu-xMg alloy system were performed by the FactSage™ (CRCT, 2009). Dashed lines indicate the Scheil cooling solidification behaviour as an illustration (non-scaled).

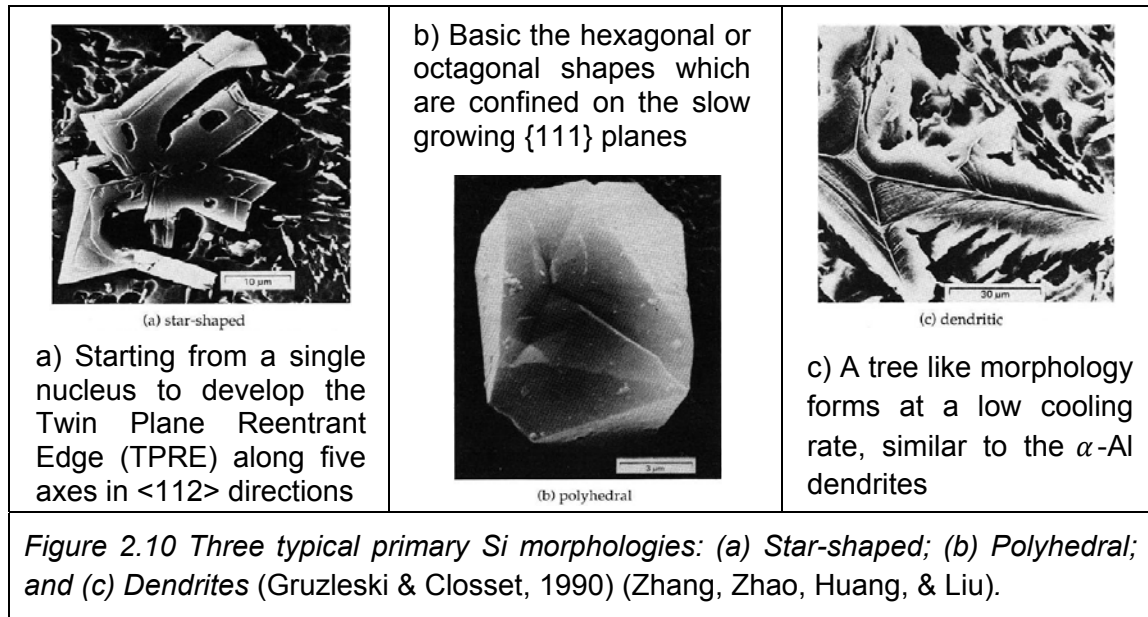


As observed in this binary phase diagram, the eutectic composition was calculated to be ~12.7 wt% Si where a eutectic microstructure of  $\alpha$ -Al + Si solidifies (Figure 2.8-c)). The solidified hypoeutectic Al-Si alloy (i.e. A356) consists of the primary  $\alpha$ -Al dendrites and the eutectic phase (Figure 2.8-b)).



However, the non-equilibrium solidification behaviour of the hypereutectic alloy (i.e. A390) is found to be different from the equilibrium case as illustrated in Figure 2.8-a)). The microstructure includes primary  $\alpha$ -Al but also primary Si and the eutectic phase (Figure 2.8-d)). For this condition, primary Si will be the first phase to be solidified (regardless of the Cu and Mg etc.), resulting in a liquid composition in rich in Al. As the Al concentration increases, the local ratio of Si to Al decreases from its hypereutectic composition until a new eutectic point is reached. In other words, the equilibrium eutectic point E has been shifted to point E' (depressed eutectic), as demonstrated in the phase diagram for the Scheil cooling solidification of A390. The Si in contact with the  $\alpha$ -Al phase

favours the eutectic reaction to take place (Gruzleski & Closset, 1990).



In Al-Si alloys,  $\alpha$ -Al and Si phases to form a binary eutectic structure as shown in Figure 2.9-a). The growing crystal consists of the non-faceted metallic mode (i.e.  $\alpha$ -Al, Figure 2.9-b), which grows randomly, and the faceted non-metallic mode (i.e. Si, Figure 2.9-c), which grows along specific planes. For normal solidification, the eutectic Si morphology grows in a faceted mode to an acicular structure via a twin formation along  $\langle 112 \rangle$  direction to cross the  $\{111\}$  planes with a  $141^\circ$  twin re-entrant angle in the form of twinned platelets (Figure 2.9-d). This results in a low ductility where cracks spread rapidly the brittle Si phases (Pekguleryuz, 2007). The acicular morphology of eutectic Si might be modified to finer fibrous structure by introducing a certain amount (p.p.m. level) of sodium (Na) or strontium (Sr).

Faceted morphology growth can occur in an anisotropic mode for high entropy phases where the solid/liquid interface is smooth on the atomic scale. Primary silicon crystallization however results in complex shapes depending on the solidification rate, local liquid composition and temperature gradient, in the form of star-shaped, polygonal, or dendritic structure (Figure 2.10-a/b/c). Under slow cooling conditions, coarse Si particles can form on only few effective nuclei since most of impurities in do not initiate Si nucleation (Gruzleski & Closset, 1990). (Weiss, 1987) reported that the primary Si in either polygonal or star-shaped can act as a seedbed to epitaxially grow the eutectic Si along the preferred directions (i.e. edges, corners, etc.).

### **2.3. Control of alloy qualities**

In practice, the solidification behaviour of hypereutectic Al-Si alloys becomes more complex with the introduction of alloying elements, i.e. 4.5 wt% Cu, 0.5 wt% Mg to A390. Although the hypereutectic Al-Si alloy system attributes unique casting and mechanical properties to the excessive Si, more care must be taken to reduce the effect of the large primary Si crystals, acicular eutectic Si precipitates, needle-liked iron intermetallic phases, and overall particle distributions on alloy performance. Also, the minimization of casting defects (i.e. porosities, inclusions etc.) is another critical factor in controlling the quality of the final products. The ideal hypereutectic Al-Si casting consists of modified fine and uniform distributed structures which result in the improved dimensional stability

even at high temperatures, excellent wear resistance, and enhanced mechanical properties. Some solutions consisting of cast alloy designs (i.e. modifications; alloying; grain refinements; and secondary phase reinforcing additions) and casting treatments (i.e. melt degassing, cleanliness, and grain refining; cast condition alternatives; heat treatment) can be applied to the quaternary Al-Si-Cu-Mg alloy system of this study.

### 2.3.1. Effect of alloying elements

The microstructures and properties of the Al-Si alloys are very sensitive to the alloying elements, which may contain not only high amount of Cu and Mg but also low or trace level of Fe, Mn, Zn, Cr, Ni, P, Sr, Na etc.. Generally, they are specific additions that are designed to modify and improve the alloy properties or alloy impurities with no major detrimental effect. One or more specific elements are selected and quantified to optimize alloy performances (Zolotarevsky, Belov, & Glazoff, 2007).

Cu improves tensile strength, machinability, and thermal conductivity but decreases ductility and corrosion resistance. Al alloys with 4-5.5% Cu results in the best age hardening response and also enhances the stability of  $\alpha$ -Al phases for either semi-solid or thixoformable Al-Si castings. Mg is important for increasing strength and hardness in heat treated Al-Si alloys and mostly use in more complex Al-Si alloys containing Cu, Ni, and other elements. The

hardening-phase  $\text{Mg}_2\text{Si}$  is more heat treatable at  $\sim 0.70\%$  Mg addition. Beyond this content either no further strengthening occurs or matrix softening takes place. Usually, the Mg content is controlled under  $0.65\%$  in hypoeutectic Al-Si alloys to reduce formation of acicular  $\text{Al}_5\text{FeSi}$ . Iron additions up to  $1.5\text{--}2.0\%$  increase the hot tear resistance and decrease the tendency of die sticking or soldering in the die casting. Above this value, the iron produces iron-based intermetallic phases such as  $\text{FeAl}_3$ ,  $\text{FeMnAl}_6$ , and  $\text{Al}_5\text{FeSi}$  etc. which are the main sources of microcrack initiations. However, Mn somewhat modifies the structure of iron-contained intermetallic phases, leading to better ductility and shrinkage resistance. Alloys with Zn addition are also heat treatable and improve alloy strength, but has negative effects on shrinkage. Ni together with Cu offers a higher hardness and strength at elevated temperatures (Pekguleryuz, 2007) (Stefanescu, 1988) (Ye, 2003). Of those alloying elements, only Si, Mg, Zn, and Cu are considered as basic additions. Mn can also be added at a level of  $\sim 1\%$  Mn in Al-Cu alloys to increase the overall thermal stability, and can reduce the negative effect of Fe intermetallic compounds.

### 2.3.2. Cast structure refining

Coarse or acicular structures can occur during the casting process, resulting in unstable properties. Commonly cast Al-Si alloys consist of a microstructure of large size grains and  $\alpha$ -Al dendrites, acicular eutectic Si, coarse primary Si, and also other harmful intermetallic phases such as needle like  $\beta$ - $\text{Al}_5\text{FeSi}$ , with

uncontrolled and unevenly distributed porosities etc. (ASTM, 2006). The solutions, which have been consequently proposed by many other researchers, are mainly focused on grain refining and modifications by the physical, mechanical, or chemical methods summarizing briefly as below.

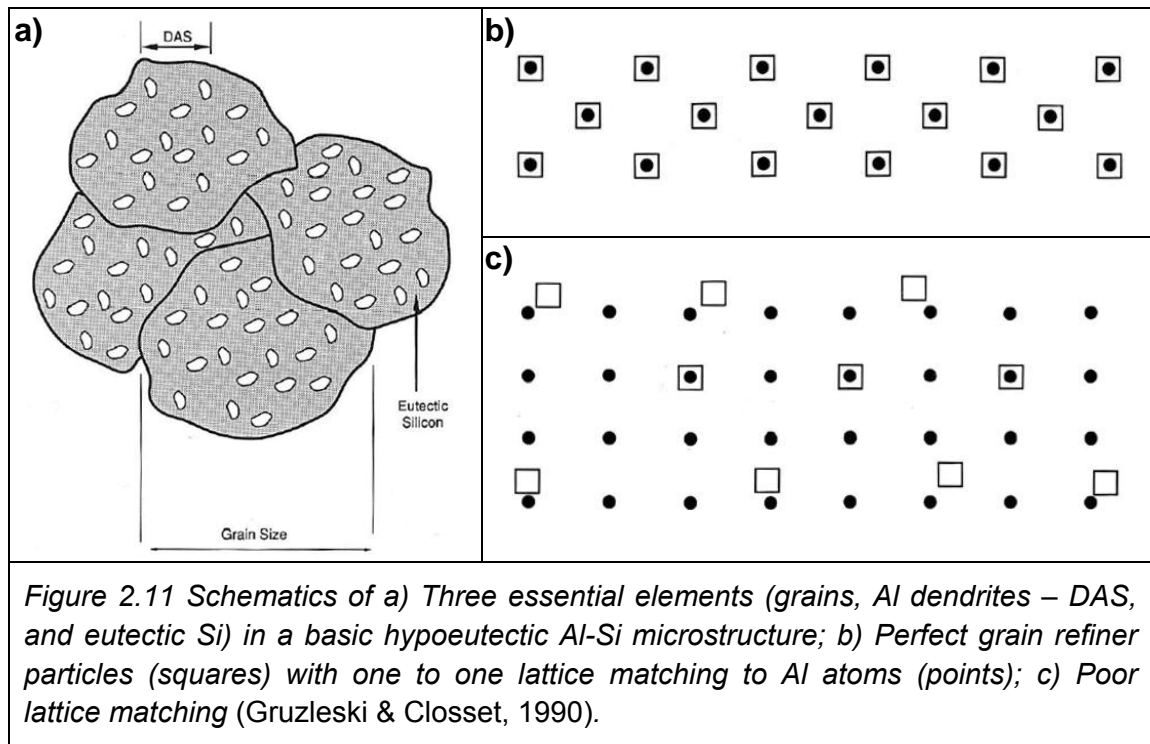
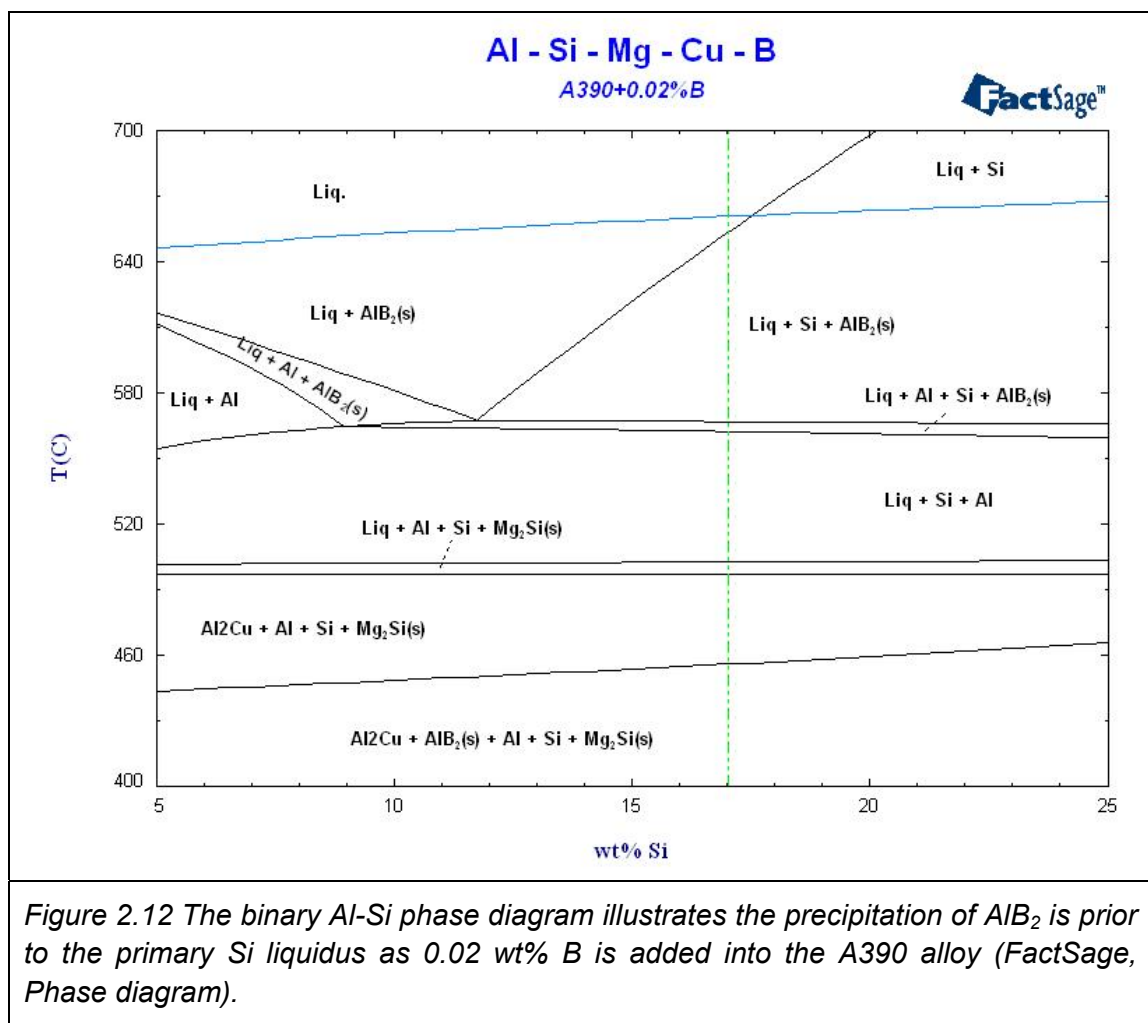


Figure 2.11 -a) indicates a basic structure of hypoeutectic Al-Si alloys consisting of grains (sizes at 1~10mm in general), dendrites (typical DAS – 10~150 $\mu\text{m}$ ), and eutectic Si which can be in acicular shapes as long as 2 mm or round particle as small as  $\phi 1\mu\text{m}$ . The DAS could be successfully reduced at higher cooling rates or by mechanic stirring. The acicular Si might be chemically modified to a fibrous morphology by using effective modifiers. Heterogeneous



nucleation should be the major approach to refine the grains, which nucleate on some of the foreign nuclei sites and grow slowly in the melt. Effective grain refiners, such as  $\text{TiAl}_3$  and  $\text{TiB}_2$ , must match their lattice perfectly coherently to the Al matrix with their lattice coherencies (Figure 2.11-b). In contrast, particles with a poor lattice matching have little influence on increasing the nucleation of grains (Figure 2.11-c), resulting in an unrefined grain structure (Gruzleski & Closset, 1990).



A major advantage of the grain refinement is the reduction of the cast hot tear tendency caused by large shrinkage porosities resulting from the lack mass feeding between the large dendrites (Pekguleryuz, 2007) (LSM, 1998). Titanium acts as the most effective grain refiner in an Al-Si alloy. It reacts with aluminum to form  $\text{TiAl}_3$  particles, which are quite favourable to nucleate on  $\alpha$ -Al, especially after a subsequent peritectic reaction of  $\text{Liq.} + \text{TiAl}_3 \rightarrow \alpha\text{-Al}$ . However, titanium is often used combining with boron ( $\text{Ti} : \text{B} = 2.22$ ) to further guarantee the process efficiency by which the boron coating protects the  $\text{TiAl}_3$  particles from early dissolution in the melt (Pekguleryuz, 2007).

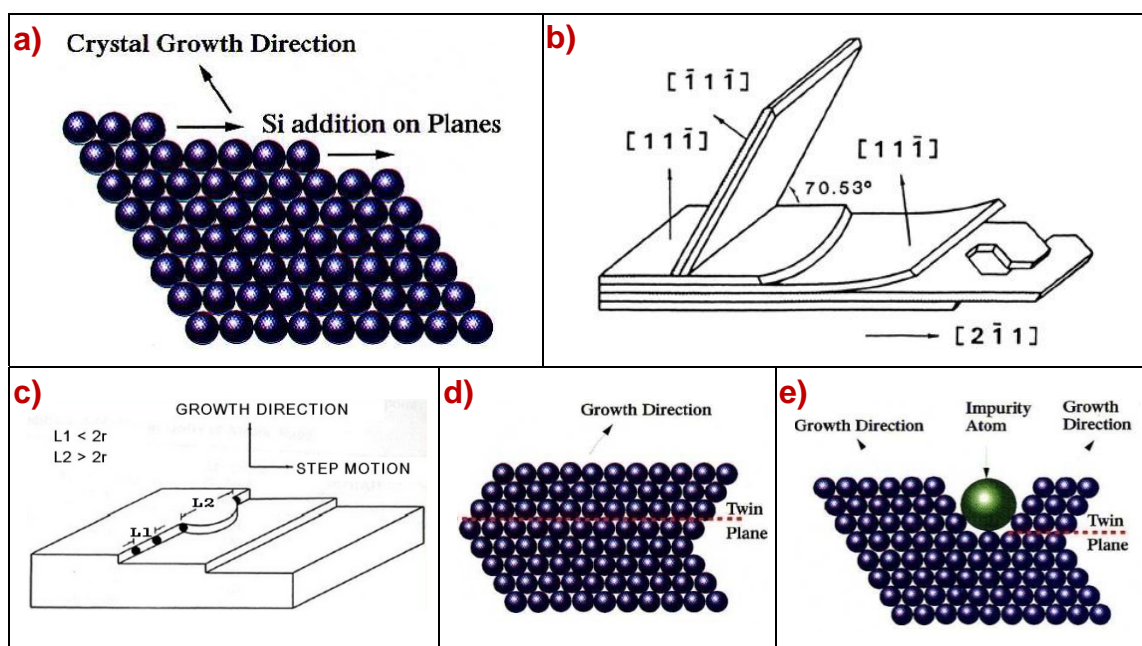
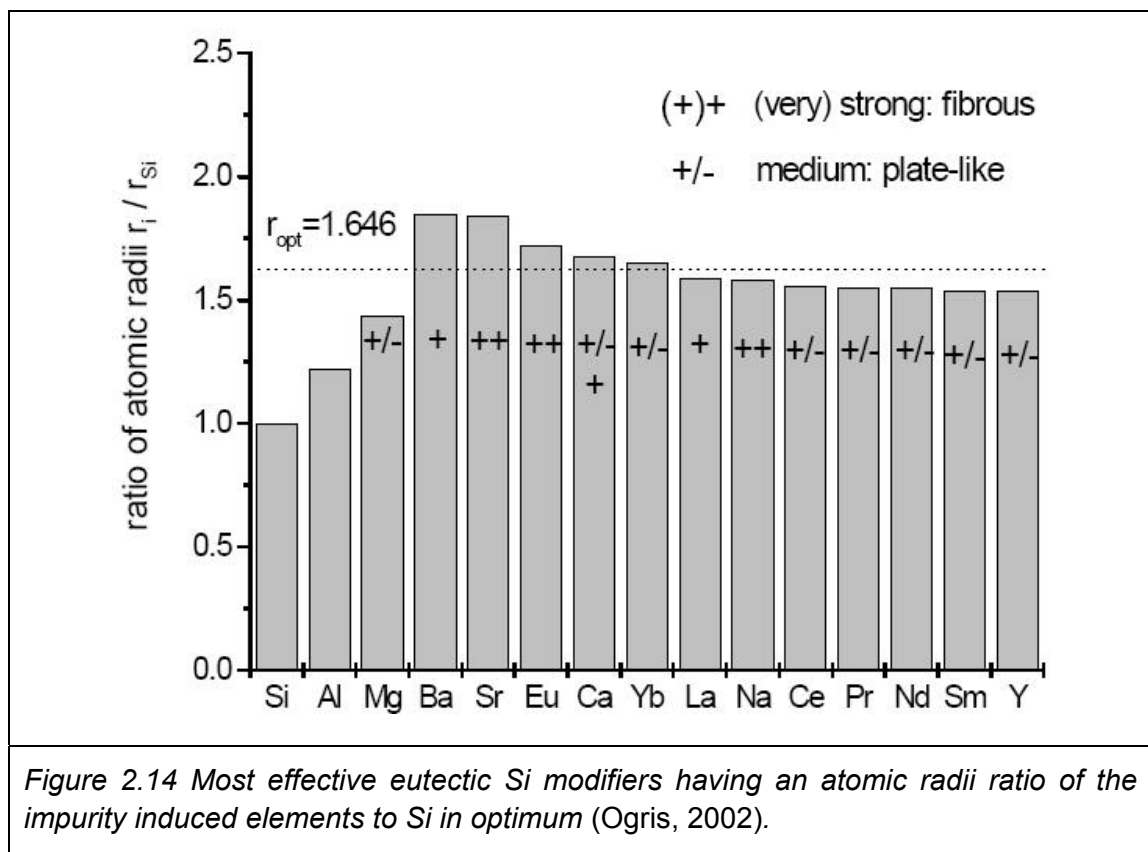


Figure 2.13 Schematics of a) Diamond Si in its standard step-growing mode (Cook, 1998); b) Branching types of the flake Si; c) Absorbed atoms effect on the monolayer steps at a growing interface where critical  $r$  determines the layer extension (Lu & Hellawell, 1995); d) Natural twin formation; e) Impurity induced twin formation (Cook, 1998).

However, boron can also act as an important independent grain refiner, i.e., a ~200ppm boron addition in the A356 alloys will change the columnar dendritic morphologies to an equiaxed structure as the  $\alpha$ -Al nucleates on the  $\text{AlB}_2$  particles (Nafisi & Ghomashchi, 2007). Likewise, the FactSage<sup>TM</sup> calculation of adding B to the hypereutectic Al-Si alloy denotes that a primary  $\text{AlB}_2$  phase occurs prior to the primary Si precipitation as shown in this binary Al-Si phase diagram (Figure 2.12). The formation of  $\text{AlB}_2$  raises the liquidus line, as a result of nucleation before the alloy solidifies.



Basically, the grain size has a smaller influence than the brittle eutectic Si and

/or the coarse primary Si on the alloy properties. The modifications of Si crystals must therefore be considered prior to grain refinement in foundry practice (Gruzleski & Closset, 1990). Either the coarse primary Si or acicular eutectic Si, which generally attain faceted flake structures with some random twins on the same close-packed [111] planes (Lu & Hellawell, 1995), might be modified, changing the Si morphologies and sizes, which can also alter the filling and feeding characters (Cook, 1998).

The addition of modifiers even at the p.p.m. level can significantly change the growth behaviour of Si phases resulting in more highly twinned branches. The normal branching mechanisms consist of large angle but also as well as of small angle branching, splitting, or overlapping (Figure 2.13-b)), which naturally occur in the Si growth process, compared to the perfect Si growth mode illustrated in the Figure 2.13-a). Repeated twinning of Si might also develop a fully oriented crystal from just one nucleation (Lu & Hellawell, 1995). Once absorbed foreign atoms have been successful bypassed by the normal growing of twin Si particles (Figure 2.13 – c), d), e)), a high density twin formation can subsequently take place. A fibrous structure therefore might be more favourable in the eutectic Si morphology. However, not all elements can act as effective modifiers, which require an optimum ratio of atomic radii at  $\sim 1.646$  between the modifier and the silicon atoms (Ogris, 2002). Figure 2.14 shows some elements that can well adapt to this impurity induced twinning theory for eutectic Si modification.

Generally, Na, Sr, or Sb are the typical modifiers used for producing the fibrous eutectic structure modification of the highly twinned Si structures while P can modify primary Si more effectively due to the nucleation of AlP, leading to an optimum particle size of 15~20µm (Gruzleski & Closset, 1990). A combination of the Si modifiers, such as P+S, P+RE<sup>f</sup>, P+Na, P+Sr, P+C, and P+S+RE etc., could be also used to achieve both finer eutectic and primary morphologies. Cancellation effects among interacting modifiers however must be avoided by adjusting the added amounts since some AlP nuclei are consumed by reactions with Sr and Na such as  $2\text{AlP} + 3\text{Sr} \rightarrow 2\text{Al} + \text{Sr}_3\text{P}_2$  and  $3\text{Na} + \text{AlP} \rightarrow \text{Na}_3\text{P} + \text{Al}$ . The modifiers to be added to the melt could be possible in the form of the pure metal (i.e. Bismuth), master alloys (i.e. Al-90Sr; Cu-8P), compounds (i.e. PCl; PCl<sub>2</sub>; PNC<sub>l</sub><sub>2</sub>), or salt mixtures (i.e. 10P-90CaCl<sub>2</sub>; 20P-70KCl-10K<sub>2</sub>TiF<sub>6</sub>; 15P-40C<sub>2</sub>Cl<sub>6</sub>-38KCl-7K<sub>2</sub>TiF<sub>6</sub>) (Zhao, 2006).

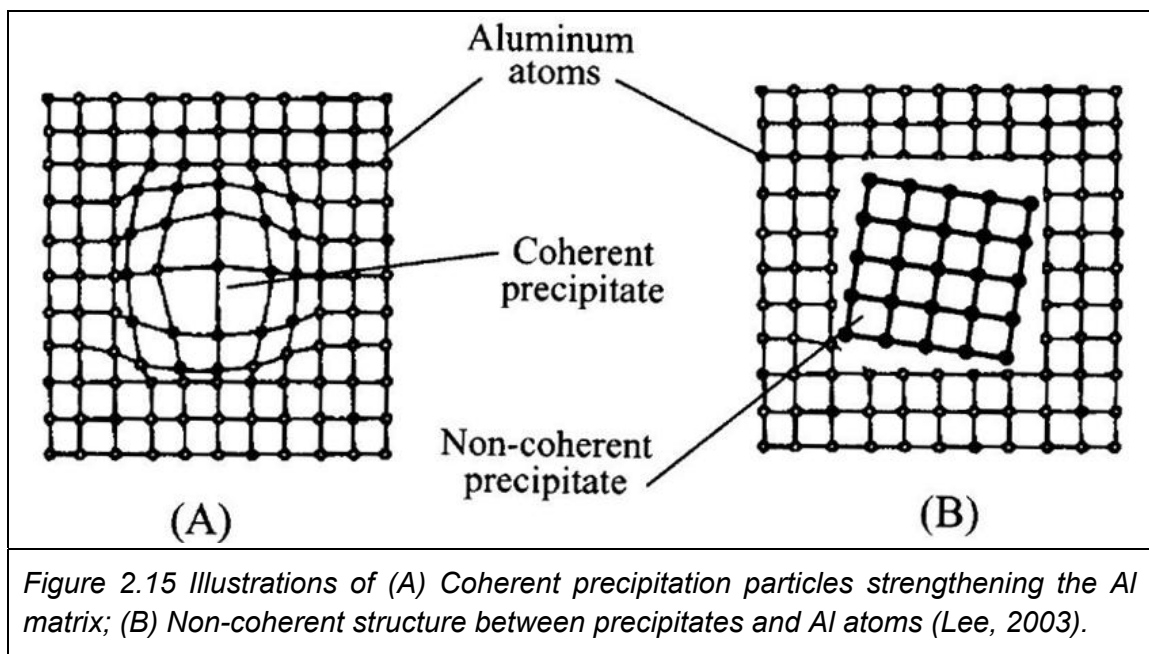
### 2.3.3. Reinforced composites

It is well known that the material properties are greatly enhanced by adding a secondary phase such as Al<sub>2</sub>O<sub>3</sub> and SiC, to the Al matrix resulting in aluminum Metal Matrix Composites (MMCs) performance at an elevated temperature could be enhanced in this way. The lattice coherency theory is again used to support the hypereutectic Al-Si alloys in its high temperature applications (230 ~ 400°C), such as diesel and direct fuel injection gasoline engine blocks (Lee, 2003). The

---

<sup>f</sup> RE – Rare Earth.

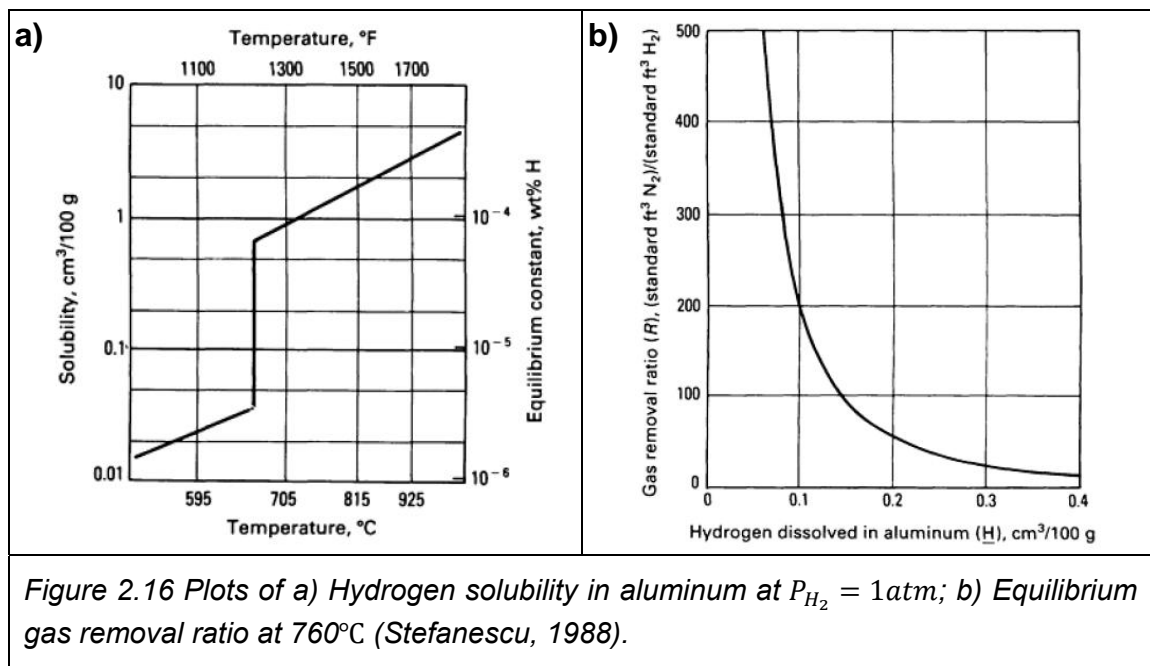
coherent precipitates produced therefore strengthen the aluminum matrix since they have similar lattice parameters as the Al atoms (Figure 2.15-A) while a mismatched non-coherent precipitate does not have the same positive effect on the material (Figure 2.15-B). Coherent particles generate the elastic coherency strains in the host Al metal to increase the dislocation resistance, which is particle spacing dependent (Pekguleryuz, 2007) (Lee, 2003).



In addition to the introduction of second phase material to the matrix, in-situ composites can be also designed to strengthen the material by the precipitation of hard phases formed spontaneously during the alloy solidification. The precipitation of  $Mg_2Si$  in a high Mg content Al-Si hypereutectic alloy has been extensively studied by (Y.G. Zhao, 2004), (Li, 2006), and (Zhang, Fan, Wang, & Zhou, 2000).

### 2.3.4. Liquid metal treatments

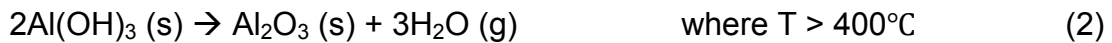
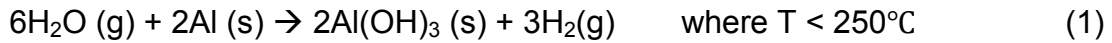
In the foundry practice, successful hypereutectic Al-Si castings produced by the conventional gravity poured process require precise control of the material compositions and of primary grain refining. This needs to be carried out with exact cast parameter surveillance, specific cooling system designed for the excess Si latent heats removal, and the right pouring and mould pre-heat temperatures control (MSFC, 1997).



Hydrogen is the major source (> 85%) of dissolvee gases in aluminum melts, exhibiting 15~20 times of solubility differences between the molten metal and solidified alloys at the temperature of fusion. As seen in Figure 2.16-a), the hydrogen content in Al melts increases rapidly from 0.034~0.05  $\text{cm}^3/100 \text{ g Al}$  in

the solid phase to  $0.65\sim 0.77\text{cm}^3/100\text{gAl}^g$  in the liquid aluminum at the melting point. Beyond that temperature, the hydrogen solubility increases linearly with increasing temperature, from 1.15 to  $1.67\text{cm}^3/100\text{gAl}$  between 750 and 800°C (Zhao, 2006).

In general, hydrogen (H) can readily dissolve from the environmental moisture ( $\text{H}_2\text{O}$ ) in contact with the solid material (<250°C) and the aluminum melt surface via the following reactions:



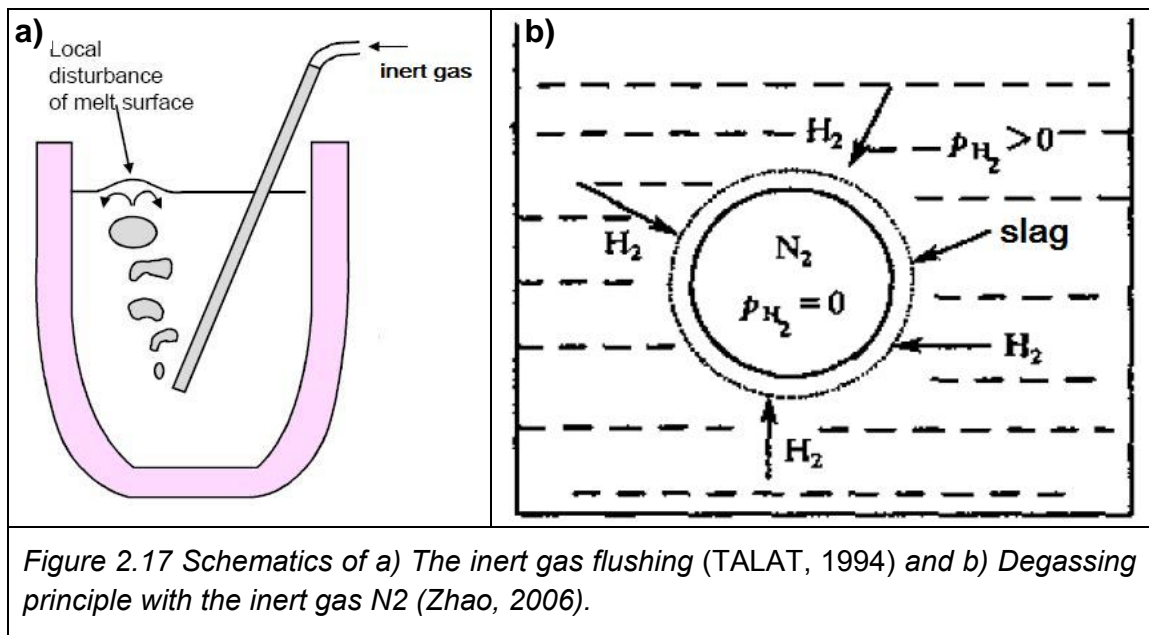
The loose layer of  $\text{Al}(\text{OH})_3$  powder is not able to prevent Al from further oxidation before the melting begins. As well, the reaction between the vapour water and the liquid aluminum are highly favourable even for very low values of vapour pressure. The solid  $\text{Al}_2\text{O}_3$  can result in inclusions while the hydrogen gas subsequently enters the liquid aluminum until the solubility limit is reached at that temperature (Zhao, 2006). Although alloying elements can reduce the hydrogen solubility above the melting point, significant gas porosity might be still present in the solid alloy without any degassing treatment due to its solubility variable directly associating with temperatures.

---

<sup>g</sup>  $1\text{cm}^3\text{H}_2/100\text{gAl}$  equals about 0.9ppm according to the hydrogen gas density 0.08988 g/L (0 °C, 101.325 kPa).



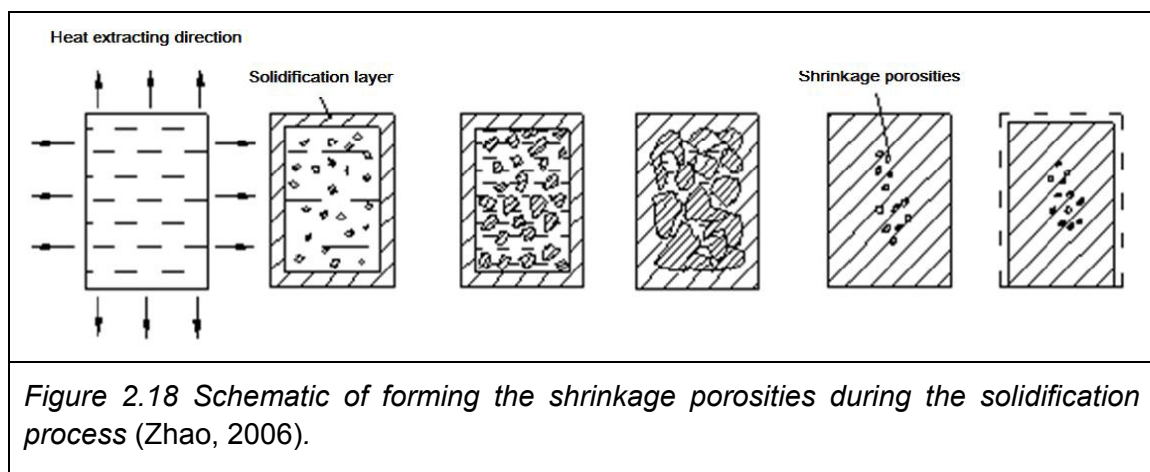
A critical size for a stable pore formation requires  $r^* = \frac{-2\sigma}{\Delta P}$ , where  $\sigma$  is the  $H_2$ /liquid aluminum interfacial energy; and  $\Delta P$  is the pressure difference between inner and outer pore. Homogeneous nucleation seems to be impossible since an extremely high  $\Delta P$  up to 30,000 atm is needed. However, heterogeneous nucleation is more feasible because the interfacial energy  $\sigma$  can be greatly reduced by wetting impurities such as inclusions and modifiers, offering favourable pore nucleation sites. The subsequent pore growth is driven by a time depended diffusion-controlled process, which implies that the faster solidification rate results in smaller pore sizes (Rin, 2005).



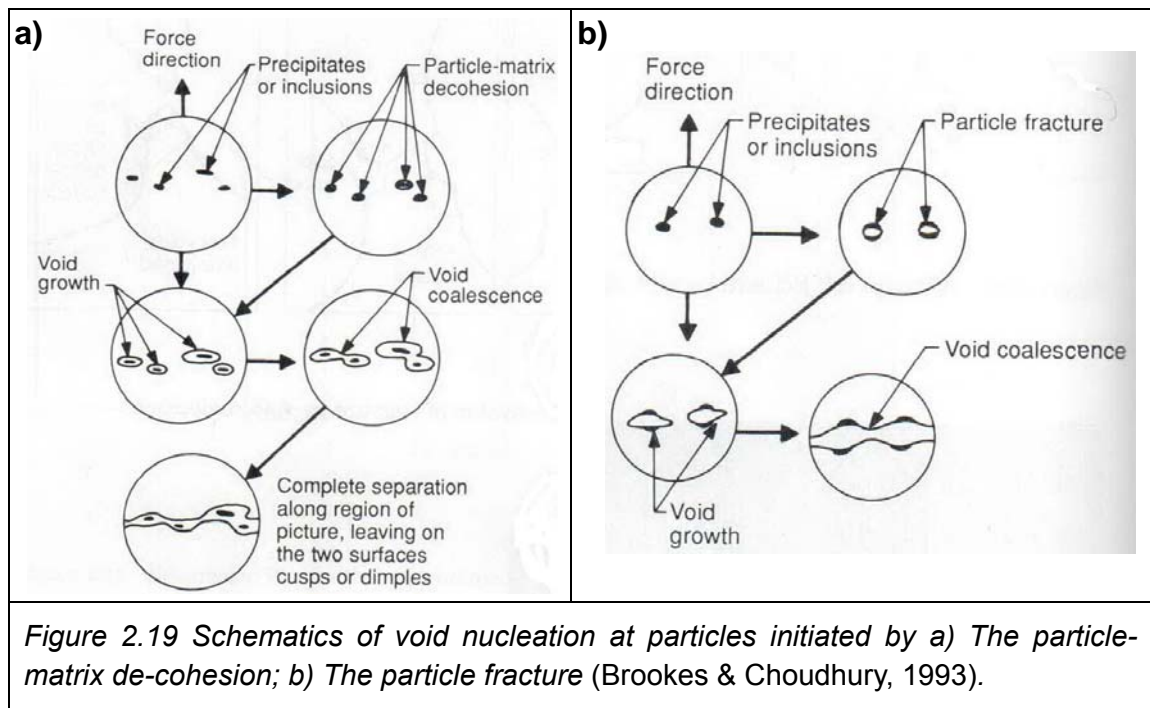
Inert gas flushing (Figure 2.17-a) is commonly carried out using  $N_2$  or Ar to remove the excessive hydrogen from the aluminum melt in order to achieve the desired alloy property. Figure 2.17-b) illustrates the effective degassing process.

The degassing principle is thus shown in Figure 2.17-b) where the floating nitrogen bubbles absorb the hydrogen which will be brought up to the melt surface (Zhao, 2006).

Different from gas porosity, the shrinkage void is another serious casting defect caused by non-sufficient interdendritic feeding or an inadequate pouring system where the last liquid solidifies in a place other than in the riser (SRS, 1999). Gas porosities can also become effective sites for the shrinkage void nucleation (Rin, 2005). Figure 2.18 illustrates the shrinkage porosity formation process during the solidification for a low temperature gradient, leading to the nearly simultaneous mass nucleation in a solidified melt. This situation therefore might be avoided in conventional gravity casting by either directional solidification with a higher temperature gradient or by the extra pressure, i.e. squeeze casting, to fill any voids caused by the shrinkages.

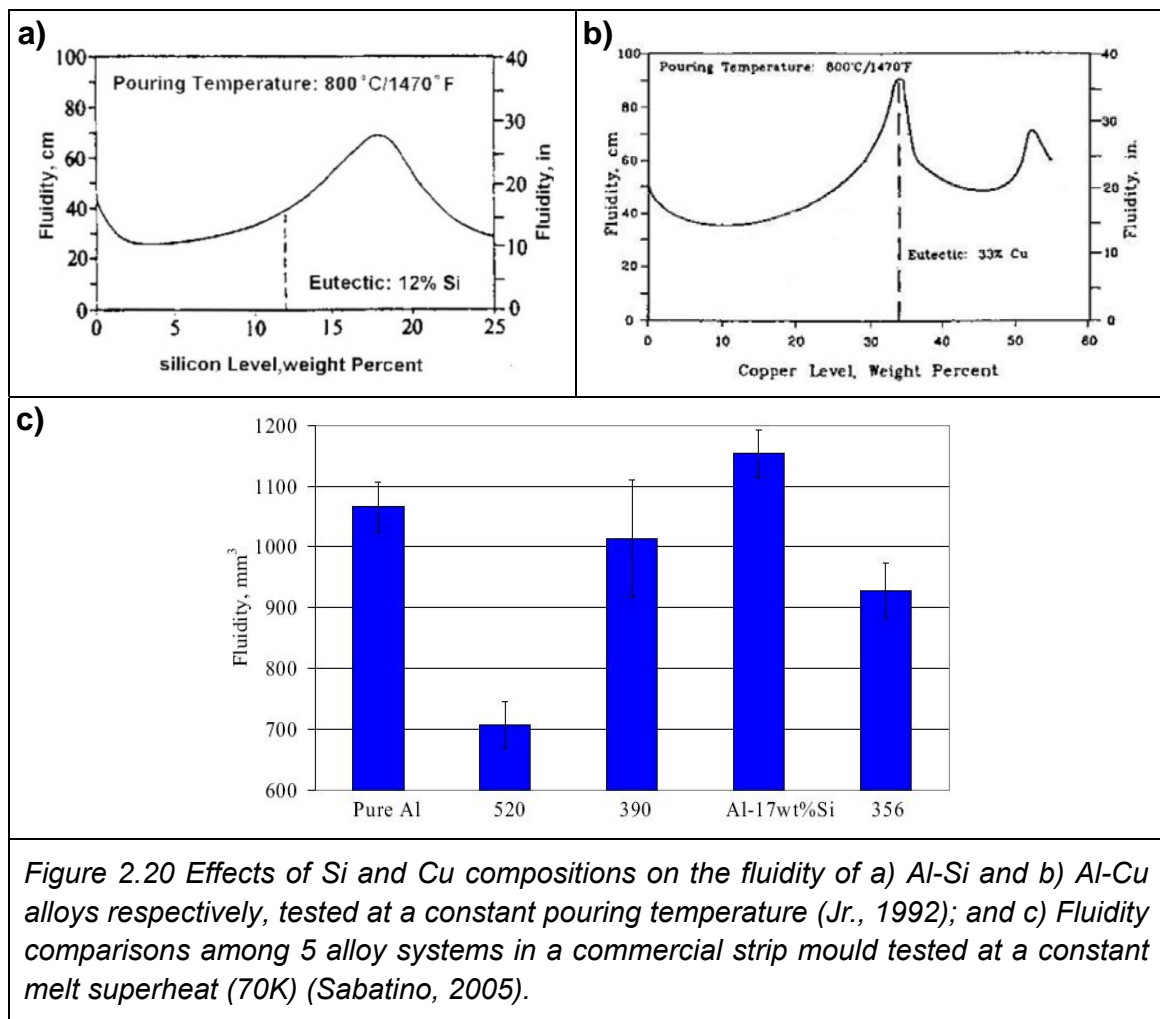


Inclusions commonly occur in casting as well, resulting in a degradation of alloy properties due to stress concentration, especially in a tensile test for the higher strength and lower ductility material. Figure 2.19 shows that the fracture occurs at particles (inclusions or precipitates) where the void coalescence is produced by either particle-matrix de-cohesion or particle fracture under an applied axial force (Brookes & Choudhury, 1993). There are two main types of inclusions that can be formed including  $\text{Al}_2\text{O}_3$  or  $\text{MgO}$ , nitrides, and sulphides, and the exogenous impurities (slag, and dross) during melt processing. The cast inclusions can be minimized by controlled casting and separation techniques including melt surface skimming and filter methods (Stefanescu, 1988), (Zhao, 2006).



### 2.3.5. Alloy fluidity

Melt fluidity is a major indication of alloy castability, directly influencing the quality of the final casting, especially for thin-wall castings. The fluidity is sensitive to a couple of variables including the alloy composition, latent heat of the fusion, superheat, grain refinement and modification, mould material, coating and pre-heating temperature, melt cleanliness, and viscosity (Sabatino & Arnberg, 2005).



For the Al-Si alloy system investigated in this study, an increase of melt temperature does increase the melt fluidity. However, this subsequently generates more gas porosities due to the increased hydrogen absorption in the molten aluminum. In a binary Al-Si system, the best melt fluidity occurs at ~17 wt% Si (Figure 2.20-a)). Higher Si contents result in fluid blockage from a large Si solid fraction although more heat is produced along with the solidification. Alloy A390 contains 17 wt% Si and combined with ~4.5 wt% Cu makes alloy heat treatable. However, Cu reduces the melt fluidity as shown in Figure 2.20 - b) and c).

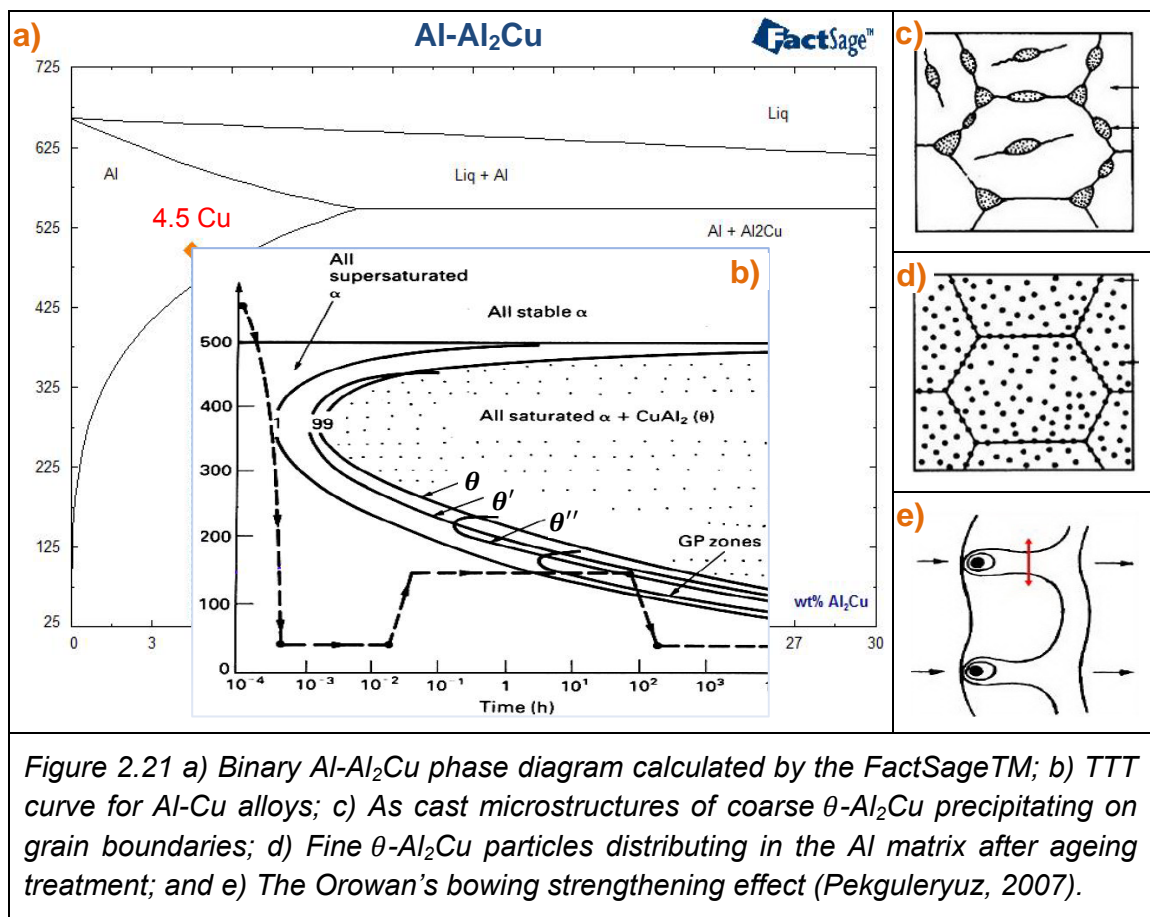
#### 2.3.6. Heat treatment

In 1906, Alfred Wilm discovered the ageing effect of an Al-3.5~5.5wt% Cu alloy results in significant improvements of strength and hardness. The material strengthening principle is based on a large solid solution deviation of the  $\theta$ -Al<sub>2</sub>Cu precipitates in the  $\alpha$ -Al as demonstrated in the binary Al-Al<sub>2</sub>Cu phase diagram (Figure 2.21-a)). Heating from ambient to a temperature below the melting point dissolves all  $\theta$  phases in the  $\alpha$ -Al completely at a composition of ~ 4.5wt% Cu. A subsequent quenching is followed by setting a cooling rate at which the nose of TTT<sup>h</sup> diagram is bypassed (Figure 2.21-b)) to achieve the supersaturated solid solution at room temperature. Furthermore, the ageing process results in fine decompositions in the  $\alpha$ -Al matrix from the metastable states until the optimum

---

<sup>h</sup> TTT - Time-Temperature-Transformation diagram.

$\theta''$  precipitates are attained. The coarse detrimental  $\theta$ - $\text{Al}_2\text{Cu}$  particles are usually distributed at grain boundaries (Figure 2.21-c)) or defects while the fine  $\theta''$  structures (Figure 2.21-d)) are homogeneously dispersed in the Al matrix after ageing, strengthening the material more efficiency as described by the Orowen pinning effects (Figure 2.21-e)).



The yield strength – microstructure relationship goes through a series of changes during the ageing process as shown in Figure 2.22 (Pekguleryuz, 2007). Initially, the supersaturated Cu atoms randomly dissolve in the FCC Al

matrix, exhibiting the solution strengthening in the alloy with a relatively low value. As the ageing process continues, high density ( $10^{18}/\text{cm}^3$ ) GP zones which are formed from ordered Cu clusters start to develop the large elastic strains since their disc shaped precipitates can match the matrix coherently in both faces (1 or 2 atom planes with a thickness at  $\sim 1\text{nm}$ ) and edges. Along with some GP zone growth, the strain mismatching occurs in their disk edges and the particles are well prepared for the  $\theta''$  nucleation, achieving optimum conditions where the Orowan's dispersion strengthening takes place to obtain the highest yield strength. Upon further holding, the  $\theta'$  phase is precipitated by nucleating at intermediate heterogeneous sites (i.e. dislocations) and becomes dominant, by losing the coherency strains relating to the non-coherent edges. Finally, the coarse  $\theta$ - $\text{Al}_2\text{Cu}$  phases are produced at the  $\theta'$  interfaces and grain boundaries, degrading alloy yield strength significantly due to their complete non-coherency (Pekguleryuz, 2007).

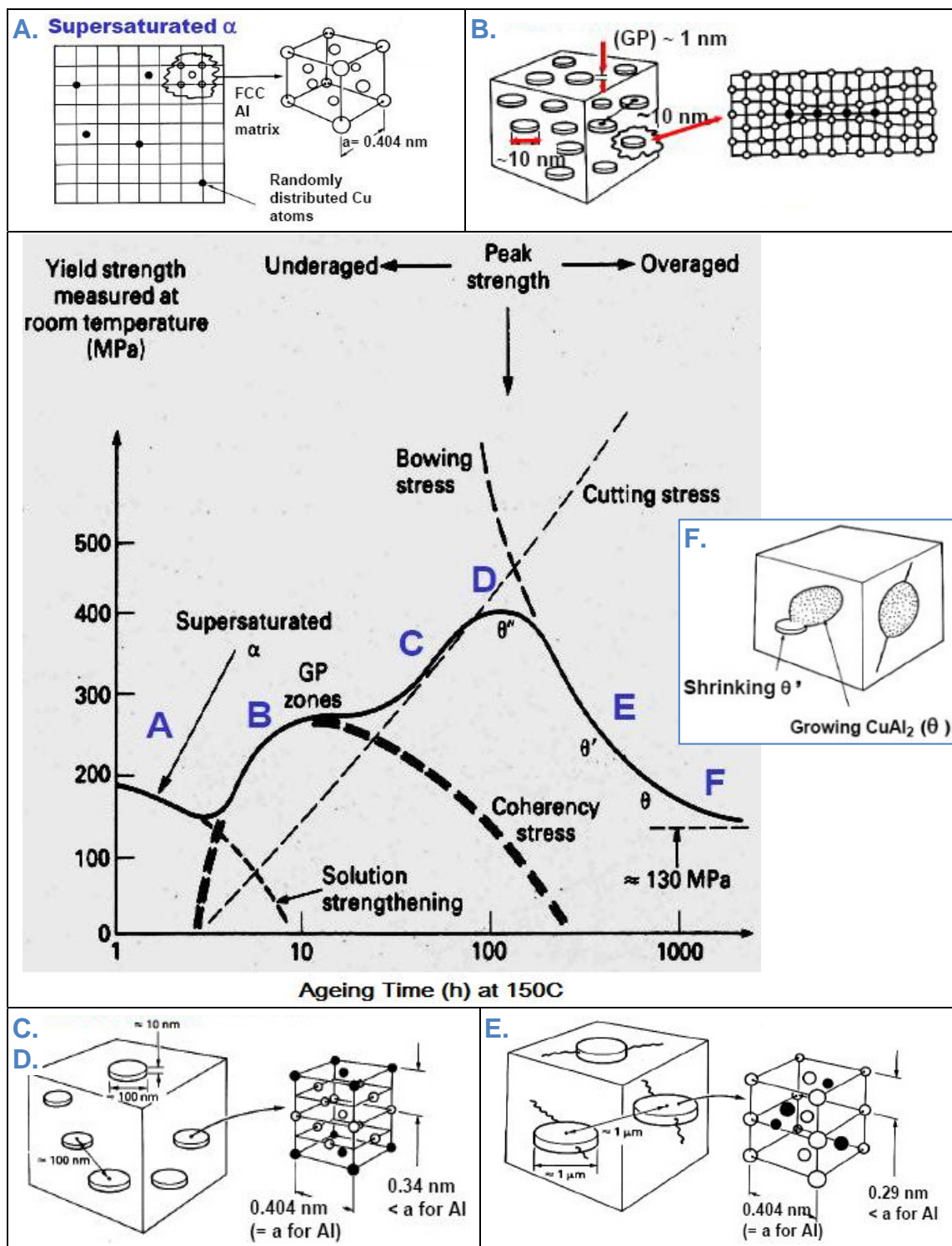


Figure 2.22 The yield strength - microstructure relationships during the ageing heat treatment process for an Al-3.5~5.5 wt% Cu alloy (Pekguleryuz, 2007).



## **CHAPTER 3. Methodology**

### **3.1. Thermodynamic calculations**

All thermodynamic calculation works were carried out using FactSage<sup>TM</sup> for the hypereutectic Al-Si-Cu-Mg alloy system with varying Mg additions in order to determine the phase diagram of these alloys. Several modules of FactSage<sup>TM</sup> 5.6 were used for this new alloy system, including “documentation”, “view data”, “reaction”, “equilibrium”, “phase diagram”, “results”, “view figure”, and “figure” etc.. Figure 3.1 shows the selected specimens of four solution phases and one solid compound derived from the FSlite database to be performed in the FactSage<sup>TM</sup> calculations.

**Reactants [4]**

(gram) 17 Si + 4.5 Cu + <A> Mg + <78.5-A> Al

**Products**

Compound species

gas ☐ ideal ☐ real 0

aqueous 0

pure liquids 0

\* + pure solids 1

☒ suppress duplicates apply

\* - custom selection species: 1

Equilibrium solidification

FSlite-LIQU

Cooling step T(C): 25

Mass(g): 0

**Solution species**

*	+	Base-Phase	Full Name
	D	FSlite-LIQU	LIQUID
	+	FSlite-AIC6	AlCu_THETA
	+	FSlite-DIAM	DIAMOND_A4
	+	FSlite-FCC	FCC_A1

Legend

D - Equilibrium solid'n ☒ Show ☐ all ☒ selected

+ - selected species: 12 solutions: 4 Select

Custom Solutions

☐ fixed activities

☐ ideal solutions

☐ activity coefficients

Details ...

Pseudonyms

apply ☐ List ...

☒ include molar volumes

Total Species (max 700) 13

Total Solutions (max 30) 4

Default

**Final Conditions**

<A> T(C) P(atm) Product H(J)

0.5 700 1

Equilibrium solidification - T(start) = 700, T(stop) = 0% liquid

**Equilibrium**

☒ normal ☐ transitions

☐ predominant ☐ open

Calculate >>

FactSage 5.6 c:\FactSage\EquiA390.DAT

Selected: 1/20

**SOLID**

+	Code	Species	Data	Phase	T	V	Code
	5	Si(s)	FSlite	si<diamond_a4>		o	
+	6	Mg2Si(s)	FSlite	mg2si		o	
	7	Cu(s)	FSlite	cu<fcc_a1>		o	

Figure 3.1 The species to be used in the FactSage<sup>TM</sup> calculations consisting of 4 solutions (FSlite-Liquid, FSlite-AIC6 < $\theta$ -Al<sub>2</sub>Cu>, FSlite-DIAM <Si>, and FSlite-FCC <Al>) and 1 compound (Mg<sub>2</sub>Si(s)) for the Al-Si-Cu-Mg alloy system in weight basis.

## 3.2. Experimental methodology

### 3.2.1. Overall experiment description

Permanent mould (PM) castings were used for casting tensile bars for mechanical properties testing of A390 alloys with increasing Mg content. Two batches (#1, #2) of tensile bar PM castings which were produced in two different

institutes: Université du Québec à Chicoutimi (UQAC) and McGill University. Tensile bars produced with circular sections (ASTM B108 – 03a) were cast of two new hypereutectic alloys with 6 and 10wt% Mg and of alloy A390 at UQAC for comparison. These specimens were also heat treated (T6) to compare their properties with the tensile bars in the as cast condition. The second set of tensile bars were cast at McGill University using a different type of metallic mould producing rectangular section tensile bar castings of the same alloys but with the addition of modifiers for the primary phase modification.

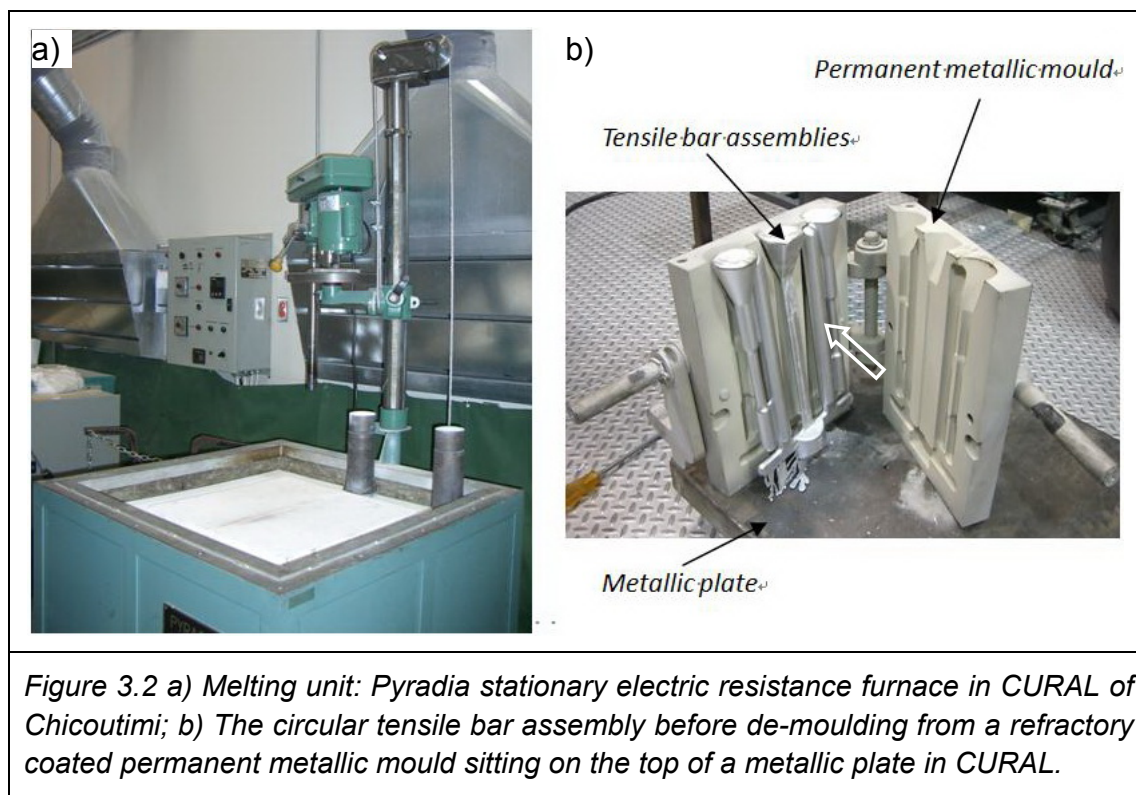
### 3.2.2. Material preparation

Alloy A390 supplied in bar ingots from Alcan® was cut into small pieces to adapt to the melting furnace and used as the base material, while a series of alloying elements and modifiers are added to the matrix either as pure metals (i.e. Mg, Cu, Si, Bi etc.) or as master alloys (i.e. Al-25Si, Al-50Cu, Cu-8P, Al-10Sr etc.) in order to obtain desired compositions. All materials used in the experiments were baked prior to the castings to avoid any hydrogen gas absorption in the melt. The chemical composition of A390 ingot is shown in the Table 3.1.

<i>Table 3.1 A390 ingot composition (source: UQAC)</i>										
Si	Fe	Cu	Mn	Mg	Cr	Ni	Zn	Ti	Ca	Al
16.81	0.13	4.27	0.005	0.29	0.001	0.003	0.016	0.10	0.087	Bal.

### 3.2.3. Castings

The first set of samples was cast using a traditional permanent mould method at the University Research Center on Aluminum (CURAL) of Chicoutimi. Three independent melts, ~20kg each of alloy (A390, 6wt% Mg, and 10wt% Mg), were prepared in the stationary electric resistance furnace (Pyradia inc., Figure 3.2-a)) by melting the base material of Alcan A390 ingot along with alloy additions of Al-25wt% Si, Al-50wt% Cu, and AZ91D to produce the 6wt% Mg alloy and of pure Si, Al-50wt% Cu, and pure Mg to make 10wt% Mg alloy.



The degassing process for A390 melt was carried out at  $\sim 730^{\circ}\text{C}$  for a period of 8 minutes using argon gas at a flow rate of 4 CFH ( $\text{ft}^3/\text{h}$ ) and 12 psi. The 6 and 10 wt% alloys were treated at the same conditions at  $760^{\circ}\text{C}$  after the addition of the designed amount of Silicon and Copper. The melt was then cooled down to  $\sim 730^{\circ}\text{C}$  followed by magnesium addition before the melts were ready.

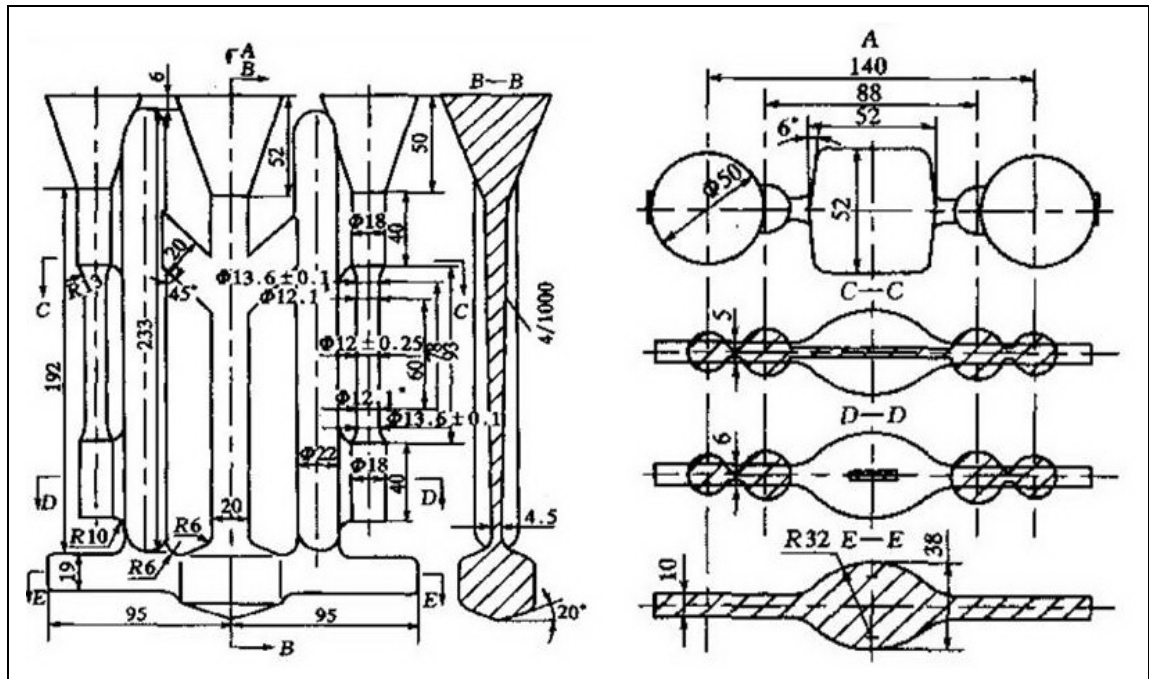


Figure 3.3 The detailed drawing of the circular tensile bar assembly (Zhao, 2006).

The pouring temperature was initially to set with  $\sim 50^{\circ}\text{C}$  superheat above the liquidus for each alloy,  $\sim 700^{\circ}\text{C}$  for A390,  $\sim 670^{\circ}\text{C}$  for 6wt% Mg, and  $\sim 690^{\circ}\text{C}$  for 10wt% Mg, according to the phase diagram prediction. However, the casting temperature was adjusted to  $\sim 700^{\circ}\text{C}$  for 6wt% Mg alloys while  $\sim 750^{\circ}\text{C}$  for 10wt% Mg alloys due to the poor fluidity of these alloys compared to A390. During the

melt preparation, no modifying component was introduced to the melt. At the end, the melts were poured into a refractory spray coated permanent metallic mould, preheated to  $\sim 400^{\circ}\text{C}$ , placed on the top of a metallic plate (Figure 3.2-b). The tensile bar assemblies were then demolded after a minimum 3~4 minutes of solidification of the melt. The total weight of the cast assembly is around 1.4kg consisting of two tensile bars as illustrated in Figure 3.3.

The second series of samples were produced using the same gravity PM casting technique but with a permanent mould for the rectangular flat tensile bars. As seen in the Figure 3.4 – a), an induction furnace (INP20-20, Norax Canada Inc.) was used as the melting unit, which provided fast heating with high power (20kw) electrical source, low voltage and high current at 5khz. The raw materials were melted in a graphite crucible with a maximum capacity of 1 kg. Figure 3.4 – b) shows the cylindrical graphite crucible,  $\varnothing 75 \times 112$  (inside dimension), containing one charge of alloy A390 bulk material ( $\sim 600$  g) to be melted. The melt temperature was precisely monitored by a chromel-alumel thermocouple (type K). All alloying materials were added to the melt at  $720^{\circ}\text{C}$  following a sequence of silicon and copper at first holding for 15 min and then magnesium for another 5 min. Structure modifying elements of either master Cu-8P alloy or pure bismuth metal were introduced at  $800^{\circ}\text{C}$  and held for 10mins before pouring. The recovery rate was found to be 100 wt% for silicon and copper, 93 wt% for magnesium, 95 wt% for pure bismuth, and 80 wt% for Cu-8P



master alloy. There was no degassing or melt filtering of the samples produced by this method.

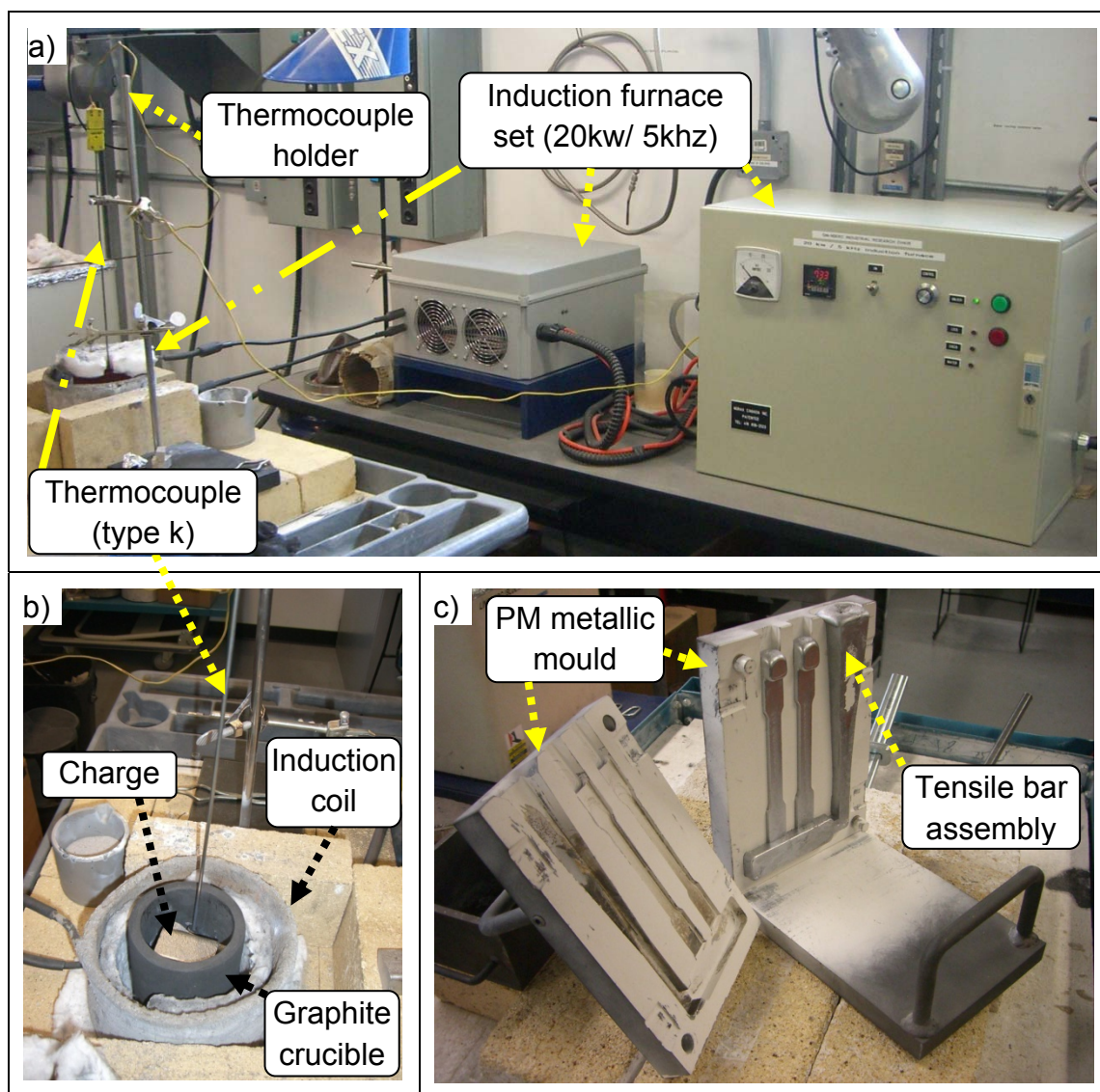


Figure 3.4 a) Induction furnace set-up (20kw/ 5khz); b) Graphite crucible with one charge of bulk A390 alloy to be melted by the magnetic field; c) Permanent Metallic mould and the rectangular cast assembly.

After skimming the melt surface, the molten metal was poured directly from the

crucible to the permanent mould, which was preheated to 400°C in a Blue M inert gas mechanical convection oven. Figure 3.4 – c) illustrates the cast assembly (~470 g) when one half of the mould is removed.

The pouring temperature was initially set at 740°C for the A390 and the 6wt% Mg alloy, and at 790°C for the 10wt% Mg alloy. However, an adjustment of the pouring temperature needed to be made for these alloys with 800°C for the previous two and 850°C for the 10wt% Mg alloy due to the decreased melt fluidity and the rapid solidification of the relatively thin sample base.

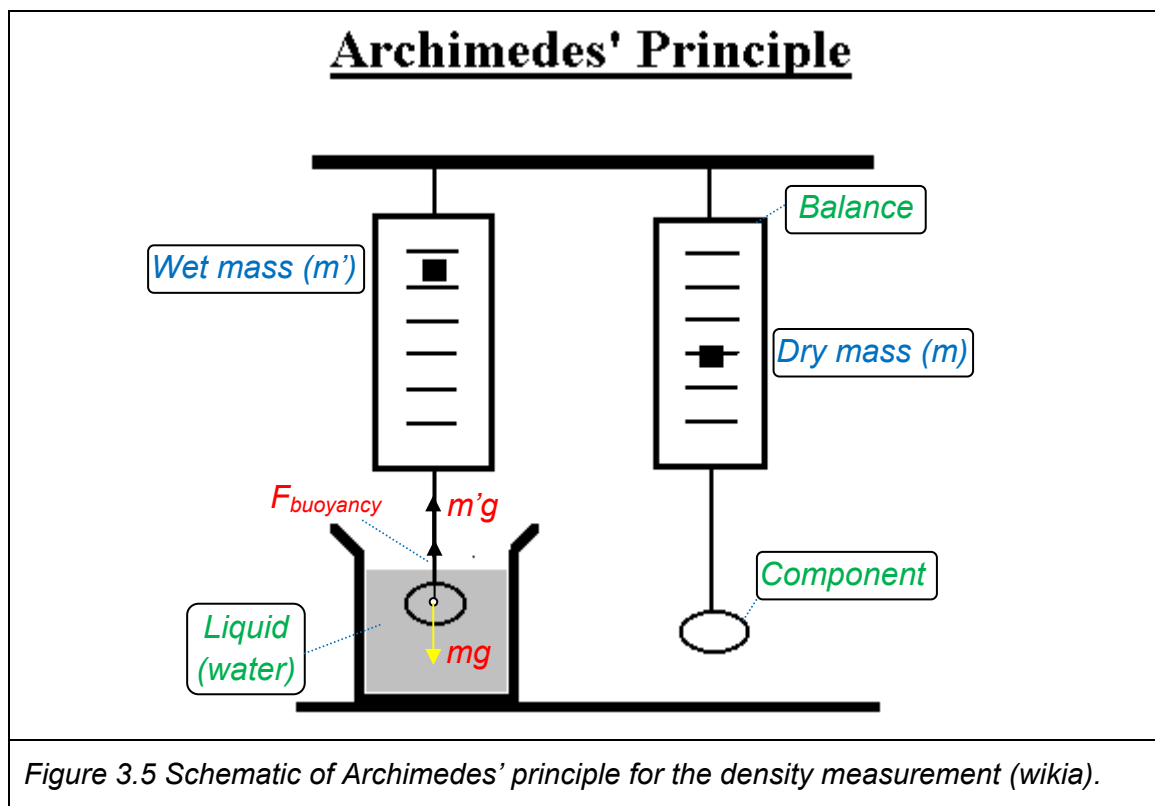
#### 3.2.4. Heat treatment (T6)

The effects of heat treatment (T6) on mechanical properties of these three alloys were investigated for the round tensile bar specimens only. The standard parameters of heat treatment applied for alloy A390 (Davis, 1990) (Jung, Seo, & Kang, 2001) was also used for other two alloys. Actually, each alloy has its own specific procedures to optimize the heat treatment effect. However, the same conditions used for parent alloy A390 was used for other two alloys, starting with solutionizing at 495°C for 8 hours in a Lindberg Blue M electric resistance furnace, followed by immediately quenching in the water (room temperature), and then ending with an artificial ageing at 175°C for another 8 hours in a Cole-Parmer electric resistance furnace.



### 3.2.5. Density determination

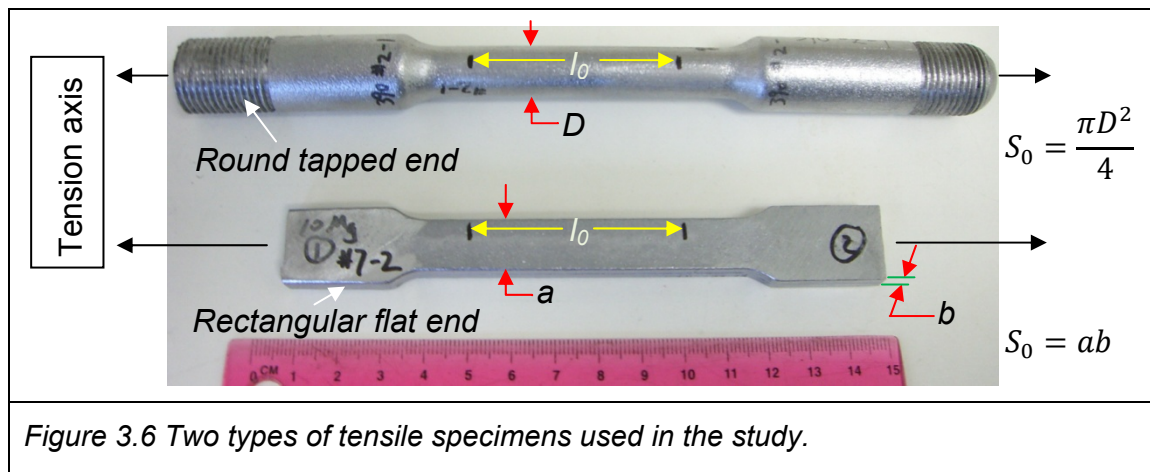
Alloy density measurements were carried out using the Sartorius CP Toploading Balance (CP 323S), which has a capacity of 320g and an accuracy of 0.001g using the Archimedes' technique where the exerted buoyancy force corresponds to the weight of the displaced liquid of the submerged object, usually water, as shown in Figure 3.5.



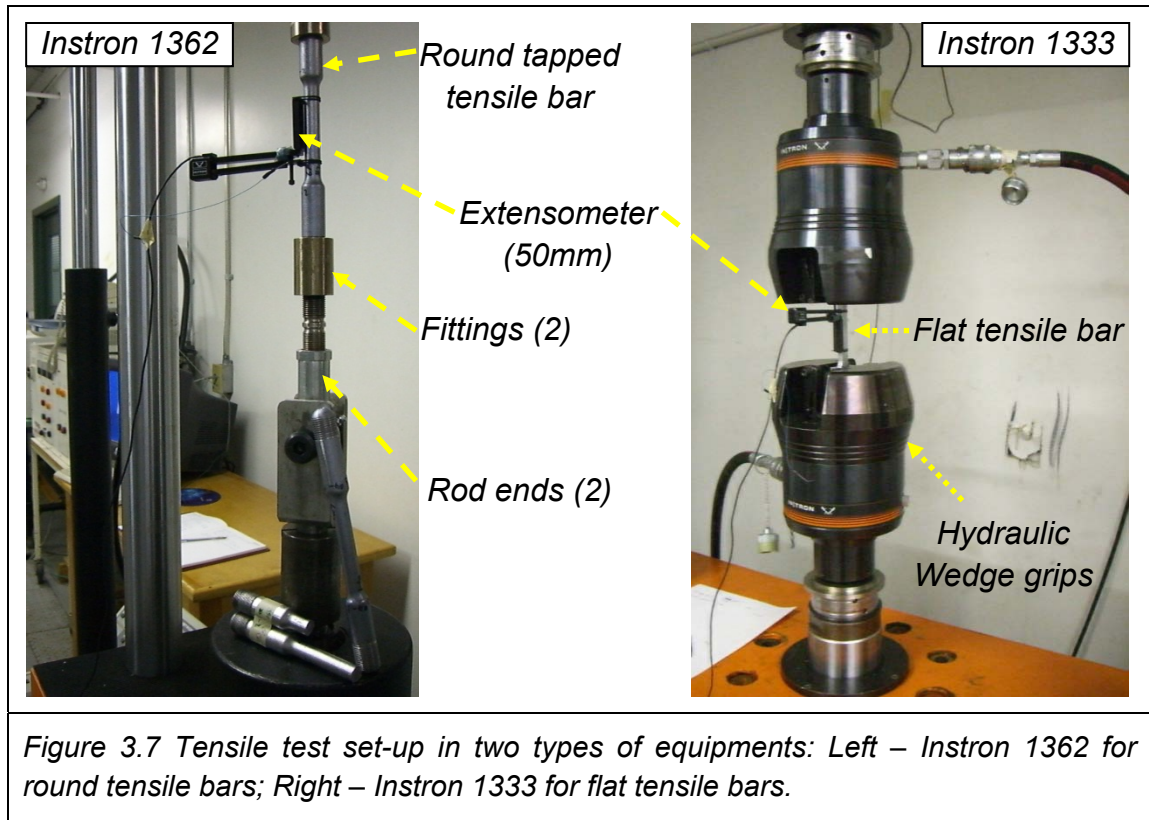
The alloy mass was recorded for both dry ( $m$ ) and submerged ( $m'$ , in water) conditions to calculate the alloy density  $\rho$  according to Equation 3.1,  $\rho = \rho_{H_2O} \cdot \frac{m}{m-m'}$ , where  $\rho_{H_2O} = 0.99905g/cm^3$  is the water density at temperature for

measurement (15.5°C). The samples were taken from the circular tensile bar specimens in the vertical runner area where the part is parallel to the tensile bars (white arrow, Figure 3.2 b)), six duplicates for each alloy including three as cast and three after T6 heat treatment.

### 3.2.6. Tensile tests



Mechanical properties are commonly evaluated by conducting a series of examinations including the tensile tests, hardness, fracture toughness, and impact tests. Only tensile strength and hardness were carried out in this study. Figure 3.6 illustrates two types of tensile bars (round and rectangular). The tensile behaviours of both types of samples were determined according to the specifications of the ASTM standard B557-06. The threaded-end round tensile bars were tested using INSTRON 1362 (Max. load: 100 KN, Figure 3.7 – left) while the flat tensile bars were tested with the INSTRON 1333 (Max. load: 244KN, Figure 3.7 – right).



Testing condition consists of a free-running crosshead speed  $V_0 = \frac{\Delta l}{\min} = \sim 0.4 \text{ mm/min}$ , respecting the maximum stress rate  $\left(\frac{\delta_{\max}}{\min}\right)$  of no more than  $10^5 \text{ psi/min}$  ( $6.9 \times 10^8 \text{ pa/min}$ ). According to Hooke's law  $\frac{\delta_{\max}}{\min} = E \cdot \frac{\Delta l / \min}{l_0}$  where E is the elastic modulus ( $E = 81.2 \text{ GPa}$  for the alloy A390 at T6 condition and  $l_0 = 50 \text{ mm}$ ). With a data storage frequency of 0.004 KHz and using Instron WaveMaker Runtime program setting up ensured that at least 200 data points were being recorded per minute. The extensometer used in the tensile testing had an equal gage length 50mm (49.7mm after the calibration) to the nominal specimen gage length as required. These conditions applied to both types of

tensile bars due to their same measuring length ( $l_0$ ) although the cross sections ( $S_0$ ) were different. The estimated maximum fracture load  $F$  was found to be ~39 KN for A390 after T6 heat treatment for the round bar specimen, and ~25 KN for the flat tensile bars.

### 3.2.7. Hardness tests

Two types of hardness testers used in the current study. A Clemex MT-2100 micro-hardness tester (Figure 3.8 – left) was used for the phases of aluminum solid solution and primary Si &  $Mg_2Si$  phase analysis, while a conventional RockWell hardness tester (Mitutoyo ATK-600, Figure 3.8 – right) was used for the bulk material determination. The micro-hardness test method followed ASTM standard E384 to measure the hardness changes of the three alloys under both as cast and T6 conditions. The measurements were taken from the area close to which the tensile fracture took place after sample polishing in order to identify the independent phases prior to the Vicker test (HV). A diamond indenter was used to evaluate the rather hard constituents such as Si and  $Mg_2Si$  with load in a range of 10~1000gf to allow a size of the indentation at ~20x20 micrometers, slowly forcing the indenter into the phases. It was found that 25gf was suitable for the  $\alpha$ -Al solid solution and the primary  $Mg_2Si$  while 100gf was used to measure the primary Si. The final readings were displayed on screen after measuring manually and stored in a computer controlled program Clemex CMT (Version 3.5.013).

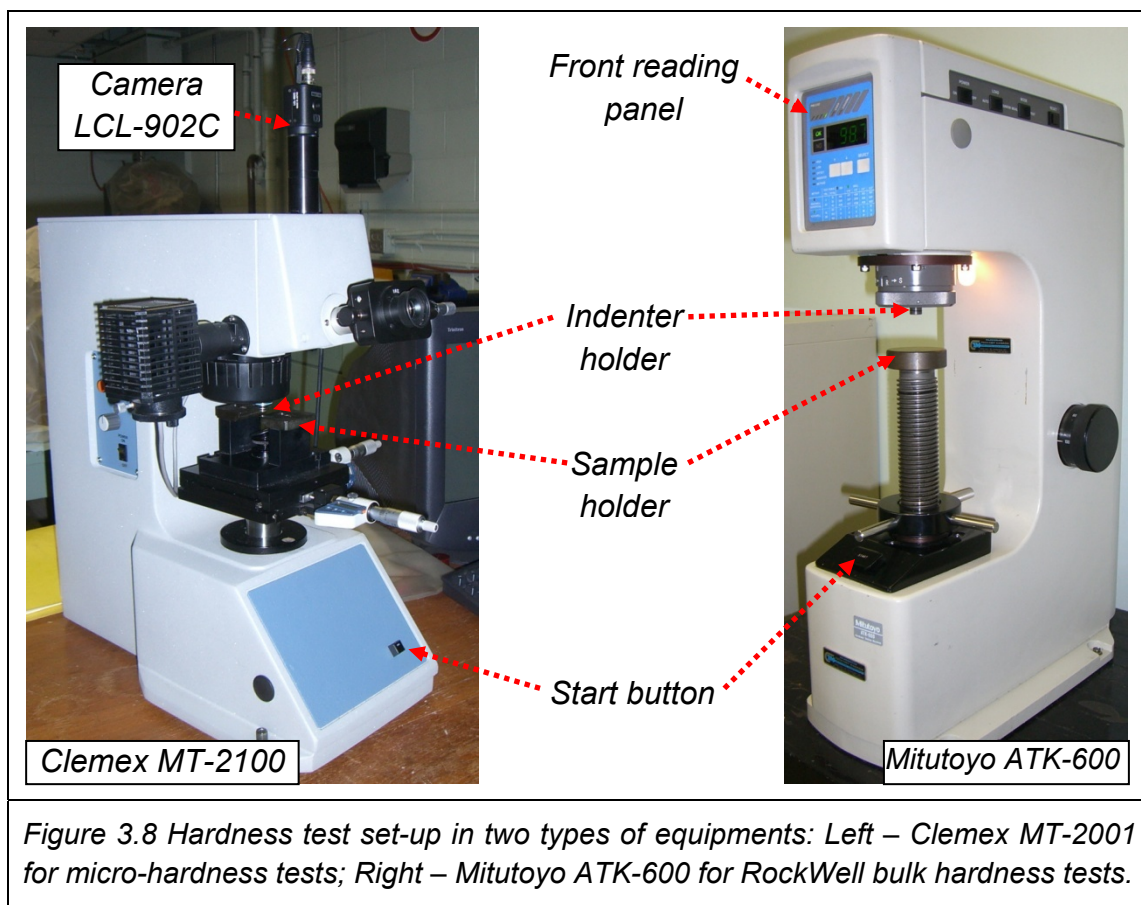
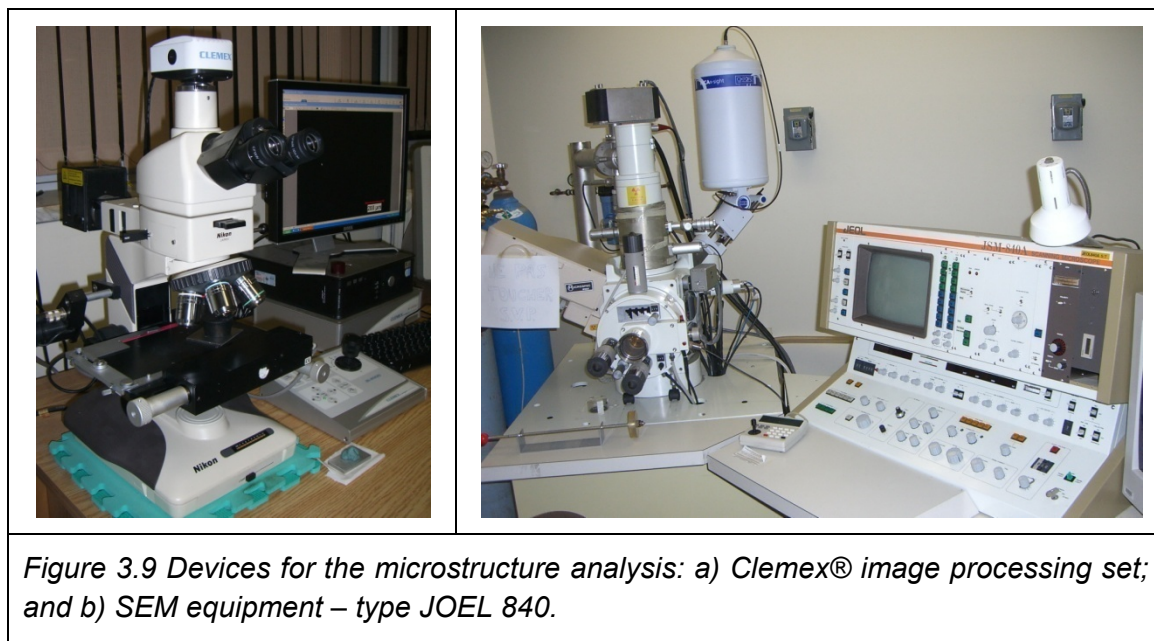


Figure 3.8 Hardness test set-up in two types of equipments: Left – Clemex MT-2001 for micro-hardness tests; Right – Mitutoyo ATK-600 for RockWell bulk hardness tests.

The Vicker's hardness which was originally reported as HV value can be converted to the GPa ( $\text{N/m}^2$ ) in SI units system by using a factor 0.009807. Therefore, a comparison can be made between the measured and reported Vicker's hardness for the primary Si and  $\text{Mg}_2\text{Si}$  phases. In addition, the overall material hardness was also measured for the same specimens using the Mitutoyo RockWell hardness tester where the load 100kgf and a ball size  $\phi \frac{1}{16}$  " (1.6mm) was used according to the RockWell B standard. These recorded values can be converted to Brinell, Vickers, Superficial, Knoop, and Scleroscope Hardness according to ASTM E140 - 07 Standard Table 2.

### 3.2.8. Microstructural examination

The microstructure of two types of tensile bars were examined by using the optical light microscope and Clemex devices (Figure 3.9 a)) in un-etched specimens cut from a transverse section closing to the fracture surface. As well, quantitative image analysis was used (Clemex Vision PE 5.0) to determine the porosities in the tensile bars for the three types of alloys (A390, 6wt% Mg, and 10wt% Mg) for the as cast and T6 samples. The average values of porosity were then calculated based on tensile bar specimens where 10 random areas in each were chosen for the analysis of porosity area percentage.



As a comparison, the tensile fracture surfaces were also examined using both optical stereograph and SEM microscopy (JOEL-840) shown in Figure 3.9 b) for

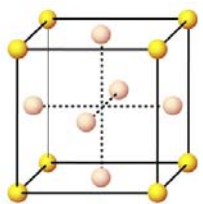
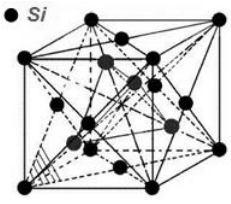
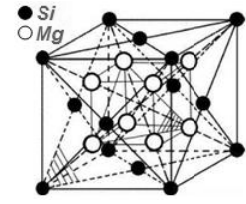
the analysis by secondary electron (SEI) and backscatter secondary electron (BSE) image and energy dispersive spectroscopy (EDS).



## CHAPTER 4. Thermodynamic calculations

### 4.1. Primary $\text{Mg}_2\text{Si}$ versus Si

The addition of Mg to the traditional hypereutectic Al-Si A390 alloy directly results in the precipitation of primary  $\text{Mg}_2\text{Si}$  as a substitute for the primary Si phases, partially or completely, depending on the amount of Mg present in the alloy.  $\text{Mg}_2\text{Si}$  is comparable to Si in both crystal structure and properties as summarized in Table 4.1 (MatWeb, 2009) (Zolotarevsky, Belov, & Glazoff, 2007) (Liao, Sun, & Sun, 2003) (WikiPedia, 2009).

<i>Table 4.1 The comparison of crystal structure and properties between Si and <math>\text{Mg}_2\text{Si}</math> (MatWeb, 2009) (Zolotarevsky, Belov, &amp; Glazoff, 2007).</i>			
	Al	Si	$\text{Mg}_2\text{Si}$
$\rho$ ( $\text{g}/\text{cm}^3$ )	2.70	2.33	1.88
$T_{\text{fusion}}(^{\circ}\text{C})$	660.37	1412	1108
Microhardness (GPa)	0.17 (WikiPedia, 2009)	12.30 (20 $^{\circ}\text{C}$ )	5.30 (20 $^{\circ}\text{C}$ )
	N/A	8.00 (300 $^{\circ}\text{C}$ , 1-hour)	1.77 (300 $^{\circ}\text{C}$ , 1-hour)
C.T.E. <sup>i</sup> ( $\mu\text{m}/\text{m} \cdot ^{\circ}\text{C}$ )	24 (0~100 $^{\circ}\text{C}$ )	2.49 (25 $^{\circ}\text{C}$ )	11.5 (20 $^{\circ}\text{C}$ )
Young's Modulus(GPa)	68	112	120
Crystal structure  (Liao, Sun, & Sun, 2003)	FCC <sup>j</sup> (Fm3m, Pm3m)	Diamond (Fd3m)	Antifluorite (Fm3m)
			

A weight reduction is achieved when Mg is added to hypereutectic Al-Si alloys

<sup>i</sup> C.T.E. - Coefficients of Thermal Expansion, the linear value is specified here.

<sup>j</sup> FCC – Face-Centered Cubic structure.



as a result of the in-situ reinforcement by primary  $\text{Mg}_2\text{Si}$  particles which have a lower density than the Si phase. Moreover, both Si and  $\text{Mg}_2\text{Si}$  have higher melting points and a higher elastic modulus than pure Al. Both Si and  $\text{Mg}_2\text{Si}$  improve wear properties but the micro-hardness of  $\text{Mg}_2\text{Si}$  is about 2.5 times lower than the Si at room temperature. In addition, 1-hour microhardness at  $300^\circ\text{C}$  indicates that  $\text{Mg}_2\text{Si}$  possess a lower level of thermal stability than Si. Alloy dimensional stability is another important factor to consider for auto applications. The coefficient of thermal expansion (C.T.E.) of  $\text{Mg}_2\text{Si}$  is 2 times lower than the Al matrix and 4 times higher than Si at room temperature. Both Si and  $\text{Mg}_2\text{Si}$  have a cubic crystal structure, the diamond A4 (Fd3m) for Si and the antiferite C2 (Fm3m) for  $\text{Mg}_2\text{Si}$ . Totally there are twelve atoms inside one  $\text{Mg}_2\text{Si}$  cubic, eight (Mg atoms) are distributed along with four body diagonals, and four others (Si atoms) on eight corners and six face centers. Whereas only eight atoms make one Si cubic since four atoms are absent from inside the cubic than the  $\text{Mg}_2\text{Si}$  (Liao, Sun, & Sun, 2003).

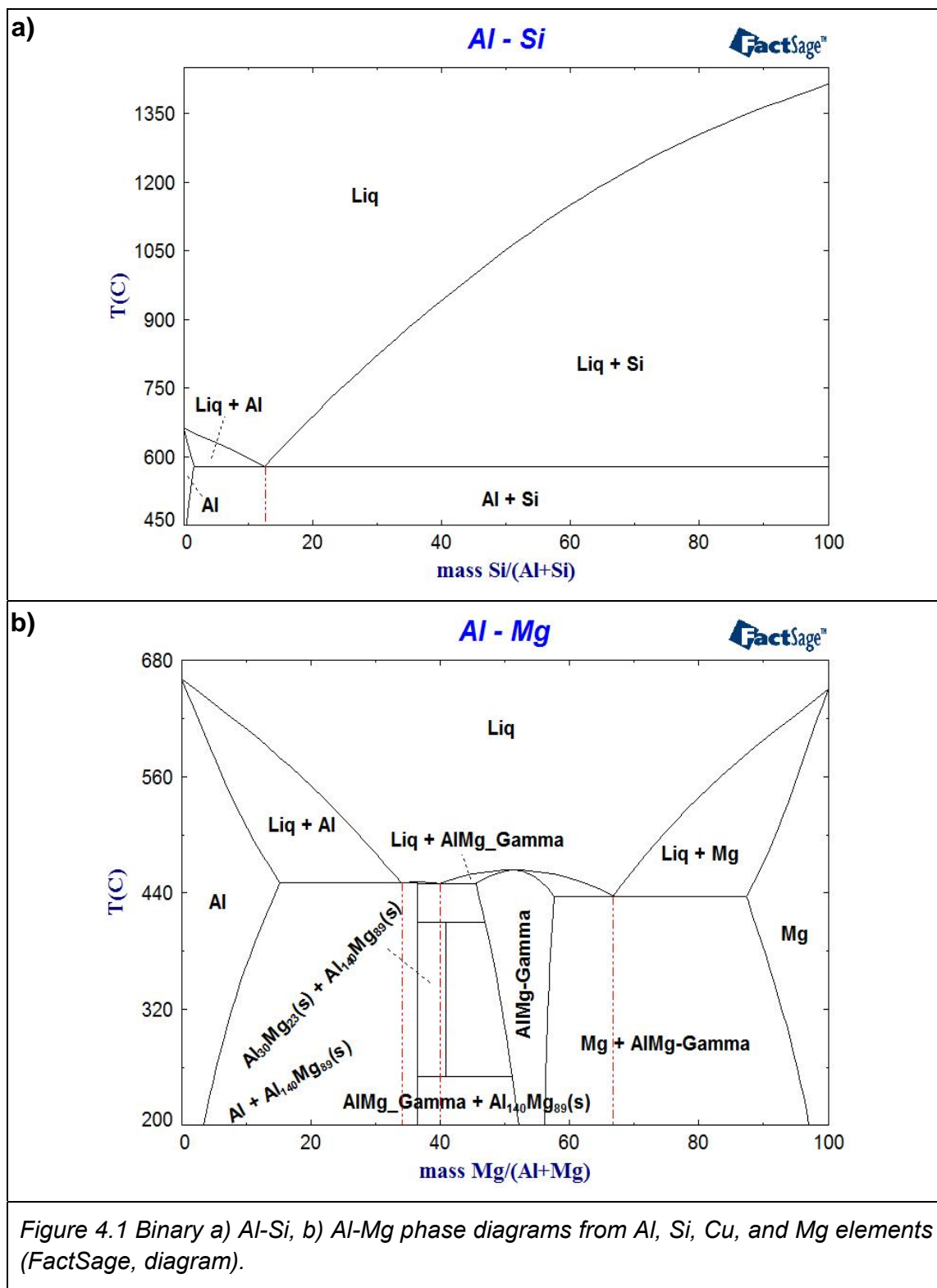
#### **4.2. Phase diagrams**

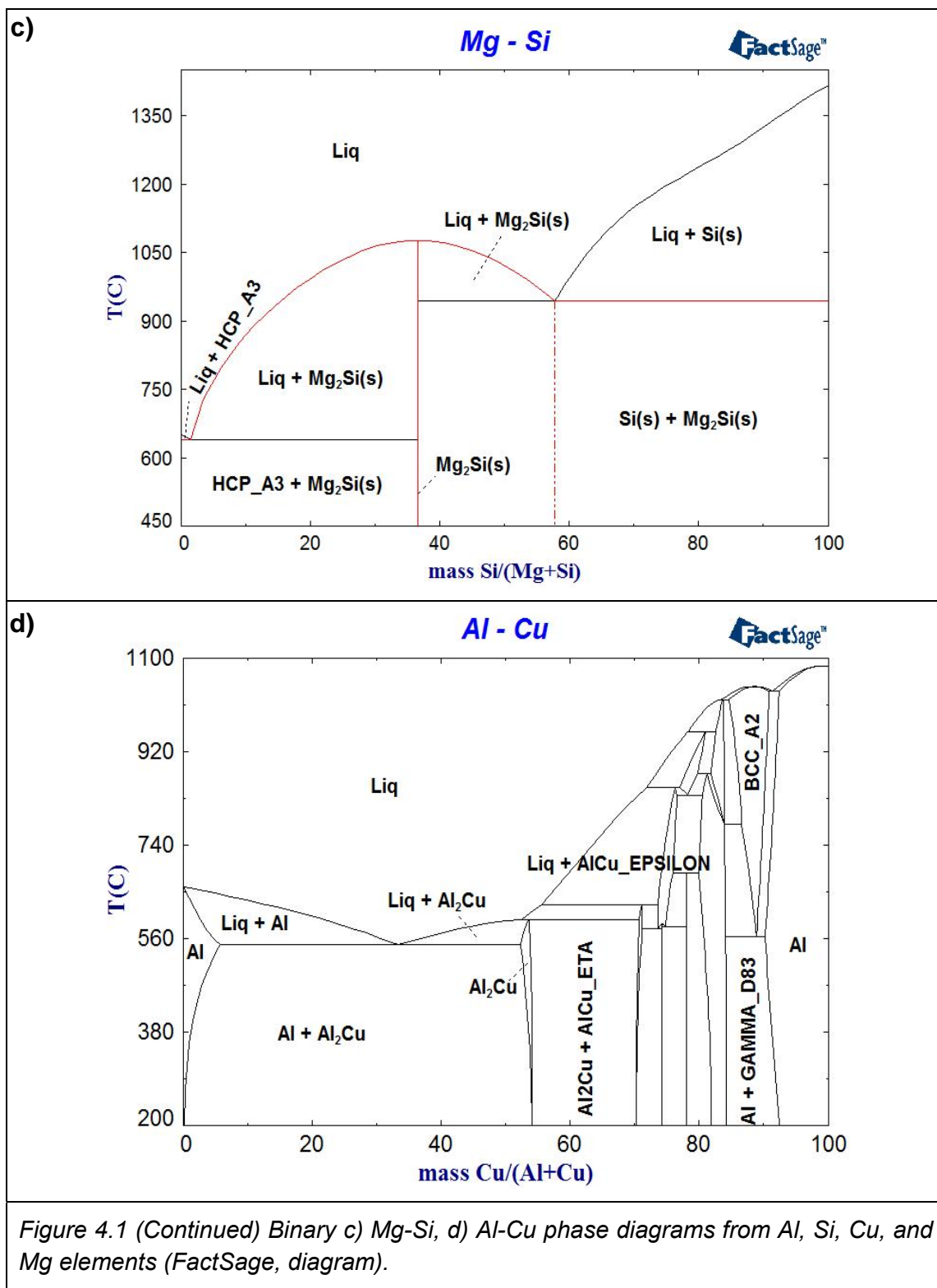
The calculations of the hypereutectic Al-Si-Cu-Mg alloy system with varying Mg addition are obtained using FactSage<sup>TM</sup>. The analysis of the thermodynamic characteristics of these alloys is used as a basis for the experimental studies. The FSLite light alloy database, which is built upon European COST Action 507, contains 117 binary, 30 ternary and 3 quaternary alloy systems relating to

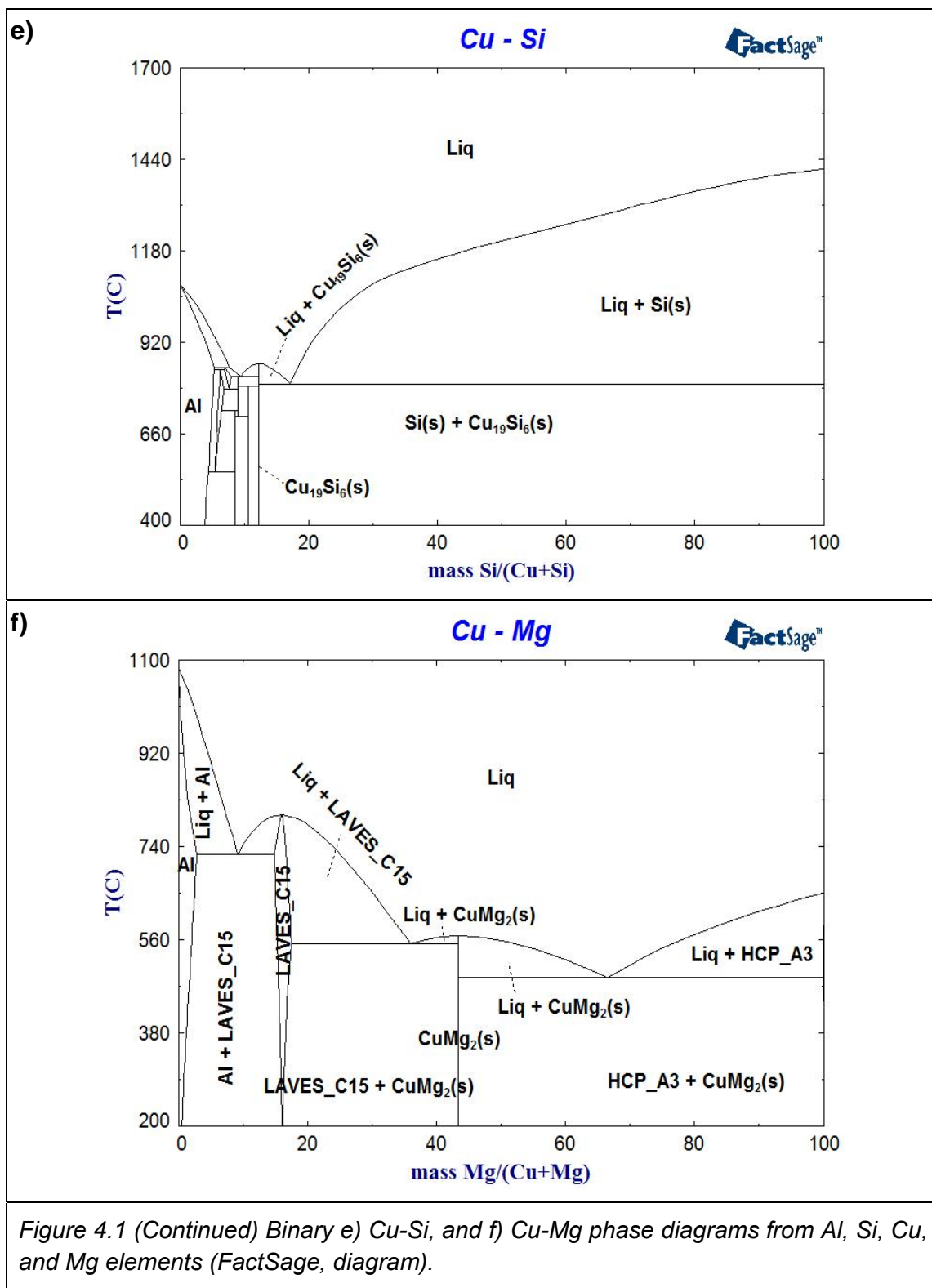
following elements: Al, B, C, Ce, Cr, Cu, Fe, Hf, Li, Mg, Mn, Mo, Nb, Nd, Ni, Si, Sn, Ta, Ti, V, Y, W, Zn, Zr etc.. The database fully describes the binary system over a complete composition/ temperature range and Al- or Mg-rich ternary alloy phases. Multi-component alloy systems, such as Al-Si-Cu-Mg, require the analysis of binary Al-Si, Al-Mg, Al-Cu, Mg-Si, Mg-Cu, Si-Cu (Figure 4.1) and ternary Al-Si-Mg, Al-Si-Cu, Al-Mg-Cu, Si-Mg-Cu, to search for all possible phases. However, the components that are included in known databases can also be included to calculate the Al-17Si-4.5Cu-xMg alloy system by constructing the ternary Al-Si-Mg isopleth phase diagram with fixed Cu at 4.5 wt%. The calculation of ternary phase diagram might be therefore more efficient by properly selecting the Cu-based phases corresponding to the composition range in each binary system, such as  $\theta$ -Al<sub>2</sub>Cu in Al-Cu system (Cu < 54 wt%), Cu<sub>19</sub>Si<sub>6</sub>(s) in Cu-Si system (Cu < 85 wt%), and CuMg<sub>2</sub>(s) in Cu-Mg system (Cu < 58 wt%).

One of solution phases Al<sub>5</sub>Cu<sub>2</sub>Mg<sub>8</sub>Si<sub>6</sub> (Q Phase), which has been documented in specimens of A390 series alloys, is absent from FSlite database. Moreover, the other minor alloying elements, i.e. Fe, Ni, Zn, Ti etc., have been also omitted in the following calculations for simplification. Phase diagrams were generated by the corresponded FactSage module for the Al-Si-Cu-Mg alloy system producing isopleths of Al-Mg-4.5wt%Cu-17wt%Si, Al-Si-4.5wt%Cu-0.5/6/10wt%Mg, Al-Mg-Si-4.5wt%Cu; the binary Al-Al<sub>2</sub>Cu etc.), which are used to analyze the alloy

characteristics and solidification behaviour. As discussed before, the four solution phases (liquid,  $\theta$ -Al<sub>2</sub>Cu, Al, Si) and one stoichiometric compound (Mg<sub>2</sub>Si(s)) included in the determination of the quasi-binary phase diagrams. Extra possible species, such as Al<sub>140</sub>Mg<sub>89</sub>(s), Al<sub>30</sub>Mg<sub>23</sub>(s), CuMg<sub>2</sub>(s), Cu<sub>19</sub>Si<sub>6</sub>(s), Al<sub>2</sub>CuMg(s), Al<sub>7</sub>Cu<sub>3</sub>Mg<sub>6</sub>(s), Al<sub>5</sub>Cu<sub>6</sub>Mg<sub>2</sub>(s), Cu<sub>3</sub>Mg<sub>2</sub>Si(s), Cu<sub>16</sub>Mg<sub>6</sub>Si<sub>7</sub>(s), and  $\gamma$ -AlMg, HCP-A3 etc., are also used to calculate the target liquidus projection as documented in the known multiple isothermal ternary phase diagrams.

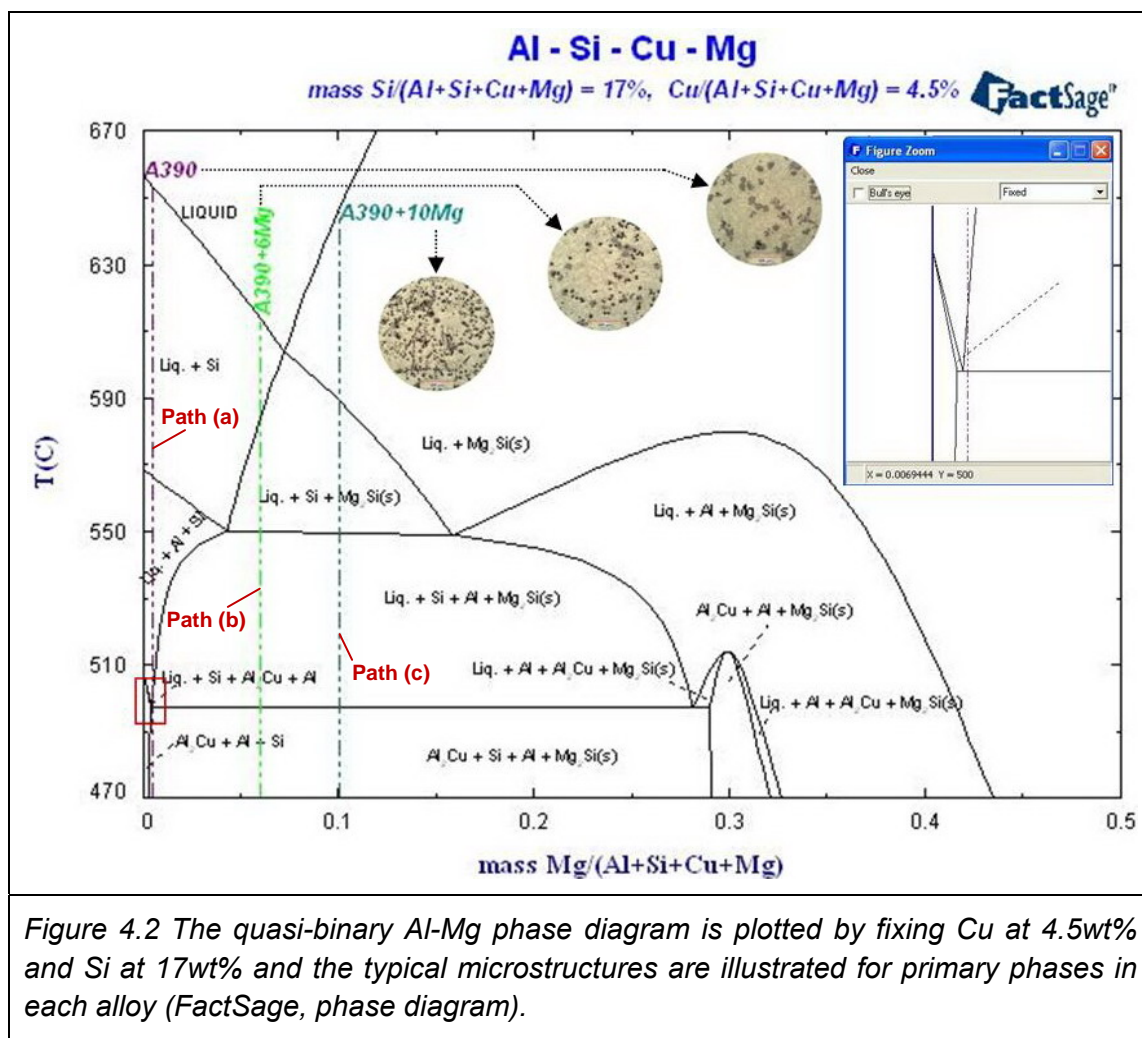






#### 4.2.1. Isopleth binary Al-Mg phase diagram

After selecting the species from “solution” and “compounds”, the variables are temperature (470~670°C) as y axis versus the Mg composition (0~50wt%) as x axis with fixed Cu (4.5wt%) and Si (17wt%). The calculated quasi-binary Al-Mg phase diagram shows the solidification path for three typical alloys, A390, 6wt% Mg and 10wt% Mg alloys, and their corresponding microstructures.

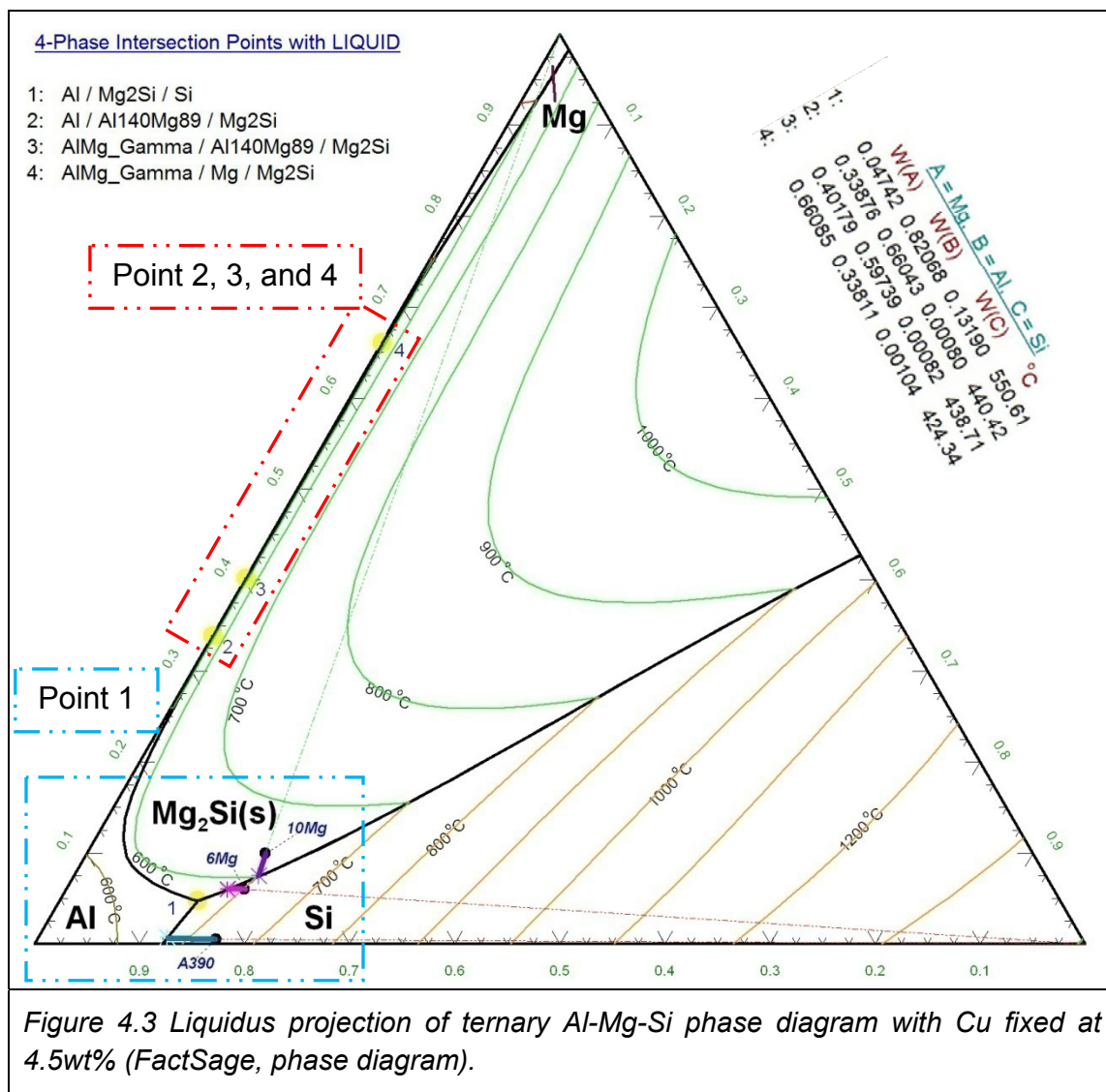


The solidification path for each alloy can be thermodynamically described in this phase diagram (Figure 4.2). Path (a) is for the A390 alloy, the first phase solidified from the liquid melt is the primary Si followed by binary eutectic of  $\alpha$ -Al and Si precipitates, continuing with a ternary decomposition where the  $\text{Mg}_2\text{Si}$  appears before finishing with a quaternary reaction forming the  $\theta$ - $\text{Al}_2\text{Cu}$  phase. Path (b) is for the 6wt% Mg alloy, primary Si will be still the first solid to form from the liquid melt along with  $\text{Mg}_2\text{Si}$  as the next primary phase before the rest of eutectic reactions take place. Path (c) is for the 10wt% Mg alloy, the solidification of the primary phases begins with  $\text{Mg}_2\text{Si}$ , and then Si, and afterward proceeding with the same decompositions as before.

#### 4.2.2. Ternary polythermal projection of liquidus surfaces

It is assumed that the alloy system consists of Al + Mg + Si + 4.5wt% Cu. Three corners of this ternary phase diagram represent pure Al, Mg, and Si at their melting temperatures. By referring the binary Al-Mg, Mg-Si, and Al-Si alloy system for the constant value of 4.5wt% Cu, a series of polythermal ternary liquidus lines are thus plotted in this ternary phase diagram showing the projected liquidus surface.





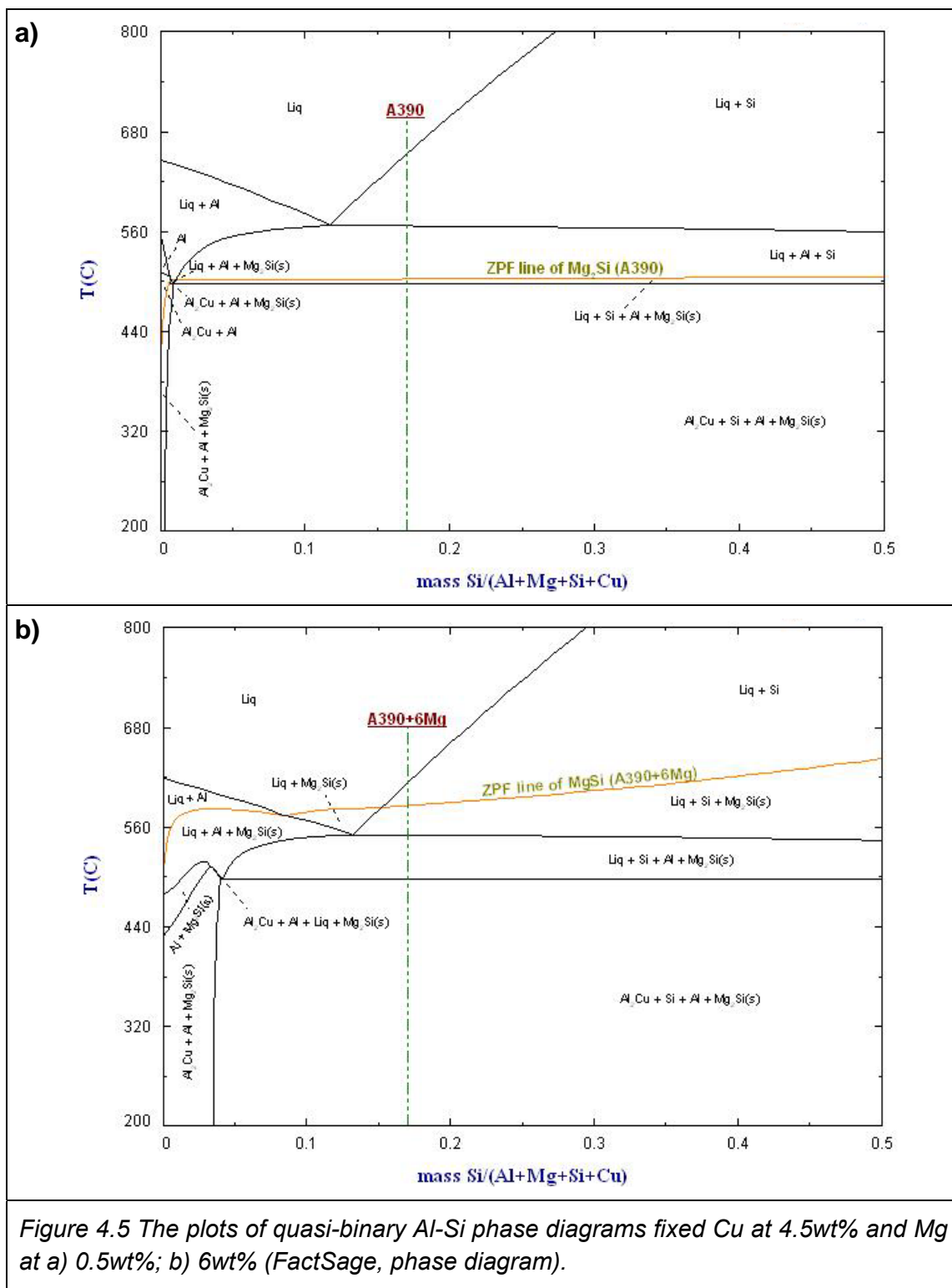
As seen in the Figure 4.3, there are four univariant points which are specified: point 1 (liquid/ Al/ Si/ Mg<sub>2</sub>Si), point 2 (liquid/ Al/ Al<sub>140</sub>Mg<sub>89</sub>/ Mg<sub>2</sub>Si), point 3 (liquid/  $\gamma$ -AlMg/ Al<sub>140</sub>Mg<sub>89</sub>/ Mg<sub>2</sub>Si), and point 4 (liquid/  $\gamma$ -AlMg/ Mg/ Mg<sub>2</sub>Si). According to the composition of Mg (up to 10 wt%), three alloy coordinates are determined in the region near the univariant point 1, illustrated in the Figure 4.4 showing a detailed view.

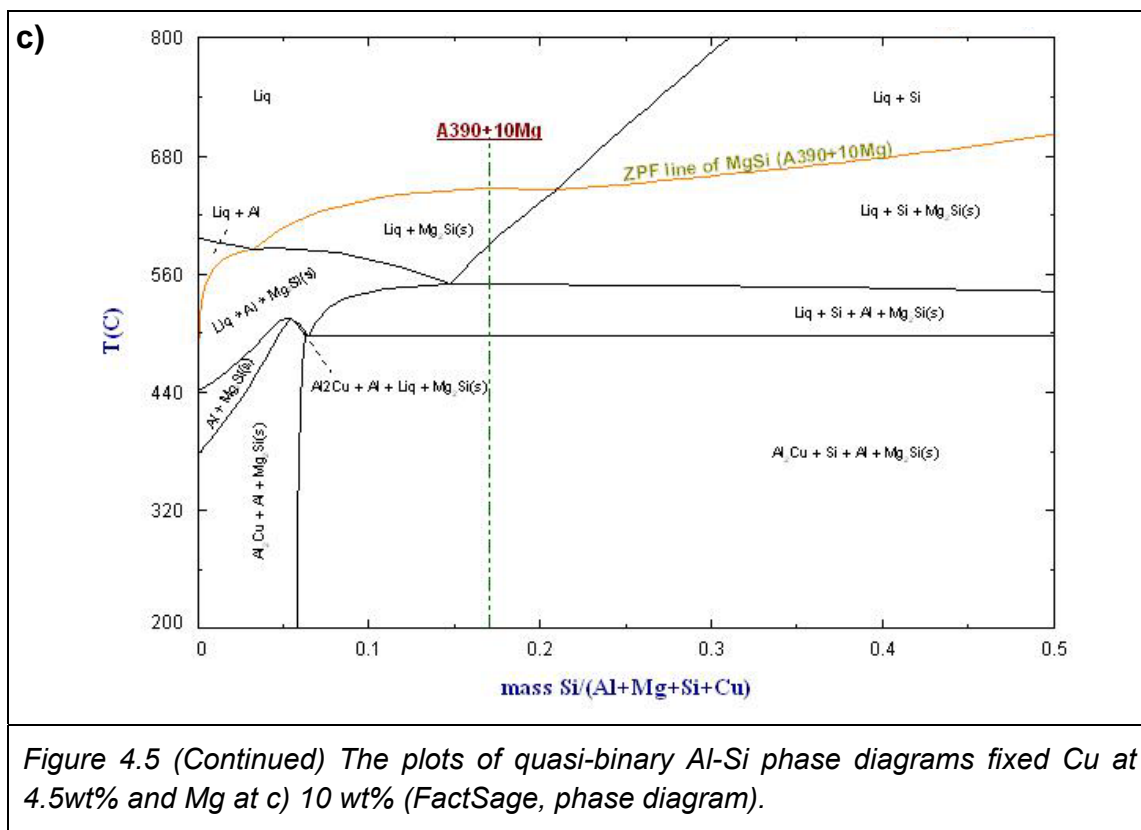
The solidification behaviour of these alloys, therefore, was studied in detail by considering precipitation sequence of the liquid alloy overall composition starting at point A, C, and F during equilibrium cooling process. For alloy A390, the solidification starts at 653.17°C from point A where primary Si is precipitated from the liquid solution on cooling, along line A-B until Al-Si eutectic point B is reached. The liquid continues solidifying forming the eutectic Al-Si along the univariant line from point B to the univariant point E where four phases (liquid/ Al/ Si/  $Mg_2Si$ ) are in equilibrium at 550.61°C. For the 6wt% Mg alloy, the starting point C at 613.27°C is still in the region where the primary Si is first crystallized along the cooling direction line C-D to point D. Next, the primary  $Mg_2Si$  begins to appear in the matrix and follows the cooling path D-E from point D to the

univariant point E. For the 10wt% Mg alloy, primary  $\text{Mg}_2\text{Si}$  first precipitates from liquid solution at  $646.18^\circ\text{C}$  at point F. Subsequently, primary Si is observed when the point G is reached along line F-G and the solidification will proceed from point F to the univariant point E where the ternary eutectic reaction  $\text{Liq.} \rightarrow \text{Al} + \text{Si} + \text{Mg}_2\text{Si}$  takes place. Note that the  $\theta\text{-Al}_2\text{Cu}$  phase is absent from this liquidus projection of ternary phase diagram because it is generally precipitated below any liquidus surfaces as seen in the binary alloy systems.

#### 4.2.3. Isopleth binary Al-Si phase diagrams

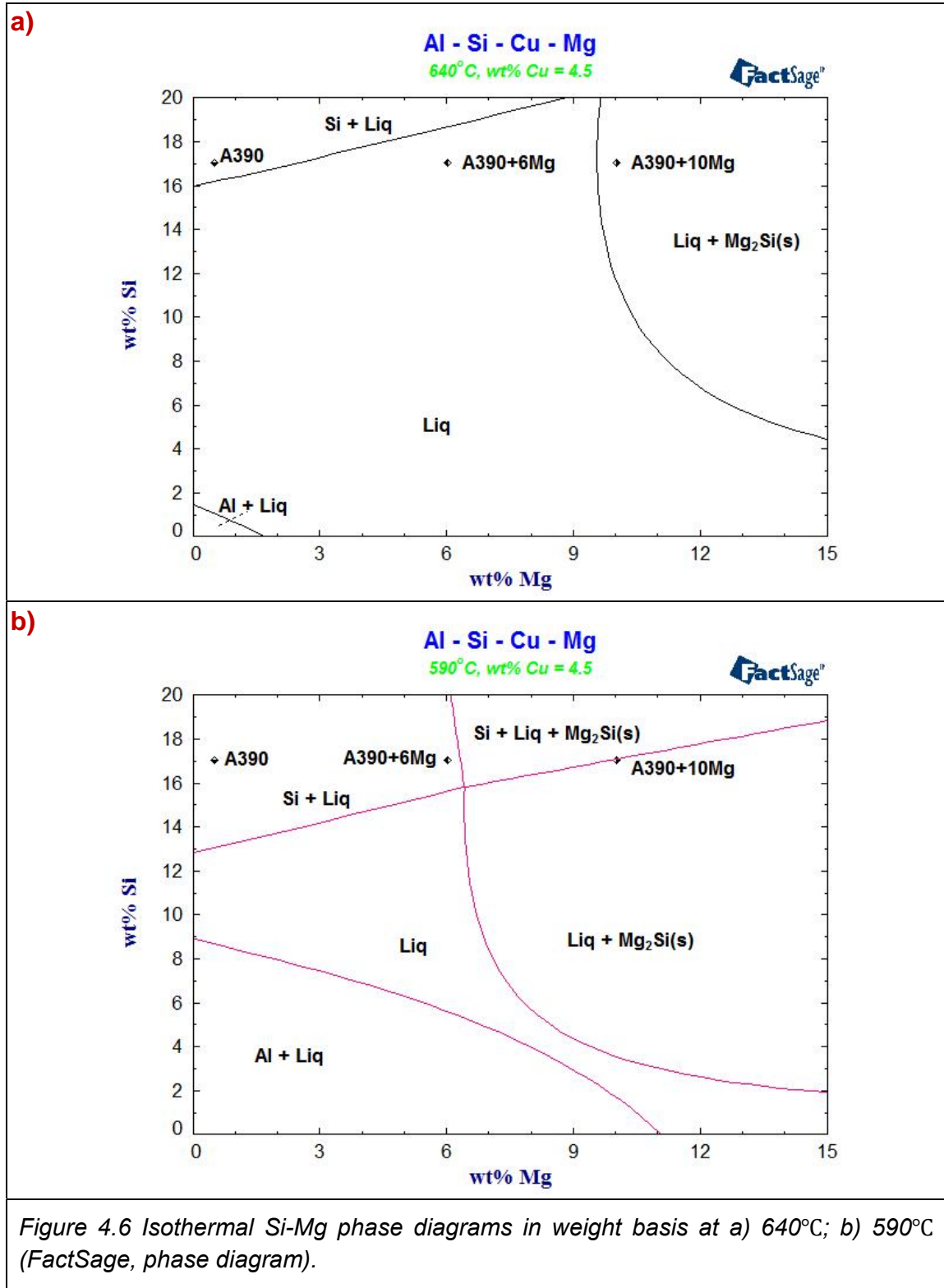
Three quasi-binary Al-Si phase diagrams are plotted at fixed Cu (4.5 wt%) with variable Mg content (0.5, 6, 10 wt%), showing the tendency of increasing the Mg value on the  $\text{Mg}_2\text{Si}$  precipitation (Ardakan, 2006). Figures 4.5 a), b), c) confirm that the precipitation course for primary phases is changed to the  $\text{Mg}_2\text{Si}$  region from the Si area with the addition of Mg. However, the binary eutectic point is also shifted to a lower temperature, which is similar to the alloy with modifiers such as sodium (Na) or strontium (Sr). These additions have no influence on the quaternary decomposition temperature ( $496.94^\circ\text{C}$  in all cases) where the last liquid is solidified.

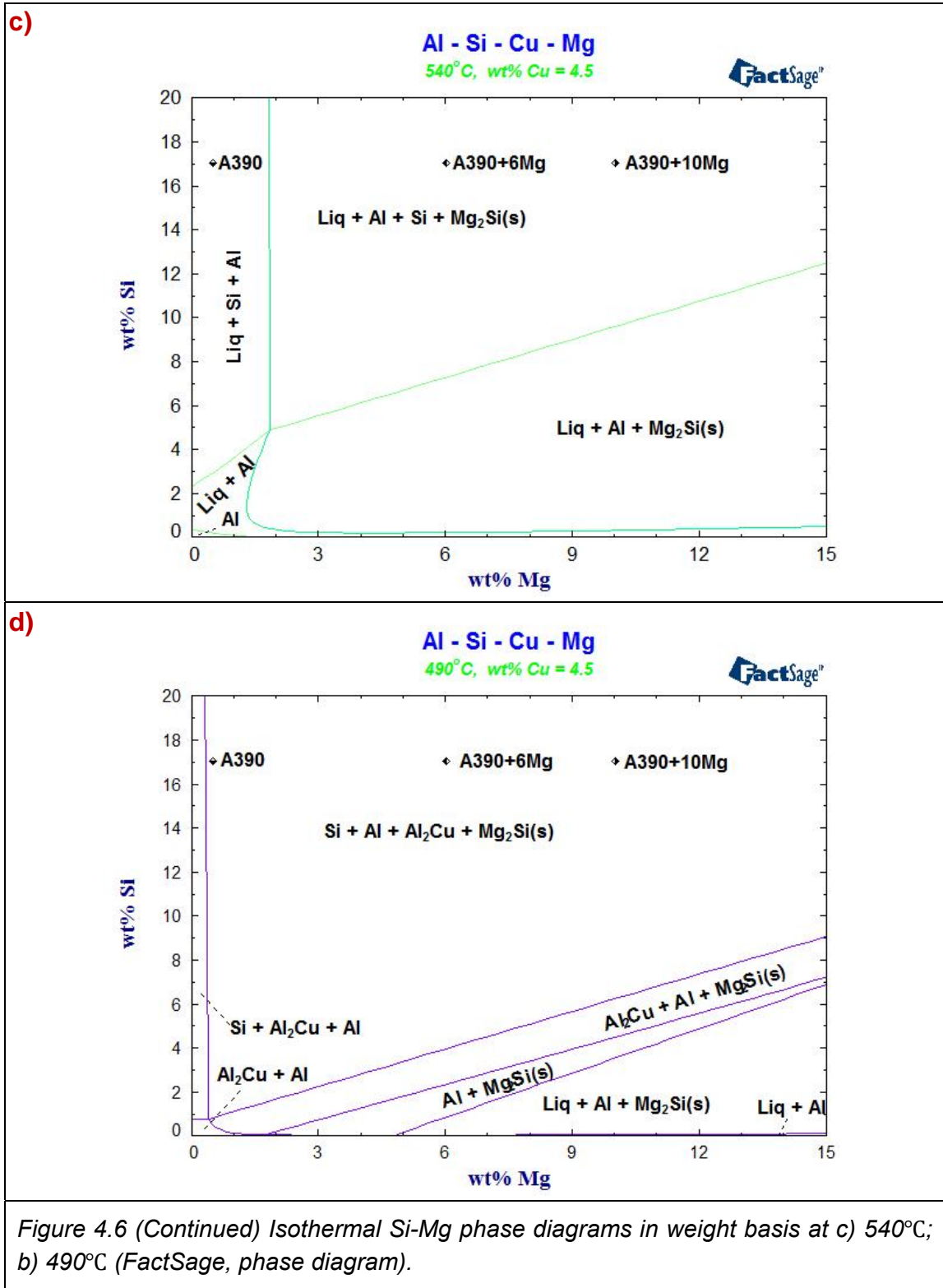




#### 4.2.4. Isothermal quasi-binary Si-Mg phase diagrams

The phase transformation from the liquid to the solid undergoes a series changes upon cooling. The stable precipitations of alloys with increasing Mg content can be expressed as the isothermal process in which the Si to Mg ratio dominates. As seen in the Figure 4.6 d), the liquid phase appears for all three alloys at 640°C, A390 alloy contains primary Si at this temperature and the 10wt% Mg alloy consists of  $\text{Mg}_2\text{Si}$ . The 6wt% Mg alloy is however entirely liquid (the liquidus temperature at 613°C).





On decreasing the temperature, the 6wt% Mg alloy precipitates primary Si at 590°C while the 10wt% Mg alloy is at the boundary where the primary Si and Mg<sub>2</sub>Si are present. The binary eutectic reaction (Liq.  $\rightarrow$   $\alpha$ -Al + Si) occurs at 540°C for A390 alloy while the ternary eutectic reaction (Liq.  $\rightarrow$   $\alpha$ -Al + Si + Mg<sub>2</sub>Si) for 6wt% and 10wt% Mg alloys occurs at same temperature. Finally, all remaining liquid will disappear at 490°C to attain the quaternary  $\alpha$ -Al, Si,  $\theta$ -Al<sub>2</sub>Cu, and Mg<sub>2</sub>Si phases for all three alloys.

#### 4.3. Equilibrium calculations – alloy decomposition behaviours

FactSage 4.6 provides a platform to calculate the alloy decompositions during the solidification process in the “Equilib” module. The species selected for this calculation also have four solution phases (FSlite-liquid, FSlite-Al<sub>2</sub>Cu, FSlite-Si, and FSlite-Al) and one compound (Mg<sub>2</sub>Si). Note that, the “FSlite-liquid” is set to the solidification target marked as “D” in the “solution” frame before going to the transition calculation with a starting temperature “700°C” and a fixed “A” value (Mg content). There are two options, equilibrium and Scheil cooling, each of which can be chosen when the “solidification” target is set, describing the different solidification behaviours in Al-17Si-4.5Cu-xMg alloy system. The Tables 4.2-4.5 and Figures 4.7-4.9 fully summarize the solidification behaviours for the three different alloys for both equilibrium and Scheil cooling conditions, denoting the transition temperature for different alloy decompositions and the fraction solids for each phase.



*Table 4.2 The summary of phase equilibrium decompositions in all transition points for Mg added A390 alloys (FactSage, Equilibrium).*

Alloy	Solidification range (°C)		Decomposition ( <b>equilibrium</b> )	Solid fraction Acc. (%)
A390	653.17 – 566.27	86.90	Liq. → primary Si	6.06
	566.27 – 502.46	63.81	Liq. → Si + Al	94.06
	502.46 – 496.94	5.52	Liq. → Si + Al + Mg <sub>2</sub> Si (eutectic)	96.08
	496.94 (iso-T)	156.23 <sup>k</sup>	Liq. → Si + Al + Mg <sub>2</sub> Si + $\theta$ -Al <sub>2</sub> Cu	100.00
A390 + 6Mg	613.27 – 584.63	28.64	Liq. → primary Si	1.98
	584.63 – 549.72	34.91	Liq. → Si + primary Mg <sub>2</sub> Si	7.24
	549.72 – 496.94	52.78	Liq. → Si + Al + Mg <sub>2</sub> Si (eutectic)	95.15
	496.94 (iso-T)	116.33 <sup>k</sup>	Liq. → Si + Al + Mg <sub>2</sub> Si + $\theta$ -Al <sub>2</sub> Cu	100.00
A390 + 10Mg	646.18 – 588.99	57.19	Liq. → primary Mg <sub>2</sub> Si	6.40
	588.99 – 549.27	39.72	Liq. → primary Si + Mg <sub>2</sub> Si	12.14
	549.27 – 496.94	52.33	Liq. → Si + Al + Mg <sub>2</sub> Si (eutectic)	94.47
	496.94 (iso-T)	149.24 <sup>k</sup>	Liq. → Si + Al + Mg <sub>2</sub> Si + $\theta$ -Al <sub>2</sub> Cu	100.00

*Table 4.3 The summary of equilibrium phase fraction solids in all transition points for Mg added A390 alloys (FactSage, Equilibrium).*

Alloy	T trans. (°C)	Phase fraction Acc. (%) ( <b>equilibrium</b> )				Liquid fraction (%)
		Si	Al	Mg <sub>2</sub> Si	$\theta$ -Al <sub>2</sub> Cu	
A390	653.17	-	-	-	-	100.00
	566.27	6.06	-	-	-	93.94
	502.46	15.89	78.17	-	-	5.94
	496.94*	16.03	79.95	0.10	-	3.92
	496.94*	16.25	81.48	0.24	2.03	0.00
A390 + 6Mg	613.27	-	-	-	-	100.00
	584.63	1.98	-	-	-	98.02
	549.72	4.35	-	2.89	-	92.76
	496.94*	12.84	73.52	8.79	-	4.85
	496.94*	13.10	75.43	8.96	2.51	0.00
A390 + 10Mg	646.18	-	-	-	-	100.00
	588.99	-	-	6.40	-	93.60
	549.27	2.57	-	9.57	-	87.86
	496.94*	10.52	68.85	15.10	-	5.53
	496.94*	10.82	71.02	15.30	2.86	0.00

<sup>k</sup> Total solidification range (°C) under equilibrium cooling condition.

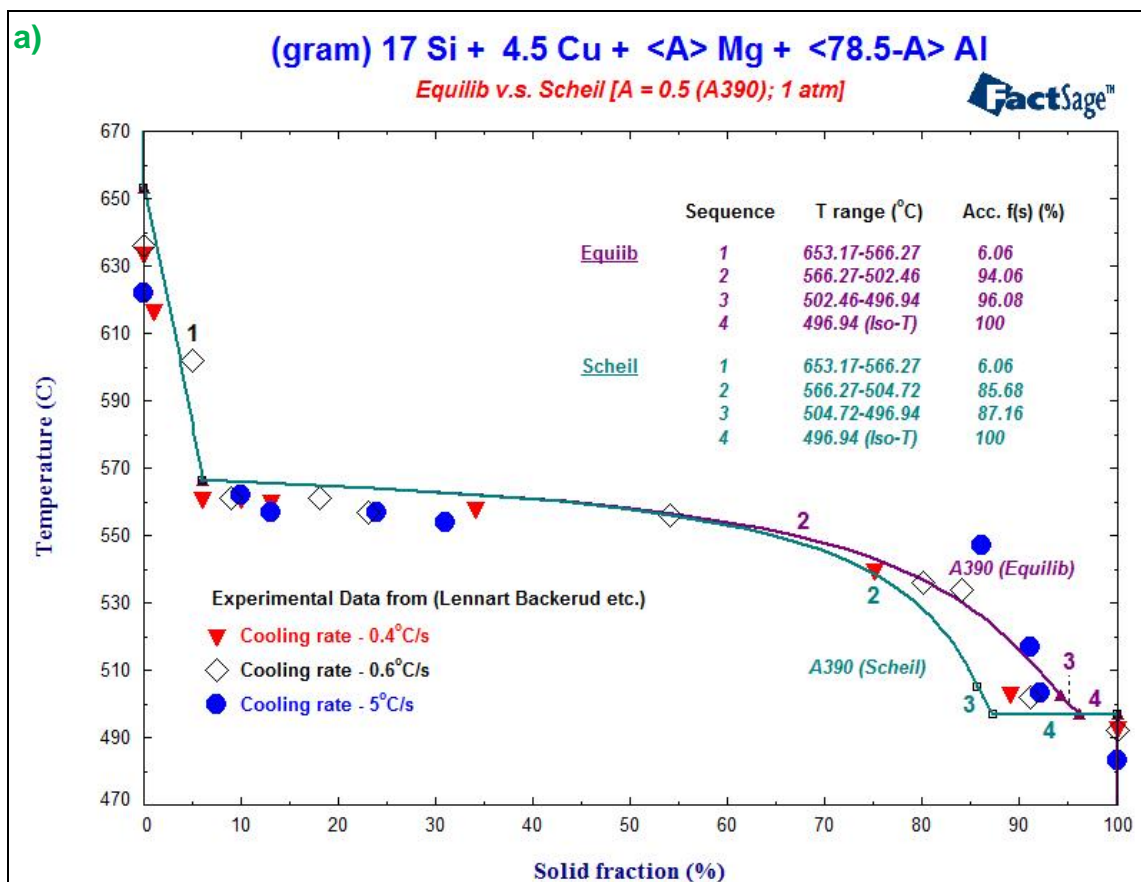
*Table 4.4 The summary of phase scheil cooling decompositions in all transition points for Mg added A390 alloys (FactSage, Equilibrium).*

Alloy	Solidification range (°C)		Decomposition ( <b>scheil cooling</b> )	Solid fraction Acc. (%)
A390	653.17 – 566.27	86.90	Liq. → primary Si	6.06
	566.27 – 504.72	61.55	Liq. → Si + Al	85.68
	504.72 – 496.94	7.78	Liq. → Si + Al + Mg <sub>2</sub> Si (eutectic)	87.16
	496.94 (iso-T)	156.23 <sup>1</sup>	Liq. → Si + Al + Mg <sub>2</sub> Si + $\theta$ -Al <sub>2</sub> Cu	100.00
A390 + 6Mg	613.27 – 584.63	28.64	Liq. → primary Si	1.98
	584.63 – 549.72	34.91	Liq. → Si + primary Mg <sub>2</sub> Si	7.24
	549.72 – 496.94	52.78	Liq. → Si + Al + Mg <sub>2</sub> Si (eutectic)	87.03
	496.94 (iso-T)	116.33 <sup>1</sup>	Liq. → Si + Al + Mg <sub>2</sub> Si + $\theta$ -Al <sub>2</sub> Cu	100.00
A390 + 10Mg	646.18 – 588.99	57.19	Liq. → primary Mg <sub>2</sub> Si	6.40
	588.99 – 549.27	39.72	Liq. → primary Si + Mg <sub>2</sub> Si	12.14
	549.27 – 496.94	52.33	Liq. → Si + Al + Mg <sub>2</sub> Si (eutectic)	86.96
	496.94 (iso-T)	149.24 <sup>1</sup>	Liq. → Si + Al + Mg <sub>2</sub> Si + $\theta$ -Al <sub>2</sub> Cu	100.00

*Table 4.5 The summary of scheil cooling phase fraction solids in all transition points for Mg added A390 alloys (FactSage, Equilibrium).*

Alloy	T trans. (°C)	Phase fraction Acc. (%) ( <b>scheil cooling</b> )				Liquid fraction (%)
		Si	Al	Mg <sub>2</sub> Si	$\theta$ -Al <sub>2</sub> Cu	
A390	653.17	-	-	-	-	100.00
	566.27	6.06	-	-	-	93.94
	504.72	14.99	70.69	-	-	14.32
	496.94*	15.13	71.93	0.10	-	12.84
	496.94*	15.83	76.97	0.56	6.64	0.00
A390 + 6Mg	613.27	-	-	-	-	100.00
	584.63	1.98	-	-	-	98.02
	549.72	4.35	-	2.89	-	92.76
	496.94*	12.24	66.41	8.38	-	12.97
	496.94*	12.95	71.51	8.84	6.70	0.00
A390 + 10Mg	646.18	-	-	-	-	100.00
	588.99	-	-	6.40	-	93.60
	549.27	2.57	-	9.57	-	87.86
	496.94*	9.97	62.27	14.72	-	13.04
	496.94*	10.68	67.39	15.19	6.74	0.00

<sup>1</sup> Total solidification range (°C) under scheil cooling condition.



## EQUILIBRIUM COOLING

b)

CONSTITUENTS AND PHASES AT 496.94 C  
(temperature of final disappearance of Liq)

CONS.	PHASE	TOTAL AMT/gram
1	1 Si	6.0570E+00
2	1 Si	9.8307E+00
2	2 Al	7.8167E+01
3	1 Si	1.4651E-01
3	2 Al	1.7772E+00
3	3 Mg2Si	1.0075E-01
4	1 Al2Cu	2.0259E+00
4	2 Si	2.1419E-01
4	3 Al	1.5402E+00
4	4 Mg2Si	1.4078E-01

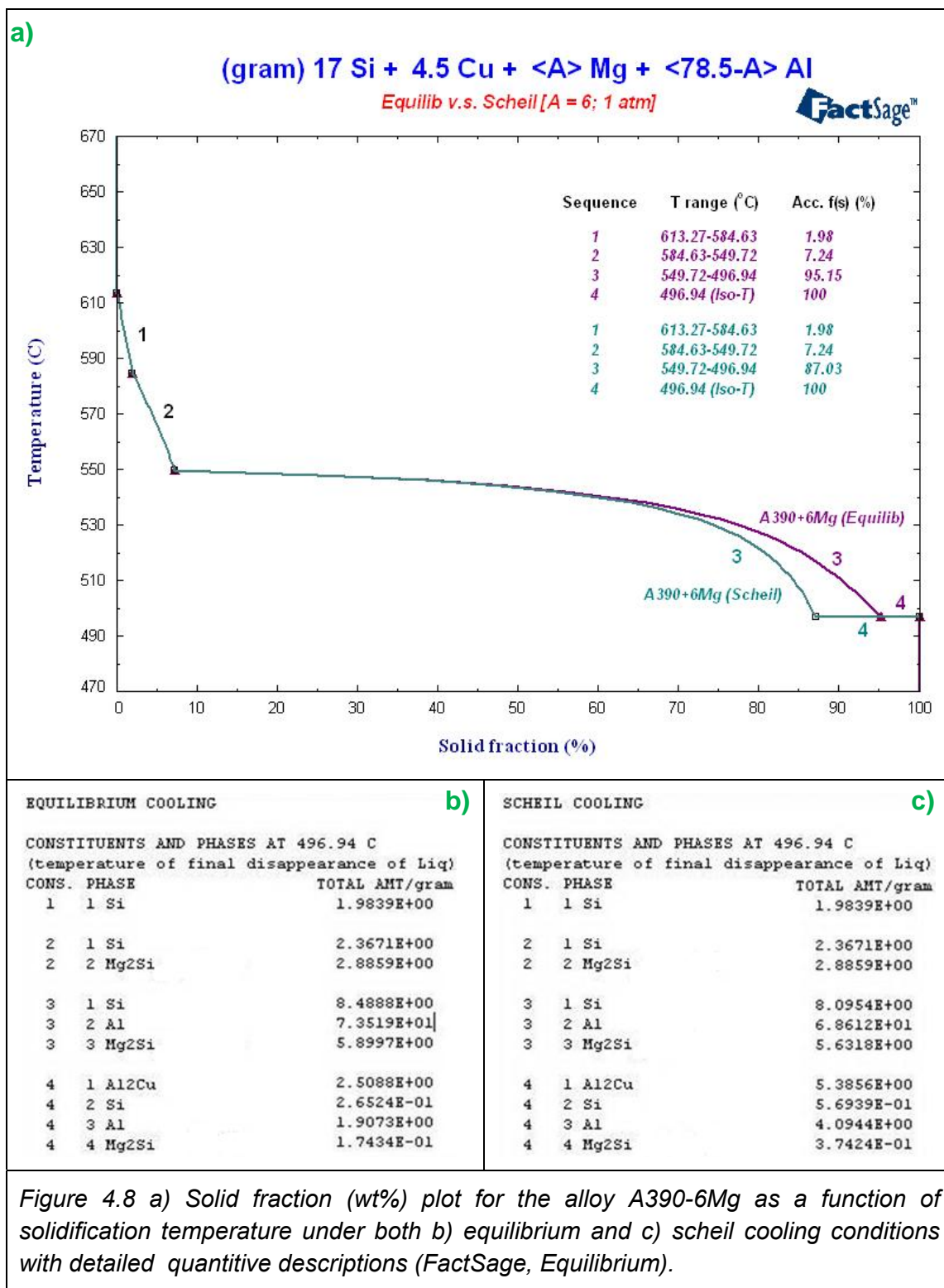
## SCHEIL COOLING

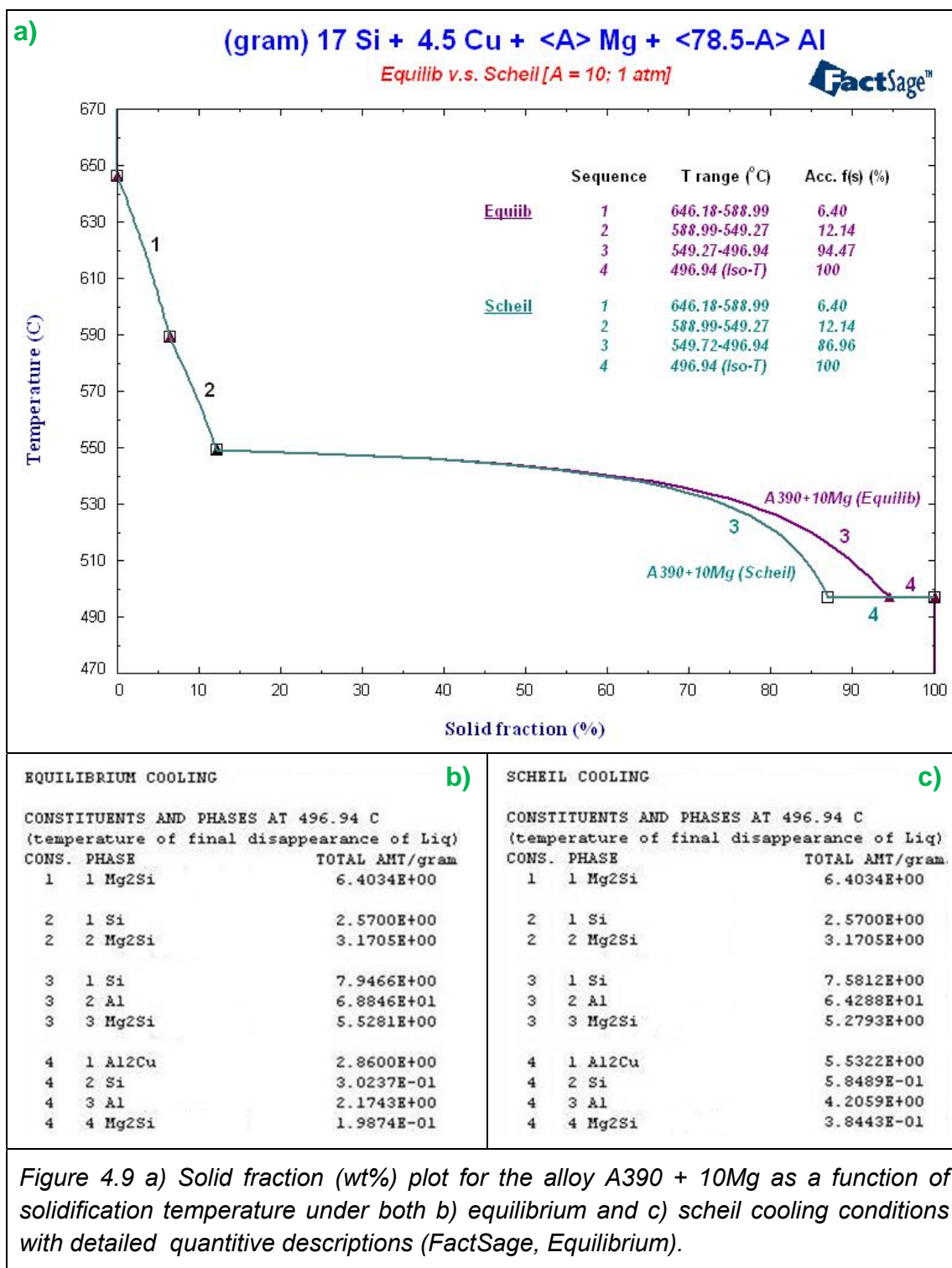
c)

CONSTITUENTS AND PHASES AT 496.94 C  
(temperature of final disappearance of Liq)

CONS.	PHASE	TOTAL AMT/gram
1	1 Si	6.0570E+00
2	1 Si	9.1139E+00
2	2 Al	7.2060E+01
3	1 Si	1.0645E-01
3	2 Al	9.5399E-01
3	3 Mg2Si	7.8318E-02
4	1 Al2Cu	6.0088E+00
4	2 Si	6.3528E-01
4	3 Al	4.5682E+00
4	4 Mg2Si	4.1755E-01

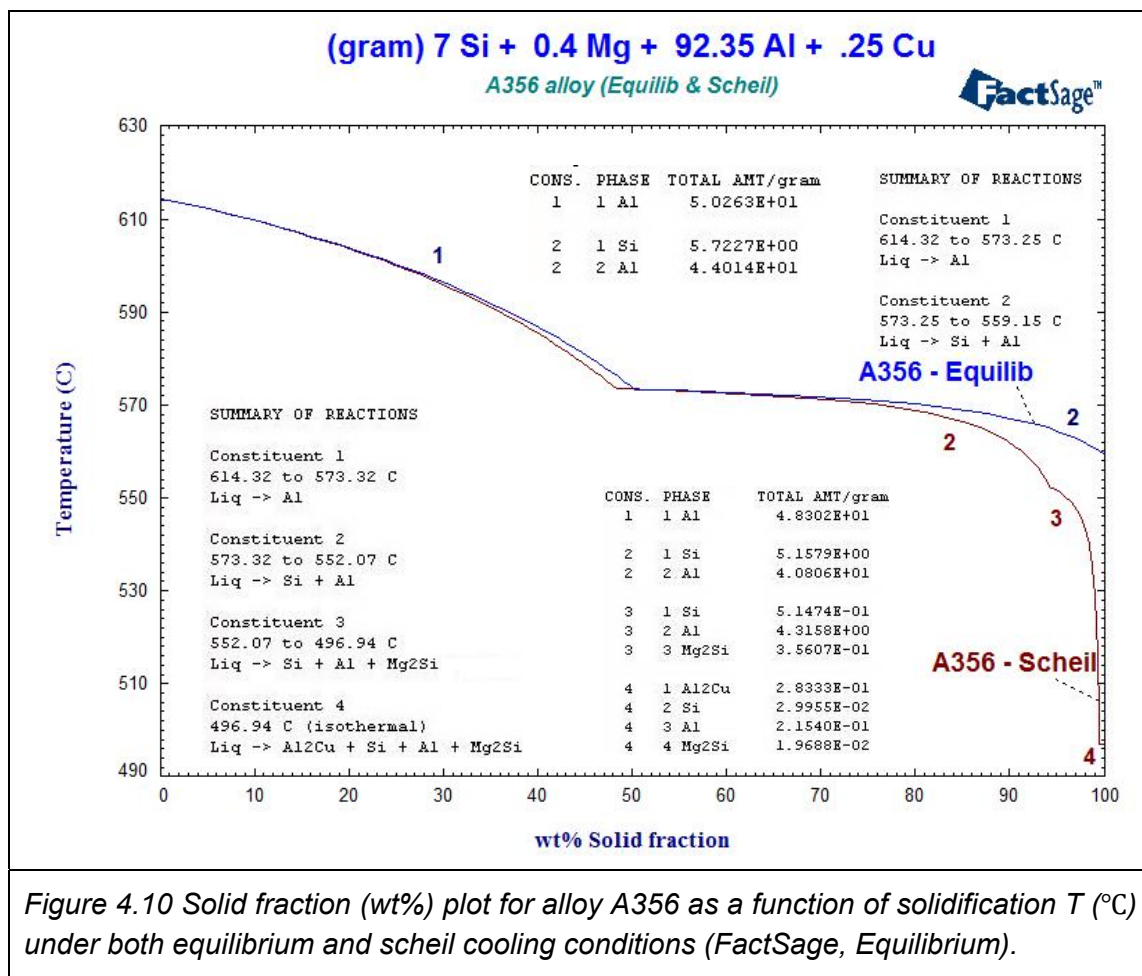
Figure 4.7 a) Solid fraction (wt%) plot for the alloy A390 as a function of solidification temperature under both b) equilibrium and c) scheil cooling conditions with detailed quantitative descriptions (FactSage, Equilibrium). In addition, a group of experimental data is also presented in three different cooling rates as a comparison (Backerud, Chai, & Tamminen, 1990).





As summarized above, the primary reaction occurs in a temperature interval of 86.90°C, 63.55°C, and 96.91°C for the alloy A390 with a solid fraction at 6.06 wt%, with 7.24 wt% for the 6wt% Mg alloy, and with 12.14 wt% for the 10wt% Mg alloy respectively. However, the subsequent eutectic decompositions of the three alloys retain solid fractions of 79.62 wt%, 79.79 wt%, and 74.82 wt% over a corresponding solidification range of 63.81°C, 52.78°C, and 52.33°C. At end of the primary reactions, the solid fraction is found to be more sensitive on further cooling. Meanwhile, only a small deviation is observed in all three alloys between equilibrium cooling and Scheil cooling conditions. There is also a small temperature region before the quaternary reactions at 496.94 °C where the equilibrium state is reached more gradually than for Scheil cooling.

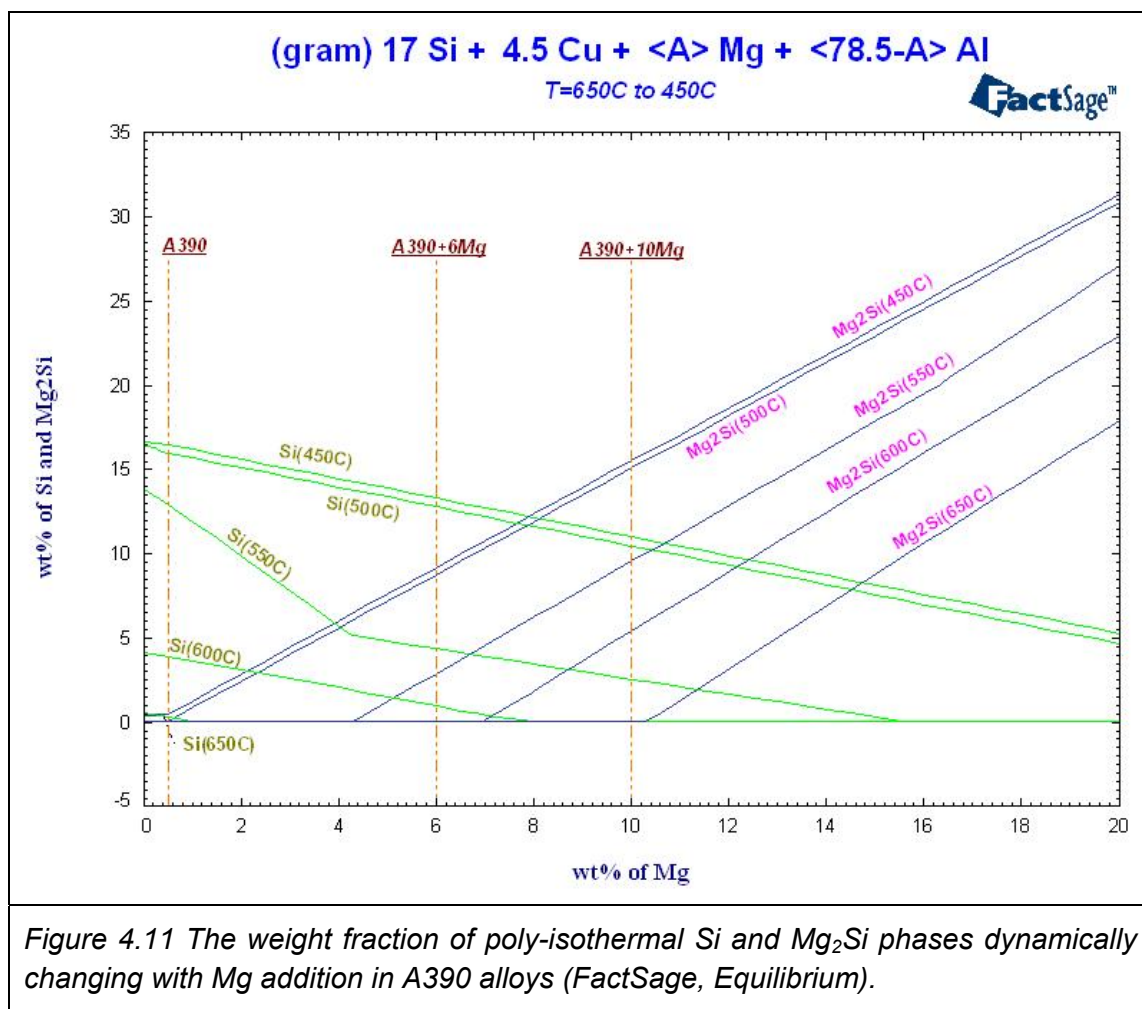
The solid fraction determination from the above analysis provides an important indication for semi-solid die casting applications in which the semi-solid slurry must be maintained in an isothermal and homogeneous state before die injection. There are two requirements for semi-solid processing (Ogris, 2002). The first is that the material used for semi-solid must have a wide solidification interval with a continuous transition from the liquid to the solid. All three alloys show a wide solidification range (156.23°C for A390, 116.33°C for 6wt% Mg, and 149.24 °C for 10wt% Mg) and have the tendency for continuous phase transformation even though there are sharp gradients for all three alloys soon after the eutectic reaction takes place (Figures 4.7-4.9).



For hypoeutectic Al-Si alloy (A356), sufficient solid 50%  $\alpha$ -Al is produced at 570°C (Figure 4.10). The solid fraction of primary Si or Mg<sub>2</sub>Si in hypereutectic Al-Si alloys is only ~6 wt% to 12 wt% solids, which require additional precipitates from the eutectic phases to be formed for semi-solid processing (C.G. Kang, 2008). This necessitates the precise control processing temperature in order to maintain the desired solid fraction, which increases sharply once the eutectic reaction begins.



Another important parameter for the semi-solid processing is to transform the dendrites to more globular morphologies by non-chemical means, such as mechanical or magnetic stirring, in order to break down the dendrites structures and release the excess heat produced during the solidification.



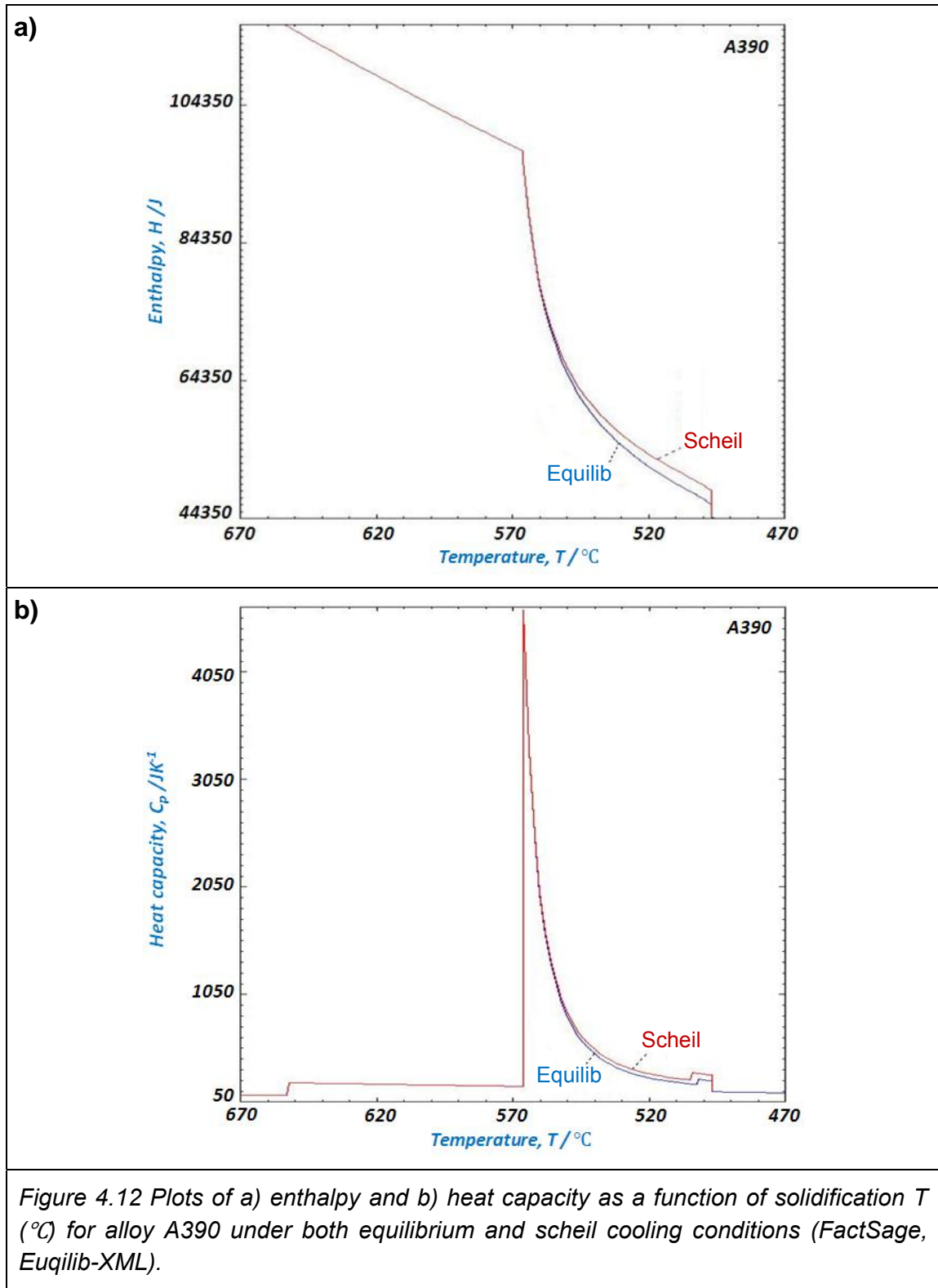
The weight fractions of the Si and  $Mg_2Si$  phases in alloys with increasing Mg content is plotted as a function of the Mg contents shown in the Figure 4.11 for a series of iso-thermal (450-650°C) conditions, driving the formation of  $Mg_2Si$

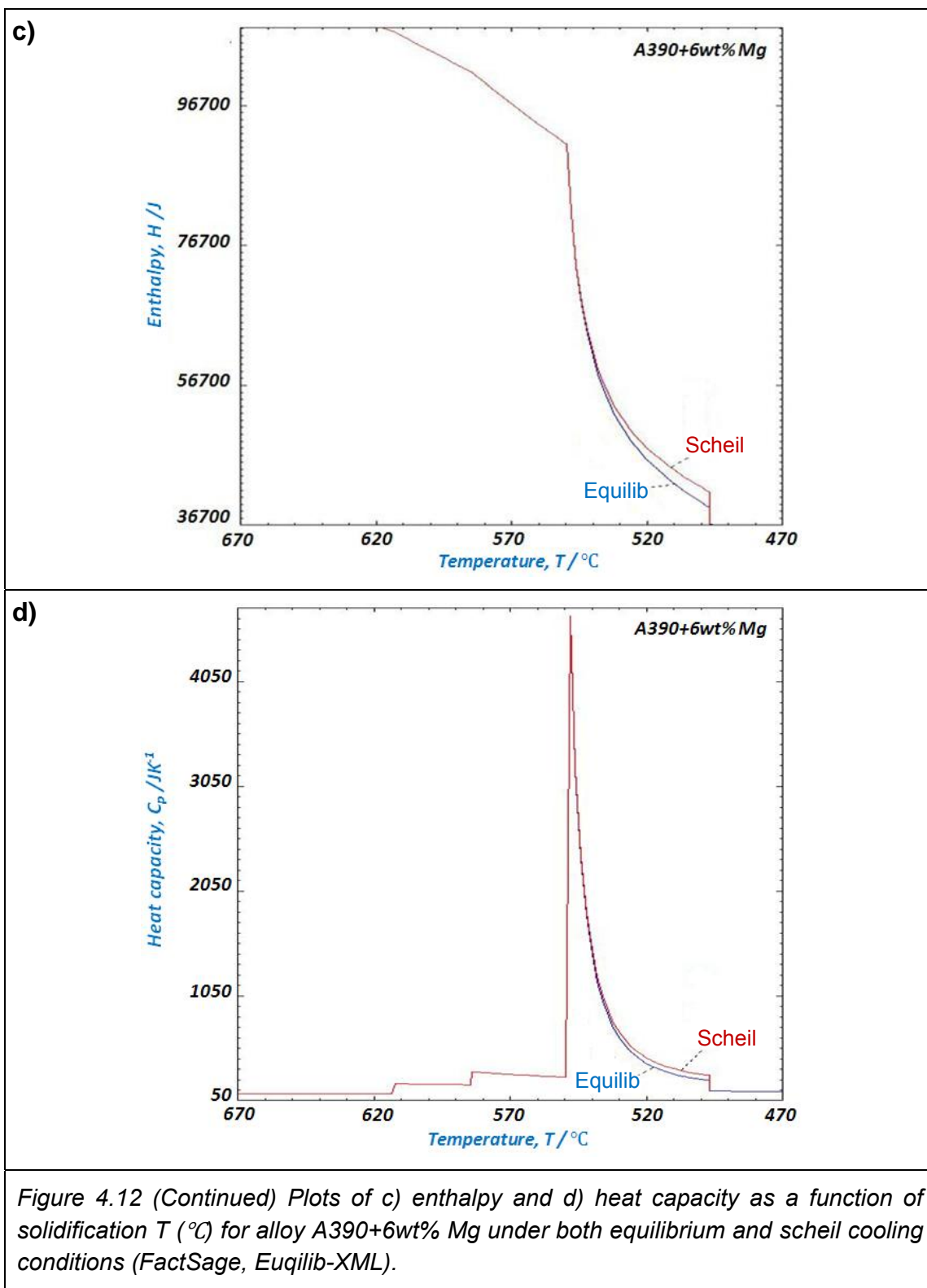


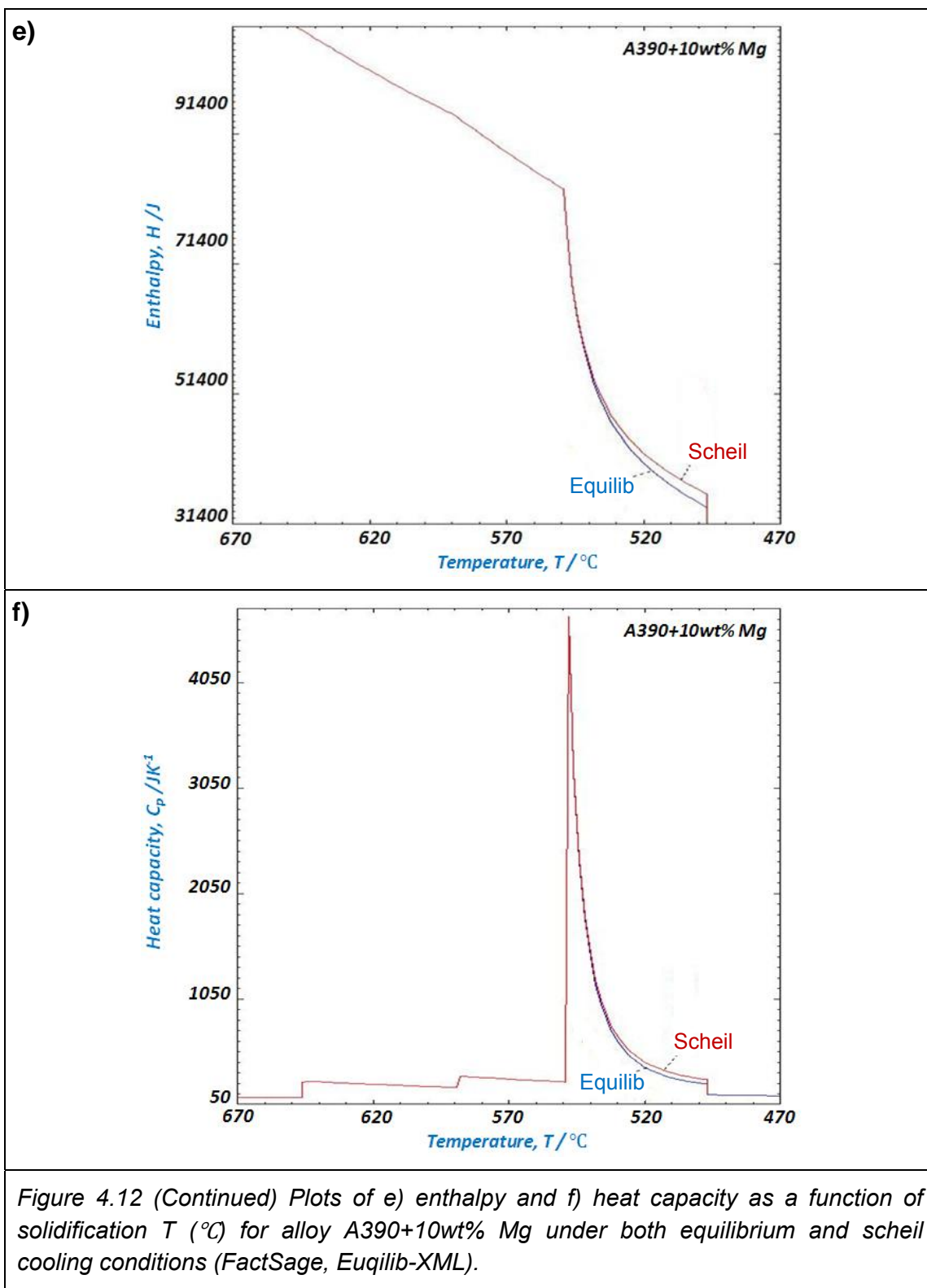
along with the disappearance of Si. By considering the single phase transformation (Table 4.3 and Table 4.5), the  $\text{Mg}_2\text{Si}$  might be produced mainly by consuming the Si portion, which is used to form the primary Si instead of the eutectic Si. The eutectic Si attains the similar solid fraction for all three alloys (9.77%, 8.60%, and 8.11wt%), differing from the primary Si (6.06%, 4.35 %, and 2.57 wt% respectively).

#### **4.4. Enthalpy (H) and heat capacity ( $C_p$ )**

The variable enthalpy (H) along the solidification path for the three alloys (A390, 6wt% Mg, and 10wt% Mg) is plotted in the Figures 4.12 a), c) and e), which exhibit a small deviation between the equilibrium and Scheil cooling conditions. The enthalpy curves for A390 alloy decrease gradually from 566°C to 496°C (binary Al-Si eutectic reactions), which fits well to the corresponding solid fraction trends plotted in the Figure 4.7. In contrast, the same type of curves for 6 and 10wt% Mg alloys show a steeper enthalpy gradient from 549°C to 496°C (ternary Al-Si- $\text{Mg}_2\text{Si}$  eutectic reactions). Moreover, there is an iso-thermal enthalpy change at 496°C where the quaternary eutectic reaction takes place for all three alloys. The ternary eutectic  $\text{Mg}_2\text{Si}$  in A390 alloy seems to have no influence on the enthalpy change as observed, which is probably because of its quite small solid concentration.







The heat capacity ( $C_p$ ) curves versus the solidification temperature ( $T$ ) for three alloys are plotted in the Figures 4.12 b), d), f), which represent more visually the enthalpy difference from the enthalpy curves in accordance with the latent heat of the freezing during the solidification. Therefore, most of the energy lost can be attributed to a single temperature where the eutectic reaction begins for all three alloys, referring to the peak in each graph.

## CHAPTER 5. Results and discussion

### 5.1. Casting practice

During casting processes, defects, such as porosities, oxide film entrapment are not easily avoided. In aluminum alloys, the alloying elements can alter the melt behaviour which influences the cast component properties. Magnesium not only plays an important role in the current alloy system for a significant structure changes, but also affects the aluminum melt with regard to castability, fluidity, surface oxide film formation, and hydrogen gas entrapment. Therefore, it is necessary to study the effects of Mg additions on aluminum alloys using sound foundry practices.

#### 5.1.1. Surface films

<i>Table 5.1 A summary of the melt oxide film forming along with Mg addition in an Al-Mg alloy system (Compbell, 2003).</i>			
wt% of Mg content	Film structure	Film thickness	Film characters
$\leq 0.005$	Pure alumina $\text{Al}_2\text{O}_3$	20~50nm	Thin & smooth as newly formed; Fine creases & folds
0.005~2	Spinel $\text{Al}_2\text{MgO}_4$	-	Crystal clusters
$\geq 2$	Pure magnesia $\text{MgO}$	200~500nm	Wrinkled oxide films

Evidence has shown that the oxide films of an aluminum melt are strongly influenced by the Mg addition as summarized in the Table 5.1 (Compbell, 2003). Alumina films ( $\alpha$ - or  $\beta$ - $\text{Al}_2\text{O}_3$ ) occur only for alloys with Mg contents smaller than 0.005 wt%. However, if the Mg is higher than 0.005 wt%, it will tend to form a spinel ( $\text{Al}_2\text{MgO}_4$ ) film for values less than 2 wt% Mg or a magnesia ( $\text{MgO}$ ) film for higher values.

Figure 5.1 shows various cast surface morphologies of both the flat tensile bars and sample overflows. The standard A390 alloy contains ~0.29 wt% Mg, exhibiting a coarse sand paper liked spinel oxide film (Figure 5.1 a) and b)) with oxide clusters floating to the melt surface. The phosphorous (0.01 wt%) modified A390 alloy showed a cellular surface profile resulted from the loss of last remaining liquids among those fast growing cellular tips (Figure 5.1 c) and d)), which is different from the conventional A390 castings. It seems that the phosphorous addition alters the temperature gradient for the A390 solidification behaviour. Surface oxide films can also consist of a thick wrinkled magnesia structure for the 6 or 10wt% Mg alloys even with bismuth modification. The melt surface formed a smooth magnesia film at beginning of the solidification in contact with the air as observed in the overflow surface. After complete solidification, however, the magnesia layer formed a corrugated surface profile (Figure 5.1 e)).

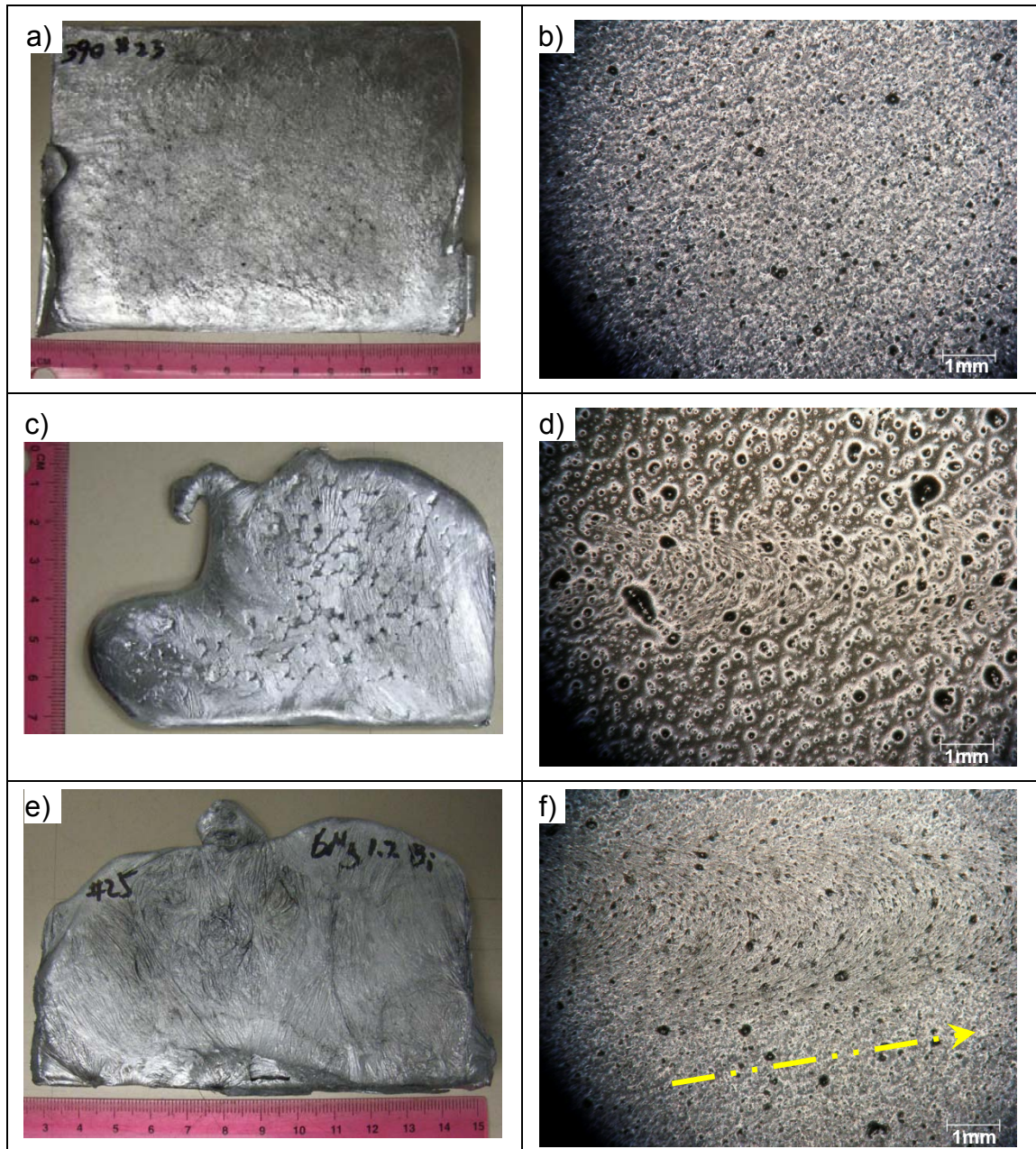
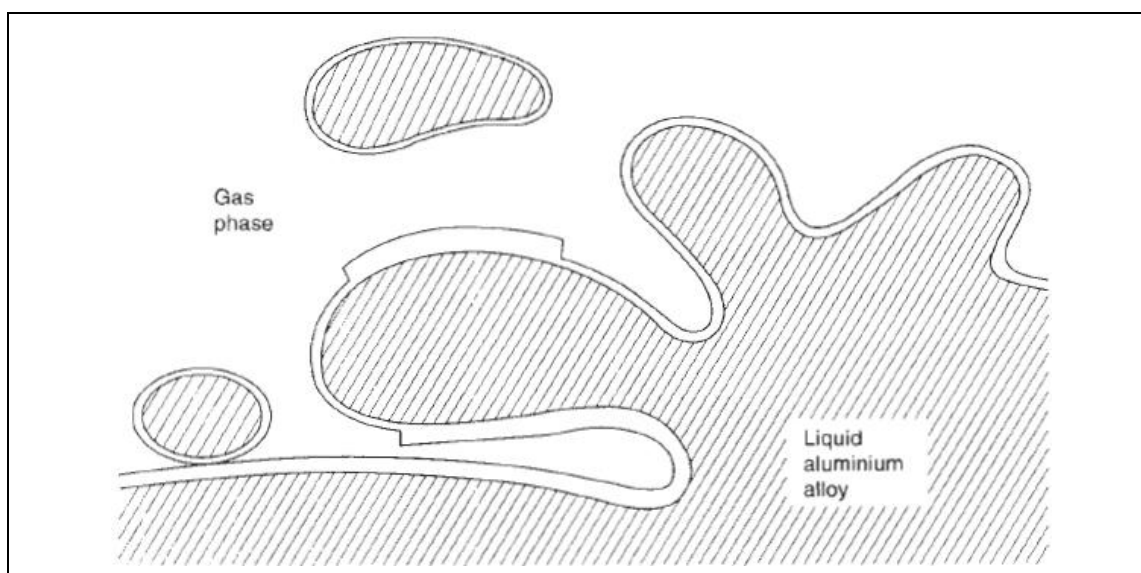


*Figure 5.1 Types of oxide film on the Mg added A390 casting surface from: melt over flow collected in a metallic basin and cast flat tensile bars for alloy a),b) A390; c),d) A390-0.01P; and e),f) A390-6Mg-1.2Bi respectively.*

If the same situation applies to solidification of the melt in a closed permanent metallic mould, the feeding liquid from the bottom to the top has to overcome the



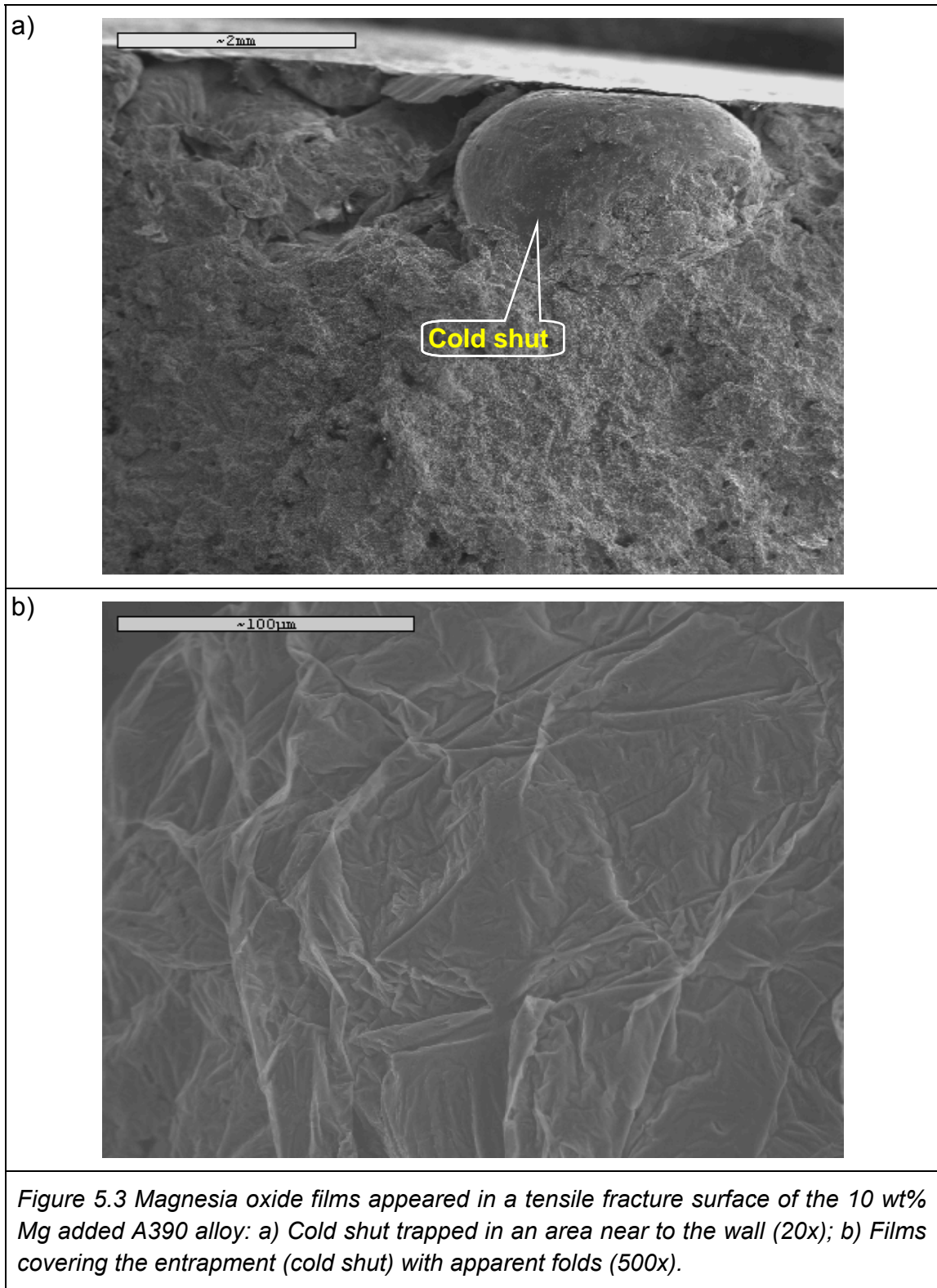
interfacial tension force exerted between the magnesia films and the metallic wall, especially for non coated moulds. Figure 5.1 f) shows this holding back phenomenon with the striation traces on the surface films of a 6 wt% Mg alloy. The arrow indicates the melt flow direction. This has a negative effect on fluidity.

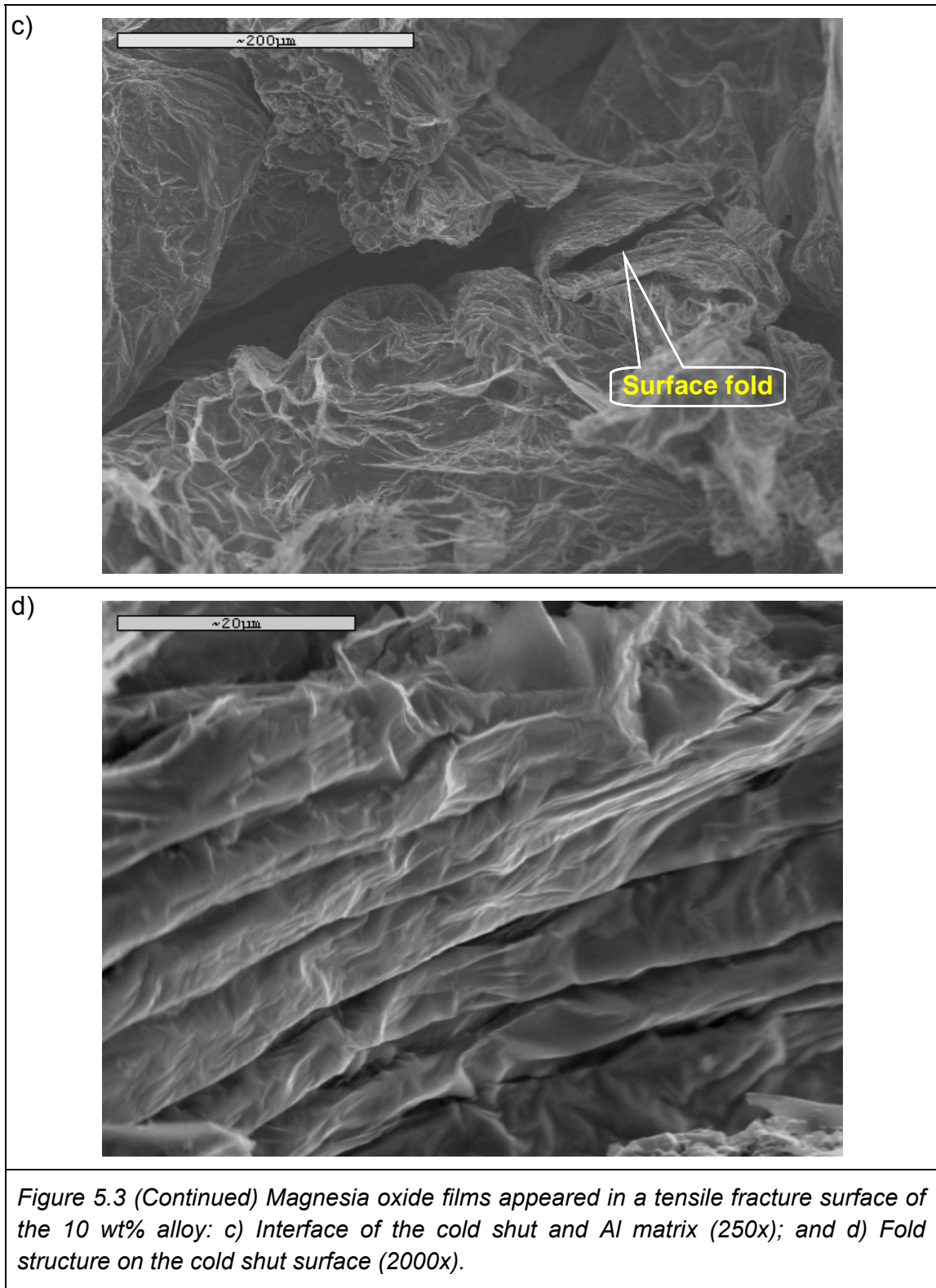


*Figure 5.2 Molten liquid with the turbulent front illustrating the mechanism of the bi-film formation and surface entrainment (Compbell, 2003).*

The mechanism of the magnesia film formation has been reported by (Compbell, 2003) resulting from the magnesium evaporation for alloys containing Mg as low as 0.4 wt% resulting in the growth of a continuous oxide film at the liquid surface. Although the oxide layer might be broken by stretching or other physical forces, a re-forming of the films often takes place instantly. These films could possibly be entrapped in the melt during the casting process combined with bubbles, inclusions or the liquid itself as shown in the Figure 5.2. Two component films,

also called bi-films, are commonly present in castings, combining with other entrapments. Figure 5.3 b) and d) illustrate an integral magnesia oxide film fully wrapping around a cold shut defect ( $\sim \varnothing 2mm$ , Figure 5.3 a)) as observed from a SEM secondary electron image of the tensile fracture surface of the 10 wt% Mg alloy casting at a position near the mould wall. This is caused by the turbulence from pouring which can cause liquid drops to form in front of the liquid surface and which can become entrapped. This can act like an inclusion. These droplets with a newly formed oxide film can separate from the liquid and contact other oxide layers at the surface. This phenomenon is difficult to control without a continued non oxidizing atmosphere. Figure 5.3 c) also shows a gap interface between the cold shut and the matrix as an evidence of a location of crack initiations. This can be the major cause for the tensile failure below the values of the accepted tensile strength.





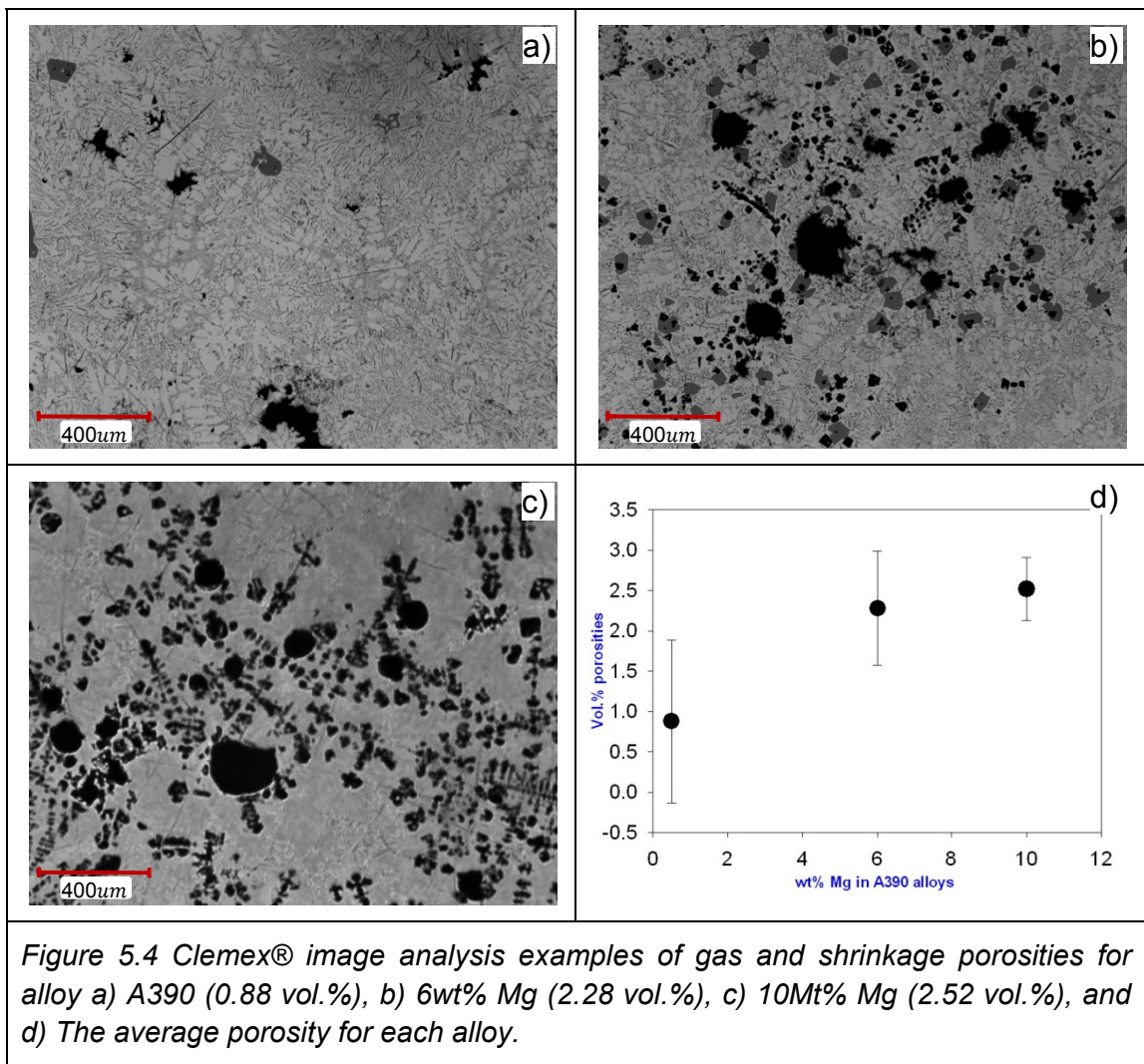
### 5.1.2. Porosities

There are usually two types of porosities found in cast components, gas bubbles and shrinkage cavities. Both contribute to reduced properties. More scattered and small in size, the gas porosities do not have negative influences as serious as the large size voids, hot tears, or irregular shaped shrinkage pores. The shape and size of the pores determine the level of stress concentration at these defect sites.

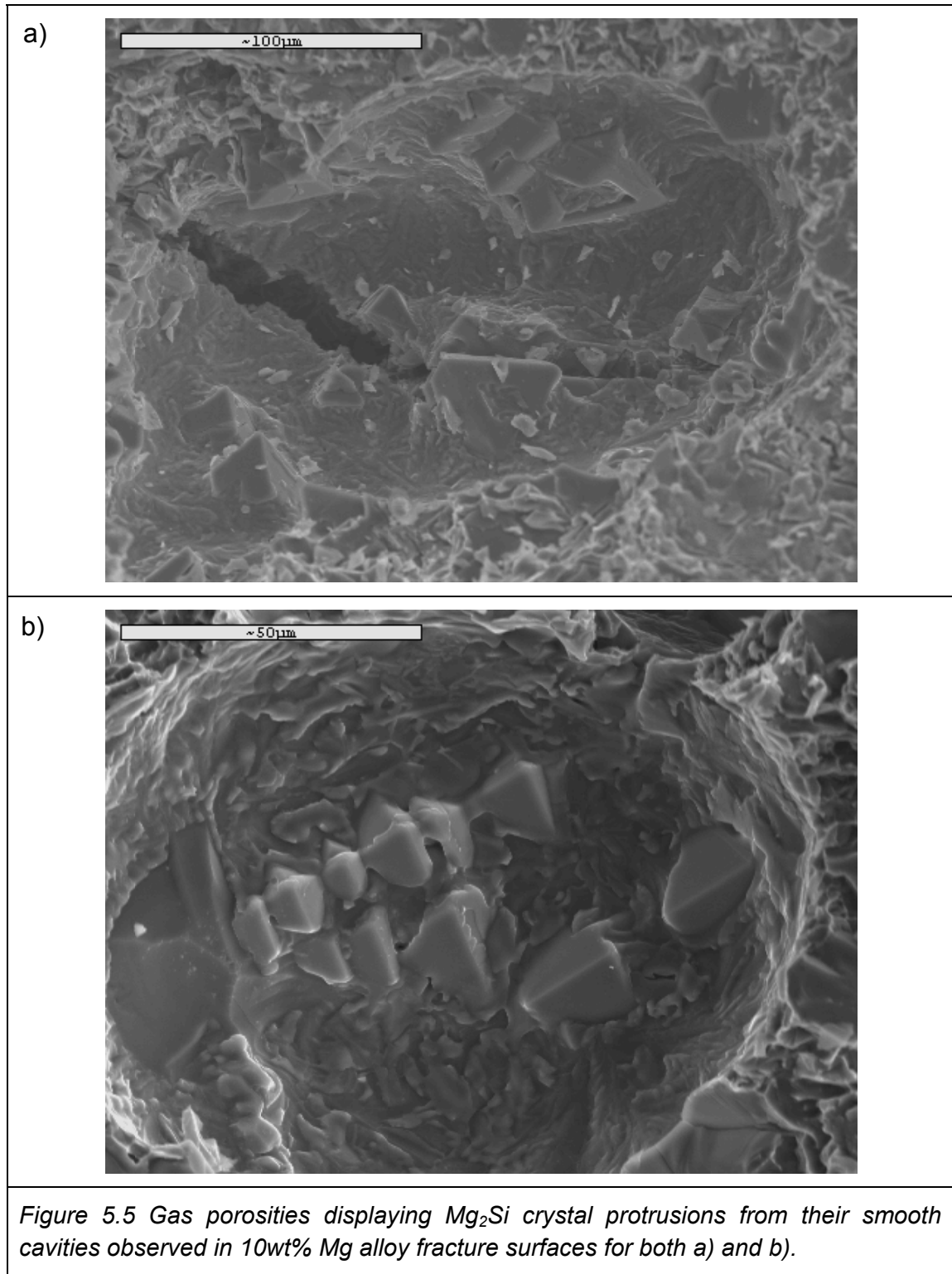
Figure 5.4 a), b), c) demonstrate that both gas and shrinkage porosities exist in the alloys of main study which were examined by using Clemex® image analysis. Finally, the porosities were measured and plotted in the Figure 5.4 d), which shows the porosity level starts to increase sharply from 0.88 *vol. %* for alloy A390, to 2.28 *vol. %* for alloy 6wt% Mg and 2.52 *vol. %* for alloy 10wt% Mg.

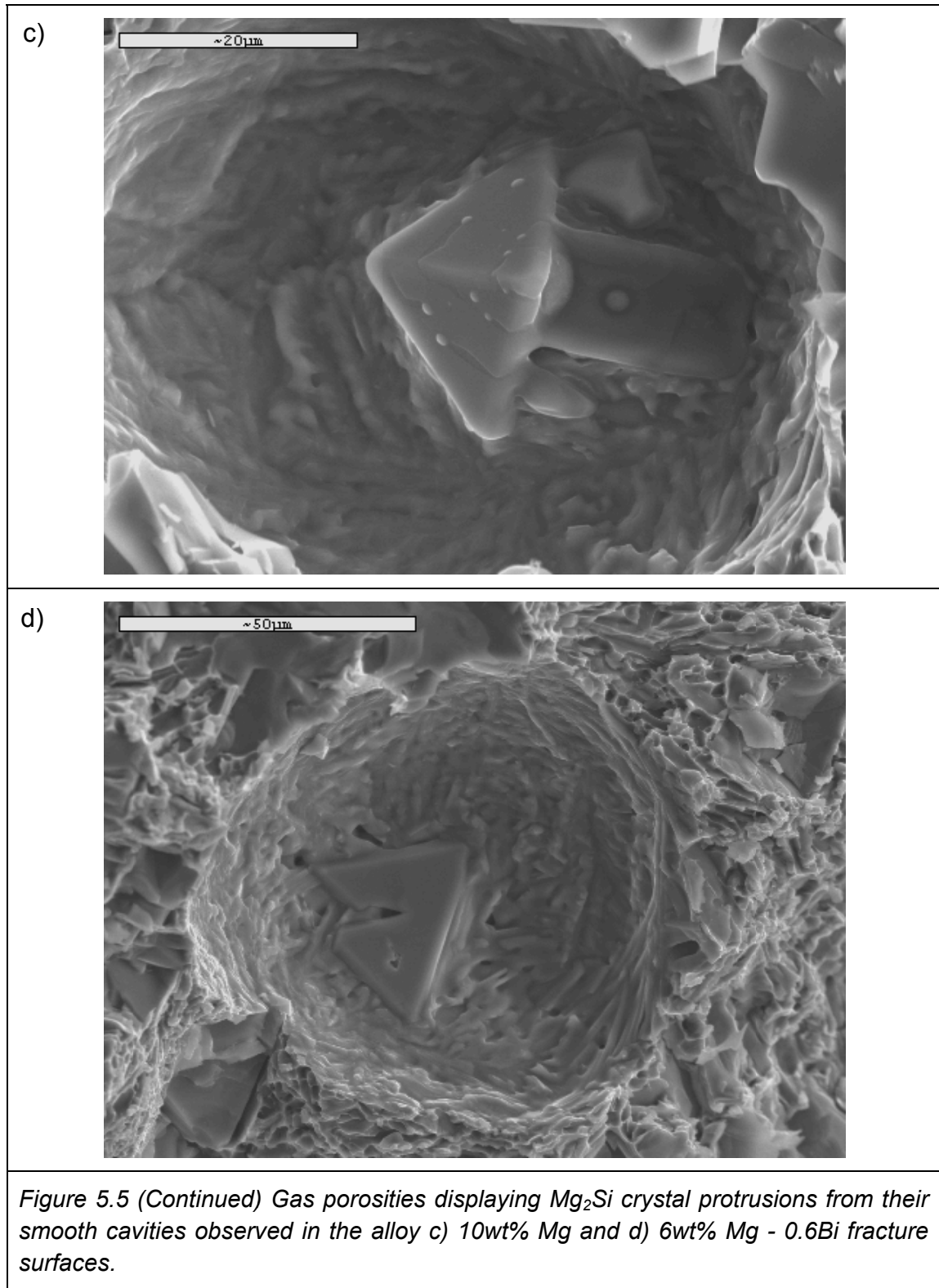
As observed from the porosity trends, a reverse relationship might be proposed between the porosity level and Mg content in Al-Si alloys using the same casting procedure. It appears that increasing Mg content increases pore formation to a certain extent. Further investigation showed that the intermetallic phase primary  $Mg_2Si$  appears in many gas pores as seen in the Secondary Electron Images (SEI) (Figure 5.5) showing four cases of gas porosities with  $Mg_2Si$  crystal protrusions in the tensile fracture surfaces of both 6 and 10 wt% Mg alloys.

This phenomenon supports pore formations relating to the Mg contents in these alloys. The possible mechanisms might be attributed to Mg vapour pressure which increases with increasing Mg content at the normal casting temperature when the Mg content is higher than 0.4 wt%.











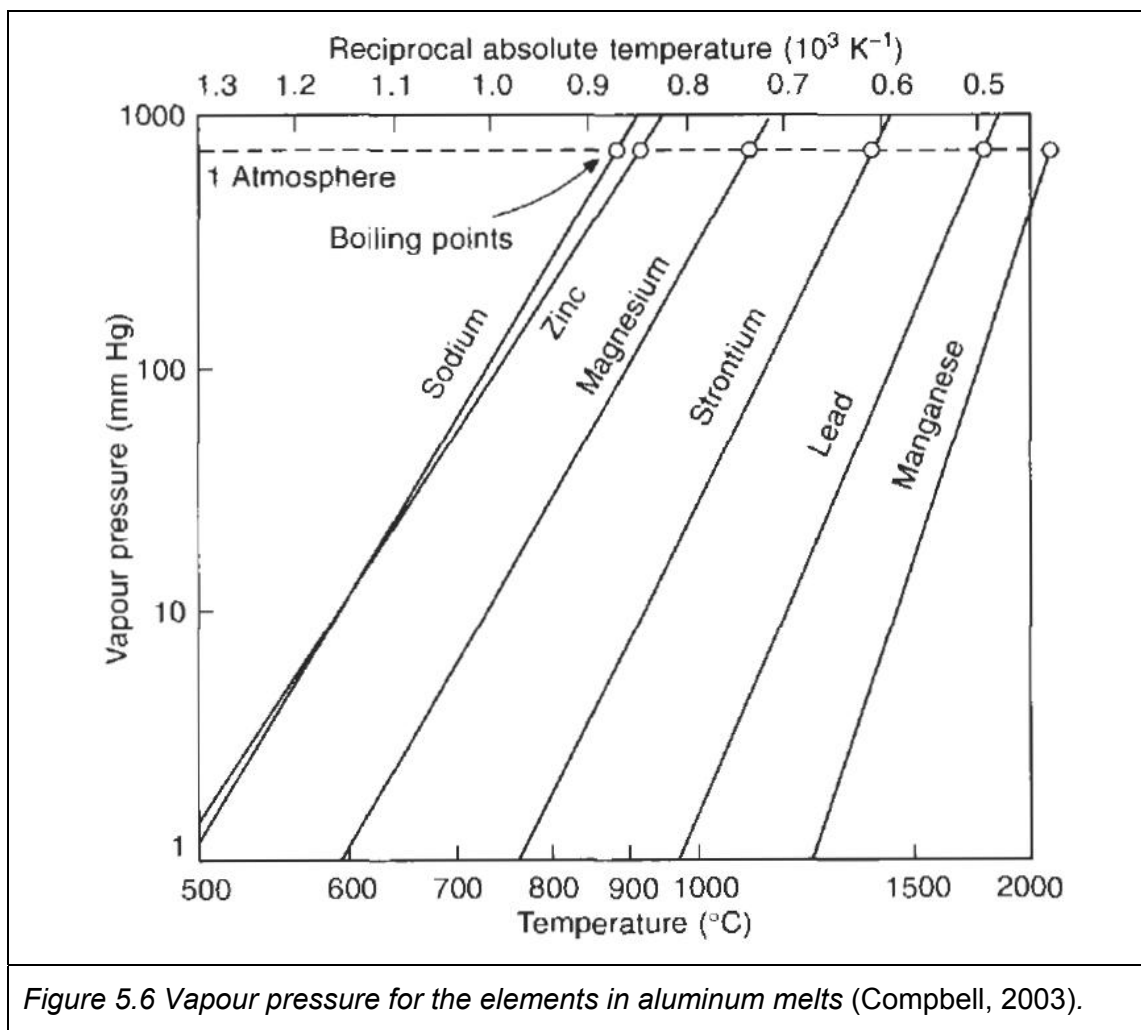


Figure 5.6 indicates that the Mg in the molten aluminum can easily vaporize, (Compbell, 2003). As discussed in the section of the surface film formation, the continuous vaporization of Mg liquid will subsequently leave vacancies or pores on solidification. Their location should be found in the high Mg enriched area where these  $\text{Mg}_2\text{Si}$  crystals are formed. Since most of the heat loss occurs at the temperature where the eutectic reactions take place as predicted by FactSage<sup>TM</sup>, some of the formed Mg vapour in the melt might not be able to

escape as the temperature changes rapidly. A void is thus left around the  $\text{Mg}_2\text{Si}$  crystal forming vapour porosity.

Another possibility could be attributed to the hydrogen solubility, which shows a quite difference between the pouring and solidification temperature. Any void caused by the Mg vaporization becomes a nucleation site. Dissolved hydrogen is also released rapidly as the melt temperature decreases. This hydrogen can readily enter a neighbouring Mg vapour void which has no hydrogen pressure originally. Continuous release of hydrogen from solutions can subsequently increase the size of Mg vapour pore.

As suggested by the Ostwald Ripening effect, the large pores continue to grow in size at the expense of small pores. This has been found to occur for the high Mg content alloys that generated in large porosities (Figure 5.4 b), c)).

There is, of course, another major type of porosity (shrinkage porosity) that was shown in the current permanent mould gravity castings. This mechanism is usually considered to be the result of the lack of liquid feeding in an area resulting in hot tears.

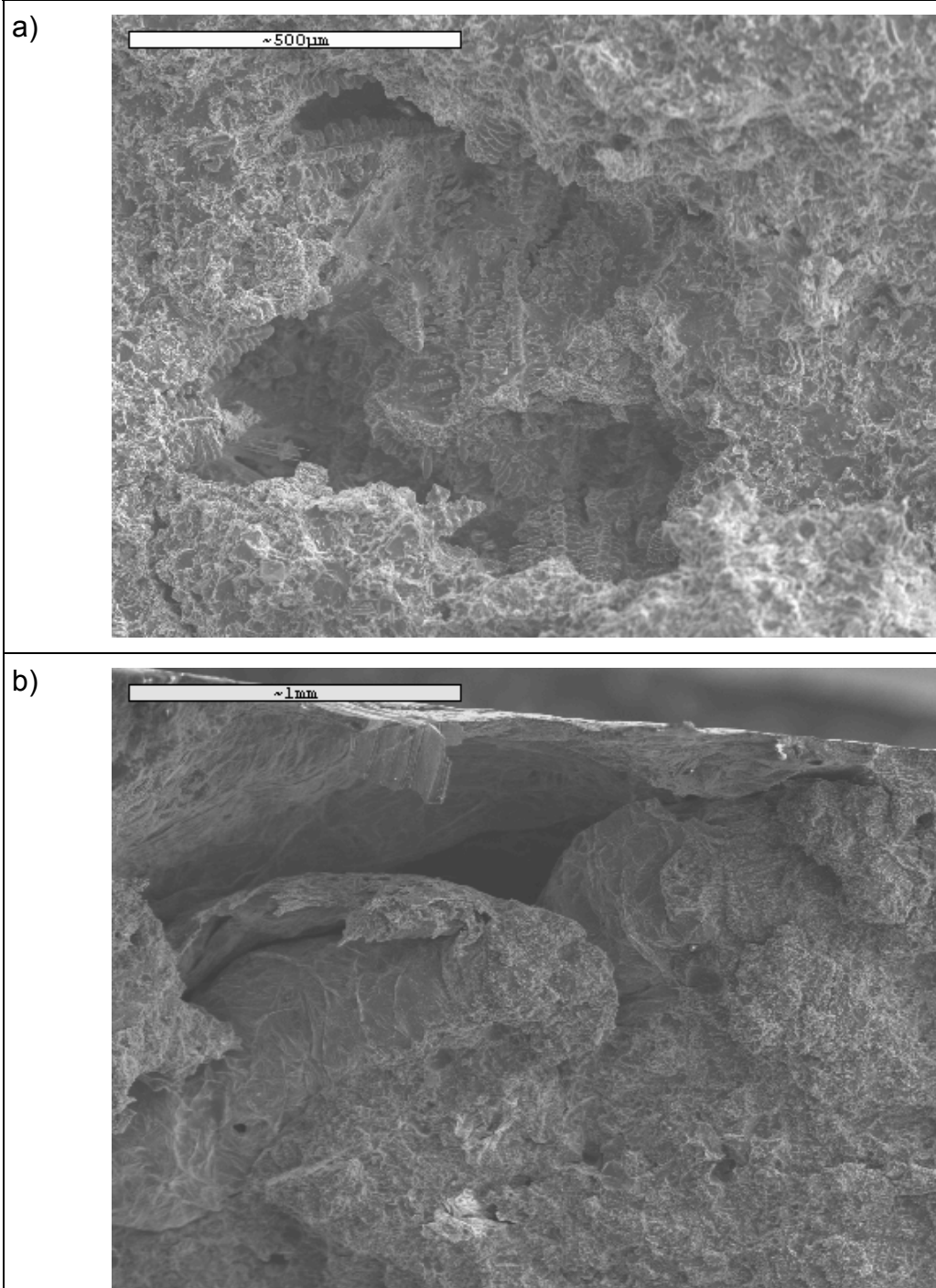
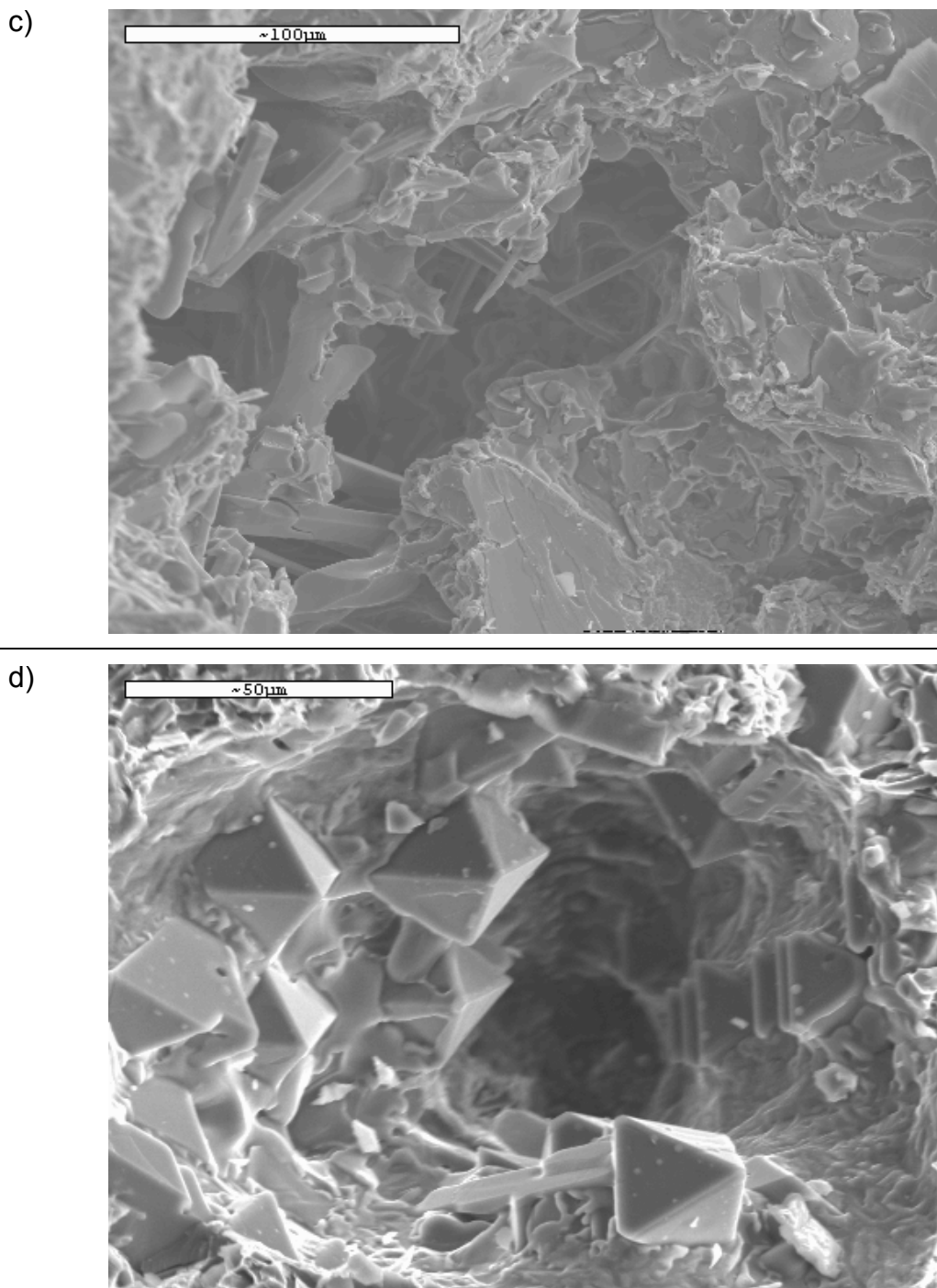


Figure 5.7 Shrinkage porosities illustrating as a)  $\alpha$ -Al dendrites in an 6wt% Mg alloy, b) Cold shut interacting with the 10wt% Mg base alloy.



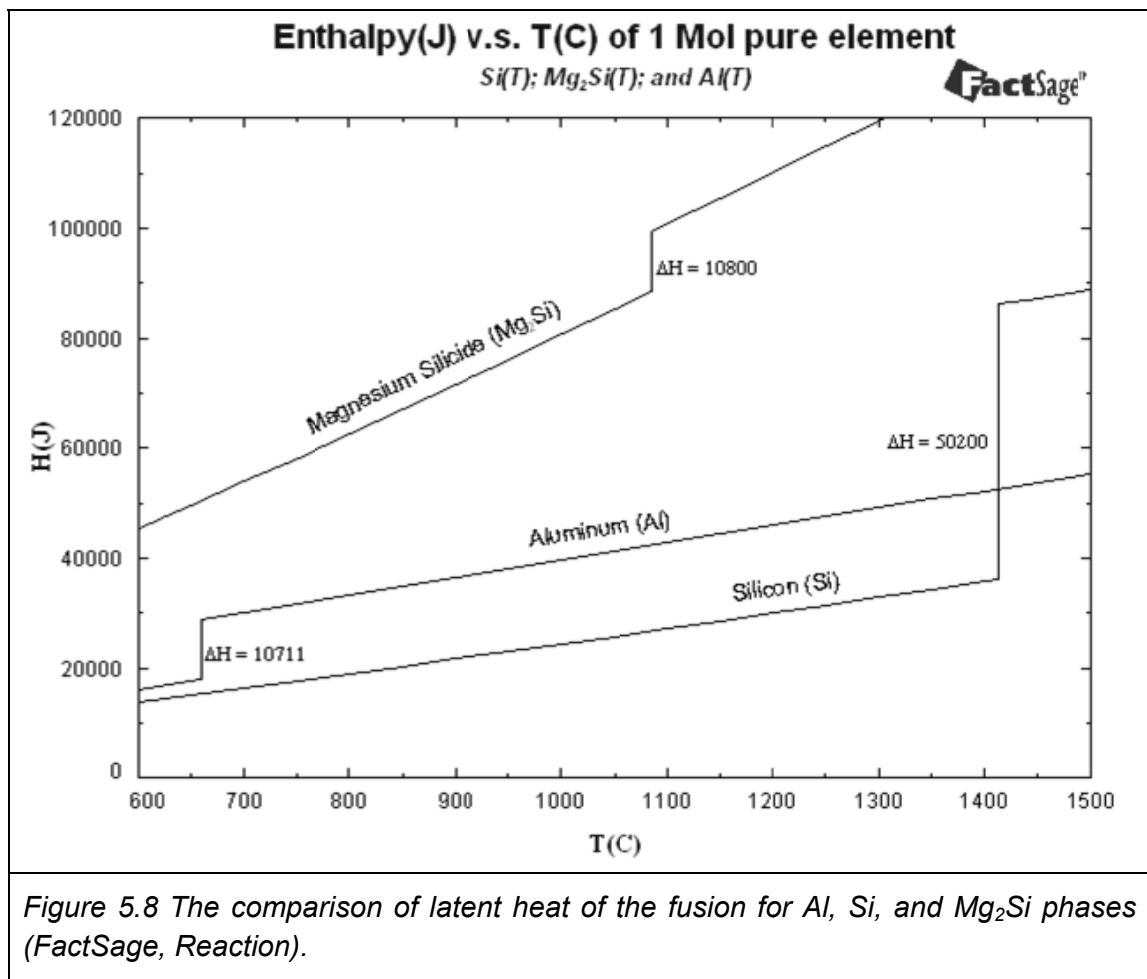
*Figure 5.7 (Continued) Shrinkage porosities illustrating c) A void containing complex constituents in an A390 alloy after T6 heat treatment, and d) A cavity surrounded with significant  $Mg_2Si$  formation in the 10wt% Mg alloy.*

Figure 5.7 illustrates different types of shrinkage related porosities, including a)  $\alpha$ -Al dendritic clusters segregated in an Al rich region forming a cavity due to the non-even composition distributed and solidification contraction; b) cold shuts interacting with the matrix blocking the liquid from filling the cavity; c) a typical last freezing area containing  $\alpha$ -Al,  $\theta$ -Al<sub>2</sub>Cu, Q-Al<sub>5</sub>Cu<sub>2</sub>Mg<sub>8</sub>Si<sub>6</sub> etc. phases in a pore; and d) another illustration of Mg vapour voids being trapped by the surrounding number of Mg<sub>2</sub>Si precipitates, combining both gas and shrinkage porosity features. It can therefore be concluded that magnesium vapour becomes an important factor altering either types of porosity formations for the high Mg content alloys.

### 5.1.3. Flow behaviour

During the solidification, the phase decomposition generally releases certain amount of enthalpy depending on the latent heat of fusion of the solidifying precipitates. It is well known that Si contributes to the melt fluidity significantly since a lot of heat is generated from the solidification of Si, which is 4.67 times higher than the value for the solidification of Al as seen in the Figure 5.8, Mg<sub>2</sub>Si is not as effective since the enthalpy of solidification is much lower. Actually, there are also other terms such as the heat loss rate during the solidification (the difference between the melting point and mould temperature,  $T_m - T_0$ ), and the pure material density ( $\rho_m$ ) that affect the melt fluidity in addition to the latent heat of the fusion (H). By combining these factors, a fluidity comparison in terms

of solidification time ( $t_m$ ) was calculated for pure silicon and pure aluminum in the Equation 5.1 (Compbell, 2003) where the Si latent heat of the fusion is ~22 times greater than the Al, contributing to better fluidity. This effect is reduced somewhat by the higher heat loss rate (~5 times) and lower density (~1.3 times). Therefore, the fluidity of the pure silicon is about 3.4 times higher than that of pure aluminum.



Likewise, the same equation was used to compare the fluidity between pure  $\text{Mg}_2\text{Si}$  and pure aluminum as shown in the Equation 5.2 where the calculated fluidity is ~33 times lower for pure  $\text{Mg}_2\text{Si}$  than the pure aluminum. Therefore, the  $\text{Mg}_2\text{Si}$  substitution for Si will significantly reduce the alloy fluidity up to ~100 times from the above analysis. Note that, the mould temperature was assumed to be the same as surrounding environment ( $T_0 = 25^\circ\text{C}$ ) during the calculations. When the mould was preheated to  $400^\circ\text{C}$  for the two types of permanent mould castings, the fluidity difference can be reduced to ~14 times from ~ 100 times worse when  $\text{Mg}_2\text{Si}$  is the primary solidifying phase. This is still a considerable difference in castability between the conventional A390 and the Mg containing alloys.

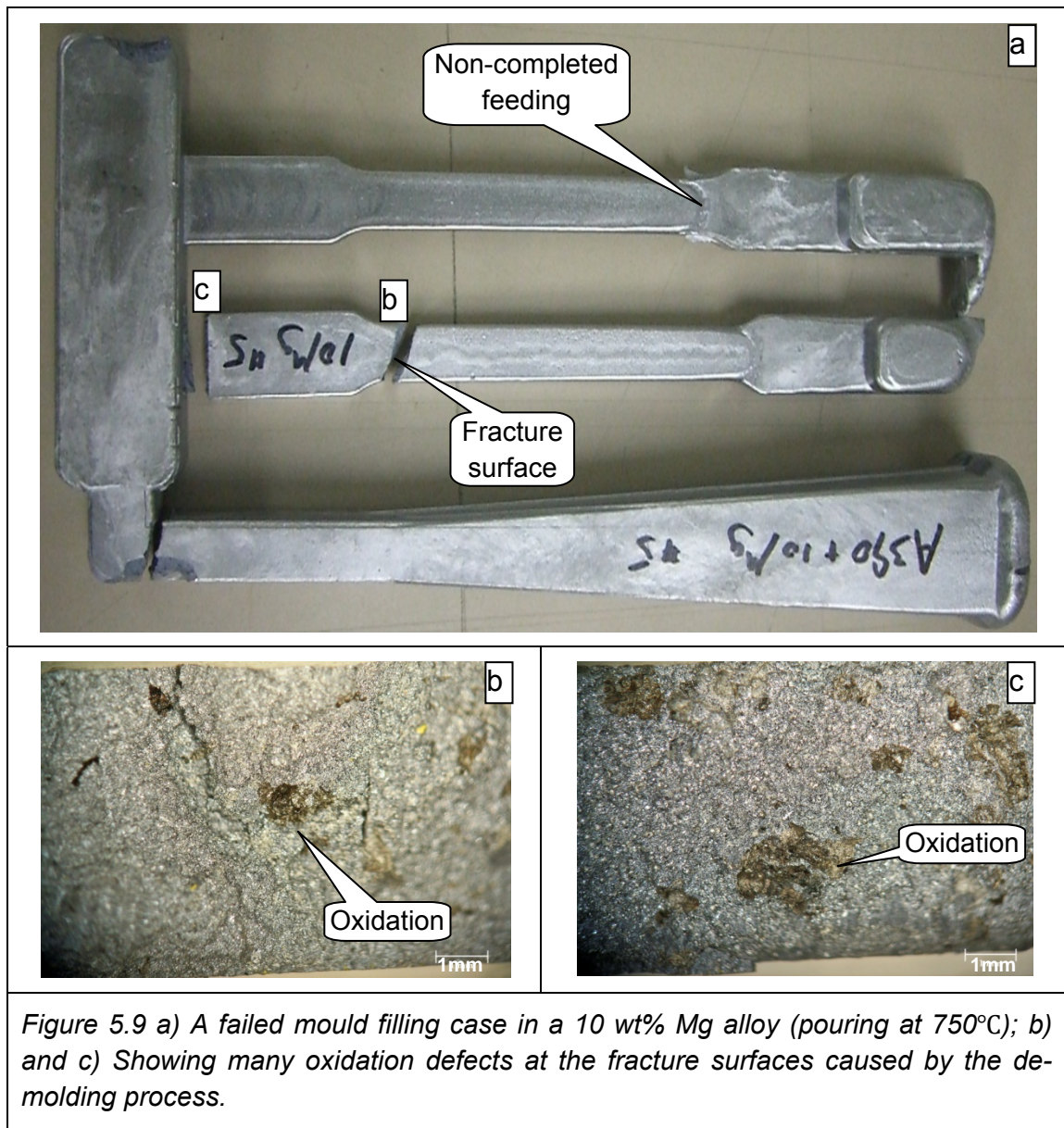
$$\frac{t_{\text{Si}}}{t_{\text{Al}}} = \left( \frac{T_{\text{Al}} - T_0}{T_{\text{Si}} - T_0} \right)^2 \left( \frac{\rho_{\text{Si}}}{\rho_{\text{Al}}} \right)^2 \left( \frac{\Delta H_{\text{Si}}}{\Delta H_{\text{Al}}} \right)^2 = 0.21 \cdot 0.74 \cdot 22.09 = 3.4 \quad \text{Equation 5.1}$$

$$\frac{t_{\text{Mg}_2\text{Si}}}{t_{\text{Al}}} = \left( \frac{T_{\text{Al}} - T_0}{T_{\text{Mg}_2\text{Si}} - T_0} \right)^2 \left( \frac{\rho_{\text{Mg}_2\text{Si}}}{\rho_{\text{Al}}} \right)^2 \left( \frac{\Delta H_{\text{Mg}_2\text{Si}}}{\Delta H_{\text{Al}}} \right)^2 = 0.12 \cdot 0.23 \cdot 1 = 0.03 \quad \text{Equation 5.2}$$

where  $T_0 = 25^\circ\text{C}$ .

In addition, the presence of surface films ( $\text{MgO}$ ) also has negative influences on the melt fluidity of high Mg content alloys whether they are surface films or oxidation inclusions. As shown earlier, the melt surface is always covered by the oxide film during the mould filling process due to the high reactivity with oxygen (air). Mould filling slows down when the narrow sections of the tensile bars are

formed in the mould. This directly results in a thicker surface film formation at the leading fluid front. A higher melt pressure exerted by the feeding liquid in the runner system is necessary in order to overcome the additional surface tension forces required for filling the mould.

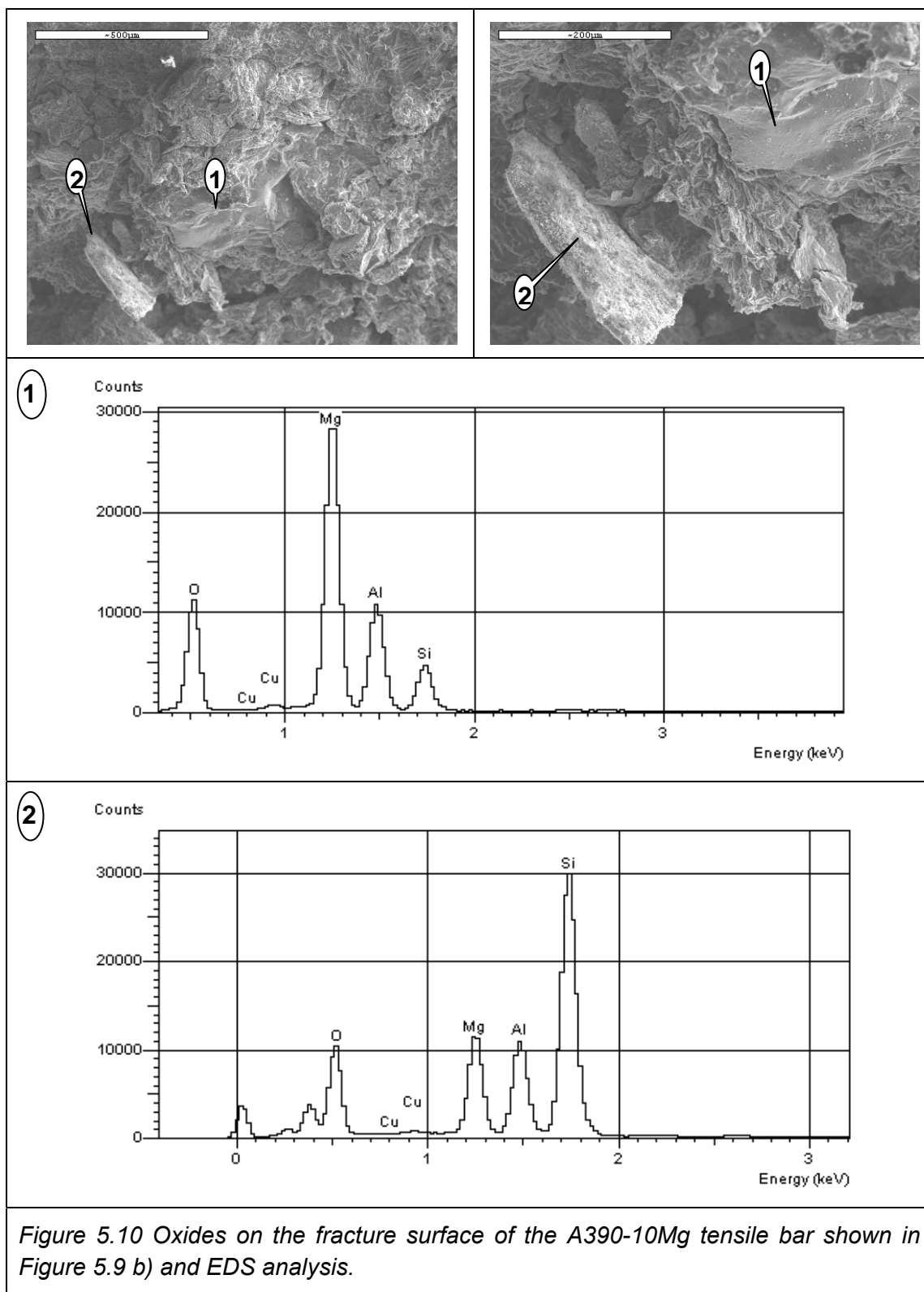




These surface films have a strong tendency to grow into thick walls leaving a series of cascading waves on the casting surfaces (Figure 5.1 f)), which indicates that the surface films present a resistance to filling the mould. Alloys with 6 and 10wt% Mg were formed to be “too sticky” because the castings were rather difficult to remove from the metallic mould. An example of 10Mg alloys is shown in the Figure 5.9 a) where both non-filled tensile bar tops and de-moulding breaks are observed. Extensive oxidation was also observed resulting in poor pouring (Figure 5.9 b), c)). The casting was poured at 750 °C representing 104 °C superheat of the alloy liquidus of 646 °C predicted by FactSage™.

However, this pouring temperature was successfully used in producing the round tensile bar castings in UQAC where a higher capacity metallic mould was used. Although the same mould pre-heating to 400°C has been adopted in both UQAC and McGill labs, apparently the smaller capacity of metallic mould in the McGill lab tended to have more rapid heat loss than the larger ones in the UQAC lab. As a result, a pouring temperature of 850°C was used to cast the flat tensile bars produced in the McGill lab.

This high pouring temperature resulted in not only more oxidation losses of the alloying elements but also in raising the hydrogen and Mg vapour porosity, further degrading the mechanical properties significantly.



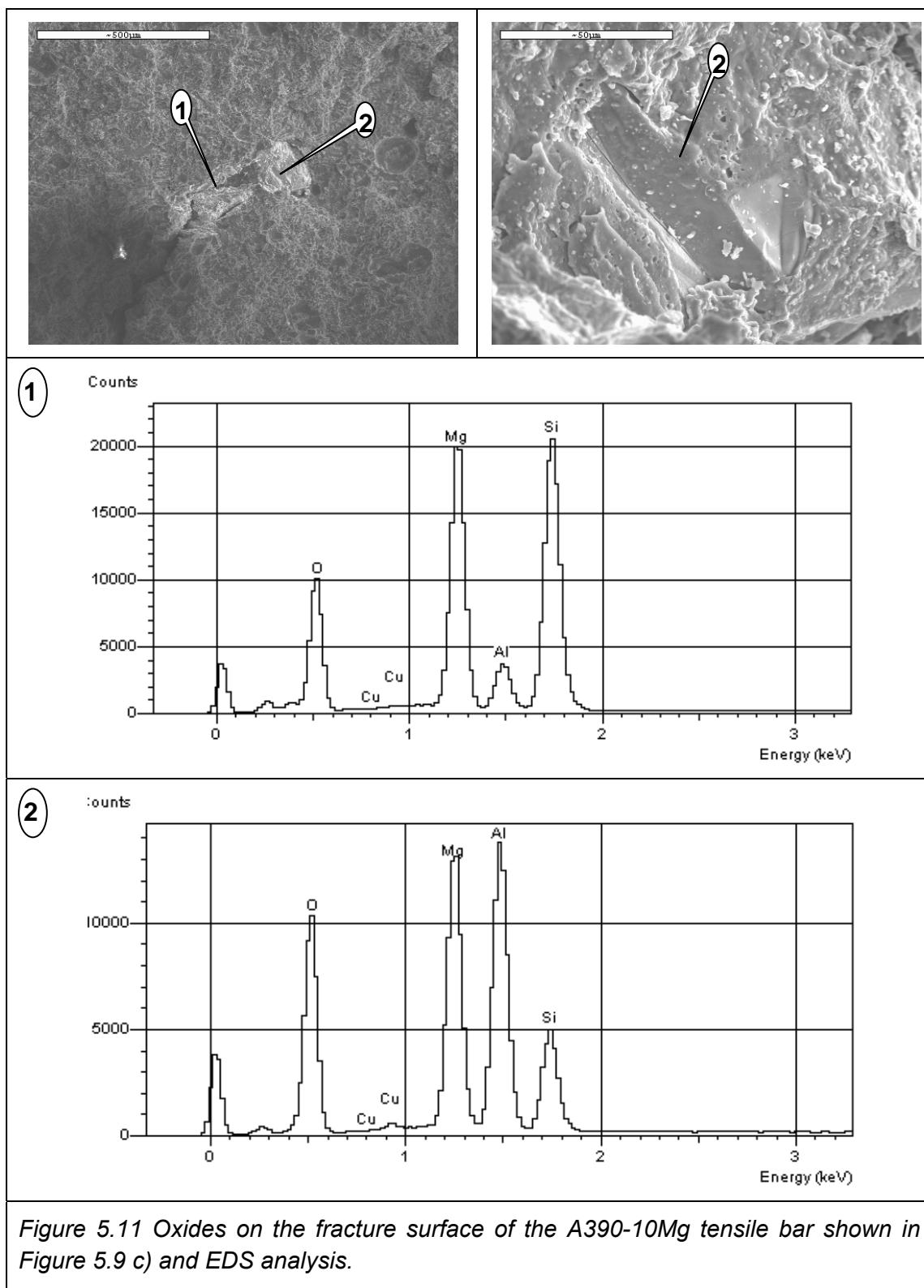


Figure 5.10 and Figure 5.11 illustrate the oxides of varying elements (Mg, Si, Al etc.) identified by using the SEI images and EDX analysis of the fracture surfaces of A390-10Mg alloy (Figure 5.9). The presence of these oxides has caused a discontinuity of the alloy matrix, reducing the melt fluidity by at least 20% (Compbell, 2003). Some of these inclusions or large surface films are enough to slow down the fluid front or even block in the narrowed area.

## 5.2. Characteristics of solidification products

FactSage<sup>TM</sup> has fully predicted the decomposition behaviour of all three Mg added alloys described in the Chapter 3. However, there are still two phases that are not predicted by thermodynamic data but which are formed in the castings. One is the primary  $\alpha$ -Al in the form of dendrites, while another one is the quaternary Q-Al<sub>5</sub>Cu<sub>2</sub>Mg<sub>8</sub>Si<sub>6</sub> phase, generally found at the final stage of solidification. It seems that it is impossible to have the primary  $\alpha$ -Al in the hypereutectic Al-Si alloy (i.e. A390), at least from equilibrium phase diagram. Using Scheil solidification shows that it does happen as previously stated in the Chapter 2.

Primary  $\alpha$ -Al can be formed in the region where an Al enriched zone can occur even in a hypereutectic Al-Si alloy. This has been observed along with the primary Si or Mg<sub>2</sub>Si precipitations.

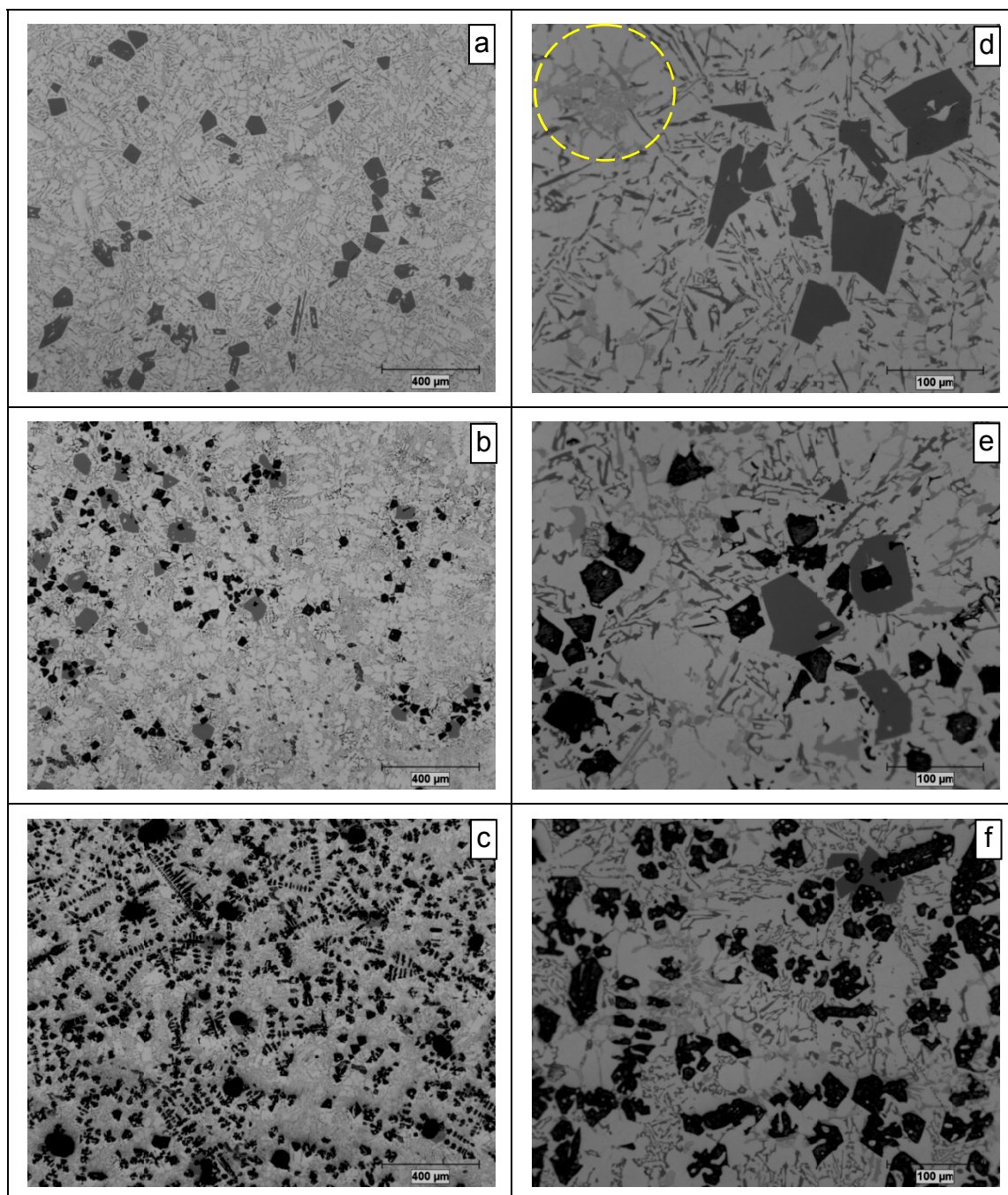
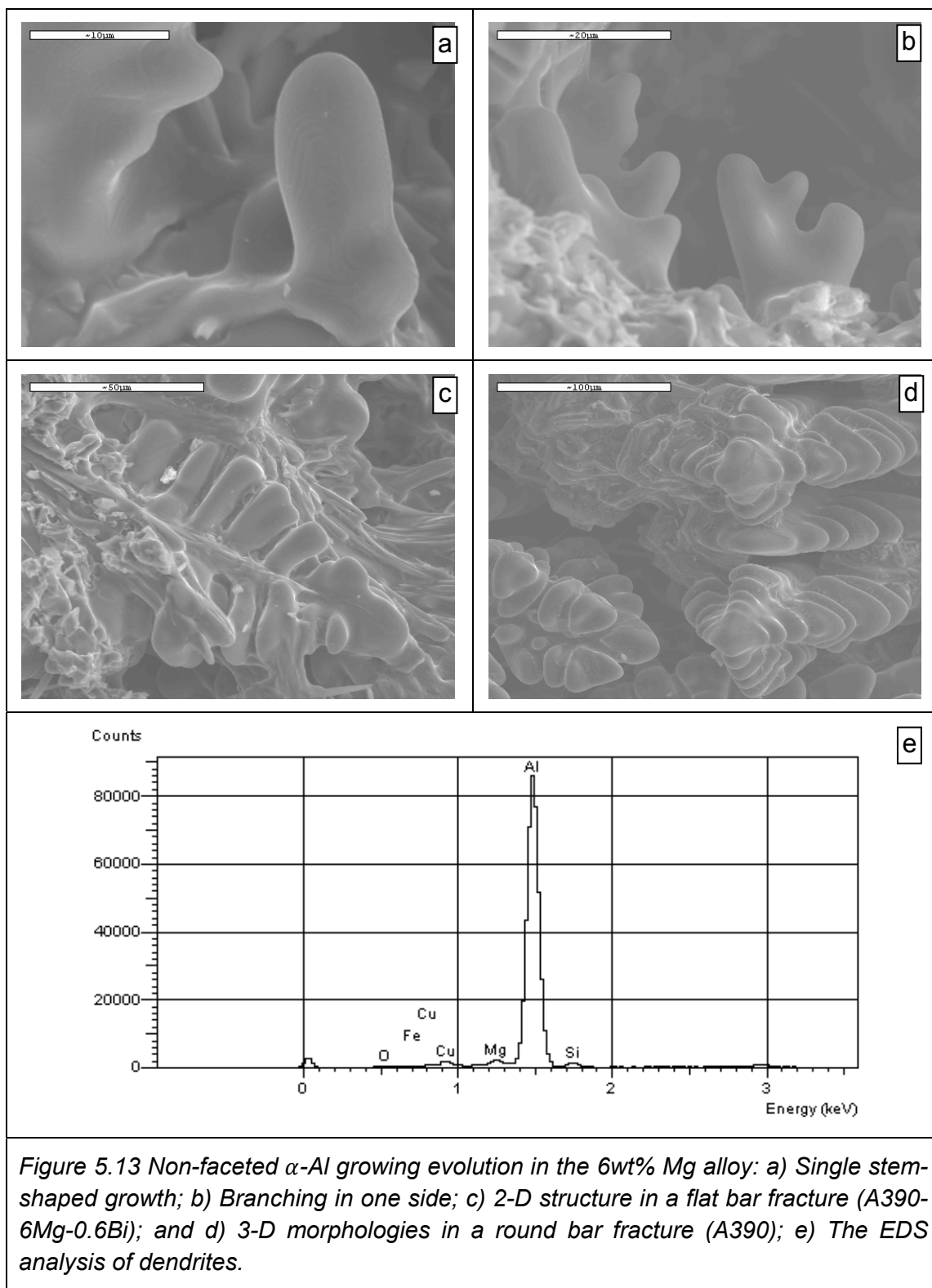


Figure 5.12 The overall morphologies of the permanent mould casting A390, A390-6Mg and A390-10Mg at a), b), c) 50X and d), e), f) 200X magnification respectively observed by OM images.



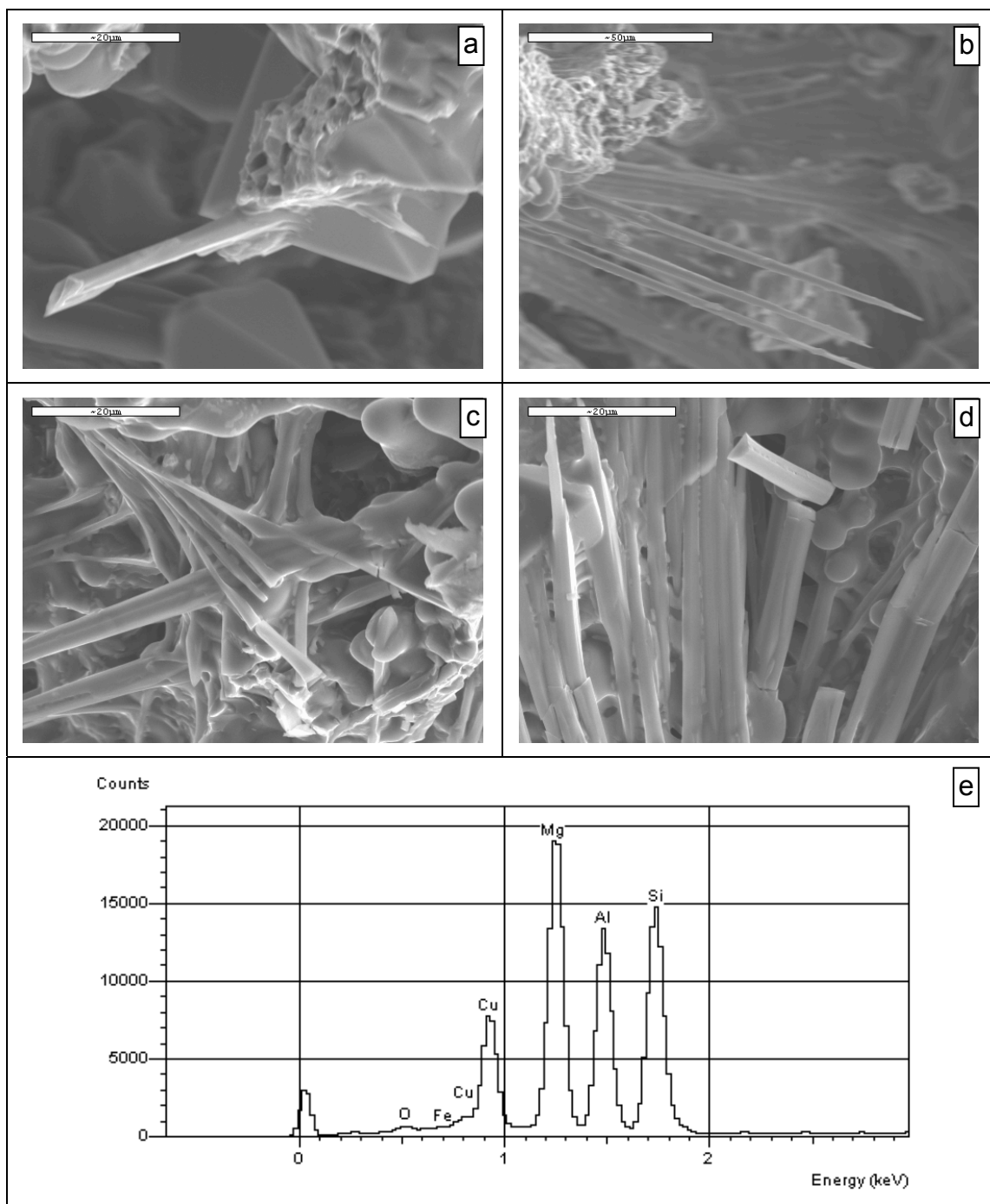
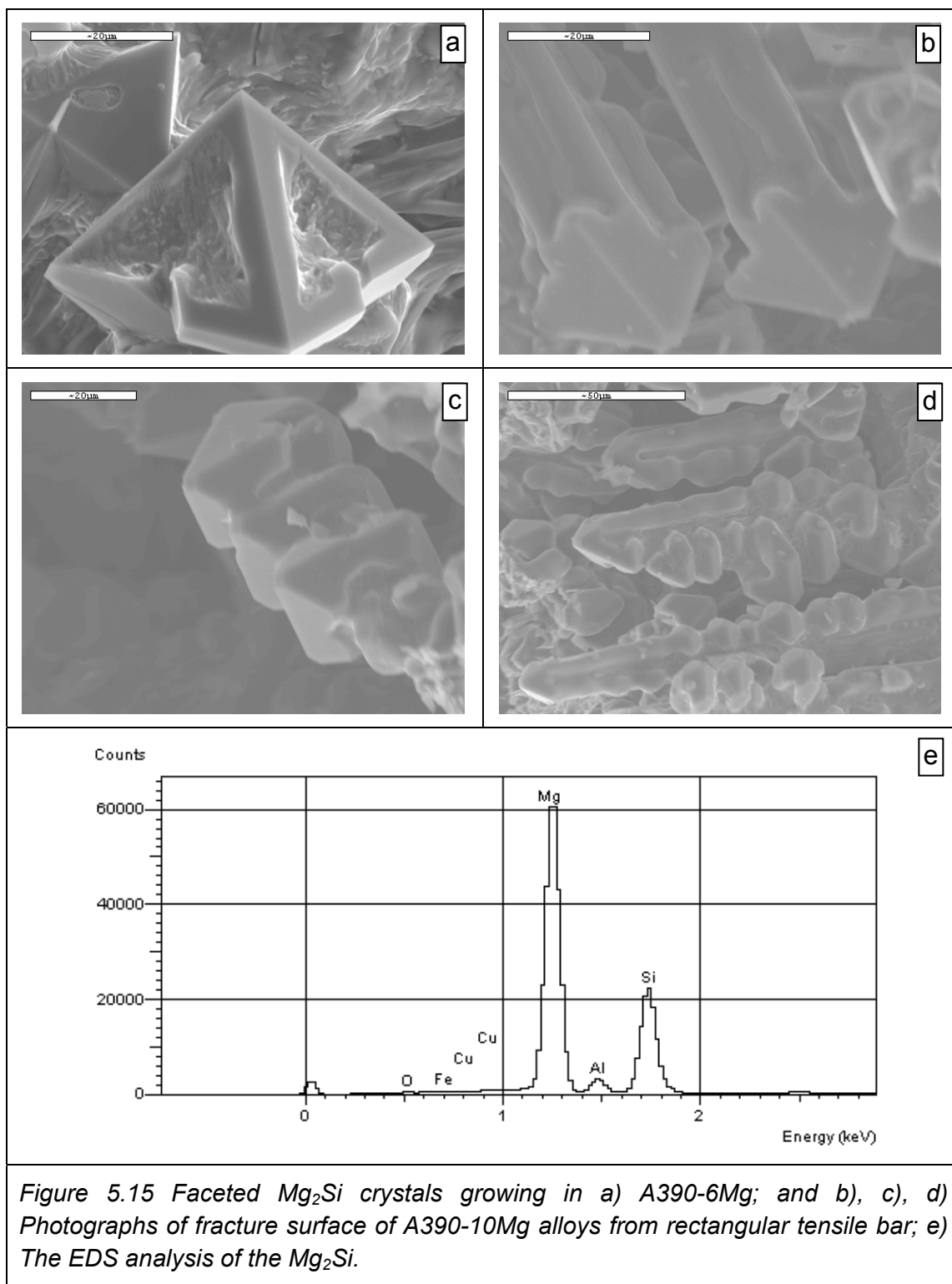
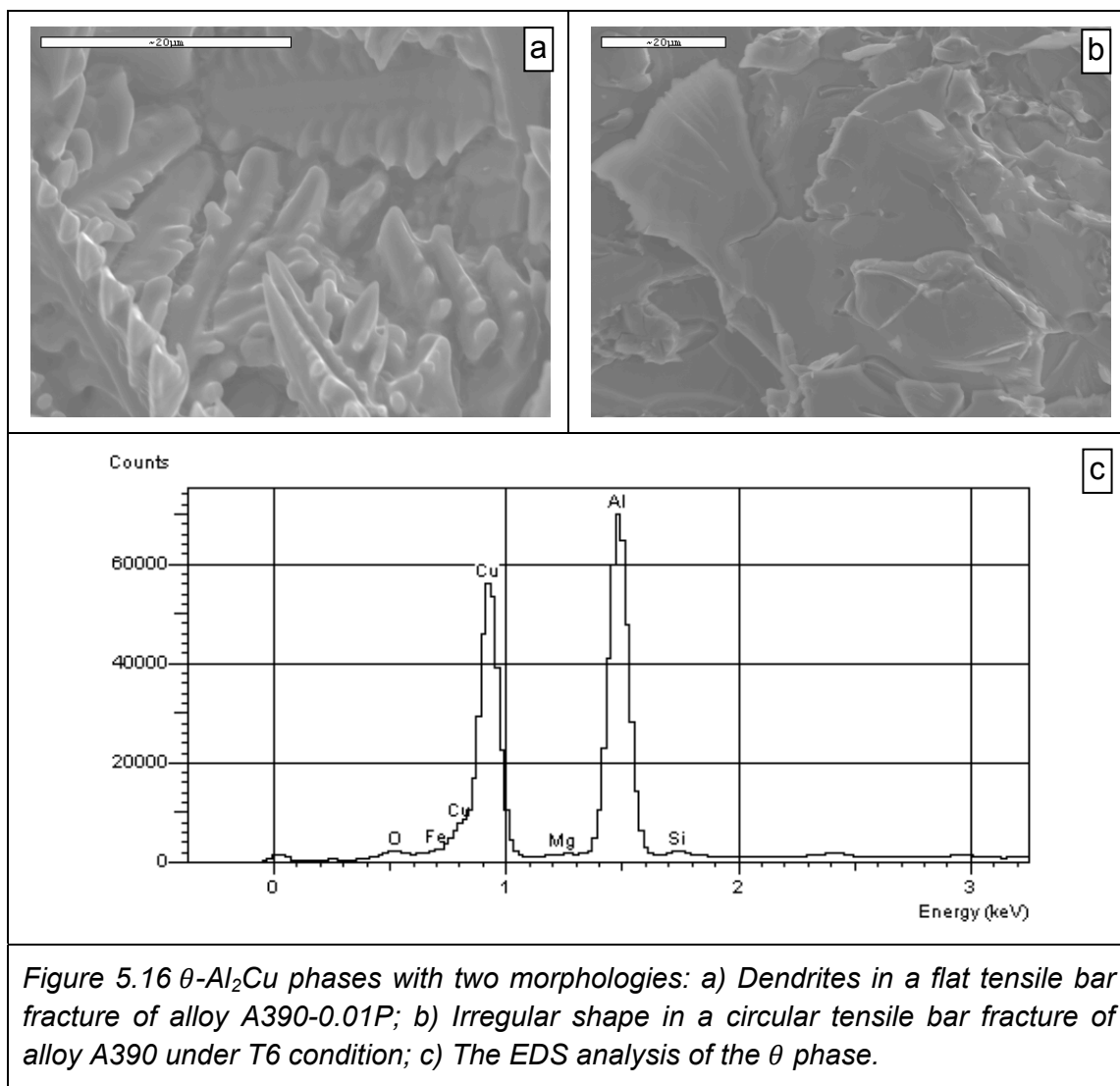


Figure 5.14 Q- $\text{Al}_5\text{Cu}_2\text{Mg}_8\text{Si}_6$  phase growing in a), b) A390-6Mg; and c), d) A390-10Mg alloys found at the rectangular tensile bar fracture surfaces; e) The EDS analysis of the Q phase "needles".







The general as cast microstructures of the 6 and 10wt% Mg alloys can be identified in OM images (Figure 5.12) where the bulk  $\alpha$ -Al and its dendrites can be found readily in the matrix. Upon further investigation, an evolution of the non-faceted  $\alpha$ -Al growth has been clearly illustrated in the SEI images (SEM) from the tensile fracture surfaces (Figure 5.13), undergoing a series of changes initially with the single stem starting to branch into a 2D structure, and finally

forming into 3D dendrite structure. The  $Q\text{-Al}_5\text{Cu}_2\text{Mg}_8\text{Si}_6$  phase is always found widely dispersed among the  $\theta\text{-Al}_2\text{Cu}$  precipitates, appearing like small round spots. However, a fracture surface has shown this phase exhibits long needle like morphologies, which might grow independently from other phases such as from  $\text{Mg}_2\text{Si}$  (Figure 5.14 a)) which can intersect each other to form a cluster (Figure 5.14 b), c), d)). Furthermore, the polished sections of the Q phase display different morphologies in between OM and SEM images. The Q phase has a density at  $2.79\text{ g/cm}^3$  close to the pure Al, with a hexagonal lattice structure of  $a = 1.032\text{ nm}$  and  $c = 0.405\text{ nm}$ . Instead of being detrimental for the material like others such as the acicular  $\beta\text{-Al}_5\text{FeSi}$  phase, the Q phase seems more heat treatable via T6 process to strengthen the alloys. Another important constituent in Mg alloys would be the  $\text{Mg}_2\text{Si}$  in either primary or eutectic form, which become major precipitates in the aluminum matrix as the Mg content increases progressively.  $\text{Mg}_2\text{Si}$  is comparable to the Si since they have similar cubic crystal structures (faceted growth) as discussed in the Chapter 3. As a consequence,  $\text{Mg}_2\text{Si}$  might be seen to grow directly on the Si crystal or vice versa (Figure 5.12 e) and f)). Actually, although the morphologies of primary Si have been reported as star-like, polygonal, and dendritic, only the first two can be observed in the current study (Figure 5.12 a) and d)).  $\text{Mg}_2\text{Si}$  dendrites are predominant in the 10 wt% alloy for the same casting conditions (Figure 5.12 c) and f)). The polygonal structure of  $\text{Mg}_2\text{Si}$  is also seen in the 6 wt% Mg alloy, with a particle size at  $\sim 2$  to 4 times smaller than the unmodified primary Si crystals

(Figure 5.12 b) and e)). Figure 5.15 shows different types of primary  $Mg_2Si$  forms observed at the tensile fracture surfaces in these new alloys, including a) the “hopper” crystal, b) the extended straight-stem with a pyramid cap, c) coalescence of three polygonal crystals, and d) the growing dendrites. Most of these were observed in or near an area where a cavity appeared.

In contrast, the integral primary Si was not observed at a fracture surface. The copper addition to this aluminum alloy results in the only Cu-bearing intermetallic phase ( $\theta$ - $Al_2Cu$ ), which plays an important role in improving the mechanical properties. This phase consists of a tetragonal lattice structure with  $a = 0.6063 \text{ nm}$  and  $c = 0.4872 \text{ nm}$  at a space group  $I4/mmm$  with 12 atoms in a cell (density:  $4.34 \text{ g/cm}^3$ ) (Zolotarevsky, Belov, & Glazoff, 2007). They are usually found at grain-boundaries or at defects (Pekguleryuz, 2007) with the cluster agglomerated structures as seen in the top-left corner of Figure 5.12 d). An interesting morphology of  $\theta$ - $Al_2Cu$  dendrite was observed at a tensile fracture surface of the as cast A390 alloy modified with 100p.p.m. phosphorous (Figure 5.16 a)). It features a compact dendritic structure with very short rounded second arm protrusions different from those observed for  $\alpha$ -Al or  $Mg_2Si$  dendrites. This form of dendrites would result in a smaller detrimental effect on the as cast alloy than  $\alpha$ -Al and  $Mg_2Si$  dendrites. T6 heat treatment, however, can dissolve and disperse them in the Al solid solution to gain a significant precipitation hardening result. Figure 5.16 b) shows another type of  $\theta$ - $Al_2Cu$

phase morphology appearing in a tensile fracture surface of the T6 heat treated A390 alloy. It looks irregular but shows more lamellar like shapes, conforming to the structure described in the stage F of the Figure 2.21, showing  $\theta$ -Al<sub>2</sub>Cu coalescence. This might occur locally since they tend to aggregate as a cluster.

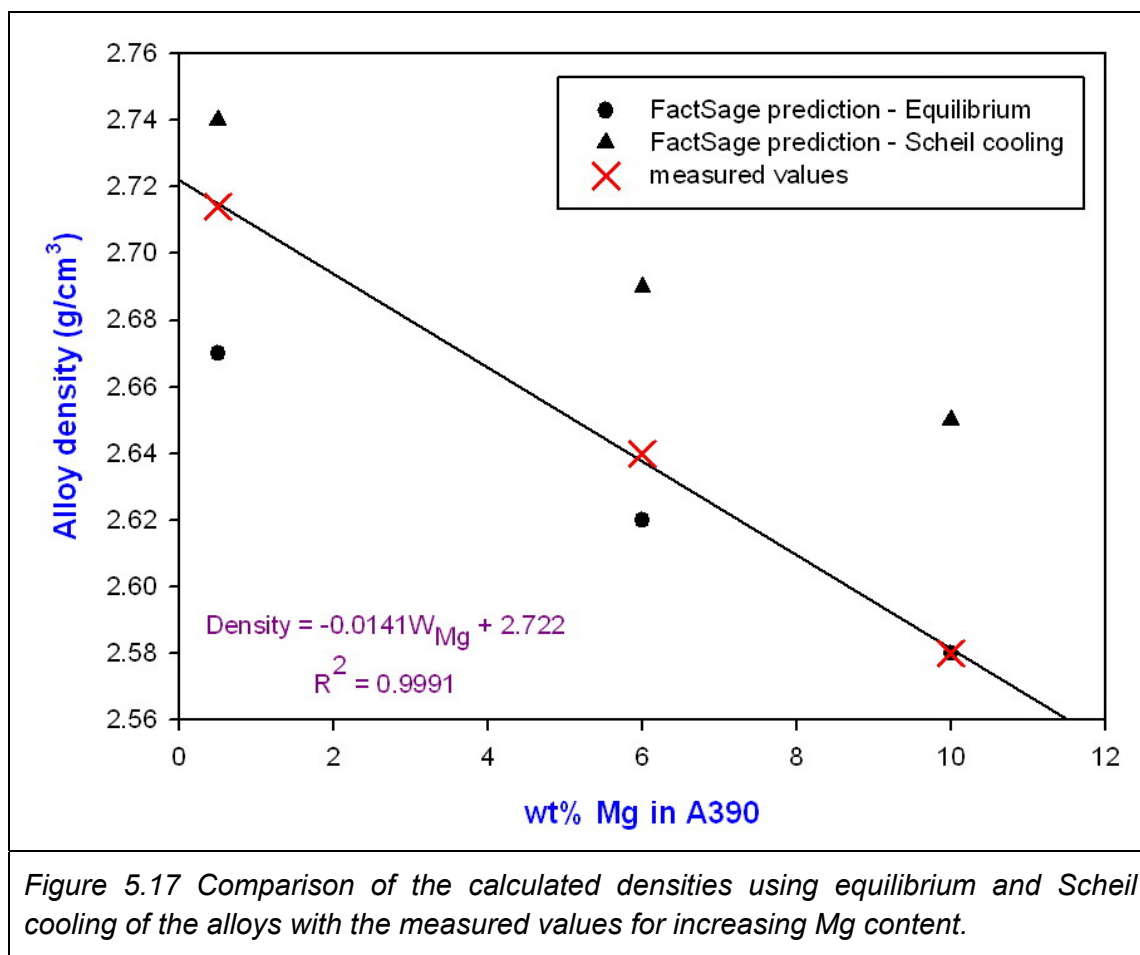
### 5.3. Density

FactSage™ was used to calculate the cumulated solid fraction for independent precipitations under both the equilibrium and Scheil cooling paths as shown in the Table 3.3 and Table 3.5. Table 5.2 summarizes the results of the calculated and measured values of the properties for 6 and 10wt% Mg alloys compared to A390.

<i>Table 5.2 An estimation of the density, porosity, and weight reduction for Mg added A390 alloys.</i>				
items		A390	A390 + 6wt% Mg	A390 + 10wt% Mg
FactSage™ Predict ( g/cm <sup>3</sup> )	Equilibrium	2.67	2.62	2.58
	Scheil cooling	2.74	2.69	2.65
Measured density ( $\rho_{meas.}$ , g/cm <sup>3</sup> )		2.690±0.044	2.580±0.011	2.515±0.021
Measured porosity (p, vol.%)		0.88±1.01	2.28±0.71	2.52±0.39
Calc. density ( $\rho_{calc.}$ , g/cm <sup>3</sup> )		<b>2.714</b>	<b>2.640</b>	<b>2.580</b>
Weight saving (wt%)		-	2.6	4.9

An approximate density can be calculated by using the equation:  $\sum W_m \cdot \rho_m$  where  $W_m$  is the mass fraction of phases (Si,  $\alpha$ -Al, Mg<sub>2</sub>Si,  $\theta$ -Al<sub>2</sub>Cu) and  $\rho_m$  is

the specific phase density. Table 5.1 shows alloy densities derived from both the FactSage™ predictions and experimental measurements using the Archimedes' principle and Figure 5.17 illustrates the comparison of the results.



However, the new alloy theoretical density is different from the measured values of the castings due to either gas entrapment or shrinkage porosity. Actually, this type of defect has been commonly observed in the high Mg alloys. The porosity volume fraction of the three alloys was also determined using quantitative image analysis, which resulted in ~0.88, 2.28, and 2.52 vol.% porosity for A390, 6Mg,

and 10Mg alloys respectively. The corrected density ( $\rho_{calc.}$ ) can be therefore calculated by using the equation  $\rho_{calc.} = \frac{\rho_{meas.}}{(1-p)}$  where  $p$  is the volume percent of porosities in alloys. This results in values of 2.714, 2.640, and 2.580 ( $g/cm^3$ ), representing a weight reduction ~2.6 wt% and 4.9 wt% for 6 and 10 wt% Mg added alloys respectively. The measured densities lie between two predictions, attaining a roughly linear relationship with increasing Mg content fitting to a regression line as shown in Figure 5.17.

#### 5.4. Hardness

The Si and  $Mg_2Si$  primary phases were initially measured for micro-hardness resulting in  $10.1 \pm 1.0 GPa$  and  $5.9 \pm 0.4 GPa$  respectively shown in the Figure 5.18, and are compared with the data published by (Zolotarevsky, Belov, & Glazoff, 2007). A deviation between measured and reported values were found to occur at room temperature conditions, with a value ~2 times higher for the micro-hardness of the primary Si compared to that of  $Mg_2Si$ . This difference is doubled (~4 times) for samples kept for one hour at 300°C, which denotes a rapid hardness reduction for  $Mg_2Si$  in a high temperature working environment. The following results for the circular tensile bars were carried out to identify the bulk material hardness changes under as cast and T6 conditions, relating to the  $\alpha$ -Al solid solution as summarized in the Table 5.3 and Figure 5.19.

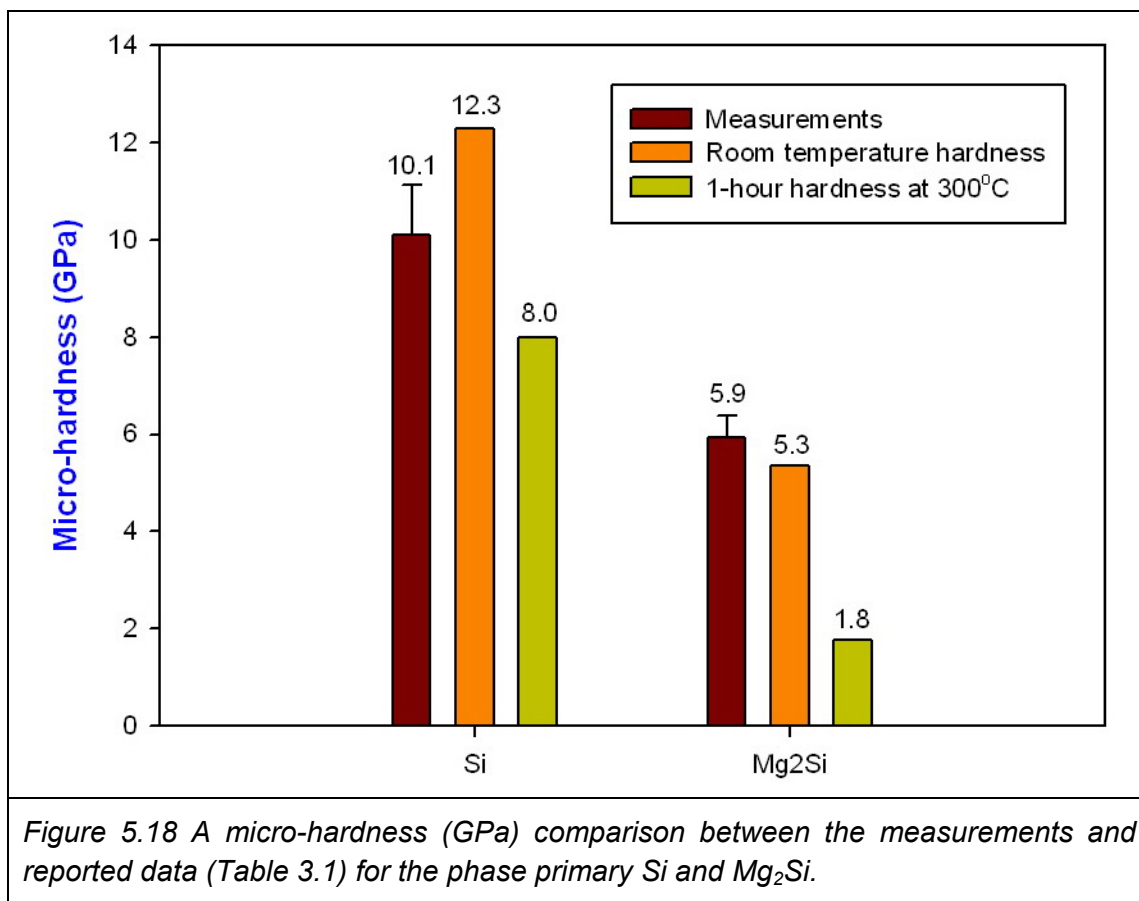
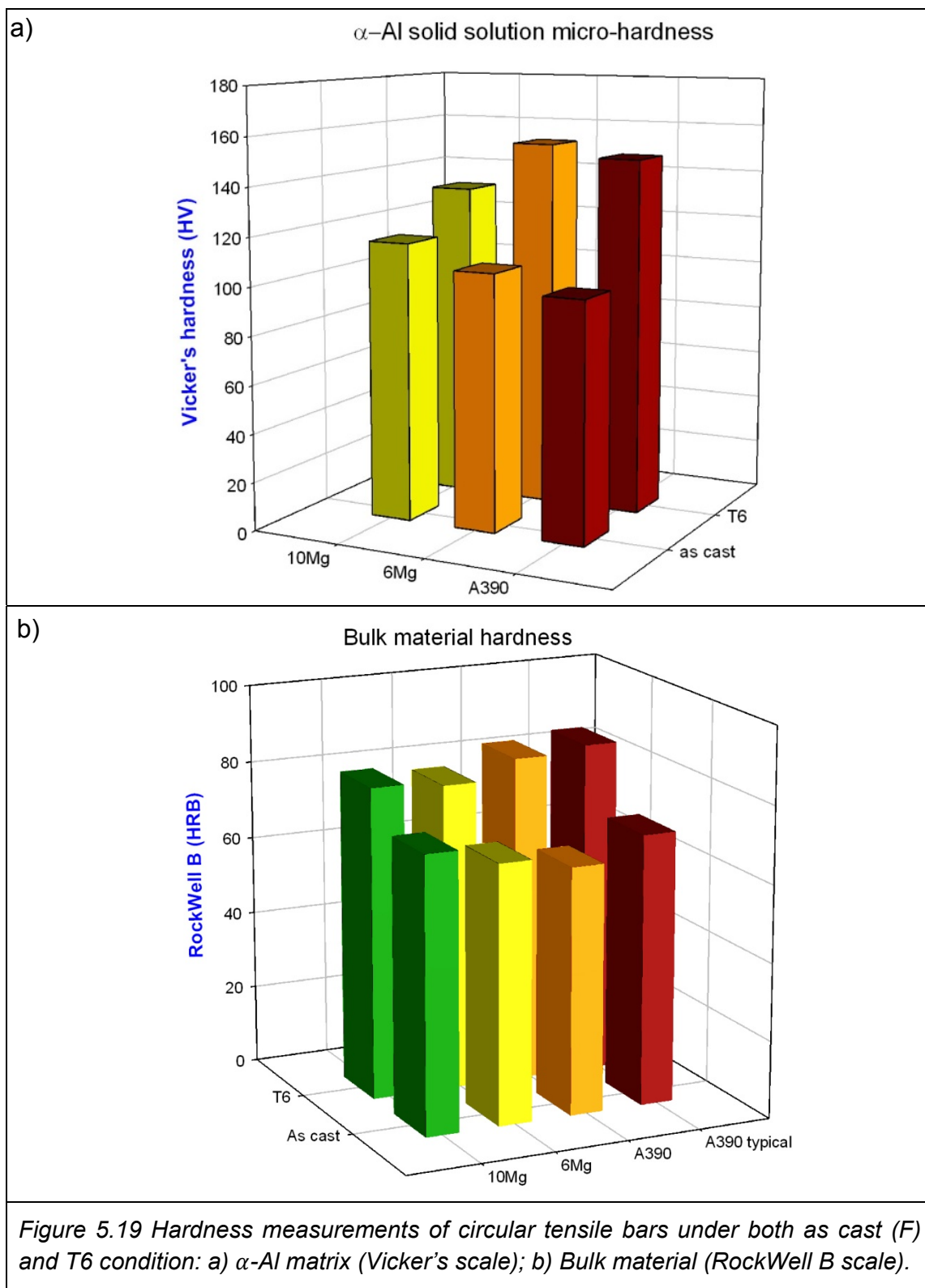
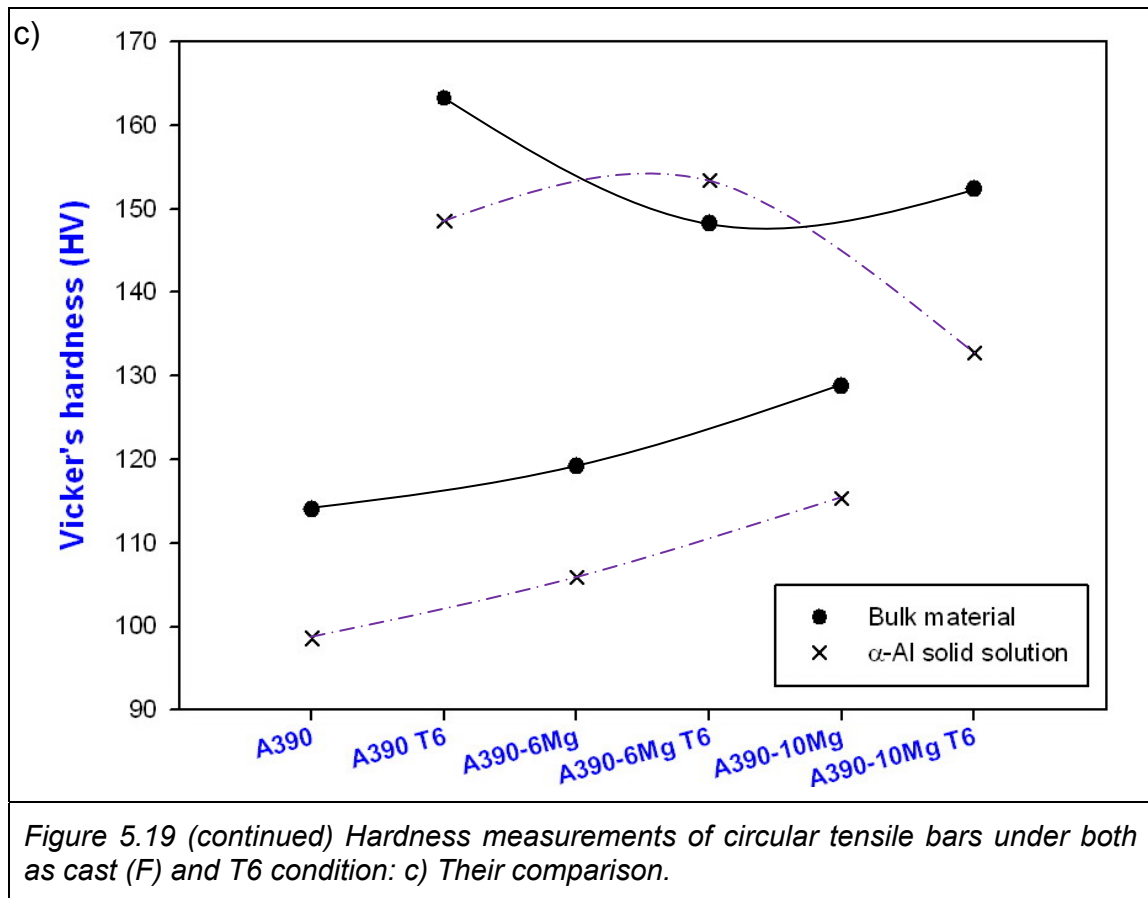


Table 5.3 An estimation of the micro-hardness for  $\alpha$ -Al matrix and the RockWell B hardness for bulk material of Mg added A390 alloys under as cast and T6 conditions.

Hardness		A390		A390+6wt% Mg		A390+10wt% Mg	
		As cast	T6	As cast	T6	As cast	T6
$\alpha$ -Al matrix	Vickers (HV)	98.6 $\pm$ 6.1	148.5 $\pm$ 6.0	105.9 $\pm$ 8.0	153.4 $\pm$ 5.1	115.4 $\pm$ 8.0	132.8 $\pm$ 9.5
Increment (%)		+50.6		+44.8		+15.1	
Bulk material	HRB	64.0 $\pm$ 3.2	84.4 $\pm$ 3.9	67.1 $\pm$ 4.2	79.4 $\pm$ 3.6	71.6 $\pm$ 2.5	80.8 $\pm$ 2.2
	HV	114.0	163.2	119.2	148.2	128.8	152.4
Increment (%)		+43.2		+24.3		+18.3	







Generally, an increase in both the bulk material and  $\alpha$ -Al solid solution hardness can be seen with Mg addition in the A390 alloy in their as cast condition. This is probably caused by the continuous increase in Mg concentration to enforce the lattice strain and pin the dislocations in the  $\alpha$ -Al matrix due to their atomic size difference. The Mg atom is larger than Al, imposing a compressive strain to limit the dislocation movement and segregating in a tensile strain field (Pekguleryuz, 2007). As a result, an additional stress is needed to overcome the attractive force between the solute Mg and dislocations, strengthening the alloy.

After T6 treatment, however, the alloys showed overall increments of the hardness for both bulk material and  $\alpha$ -Al matrix.

After T6 heat treatment, the conventional A390 alloy has excellent RockWell B hardness (43% increment) and the 6 and 10Mg alloys increase the hardness only slightly (24% and 15% increment respectively) when compared to the as cast conditions. Micro-hardness of  $\alpha$ -Al matrix increases nearly 50% for the A390 and also for the 6Mg alloy due to the precipitation hardening of the  $\alpha$ -Al phase, which indicates the heat treatment parameters of this 6Mg alloy approach their optimum value. A smaller increase of 24% for the bulk hardness of the 6Mg alloy might be related to both the relative higher initial as cast value due to the harder  $\text{Mg}_2\text{Si}$  phase present and the lower T6 valuations which are probably caused by the micro-porosity appearance under the measured surface. An increase in hardness of both the  $\alpha$ -Al matrix and bulk material is also observed in the 10Mg alloy, but only ~15% higher than the value of the as cast alloy. These results show that the T6 heat treatment conditions need to be modified in order to achieve optimized values.

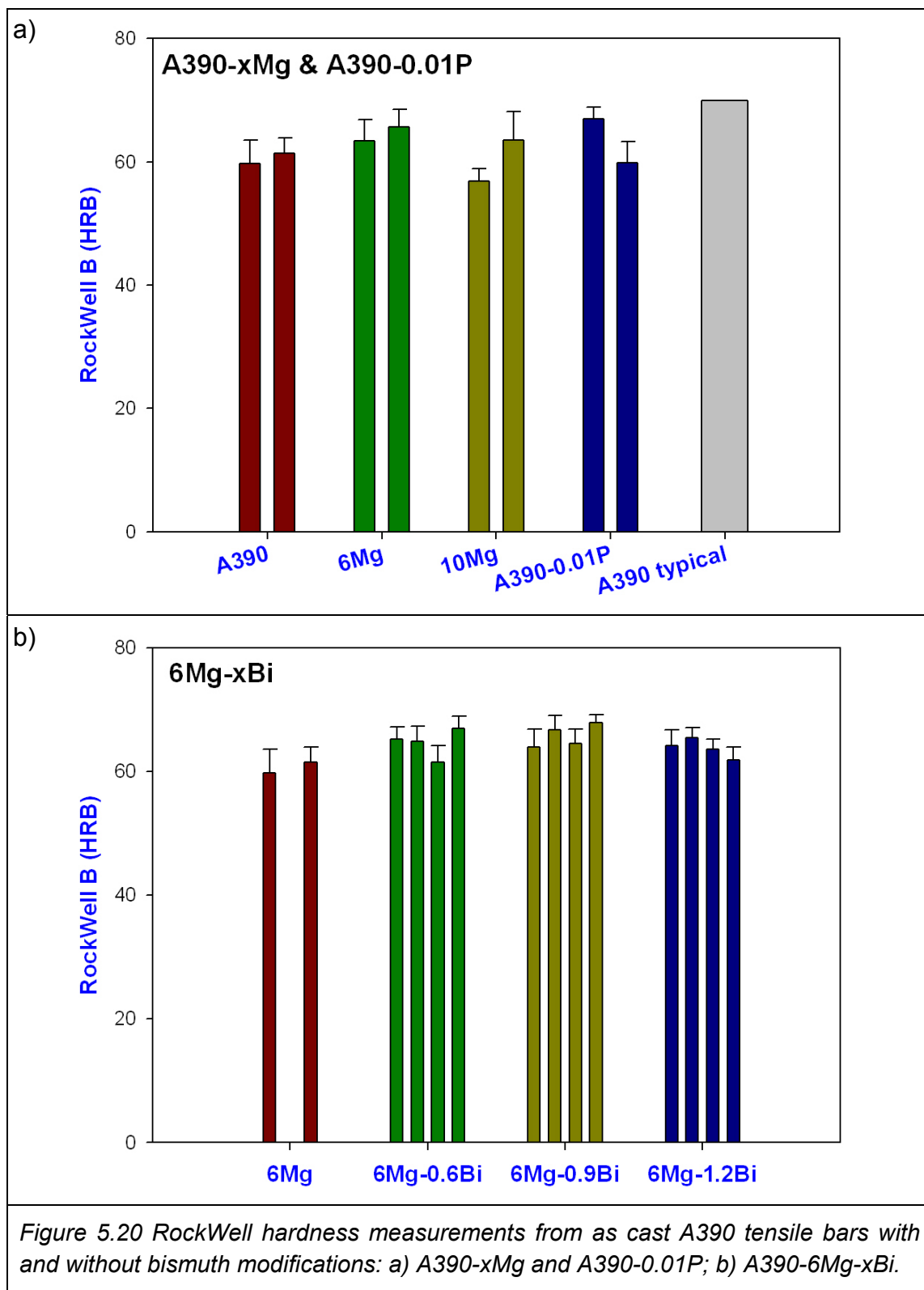
*Table 5.4 RockWell B hardness measurements of the rectangular Mg added A390 tensile bars with and without modifications.*

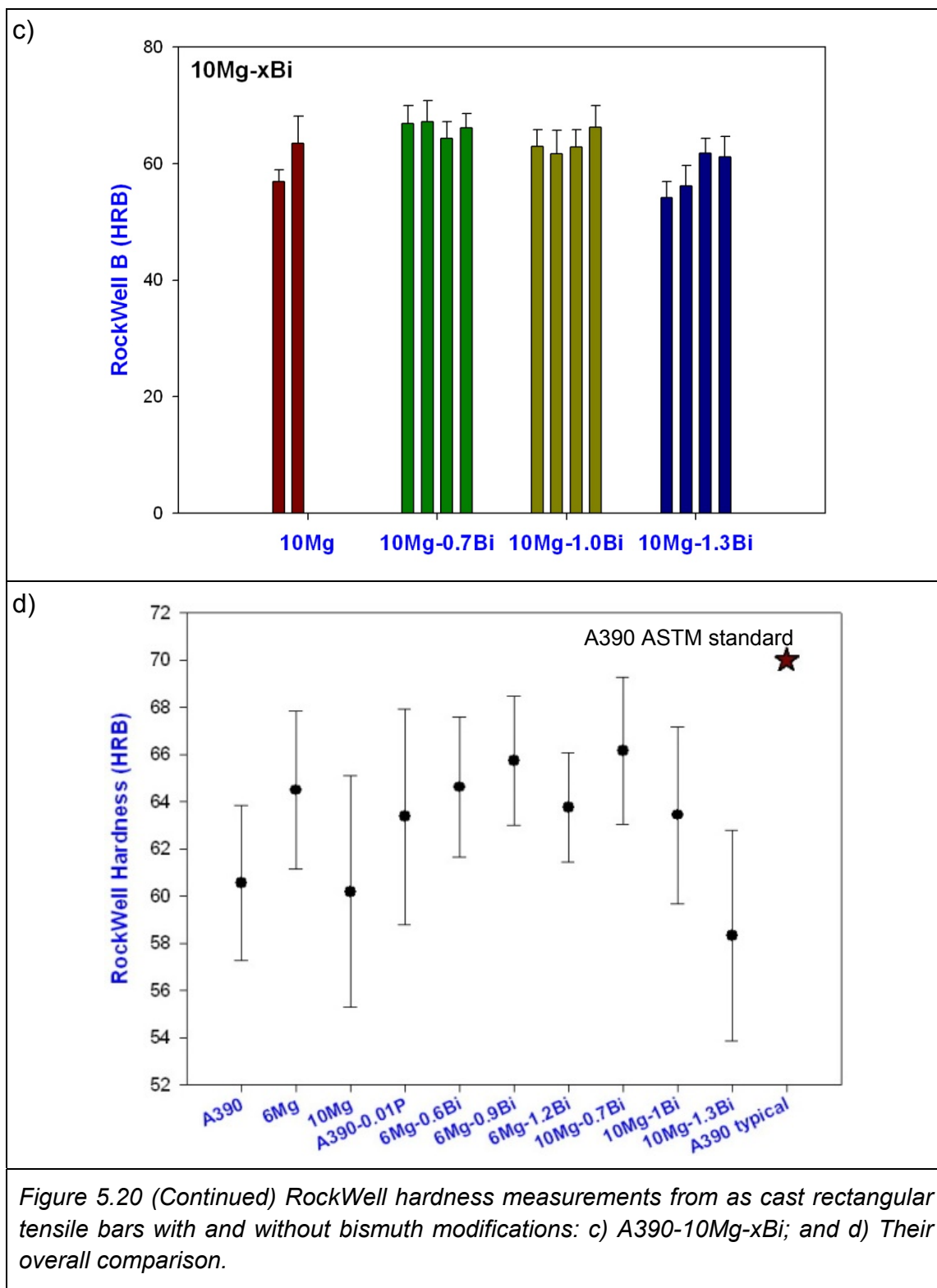
A390	60.6 $\pm$ 3.3	A390-6Mg	64.5 $\pm$ 3.3	A390-10Mg	60.2 $\pm$ 4.9
+0.01P	63.4 $\pm$ 4.6	+0.6Bi	64.6 $\pm$ 3.0	+0.7Bi	66.2 $\pm$ 3.1
—	—	+0.9Bi	65.7 $\pm$ 2.7	+1.0Bi	63.4 $\pm$ 3.7
—	—	+1.2Bi	63.8 $\pm$ 2.3	+1.3Bi	58.3 $\pm$ 4.4

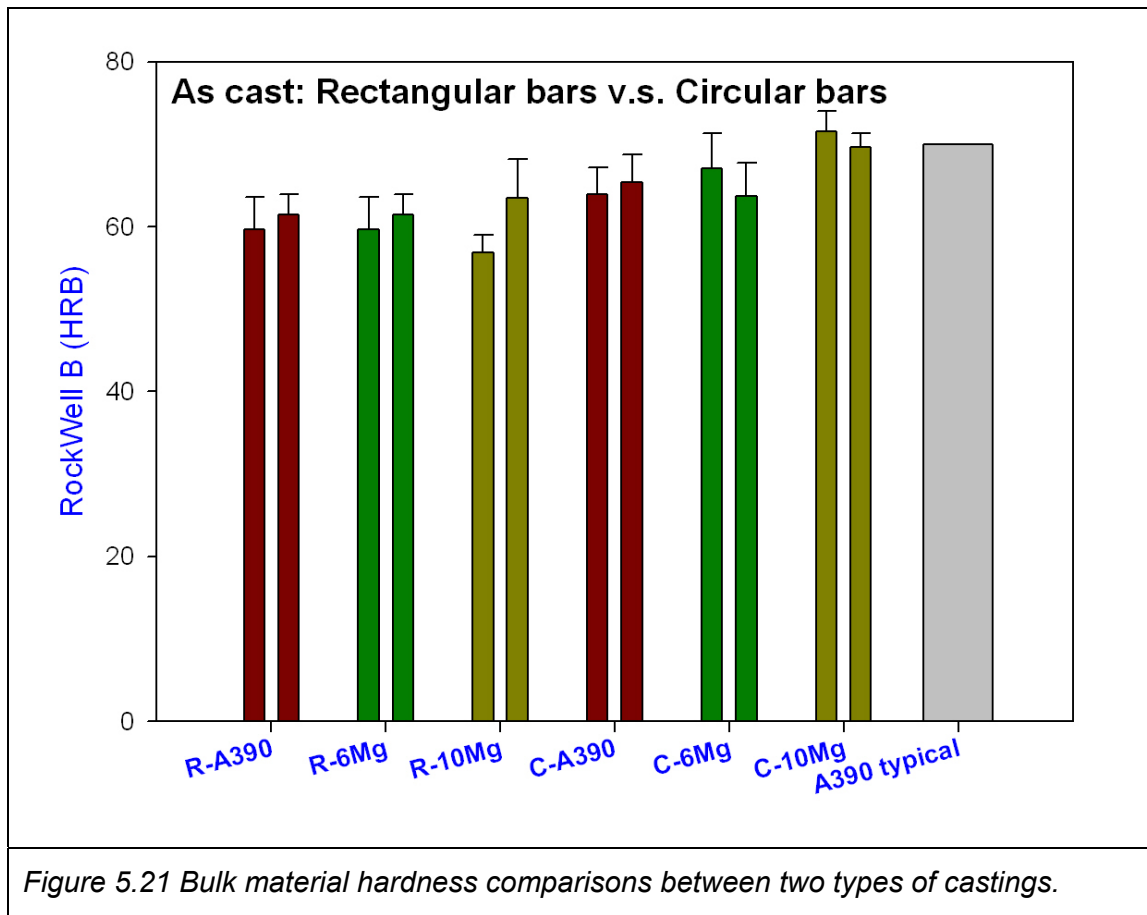
RockWell B hardness measurements are reported in Table 5.4 and Figure 5.20 for the rectangular tensile bars to illustrate the difference before and after the structure modification. Phosphorus (~ 100 p.p.m.) is added into the A390 alloy to modify the primary Si. The alloy hardness improvement might be due to the finer hard primary phases floating in the matrix.

Furthermore, the 6Mg alloy becomes harder than the A390 while the 10Mg alloy hardness decreases a little. This appears contrary to the result derived from the circular tensile bars could be attributed to the pouring condition difference used. The rather high overheat value of ~200°C used at McGill might be the major cause for this difference, degrading the properties. In the modification with bismuth for the 6Mg alloy, an overall enhancement of the alloy hardness can be seen in the Figure 5.20 b) and d). Of the three different Bi contents (0.6, 0.9, and 1.2 wt% as target values), the 0.9% Bi appears to be the best. The 10Mg alloy is also found to increase in hardness by the introducing the bismuth, with optimum effects at 0.7 and 0.9 wt% Bi (targets).

The comparison of as cast specimens produced in McGill and UQAC is shown in Figure 5.21. It can be seen that the rectangular bars have slightly lower hardness value for all three alloys, probably due to more casting defects of the smaller rectangular samples.







### 5.5. Tensile properties

Standard uni-axial tensile tests were used to measure the resistance of both circular and flat rectangular specimens. A subsequent T6 heat treatment was carried out on some of the former type of specimens to compare their tensile properties with the values for the as cast condition. The results are shown in Table 5.5 and Figure 5.23. The same tensile tests were also performed for rectangular samples, with and without the additions of structure modifiers (phosphorus in A390 and bismuth in Mg alloys) and without heat treatment. The

results are present in Table 5.6 and Figure 5.24 and the overall comparison graphs are shown in Figure 5.25 for the two types of the tensile bars.

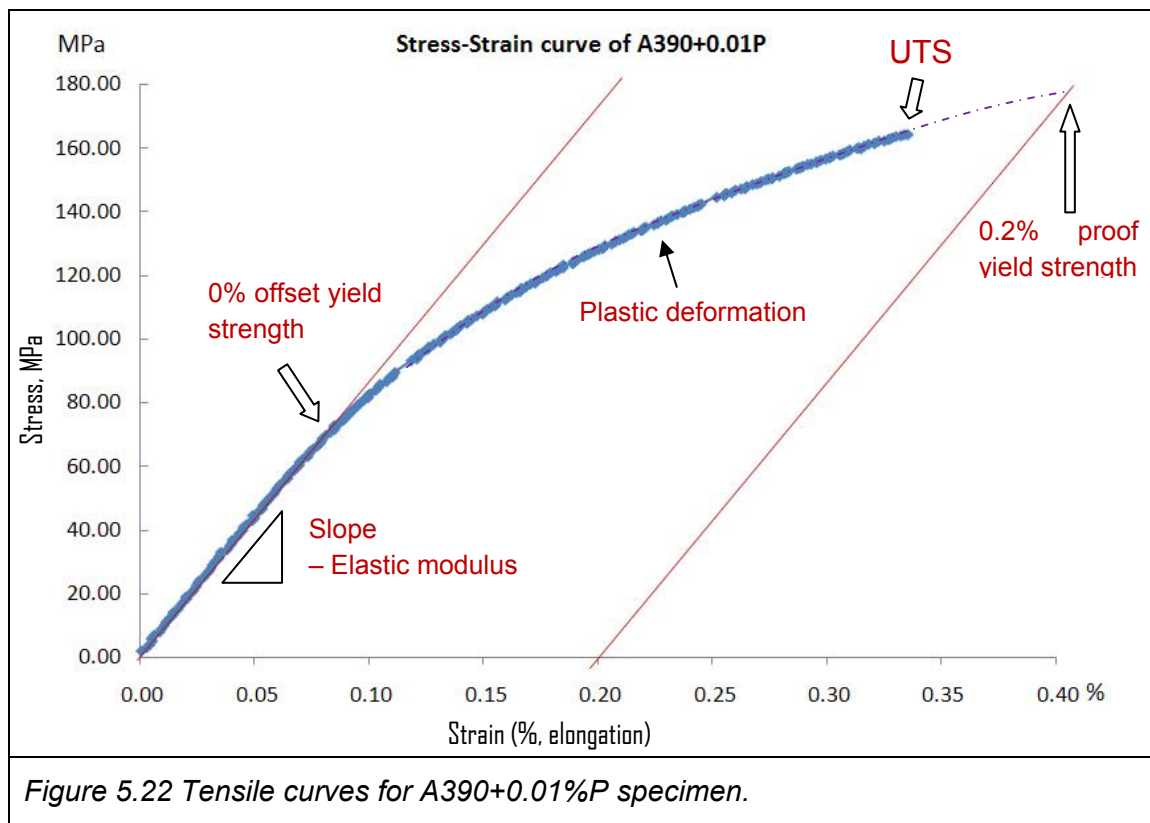


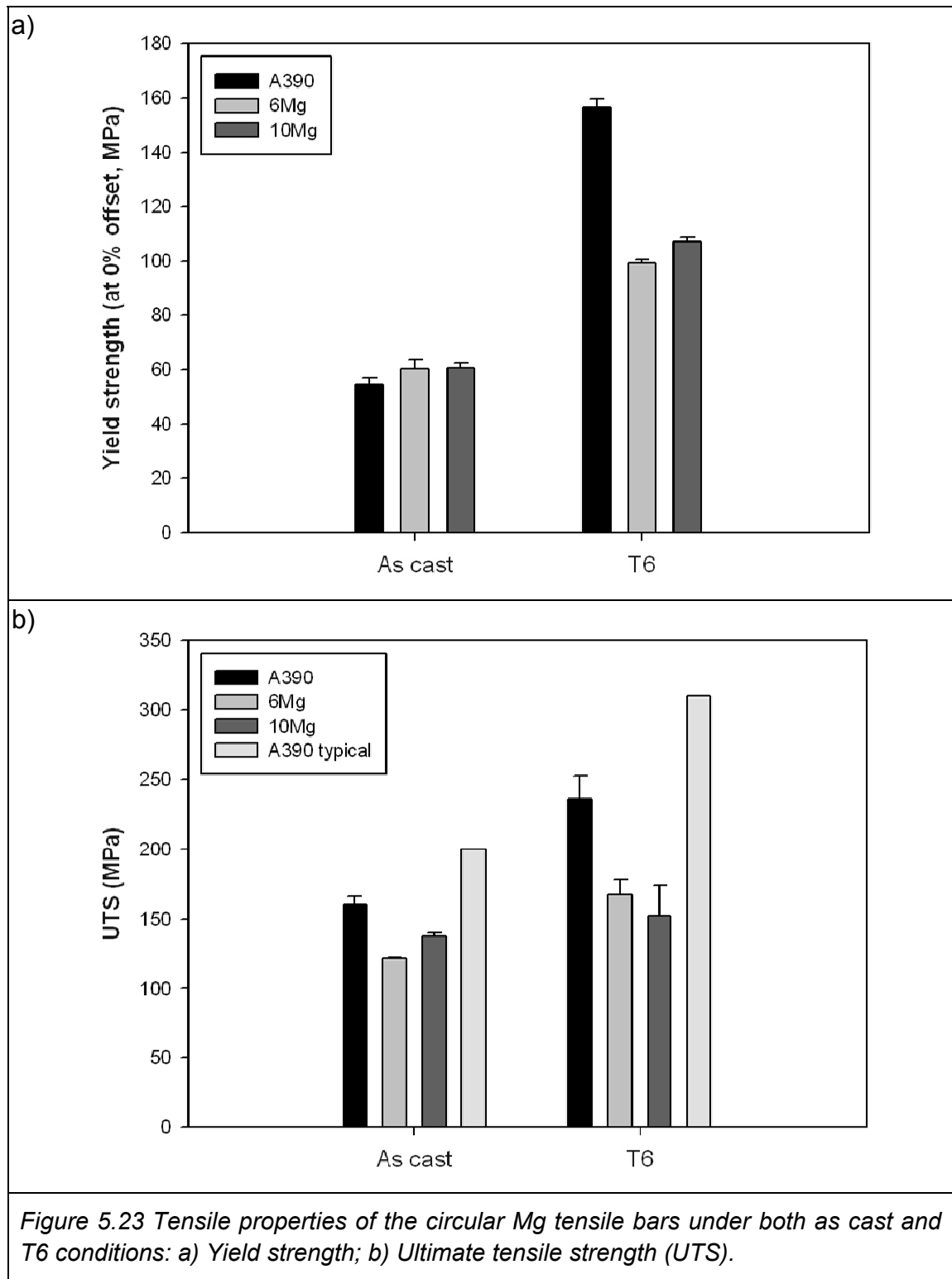
Figure 5.22 describes the method used in determining the tensile properties, including the yield strength (at 0% offset), UTS (ultimate tensile strength), and elastic modulus etc., using the results of the rectangular tensile bar for the alloy A390-0.01P. Note that the 0% offset was selected instead of the conventional 0.2% offset to estimate the alloy yield strength since all samples encountered brittle fracture before reaching the 0.2% strain value. The value for 0% yield strength, however, is difficult to evaluate in a stress-strain curve where the

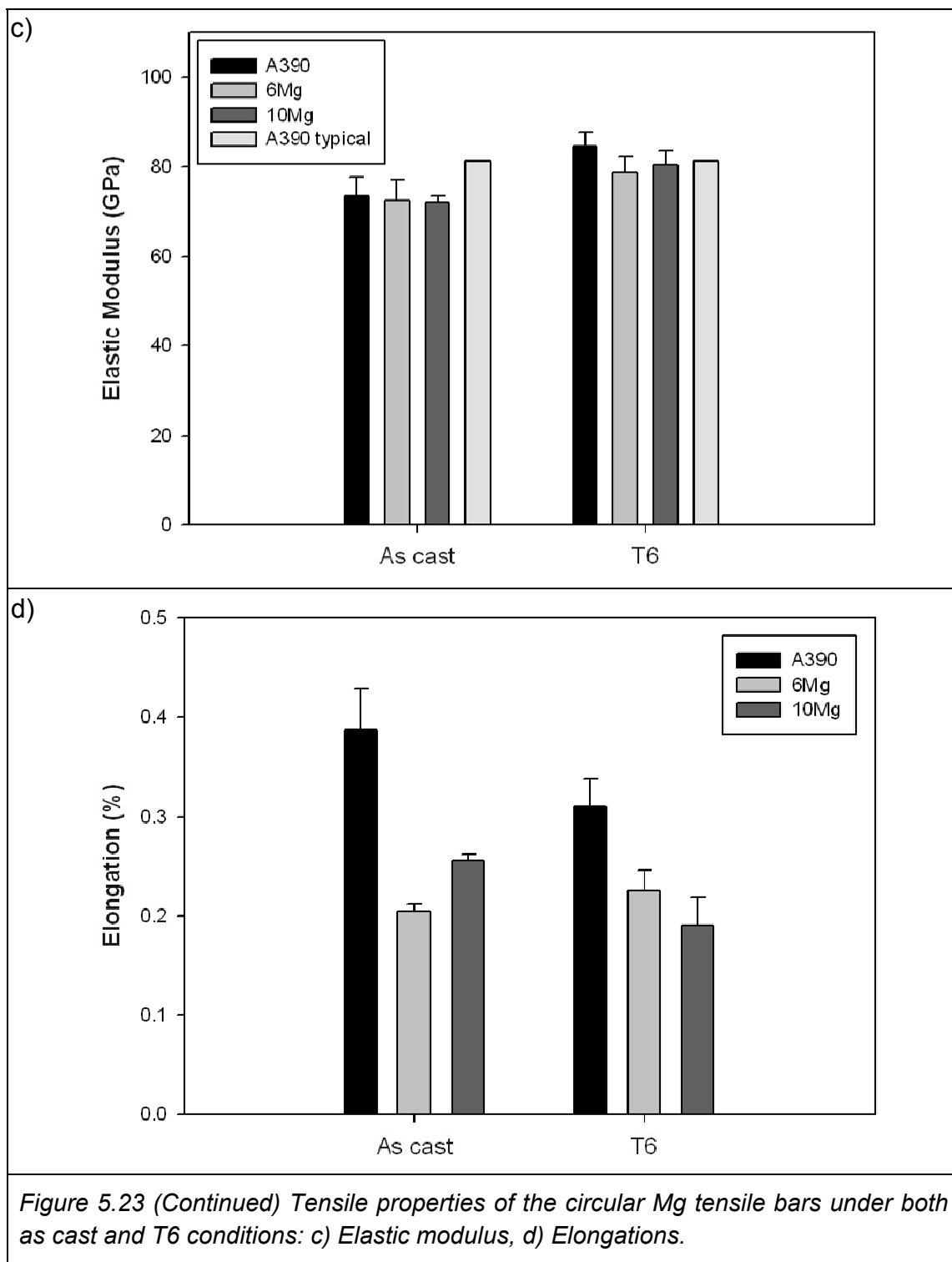
transition of the elastic to plastic deformation changes gradually. As a result, the ASTM standard suggests using the UTS as the material yield strength. A typical value of 200 MPa UTS was reported by (Davis, 1990). Although the measurements for the UTS show some variation caused by porosities and other casting flaws, the comparisons of the mechanical properties and trends among different types of Mg alloys are still very significant.

<i>Table 5.5 Tensile properties of the circular Mg tensile bars for both as cast and T6 conditions.</i>					
Tensile properties		Yield strength (0% offset, MPa)	Tensile strength (MPa)	Fracture elongation (%)	Elastic modulus (GPa)
A390	As cast	53.6 $\pm$ 2.1	160.4 $\pm$ 6.1	0.41 $\pm$ 0.01	71.4 $\pm$ 1.9
	T6	156.7 $\pm$ 3.1	235.7 $\pm$ 16.7	0.31 $\pm$ 0.03	84.6 $\pm$ 3.2
6Mg	As cast	60.4 $\pm$ 3.5	121.2 $\pm$ 0.8	0.21 $\pm$ 0.01	72.6 $\pm$ 4.5
	T6	99.2 $\pm$ 1.5	167.4 $\pm$ 10.5	0.23 $\pm$ 0.02	78.7 $\pm$ 3.5
10Mg	As cast	60.6 $\pm$ 1.7	137.4 $\pm$ 3.1	0.26 $\pm$ 0.01	72.2 $\pm$ 1.3
	T6	107.1 $\pm$ 1.7	152.3 $\pm$ 21.5	0.19 $\pm$ 0.03	80.4 $\pm$ 3.0

As observed in the Figure 5.23 a), both the as cast 6 and 10wt% Mg alloys increased in yield strength to the same level, which denotes that the solid-solution strengthening mechanism is attributed to the Al matrix via the Mg additions.







The results show that A390 doubled its yield strength after T6 heat treatment while the other two alloys resulted in smaller increases. One of reasons for the latter case might be related to the insufficient heat treatment effects. This can be explained by amount of the heat treatable Al in the solidified matrix which decreases with Mg additions, ~77 wt% for A390, ~71 wt% for 6Mg and ~67 wt% for 10Mg, as predicted by FactSage™ shown in Table 3.5. Another factor is related to casting defects, porosities and/ or oxidation inclusions, which are more prevalent in the Mg added A390 alloys.

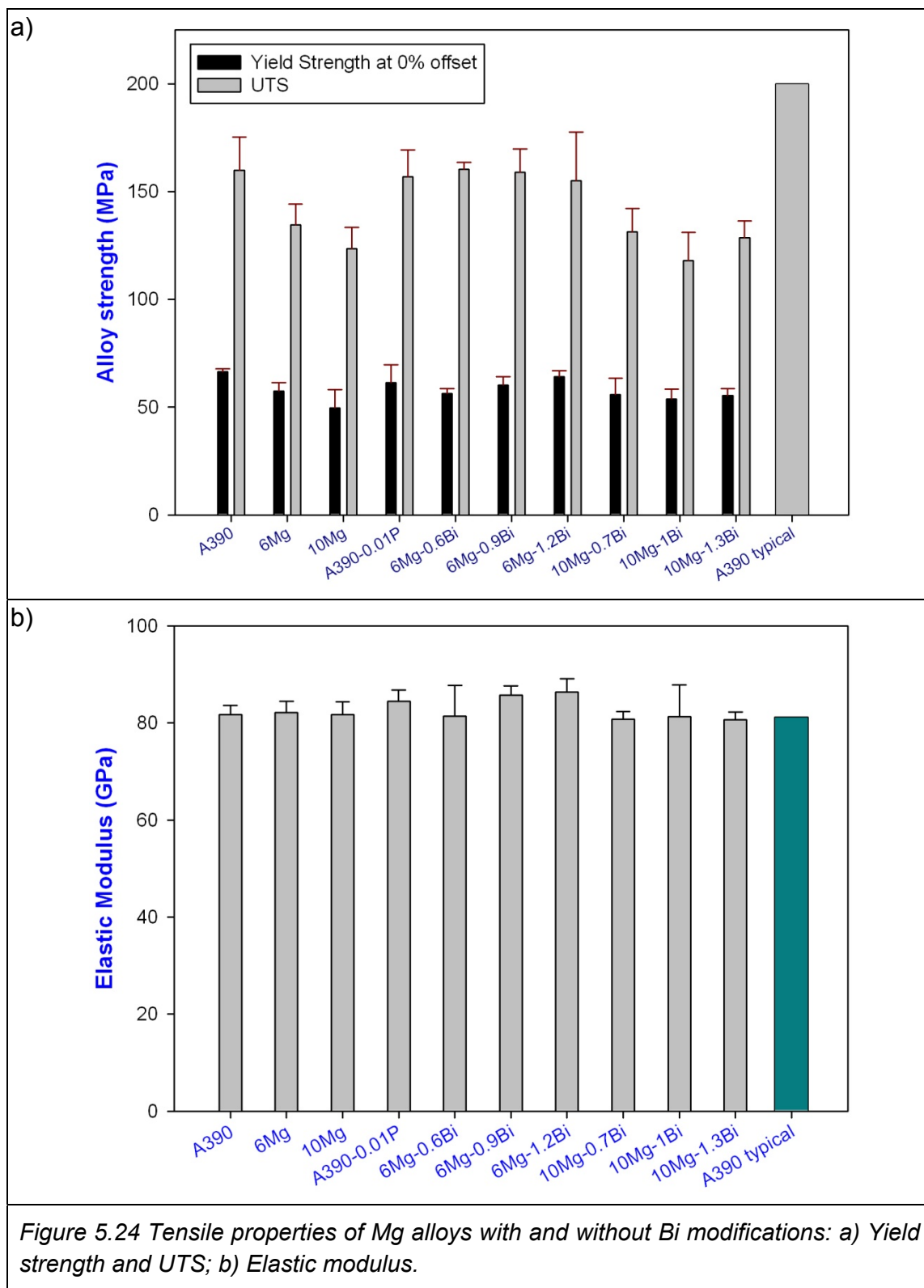
<i>Table 5.6 Tensile properties of the rectangular Mg added tensile bars with and without structure modification additions.</i>				
Tensile properties	Yield strength (0% offset, MPa)	Tensile strength (MPa)	Fracture elongation (%)	Elastic modulus (GPa)
A390	66.3±1.5	159.9±15.5	0.37±0.09	81.7±1.9
A390-0.01P	61.2±8.4	156.9±12.3	0.32±0.06	84.4±2.3
6Mg	57.4±4.0	134.5±9.8	0.26±0.04	82.2±2.3
6Mg-0.6Bi	56.2±2.4	160.2±3.4	0.36±0.03	81.4±6.4
6Mg-0.9Bi	60.2±3.9	159.0±10.7	0.35±0.07	85.7±1.9
6Mg-1.2Bi	64.2±2.7	155.1±22.4	0.33±0.10	86.3±2.8
10Mg	49.6±8.6	123.4±10.1	0.23±0.05	81.7±2.6
10Mg-0.7Bi	55.9±7.6	131.4±10.8	0.23±0.02	80.8±1.6
10Mg-1.0Bi	53.7±4.6	118.1±13.0	0.20±0.03	81.3±6.6
10Mg-1.3Bi	55.3±3.3	128.6±7.8	0.23±0.04	80.6±1.6

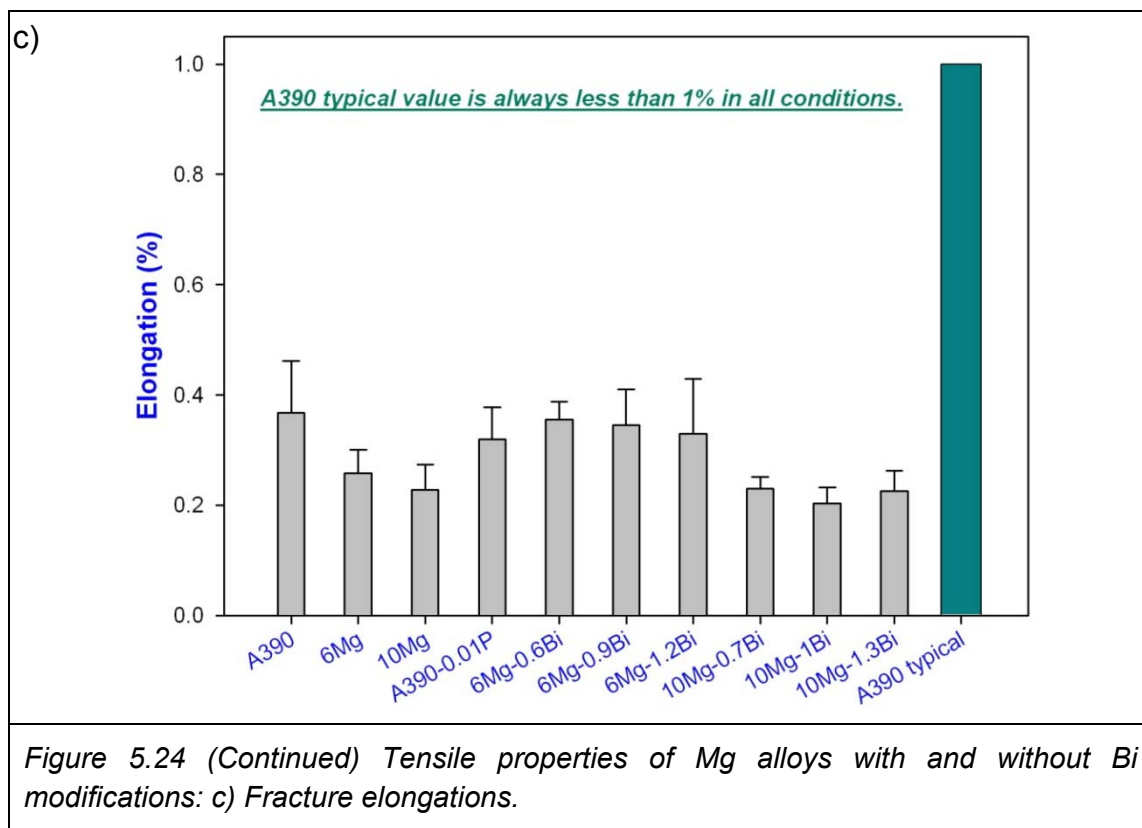
Figure 5.23 b) shows results of the tensile strength of the as cast and T6 samples. None of the samples exceeded the values of the standard A390 alloy. This would indicate that the casting qualities can be improved. Figure 5.23 c)

compares the elastic modulus for all alloy compositions and no significant deviation was found between the two sample geometries. It appears that A390 results in better properties after T6 heat treatment where precipitation hardening was optimized. Fracture elongations are also presented in Figure 5.23 d), which shows once again the alloy A390 attains a higher value than the high Mg alloys.

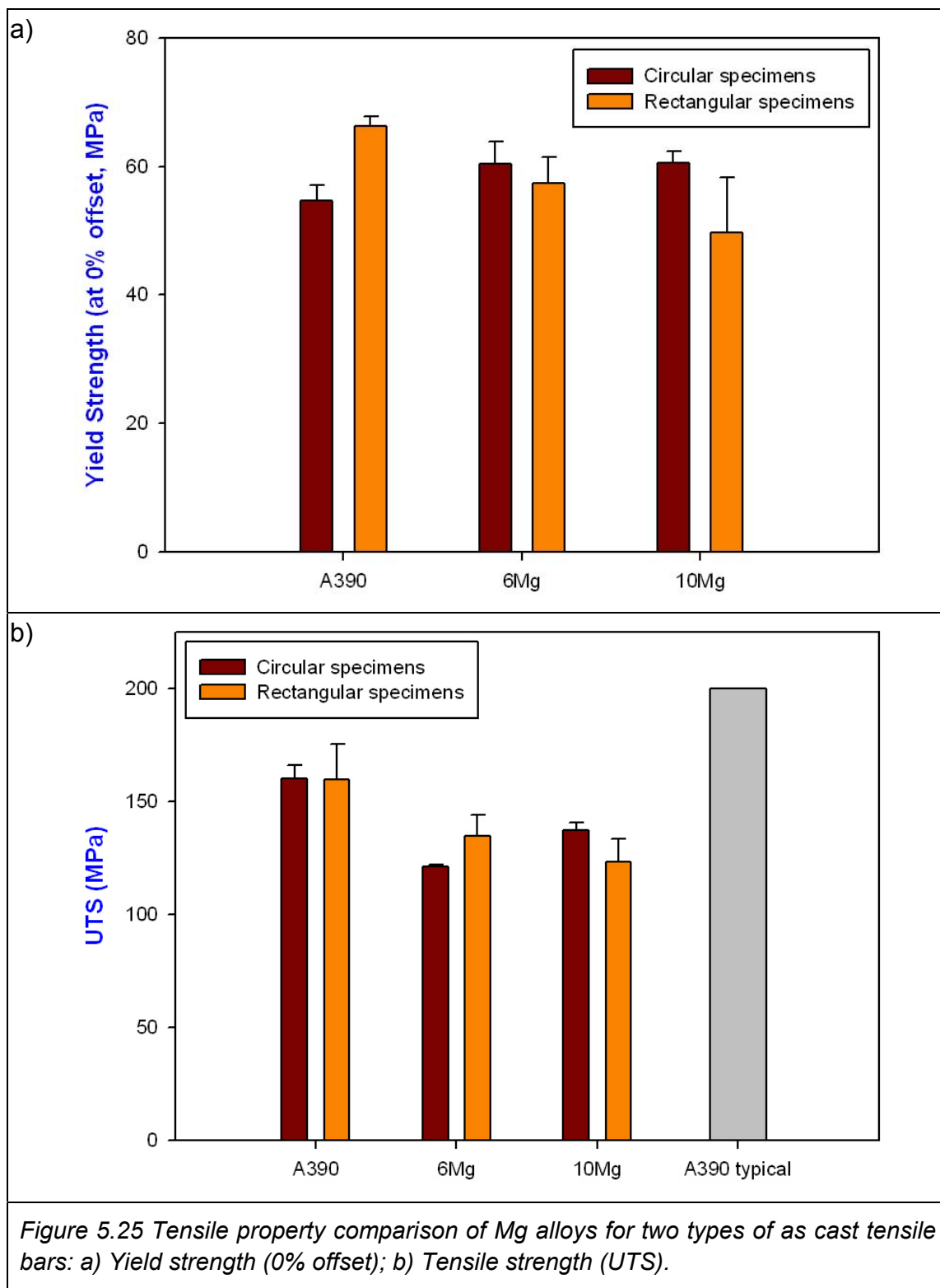
Figure 5.24 a) shows both yield strength and UTS determined for all of the rectangular tensile bars. For the case without modification, a progressing decrease in yield and tensile strength was observed with increasing Mg addition. This can also be attributed to the casting defects. The modification using 100 p.p.m. (0.01%) phosphorus in A390 showed very little changes in tensile properties.

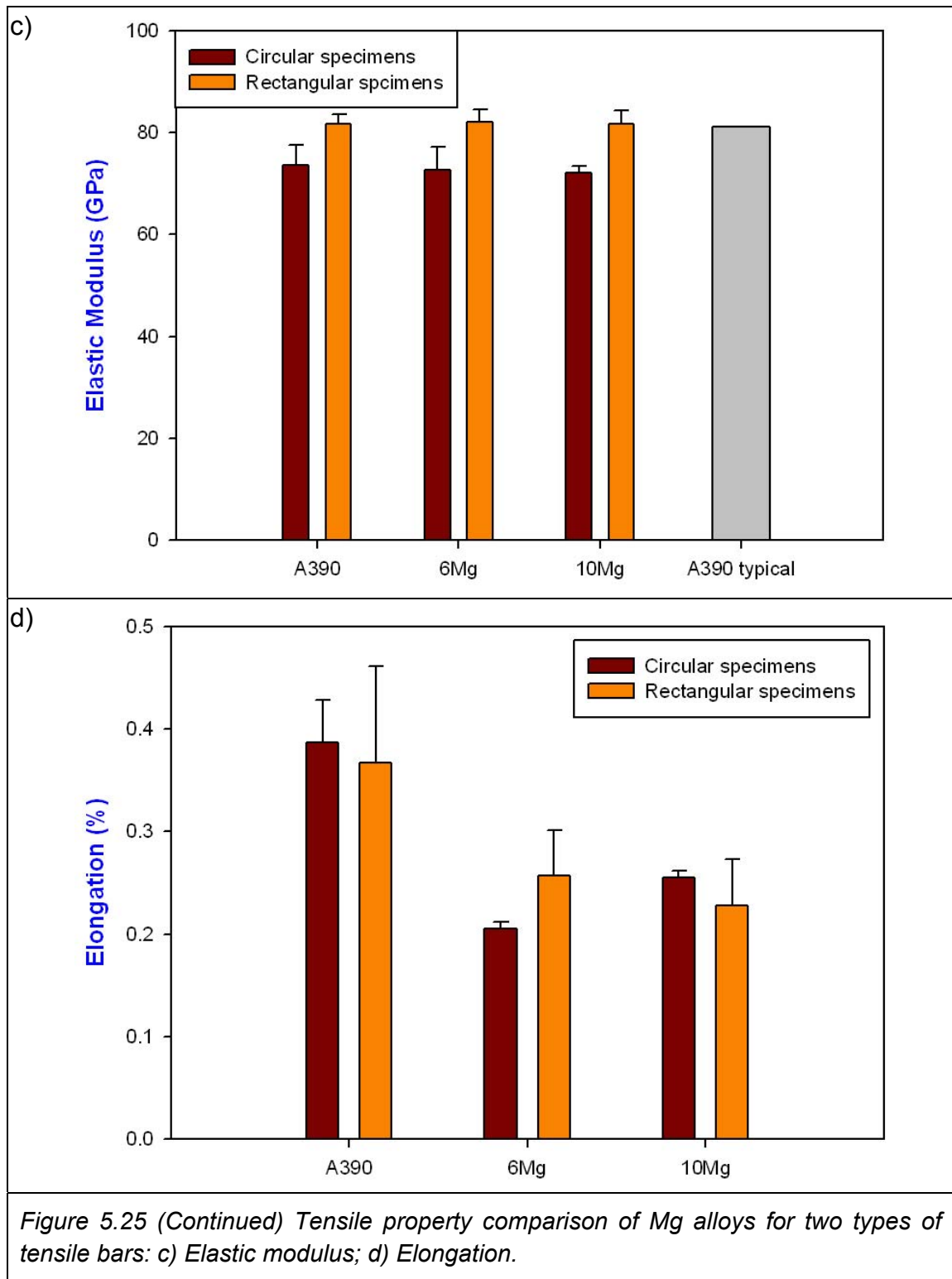
The bismuth additions to these high Mg alloys however showed an overall enhancement in tensile properties. By increasing in the Bi contents from 0.6 to 1.2 wt% (targets), the yield strength was increased while the corresponded ultimate tensile strength decreased. It seems that the alloy 6Mg-0.9Bi shows an optimum modification effect when comparing the elastic modulus and elongations properties.





The results of the fracture tensile strength in the 10Mg alloy are not consistent due to the rather difficult casting characteristics. Figure 5.24 b) shows a similar elastic modulus for all alloys, except for the 6Mg alloy with 0.9 and 1.2 wt% Bi where these additions result in a slightly higher value than the average. Figure 5.24 c) shows that the effect of Bi modification in the 6Mg alloy on elongation is higher than the average. The tensile property comparison between two types of the tensile bar specimens is shown in Figure 5.25 a), b), c) and d) for the as cast conditions.





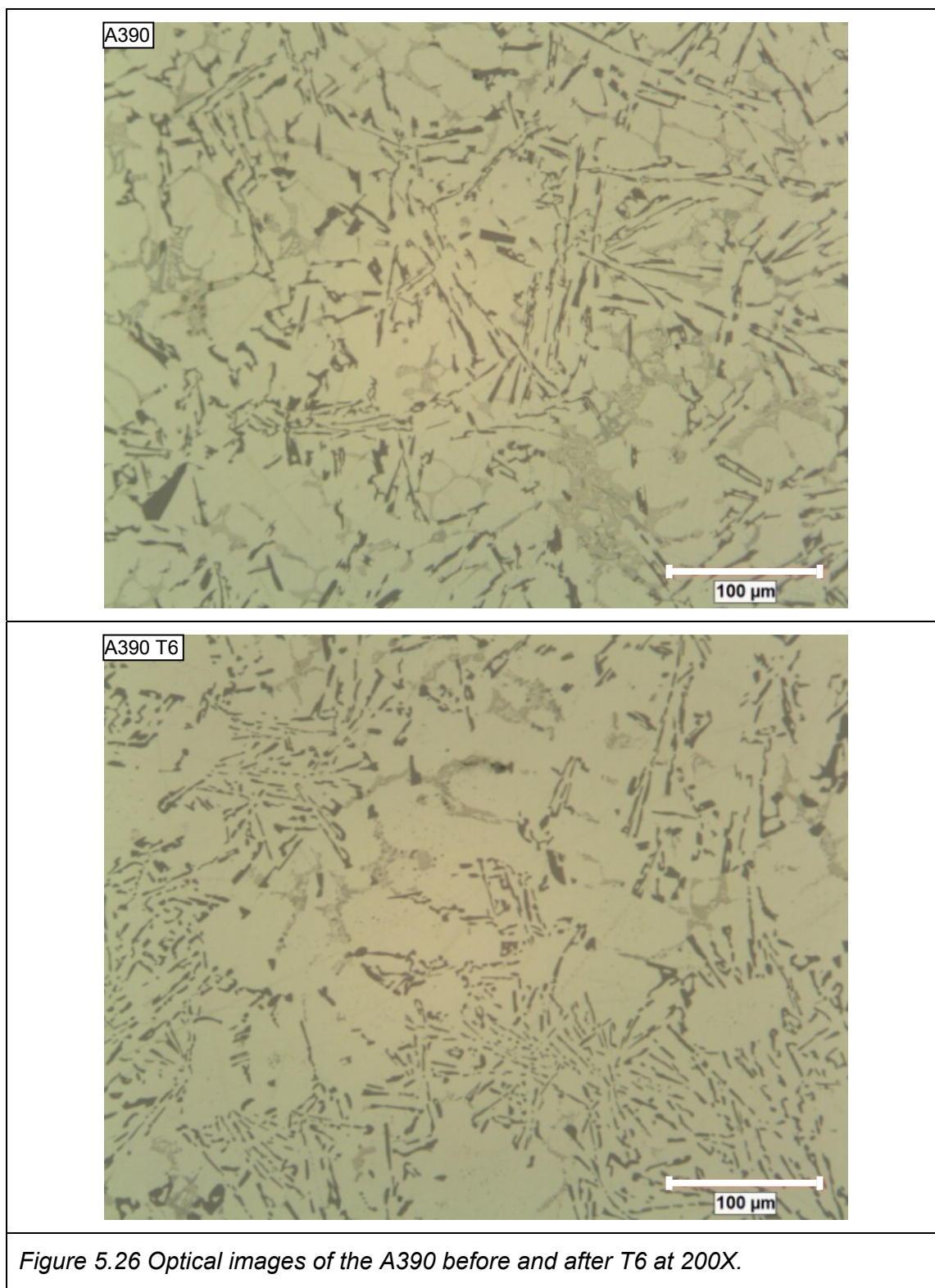


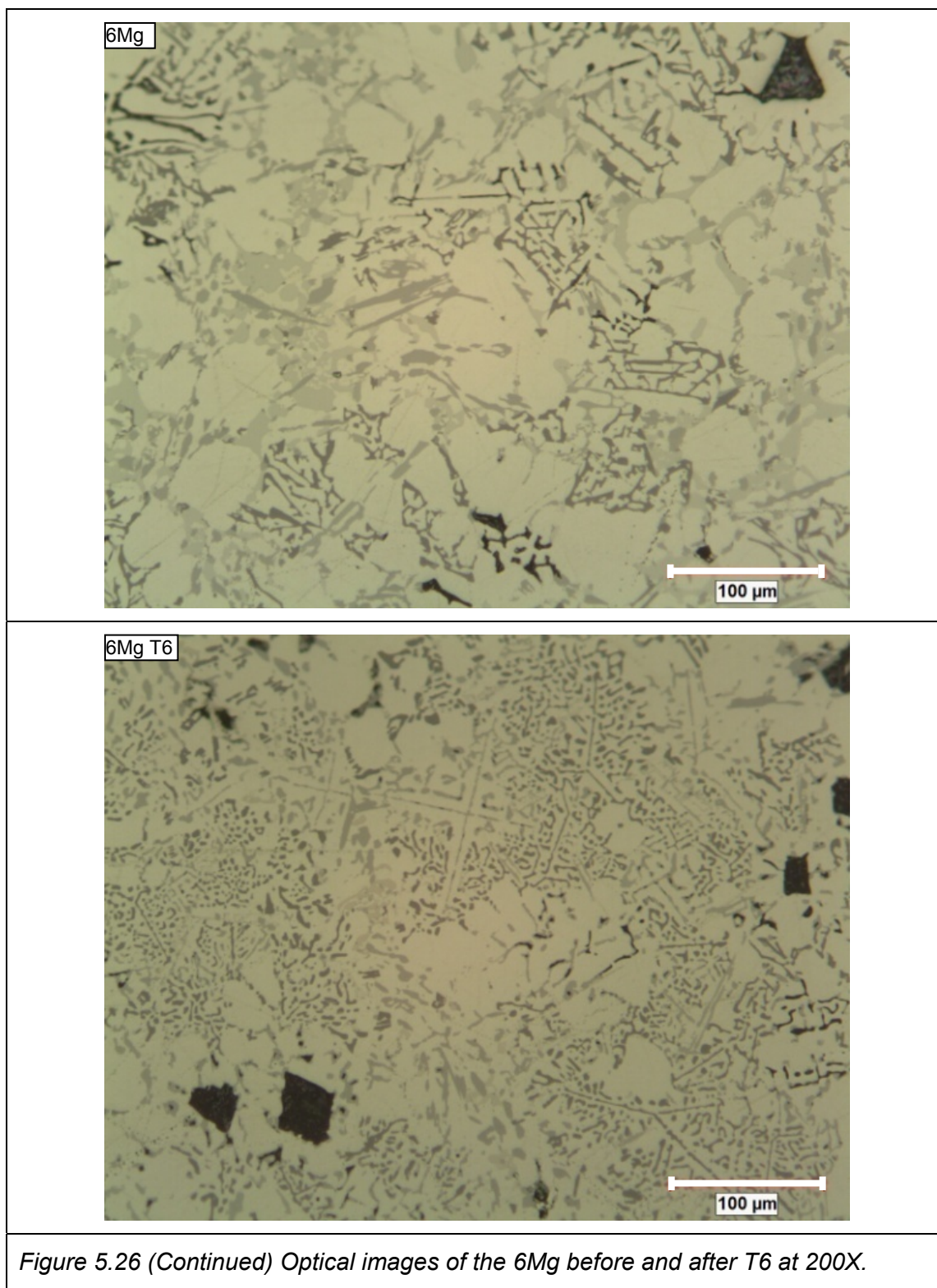
It can be seen that the yield strength of these high Mg alloys have slightly better results for the circular tensile bars than for the rectangular ones, whereas the UTS, the A390 alloy attains the same value for both types of tensile bars. However, the 6Mg alloy shows overall increase for the rectangular bars, also observed for the 10Mg alloy. All measured elongations were below 0.5% indicating a brittle feature for these alloys. And the elastic modulus of the two types of specimens roughly agreed with each other.

## **5.6. Microstructures**

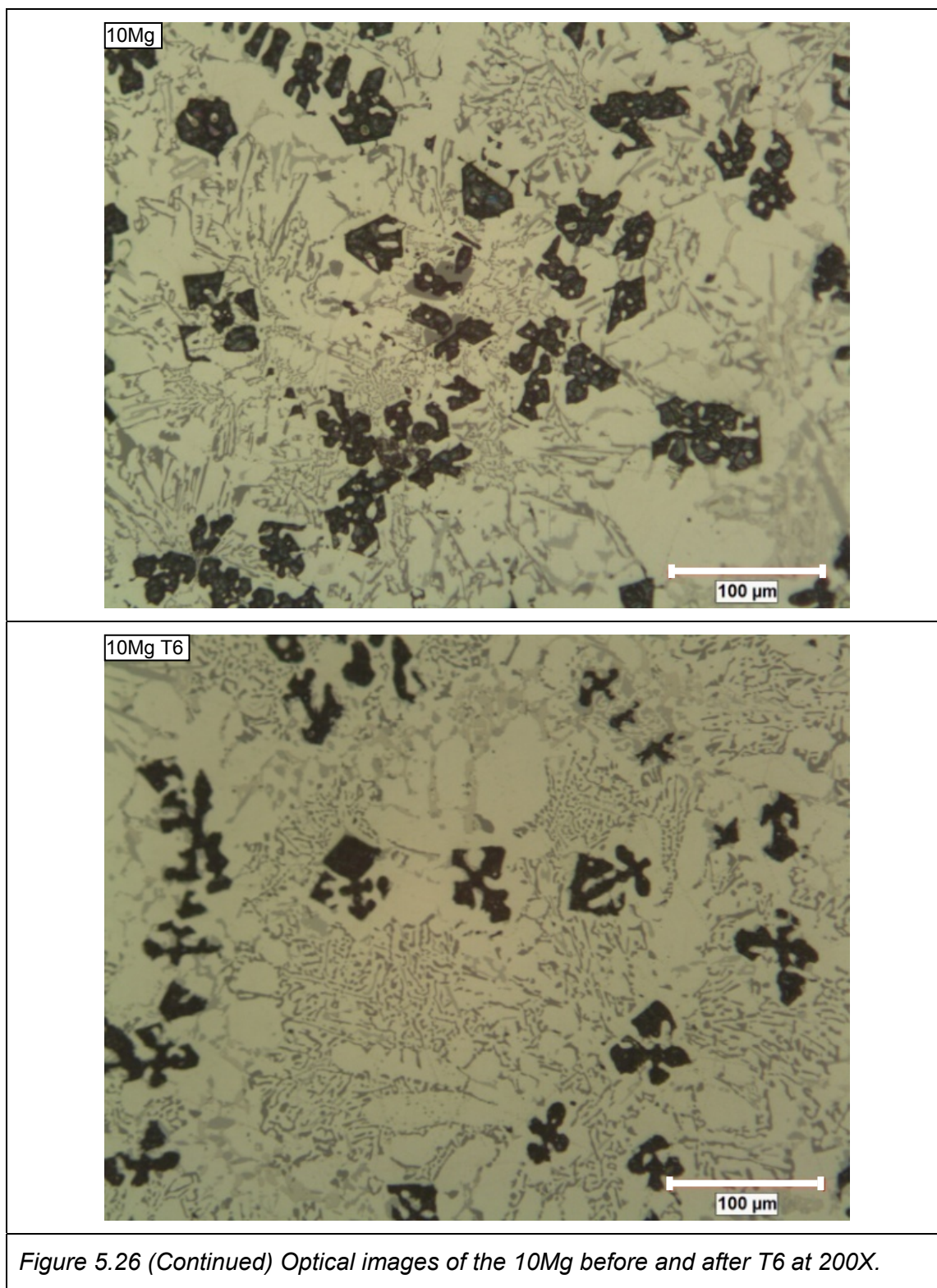
### **5.6.1. Effects of T6 heat treatment**

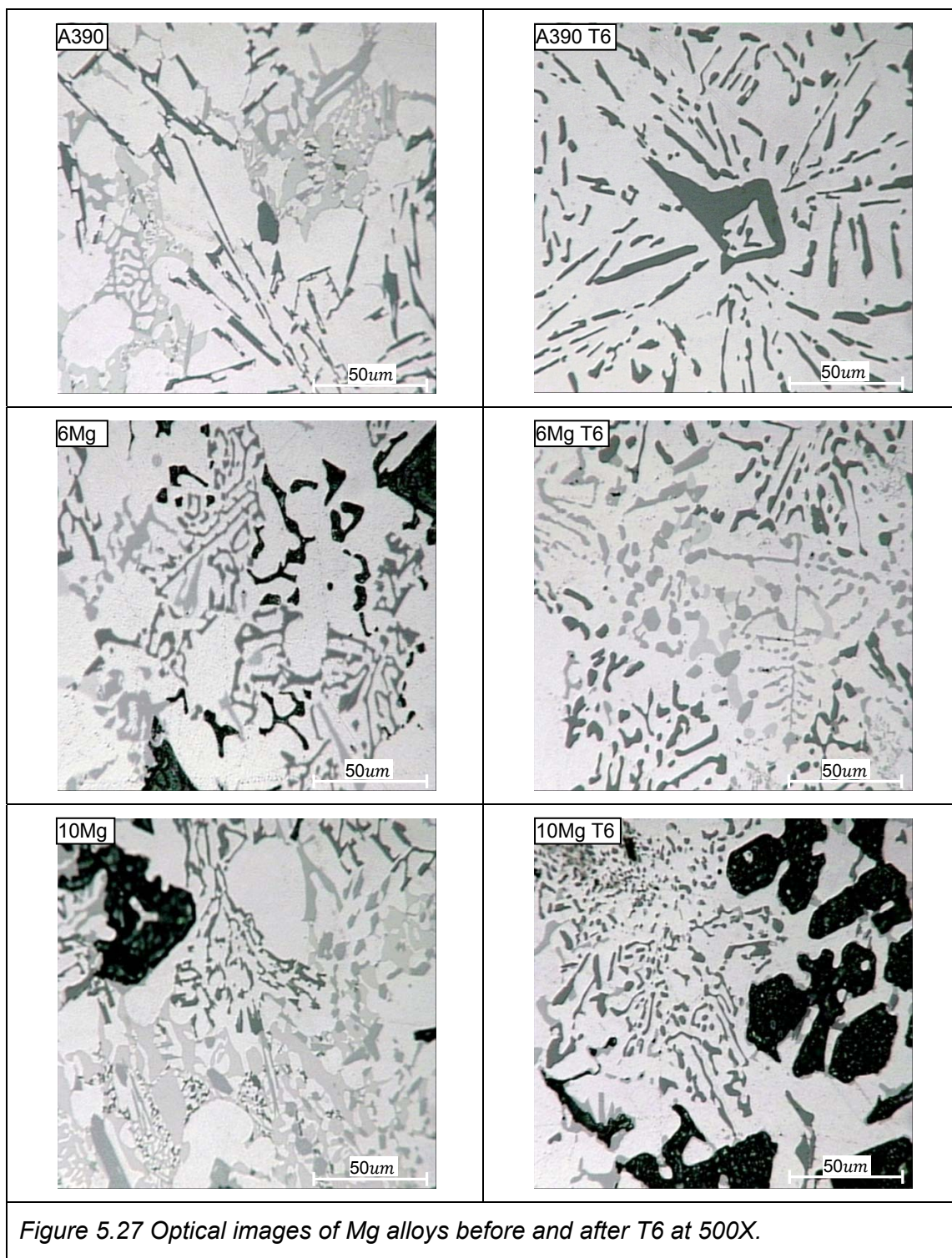
Typical optical microscope (OM) images are shown in the Fig.26 (200X) and Fig.27 (500X) illustrating the microstructural changes due to the T6 heat treatment for all three alloys. It can be seen that the primary phases of either Si or  $Mg_2Si$  tend to segregate in the regions close to the wall of permanent mould instead of the center zone where a smaller temperature gradient occurs.











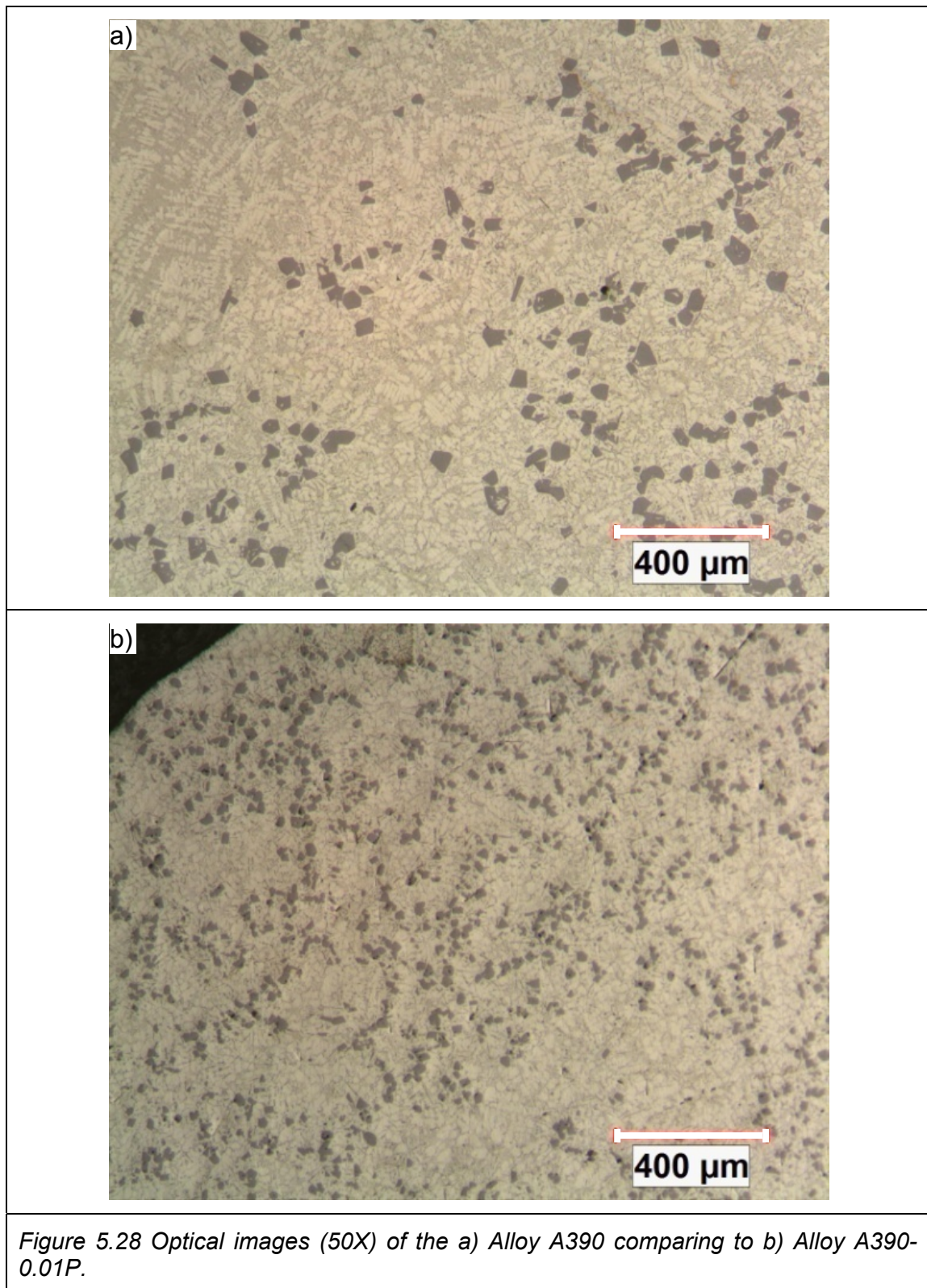
The optical images indicate that the size and distribution of the primary phase changed very little for these alloys after T6 heat treatment, compared to their as-cast condition, while the morphologies of primary  $\text{Mg}_2\text{Si}$  in the 6Mg and 10Mg alloys become more rounded and compact. However, the eutectic phases presented more complex microstructure variations in all three alloys between as cast and T6 conditions. Both the acicular eutectic Si in A390 and the skeleton eutectic Si in the 6Mg or 10Mg alloys were partially broken down into a series of small rounded particles, probably due to the effects of spheroidization and ripening during the solutionizing. Similar fractures can be found in the long needle-like  $\text{Q-Al}_5\text{Cu}_2\text{Mg}_8\text{Si}_6$  intermetallic phase particles for the T6 samples (Figure 5.27 – 6Mg T6). These changes certainly play a role in strengthening the alloys in addition to the  $\theta\text{-Al}_2\text{Cu}$  phase which results in the most effective precipitation hardening. As discussed in the Chapter 3, the as cast  $\theta\text{-Al}_2\text{Cu}$  particles will go through the supersaturated solid solution and Cu enriched GP zones are formed before reaching the metastable  $\theta''$  precipitates which are the most efficient hardening agents. At this point, the particle size is usually as small as  $100\text{nm}$ , which is not easy to be identified by OM or SEM means. It was observed that the  $\theta\text{-Al}_2\text{Cu}$  phases do not seem to be dissolved completely in the  $\alpha\text{-Al}$  matrix since they were still visible in the T6 specimens. This might be caused by the original  $\theta\text{-Al}_2\text{Cu}$  particles which are too coarse to disappear readily or by the over ageing to reform  $\theta\text{-Al}_2\text{Cu}$  in the matrix again. However, the heat treatment factors have to be controlled precisely in order to achieve the

expected alloy properties. Other intermetallic phases such as  $\beta$ -Mg<sub>2</sub>Si and Q-Al<sub>5</sub>Cu<sub>2</sub>Mg<sub>8</sub>Si<sub>6</sub> are also heat treatable, resulting in similar precipitation effects, but were not investigated in this analysis.

#### 5.6.2. Effect of structure modifiers

Primary phase structure modification experiments were carried out by adding phosphorus to the A390 alloy for the primary Si modification. The addition of bismuth to Mg alloys for the modification of primary Mg<sub>2</sub>Si has not been reported before and the corresponding microstructures were investigated in order to determine their property influencing factors. Phosphorus and bismuth were added to the alloys to produce permanent mould tensile bar castings. Figure 5.28 shows that both the primary Si size and distribution were altered by modifying the alloy A390 with a 0.01 wt% P addition. A size reduction of one half or one third of the original size ( $\sim 40 - 50\mu\text{m}$ ) was observed depending on the amount of modifiers that were added. This indicates the phosphorus-bearing compound AlP, which was formed according to the reaction  $\text{Cu}_3\text{P(l)} + \text{Al(l)} \rightarrow \text{Cu(l)} + \text{AlP(s)}$  (Zhao, 2006), acts as an effective nucleation agent of the primary Si, since their cubic structures have the similar lattice parameters of 5.42Å for Si and 5.45Å for AlP (Zhang, 2007). Nucleation of the primary Si crystals is facilitated by the addition of the master alloy (P-8Cu) to hypereutectic Al-Si melts, resulting in typical heterogeneous nucleation behaviour.







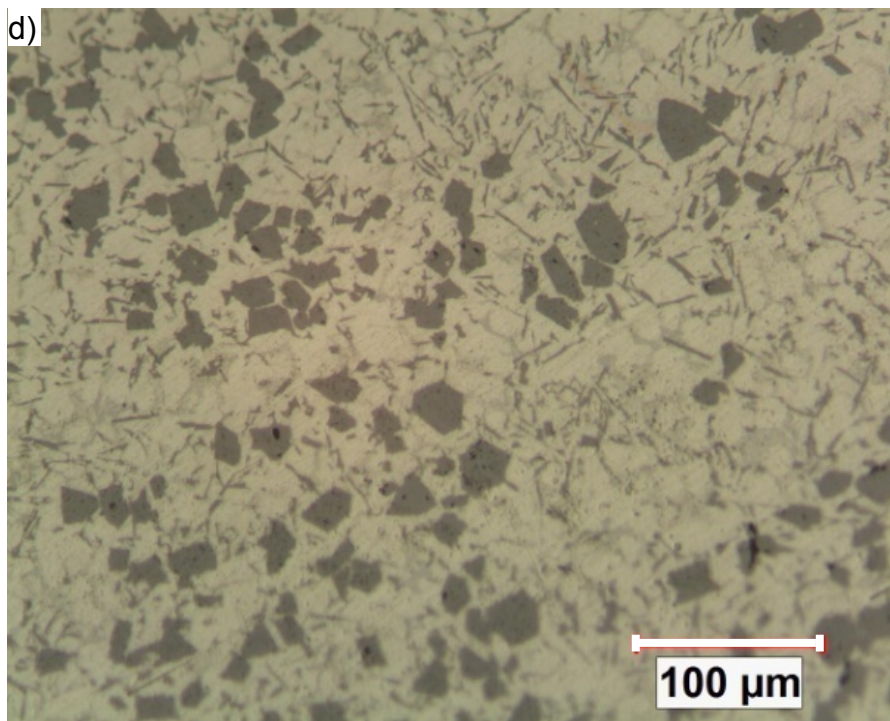
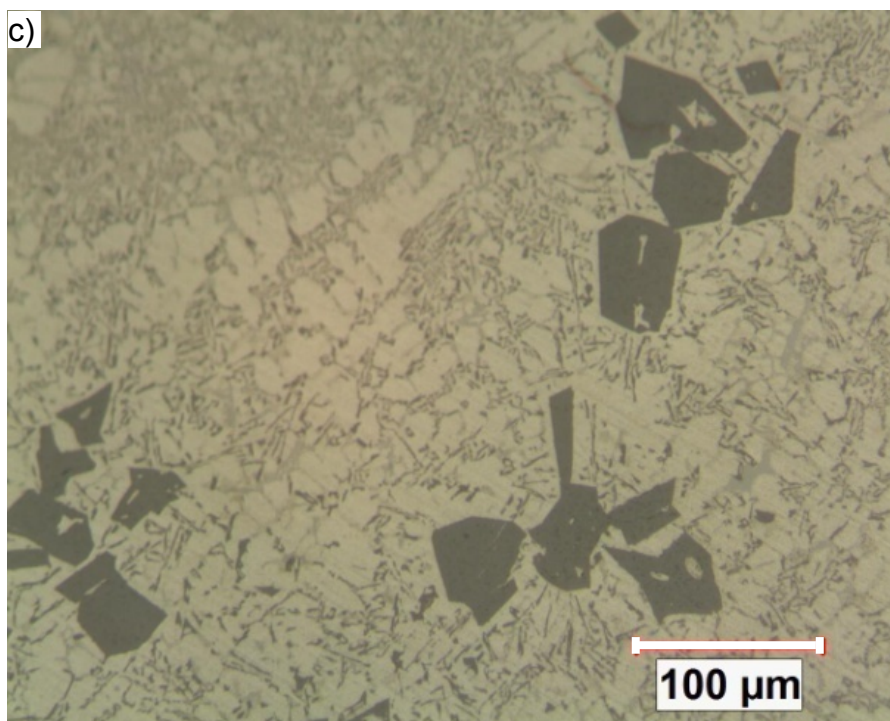
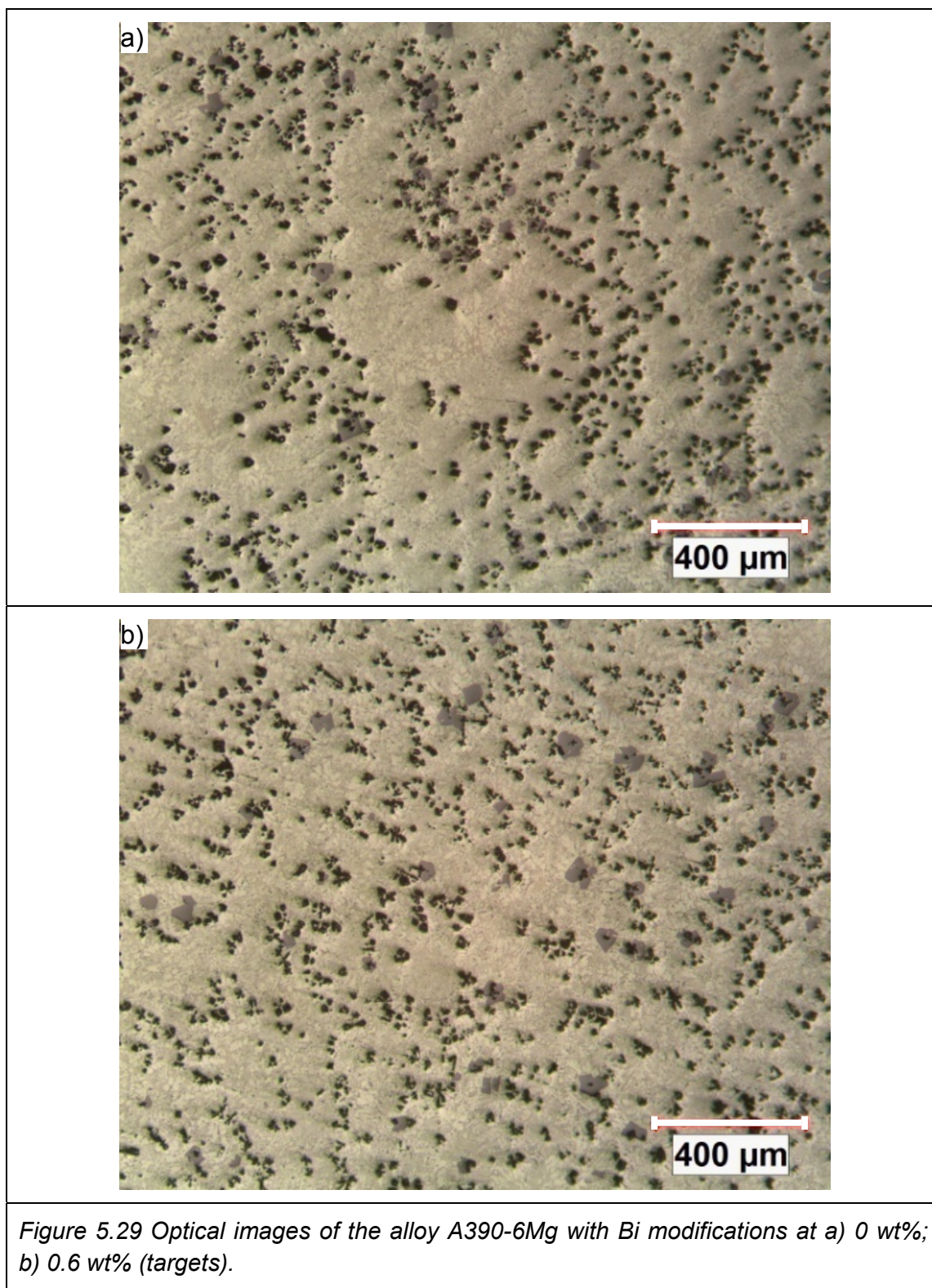


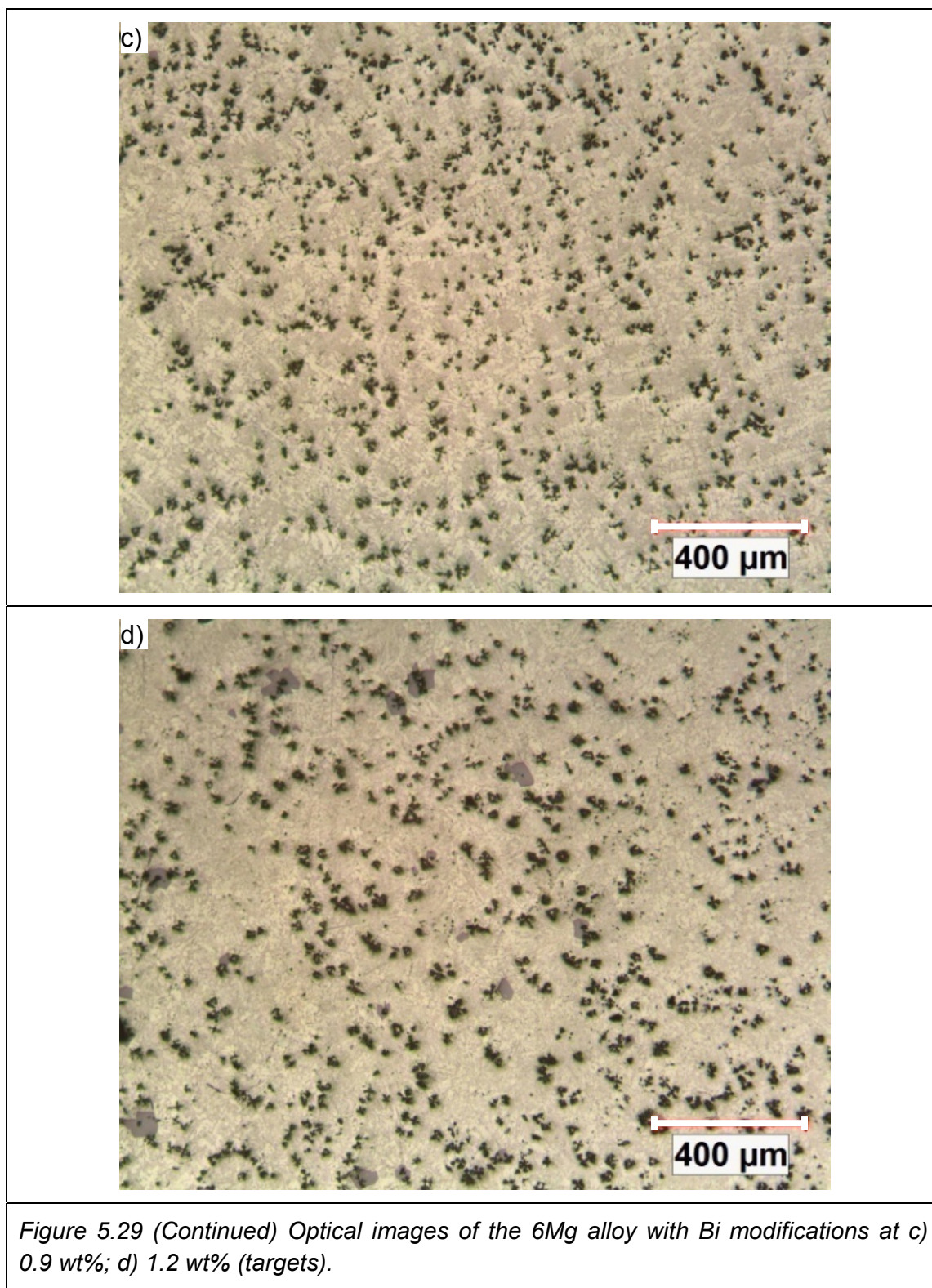
Figure 5.28 (Continued) Optical images (200X) of the c) Alloy A390 comparing to d) Alloy A390-0.01P.

A more dispersed primary Si distribution was also observed in the modified microstructures when compared to the non modified case in which agglomeration of the coarse primary Si obviously occurred. The morphologies of the primary Si appear to change to polygonal shapes after modification. However, there was no increase in tensile properties for the phosphorus addition in the current study. This is probably due to the casting quality variations for the A390 alloys.

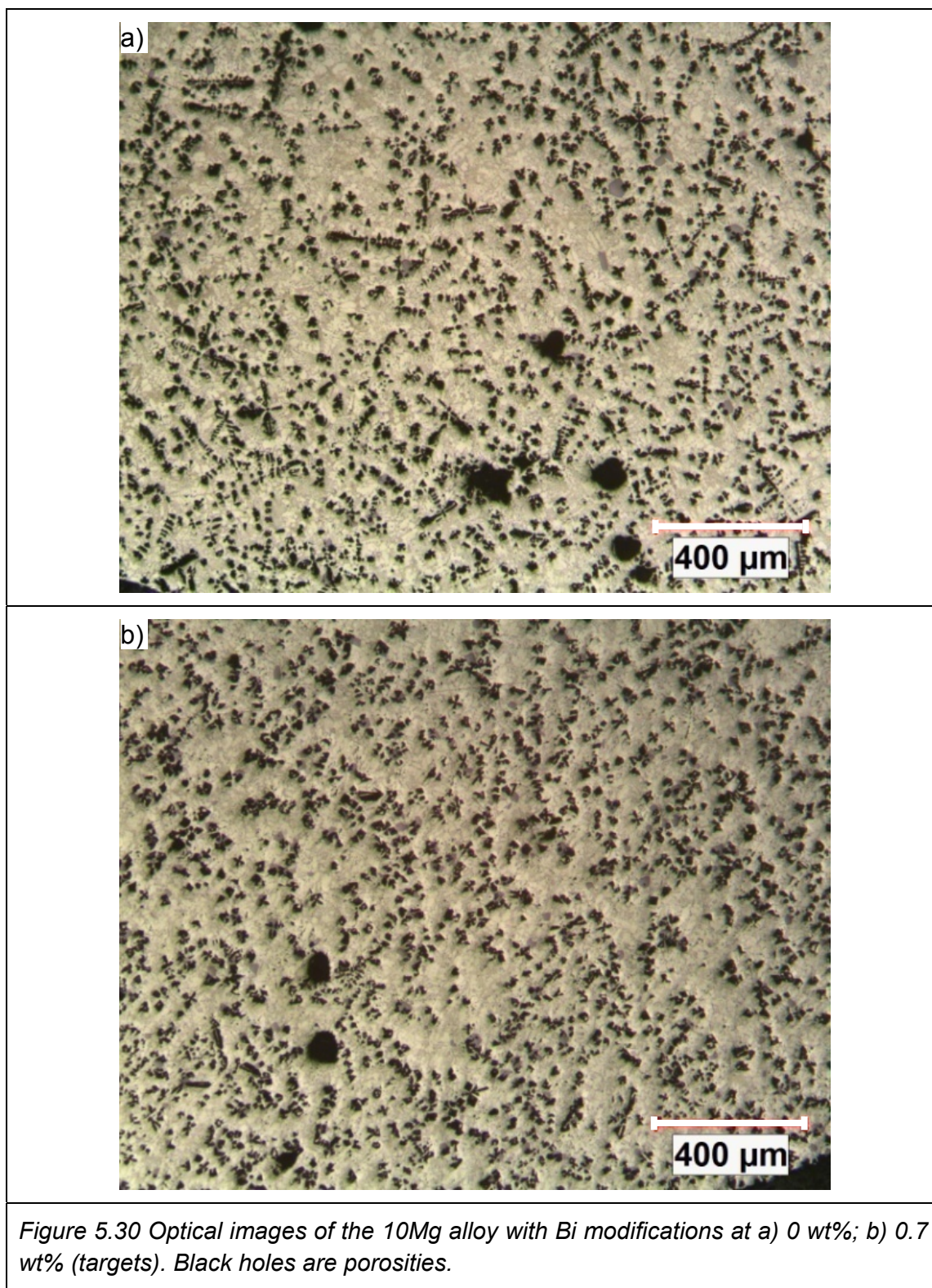
A new structure modifying element (Bi) was selected to determine its influence on the primary  $\text{Mg}_2\text{Si}$  phases formed in the 6 and 10 wt% Mg alloys. Figure 5.29 and Figure 5.30 are optical image microstructures of the effect of bismuth additions on the 6Mg and 10Mg alloy matrix respectively, showing a series changes of the primary  $\text{Mg}_2\text{Si}$  under 50X magnifications. Of the three levels of Bi additions (0.6, 0.9, and 1.2 wt% as targets) to the 6Mg alloy, it seems that the 0.9 wt% addition had the best effect on the primary  $\text{Mg}_2\text{Si}$  phase with an obvious size reduction as shown in the Figure 5.29 c). For the other two Bi concentrations, an uneven size distribution can be observed in the matrix although it displayed some smaller precipitations. A more detailed series of tests need to be carried out in order to determine the optimal Bi addition with a precise control of the casting conditions. However, an increase of their tensile properties was observed for the 6Mg alloy for all three levels of Bi content.



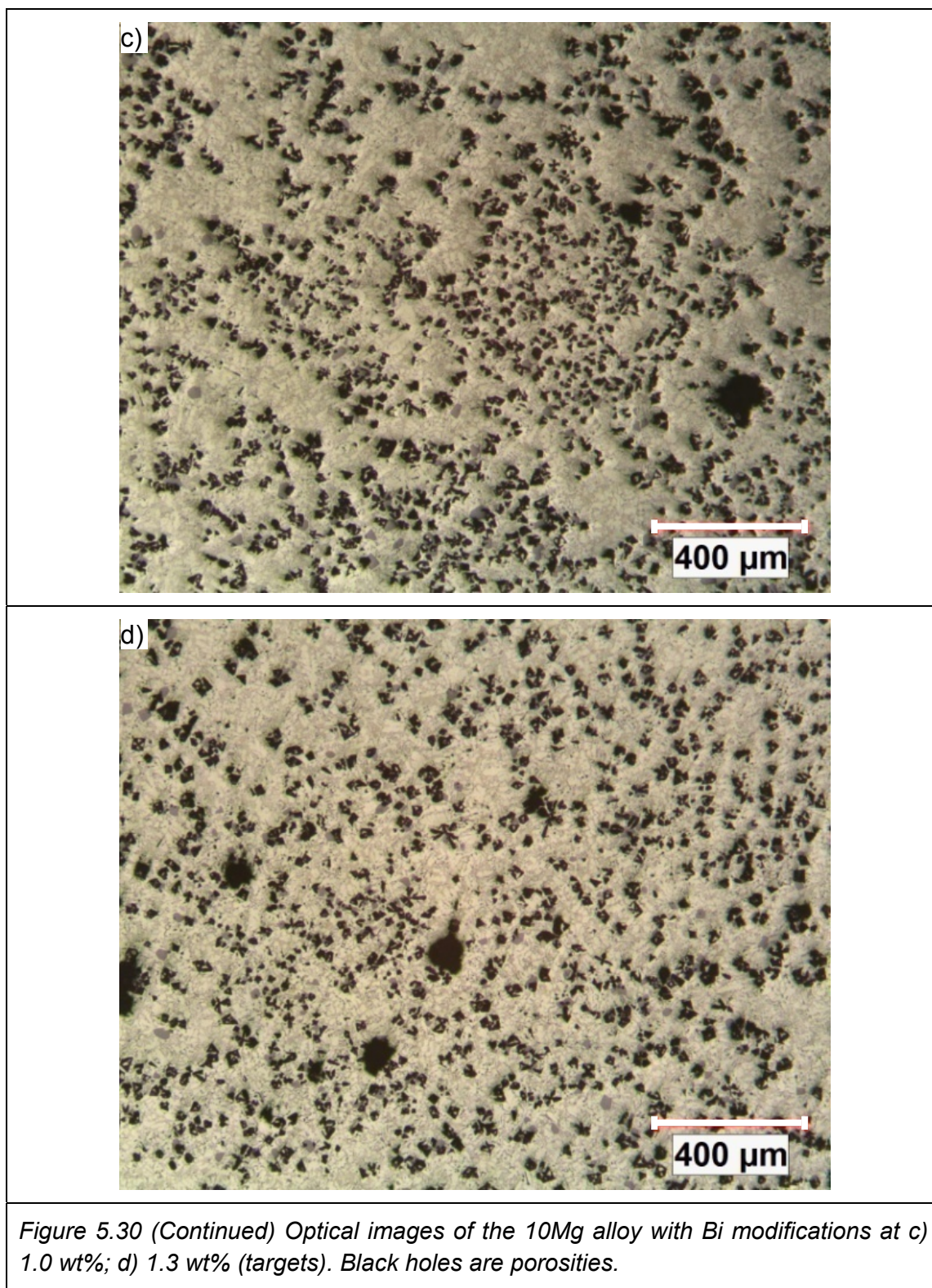


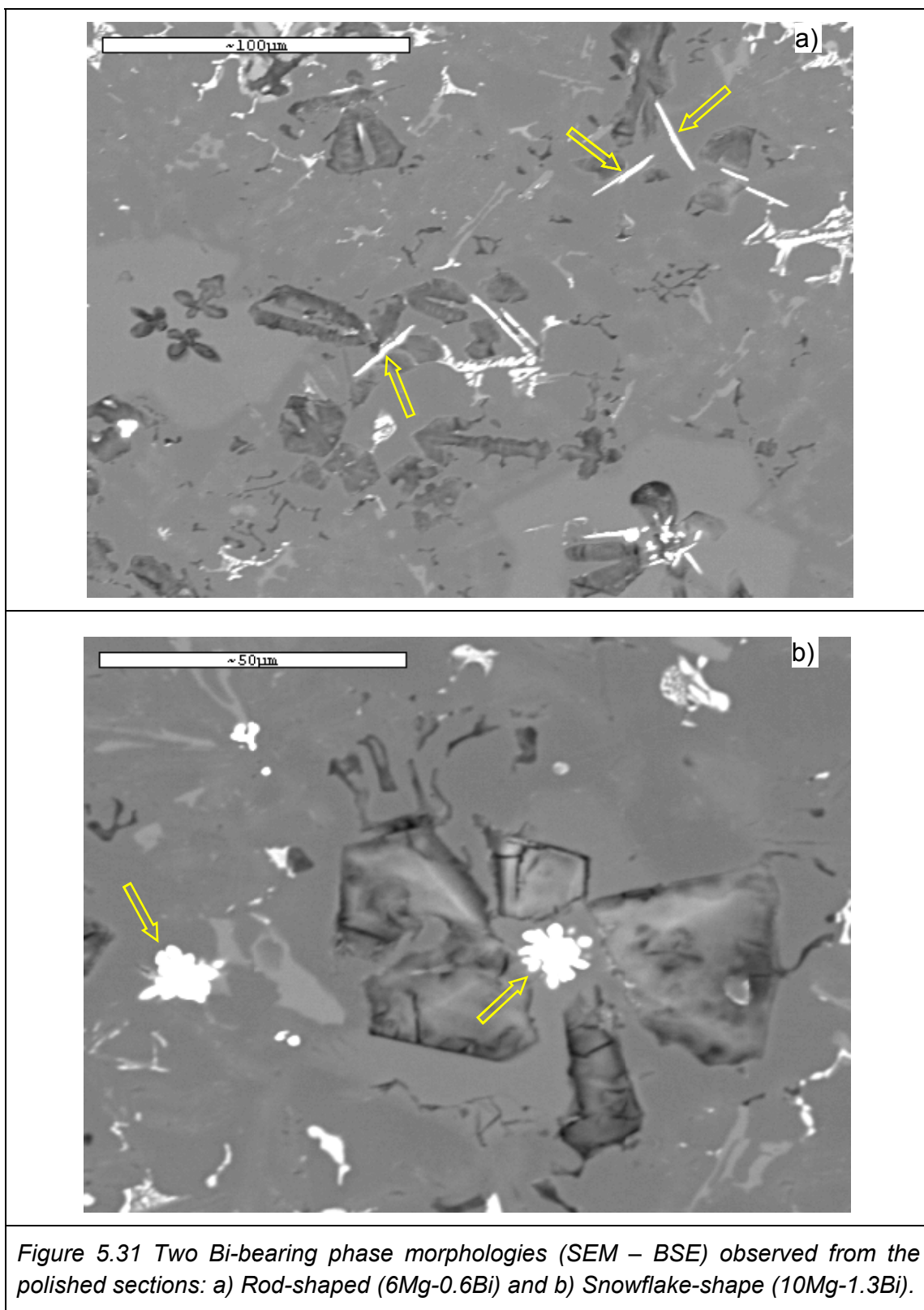


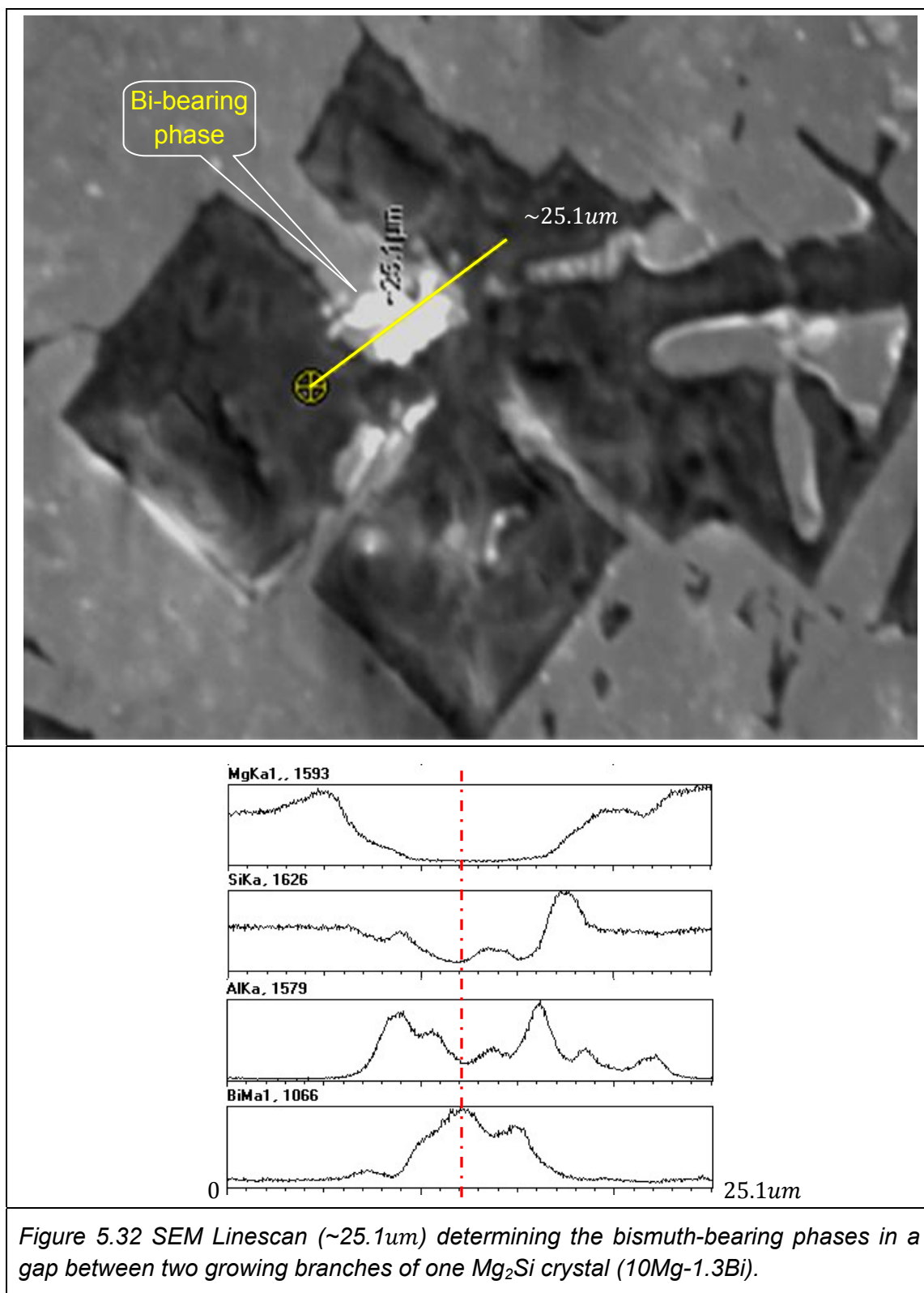










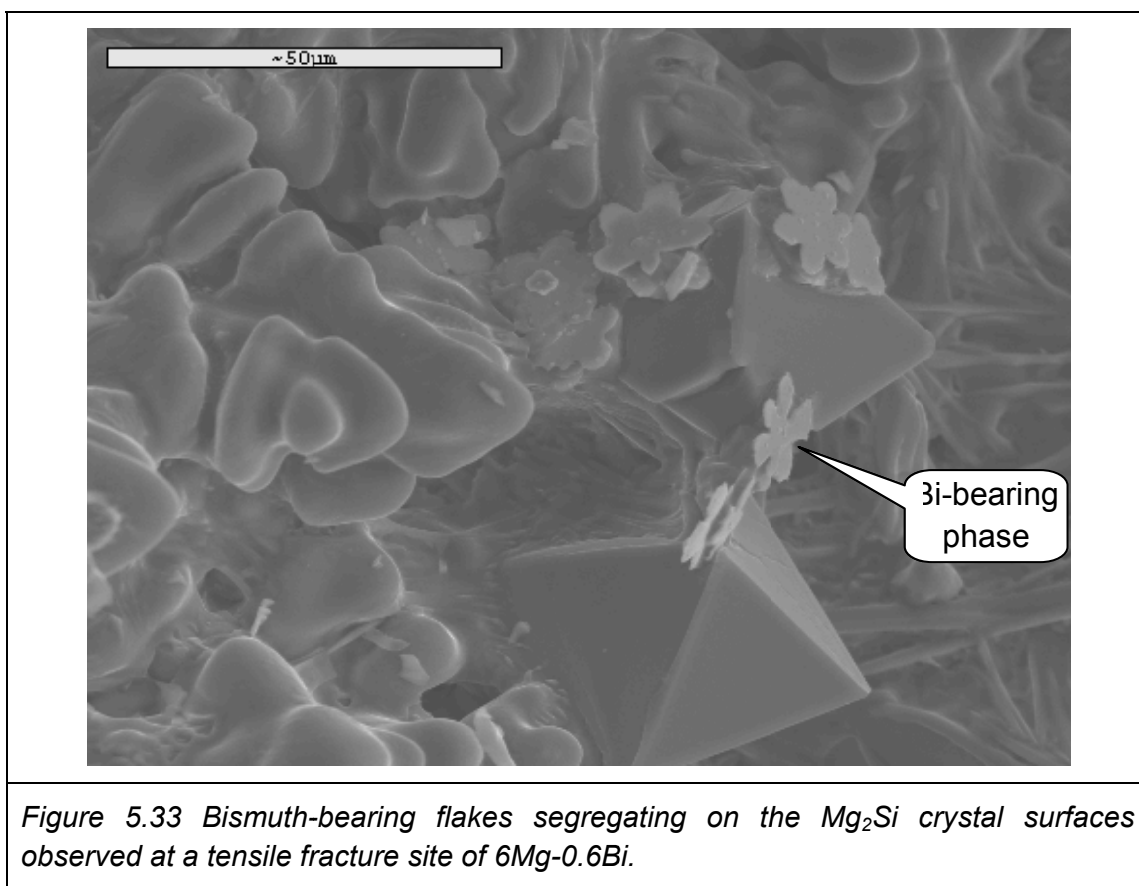




For the 10Mg alloy, the bismuth additions could cause a discontinuity of the primary  $\text{Mg}_2\text{Si}$  dendrites, forming more equiaxed precipitations as seen in the Figure 5.30. Dendritic shapes and non-uniform distributions of the primary  $\text{Mg}_2\text{Si}$  were also observed in the microstructures of the Bi modified 10Mg alloy. Figure 5.30 c) shows the central region attaining finer structures than the surroundings, displaying the segregation features of the Bi modification. There were no benefits obtained from Bi modifications for the 10Mg alloy as seen in the tensile properties. It should also be noted that these alloys were very sensitive to the casting defects. The same possible explanations used for the 6Mg alloy can also be applied to the 10Mg alloy. A more detailed Bi modifying mechanism for the primary  $\text{Mg}_2\text{Si}$  crystals will require the further investigations.

The Figure 5.31 indicates two different morphologies of the same Bi-bearing phases formed in the polished sections. Depending on the section angle of the specimens, it can take the form of thin rod-shaped (Figure 5.31 a)) or snowflake-like structures (Figure 5.31 b)). Although the exact phase compositions are difficult to determine due to the size of these precipitates and the limits of EDS analysis, the bismuth concentration was confirmed in this phase by using the SEM linescan technique as shown in the Figure 5.32. These phases can be readily observed in all Mg added A390 alloys with any level of bismuth modifications, distributed mostly in an area where the primary  $\text{Mg}_2\text{Si}$  crystals are present. Figure 5.31 b) illustrates one bright Bi-contained phase at the center of

at least four  $\text{Mg}_2\text{Si}$  crystals.



Bismuth is believed to react with magnesium to form an intermetallic compound  $\text{Mg}_3\text{Bi}_2$ , which has a hexagonal structure of  $D5_2$  (Yuan, 2001) and a melting point of  $821^\circ\text{C}$  (Ryabchikov, 2007), and can be formed at the early stages of solidification in Mg alloys. A similar morphology has been reported as a rod-shaped  $\text{Mg}_3\text{Bi}_2$  in an AZ91 Mg alloy with bismuth addition (Yuan, 2001). This Bi-bearing phase is therefore considered to be the  $\text{Mg}_3\text{Bi}_2$  intermetallic compound, although its crystal structure is reported as Rhombohedral-A7 by FactSage<sup>TM</sup>.

However, the intermetallic compound  $\text{Mg}_3\text{Bi}_2$  does not appear to be a favourable heterogeneous nucleation site for primary  $\text{Mg}_2\text{Si}$  formation due to their crystal structure differences.

One of possible explanations might just simply relate to the nucleation of Bi-bearing particles (i.e.  $\text{Mg}_3\text{Bi}_2$ ) segregating onto the primary solidifying  $\text{Mg}_2\text{Si}$  crystals which can deter their growth. Figure 5.33 shows the presence of snowflake-like particles at the surface of the  $\text{Mg}_2\text{Si}$  crystals which may retard or even stop their growth in certain directions. Also, the bismuth introduction might also shift the eutectic point, similar to the effect of strontium in the hypoeutectic Al-Si alloys, to decrease the solidification temperature for the primary  $\text{Mg}_2\text{Si}$  decompositions. This phenomenon occurs locally if a non-uniform distribution of Bi atoms is present in the liquid. Another possibility could also be due to the relatively high solid solubility of Bi ( $\sim 1.3$  at%) in the  $\text{Mg}_2\text{Si}$  crystals where the silicon sites can be substituted by the Bi atoms (Tani & Kido, 2005), further altering the crystal growing modes via the substituted crystal sites.

#### 5.6.3. Tensile fractography

A technique to identify the fracture mechanisms is usually called “fractography” (Brookes & Choudhury, 1993), including both the macro-fractography in which the low magnification of the fracture surface topography is examined and the micro-fractography where the fracture mechanism is directly revealed by their

fine topographies using SEM and TEM analysis methods. Structure variations relating to the mechanical properties of the Mg hypereutectic Al-Si permanent mould tensile bar castings were studied using fracture surface analysis.

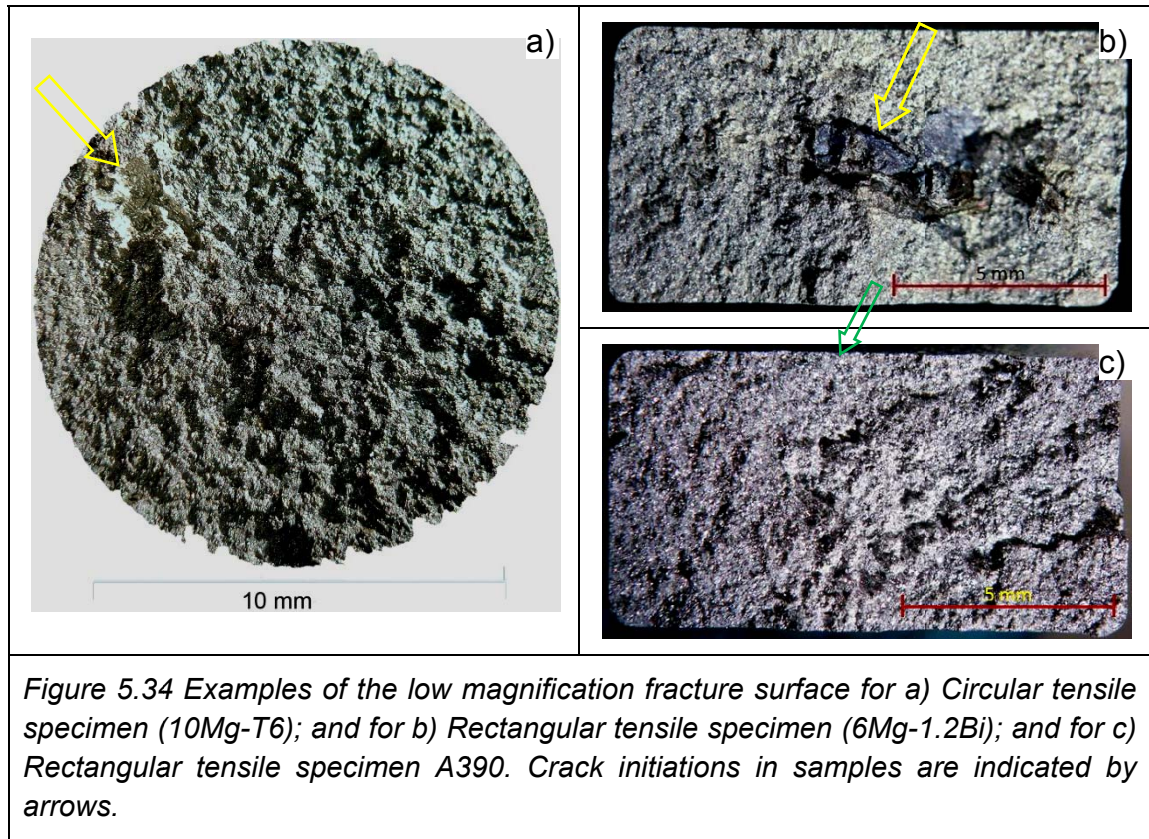
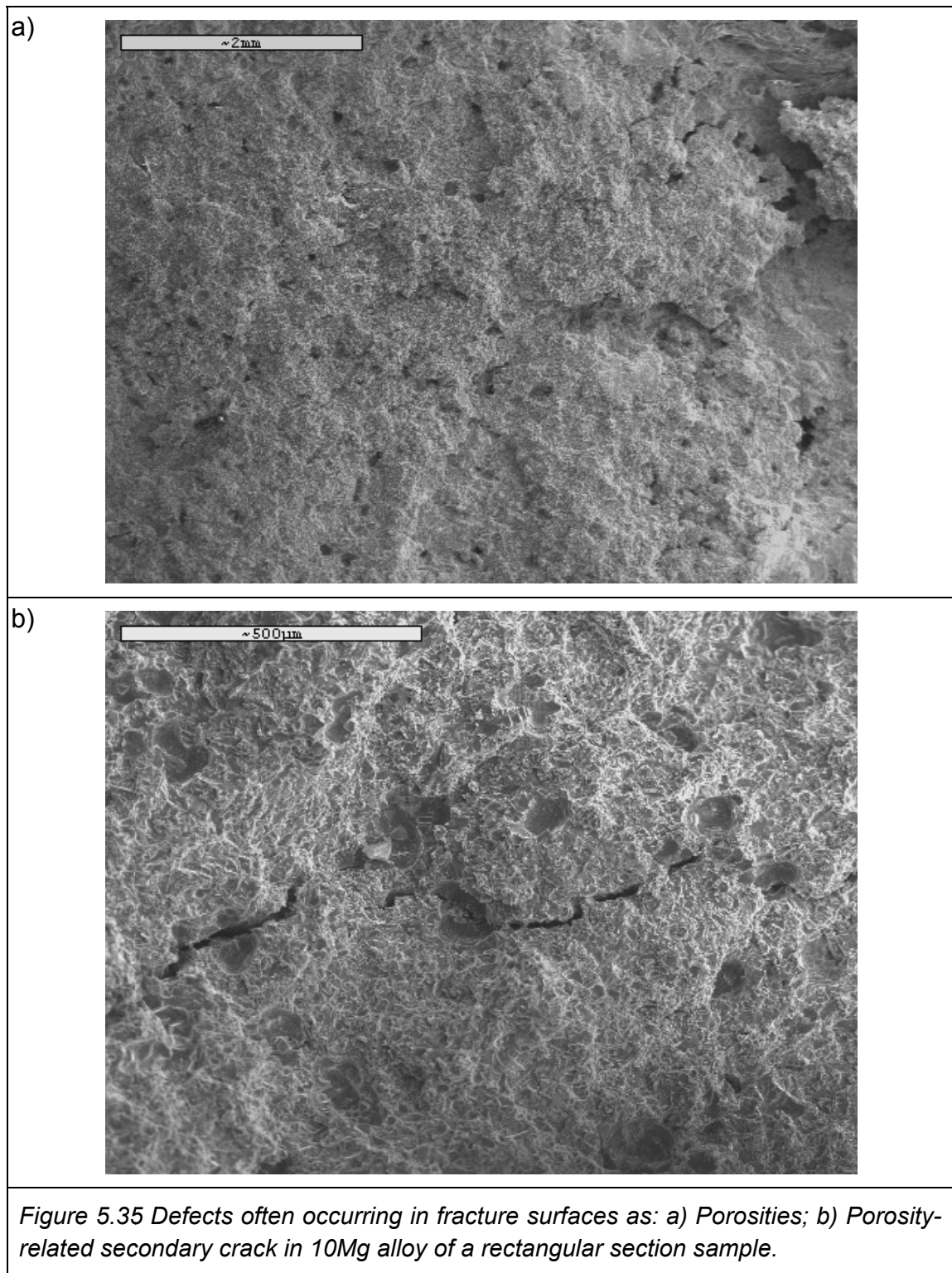
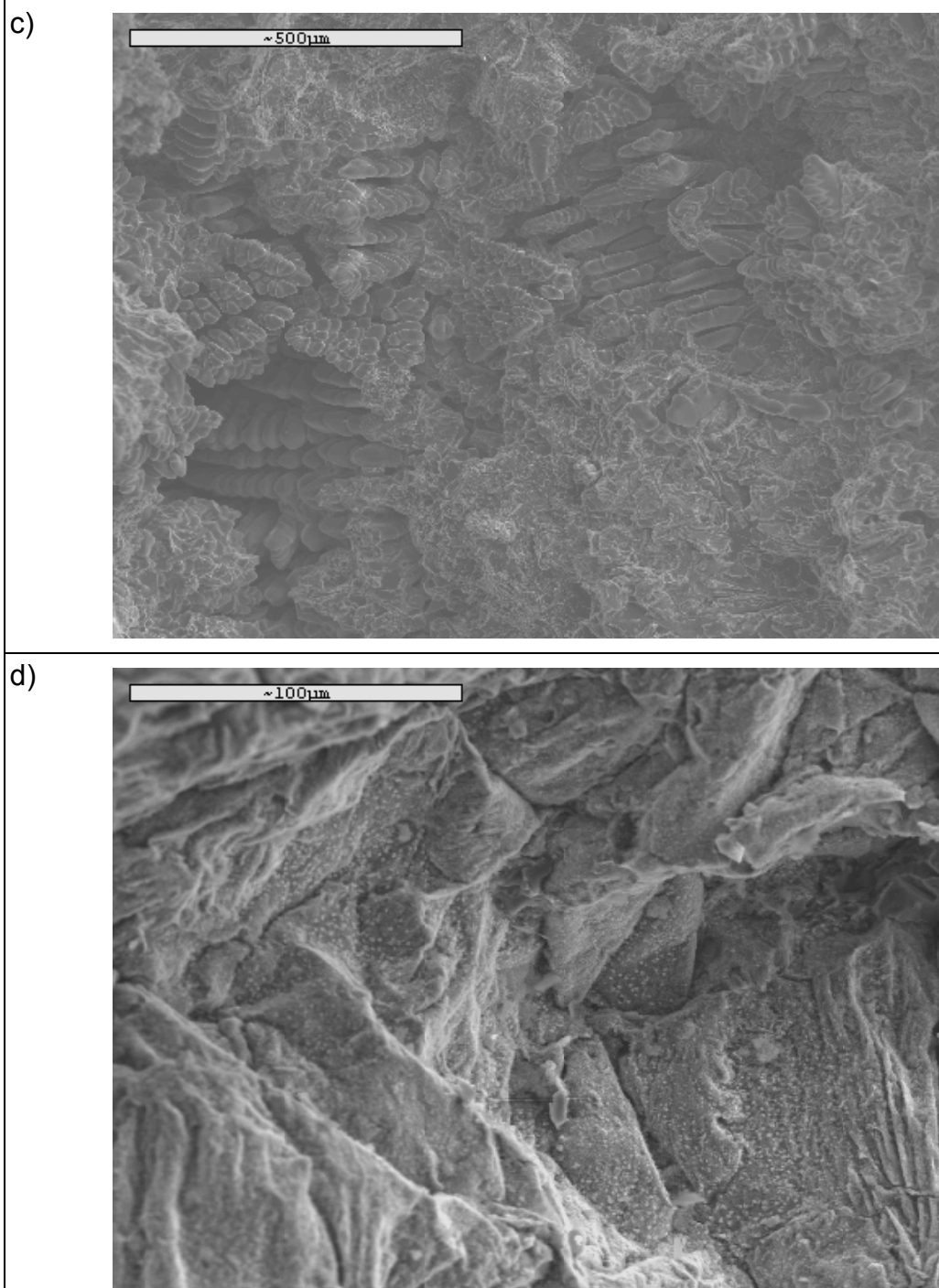


Figure 5.34 illustrates tensile fracture surfaces and locations of probable crack initiation and propagation sites under the low magnification optical stereo photos. All specimens show brittle fracture characteristics since there was no visible shrinkage neck observed. Samples with less than 0.5% elongations do not exhibit any measurable stretching. Most brittle fractures can be found to be initiated by cracks corresponding to the casting defects such as obvious

porosities (Figure 5.34 a)), oxide inclusions (Figure 5.34 b)), or micro imperfections associated with the weakest atom bonding, as shown in Figure 5.34 c). These overall fracture features are general indications of the fracture types, initiation, and crack growth paths. However, examination at higher magnification is necessary to understand the failure mechanism.

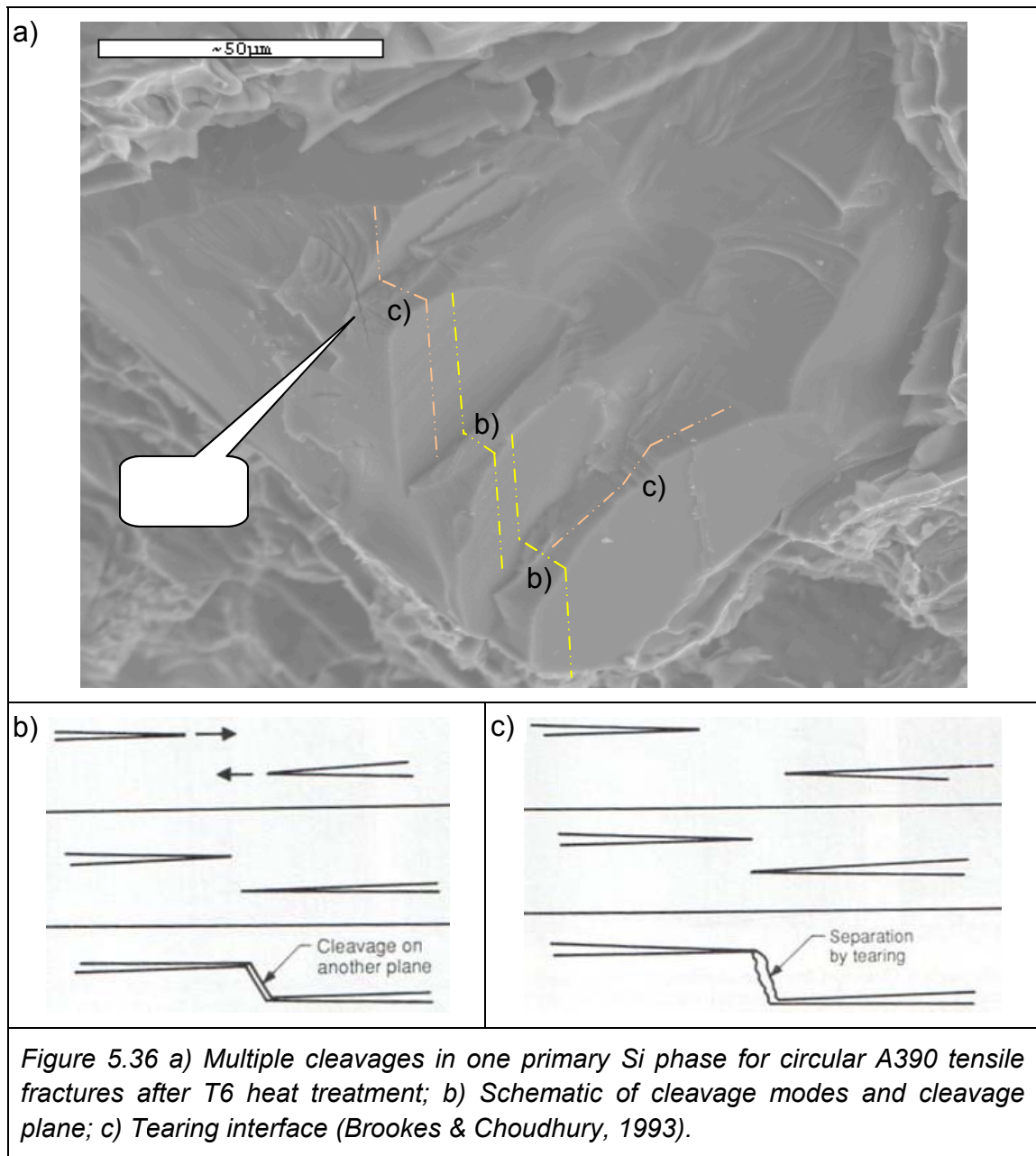
Casting defects can be readily observed in great detail by using the SEM. Figure 5.35 a) shows significant porosities appearing on the fracture surface of 10Mg alloy while Figure 5.35 b) exhibits a secondary discontinuous crack associated with porosities in the alloy. This strongly confirms that the porosities are associated with crack formation and growth. Oxidation inclusions and cold shut defects have also become important sources of crack formation. Figure 5.35 c) presents several  $\alpha$ -Al dendrites at porosities formed by shrinkage cavities at a fracture surface of A390 alloy. The shrinkage usually corresponds to the last freezing area during the solidifications. In addition to the  $\alpha$ -Al dendrites, other constituents could also be found in the shrinkage voids, such as  $\theta$ -Al<sub>2</sub>Cu, Mg<sub>2</sub>Si, and Q-Al<sub>5</sub>Cu<sub>2</sub>Mg<sub>8</sub>Si<sub>6</sub> etc., independently or in combination.





*Figure 5.35 (Continued) Defects occurring in fracture surfaces as: c)  $\alpha$ -Al dendrite-related shrinkage cavity (circular specimen, A390); d) Impurity or oxidation particles distributing in an area where an intergranular fracture took place (rectangular specimen, 6Mg-0.6Bi).*





Intergranular fracture might occur if there are impurities or oxide particles distributed at the grain boundaries. Such a case can be seen in the Figure 5.35 d) where the fracture surfaces were surrounded by numerous small oxide particles. As a consequence, their bonding energies can be reduced sufficiently



so as to initiate a crack easily along the grain boundaries instead of transgranularly propagation. However, transgranular cleavage of the primary Si or  $\text{Mg}_2\text{Si}$  crystals are most often seen at the fracture surfaces of these alloys. They usually display smooth bright facet topographies, which indicate that the cleavages take place along certain facet planes where the lowest cleavage energy occurs. Multiple cleavage facets are more common than single cleavage planes since lattice defects (i.e. dislocations) are always present. Multiple cleavage locations can be thus initiated and propagated at several levels (Brookes & Choudhury, 1993). As shown in the Figure 5.36 a), multiple cleavages occurred at the same time showing many parallel facet planes propagating from one surface to another along the interface in either the cleavage mode (Figure 5.36 b)) or the tearing mode (Figure 5.36 c)).

Many other types of cleavage mechanisms might also occur for single or multiple Si crystals. Figure 5.37 a) illustrates the cleavage perpendicular to two adjacent crystals and propagating along their grain boundaries (arrow direction). Grain boundaries can stop or retard the crack propagation. It seems that the presence of the multiple grain boundaries might lead to a block-like cracking pattern (Figure 5.37 b)) in the same parallel facet planes. The cracks are generally initiated at locations of the weakest atomic bonding which can occur at multiple levels, while the typical cleavages could still form at the same time. If a torque force is exerted on a crystal, a spiral cleavage can also occur as seen in

the Figure 5.37 c) where the upward cleavage steps are clearly demonstrated. In another case, a herringbone cleavage structure was observed (Figure 5.37 d)) where cleavages crossed a twin silicon crystal. The symmetric cleavage was thus propagated along the twin. Figure 5.37 e) shows a cascading cleavage pattern formed at a low-angle boundary where numerous new cracks are aligned and propagate into a series cleavage steps at different plane levels, identified as a river “downstream” mechanism (Brookes & Choudhury, 1993).

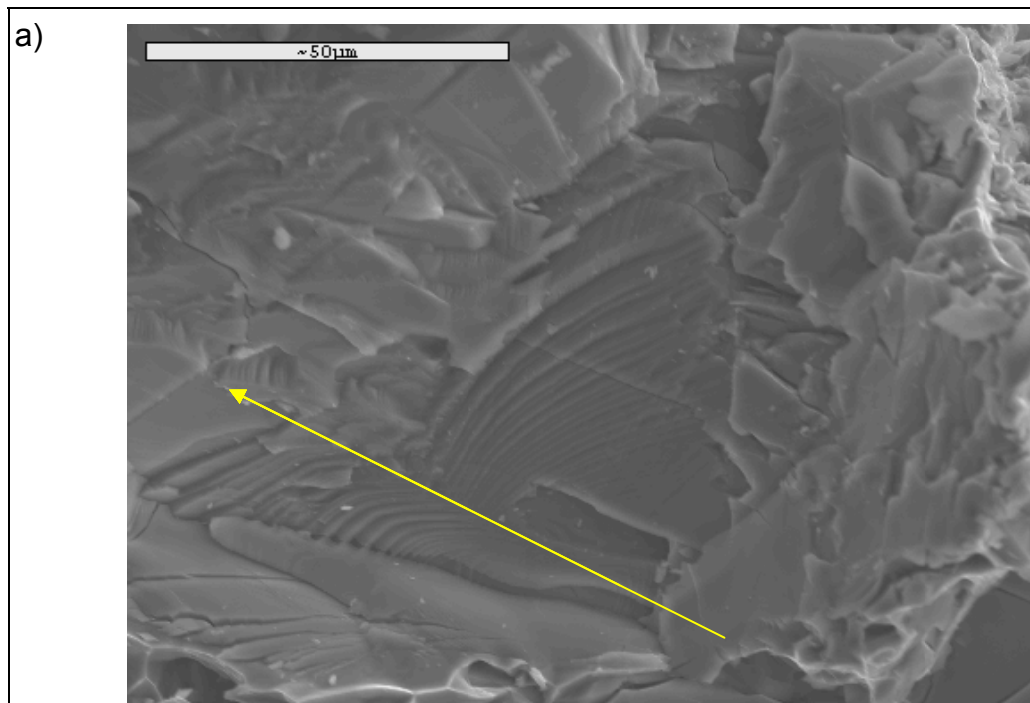


*Figure 5.37 Primary Si cleavages of circular A390 (T6) test specimens: a) A typical grain boundary slowing down the crack propagation.*

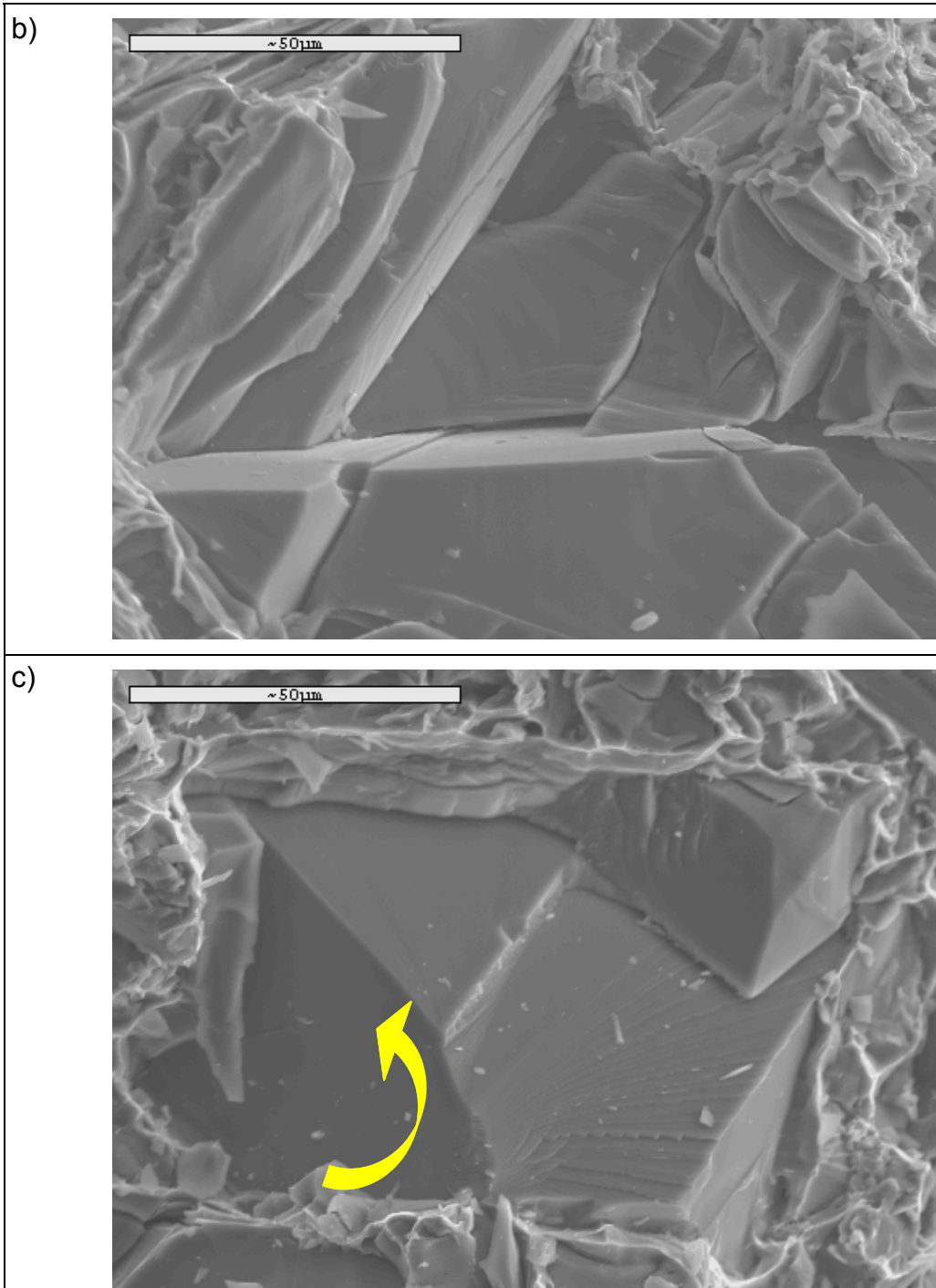


*Figure 5.37 (Continued) Primary Si cleavages of b) circular A390-T6 test specimens: A block-like cracks; and of c) circular A390 test specimens: A spiral crack propagation in a single Si crystal.*

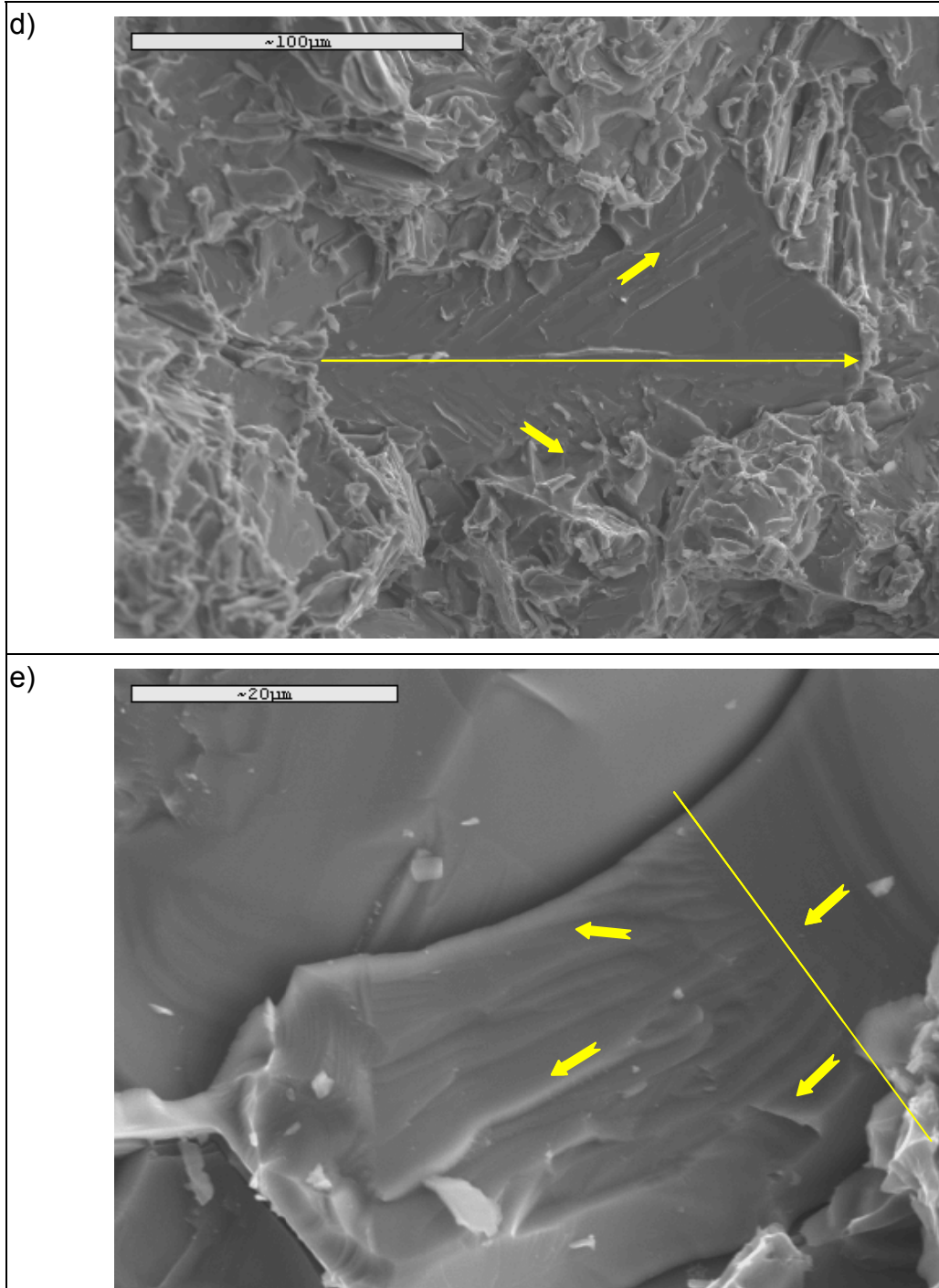
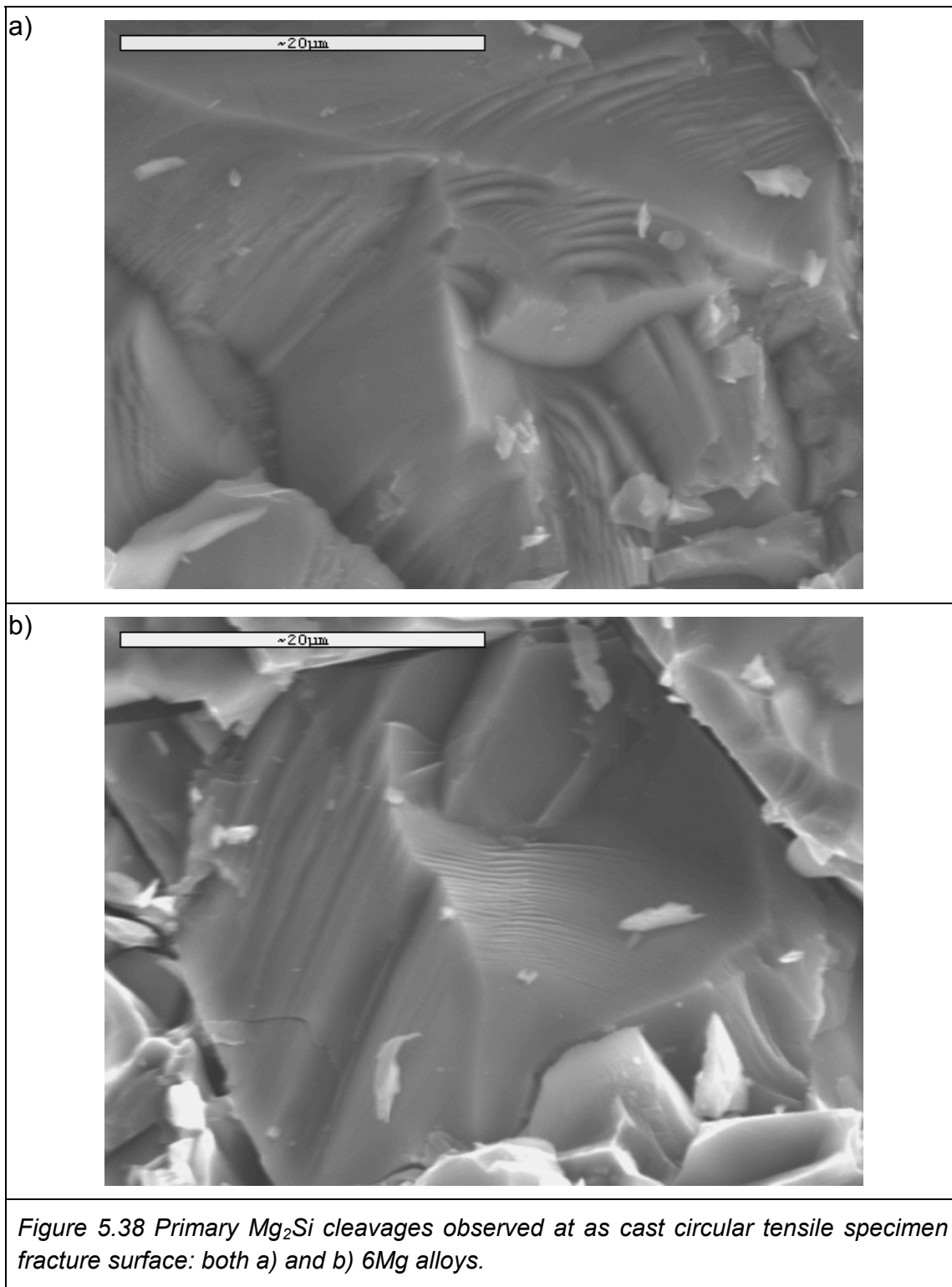
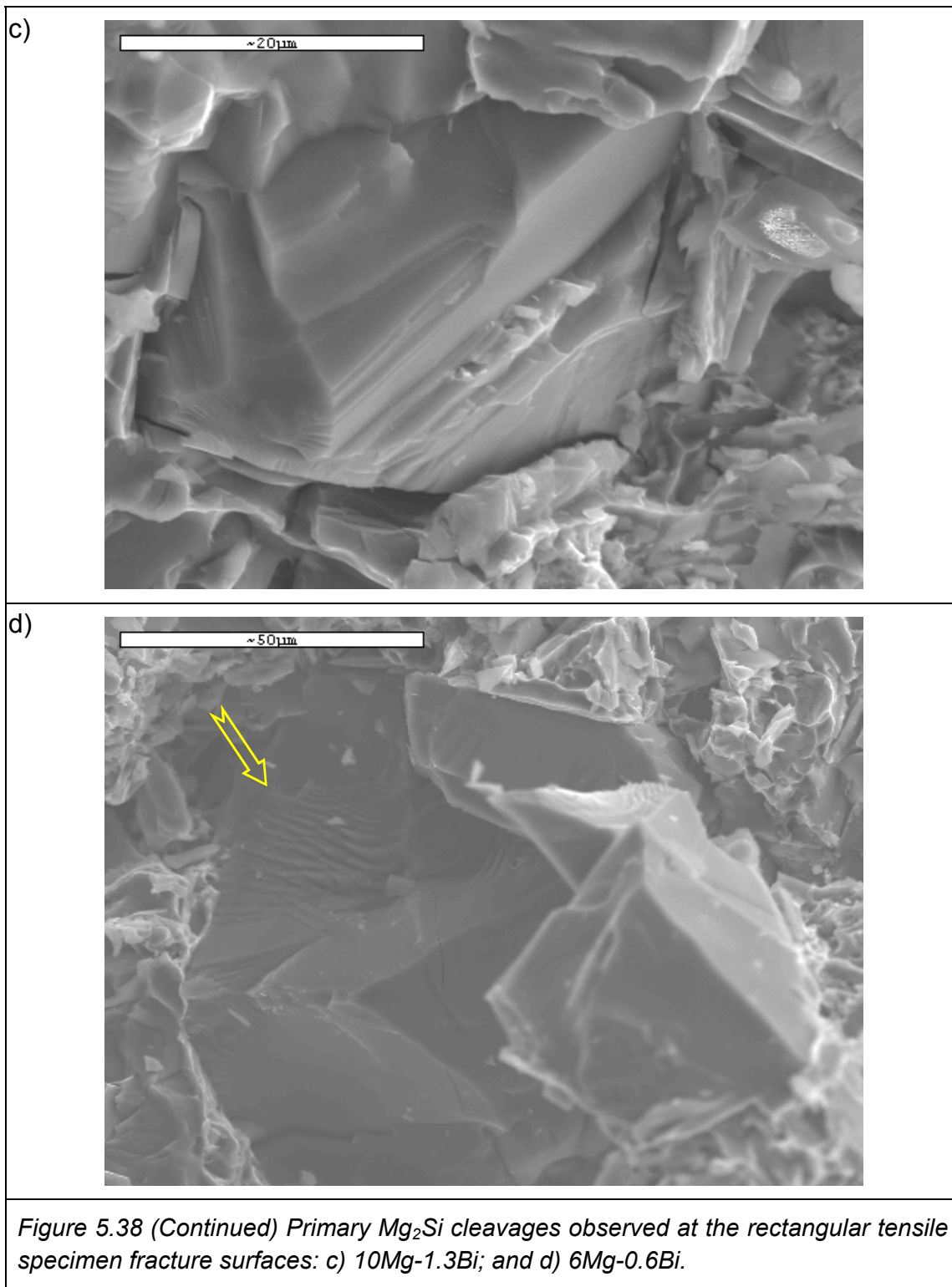


Figure 5.37 (Continued) Primary Si cleavages of d) Circular A390 test specimens: Herringbone structure from plane cleavage; and of e) Circular 6Mg test specimens: A cascading pattern fracture.





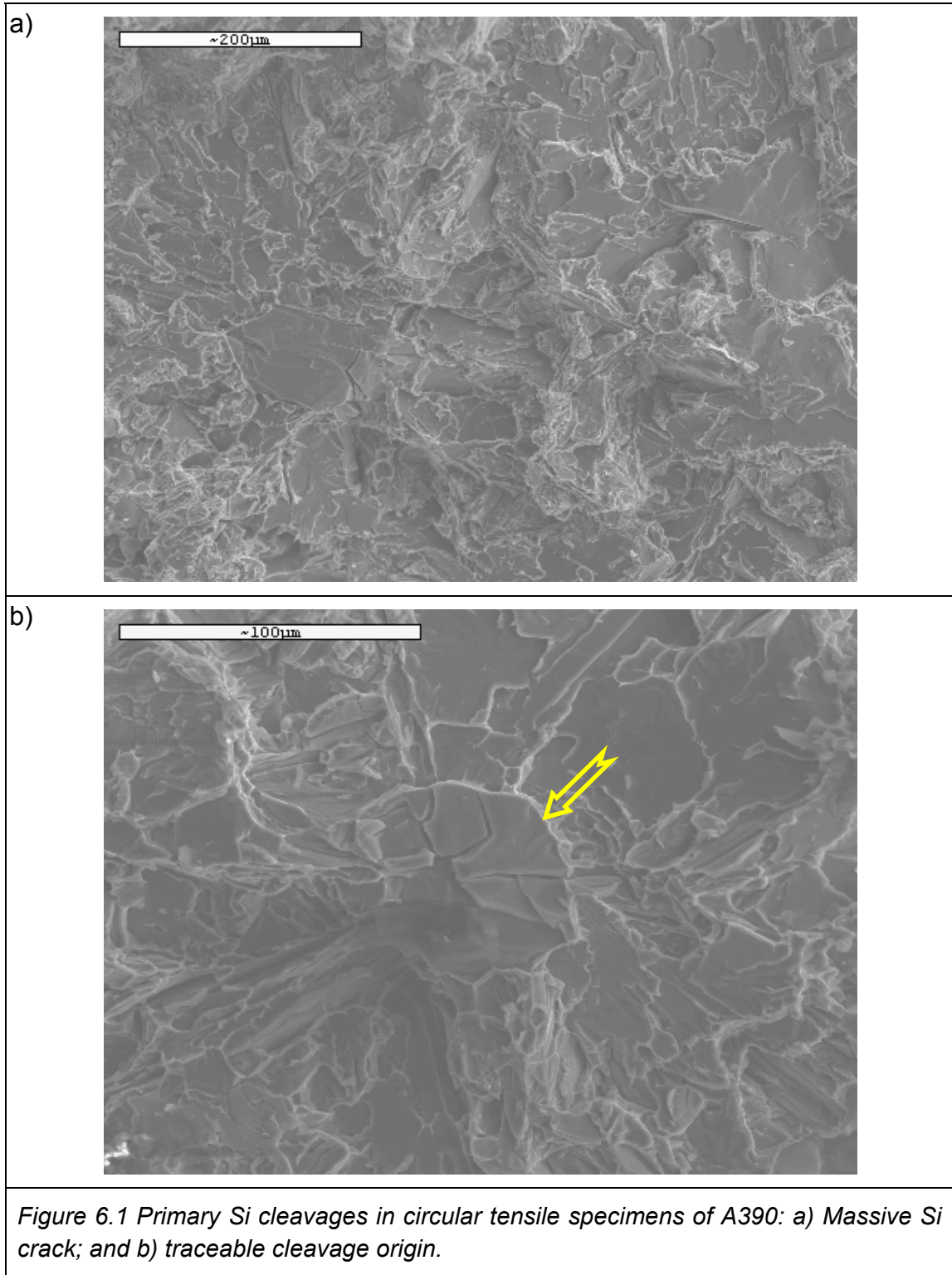
Similar cleavage features can also be found in the Figure 5.38 (a), b), c) and d)) for the primary  $\text{Mg}_2\text{Si}$  phases because of their similar crystal structures. There are some differences, however, such as the rare occurrence of straight faceted cleavage planes in the  $\text{Mg}_2\text{Si}$  crystals and the less sharp crack edges of the  $\text{Mg}_2\text{Si}$  when compared to the Si crystals. The cleavage surfaces indicate a certain extent of plastic deformation as shown in Figure 5.38 d). The fracture surface of the  $\text{Mg}_2\text{Si}$  crystals have curved contours indicating some ductility of the  $\text{Mg}_2\text{Si}$  crystals in contrast to the Si phases.

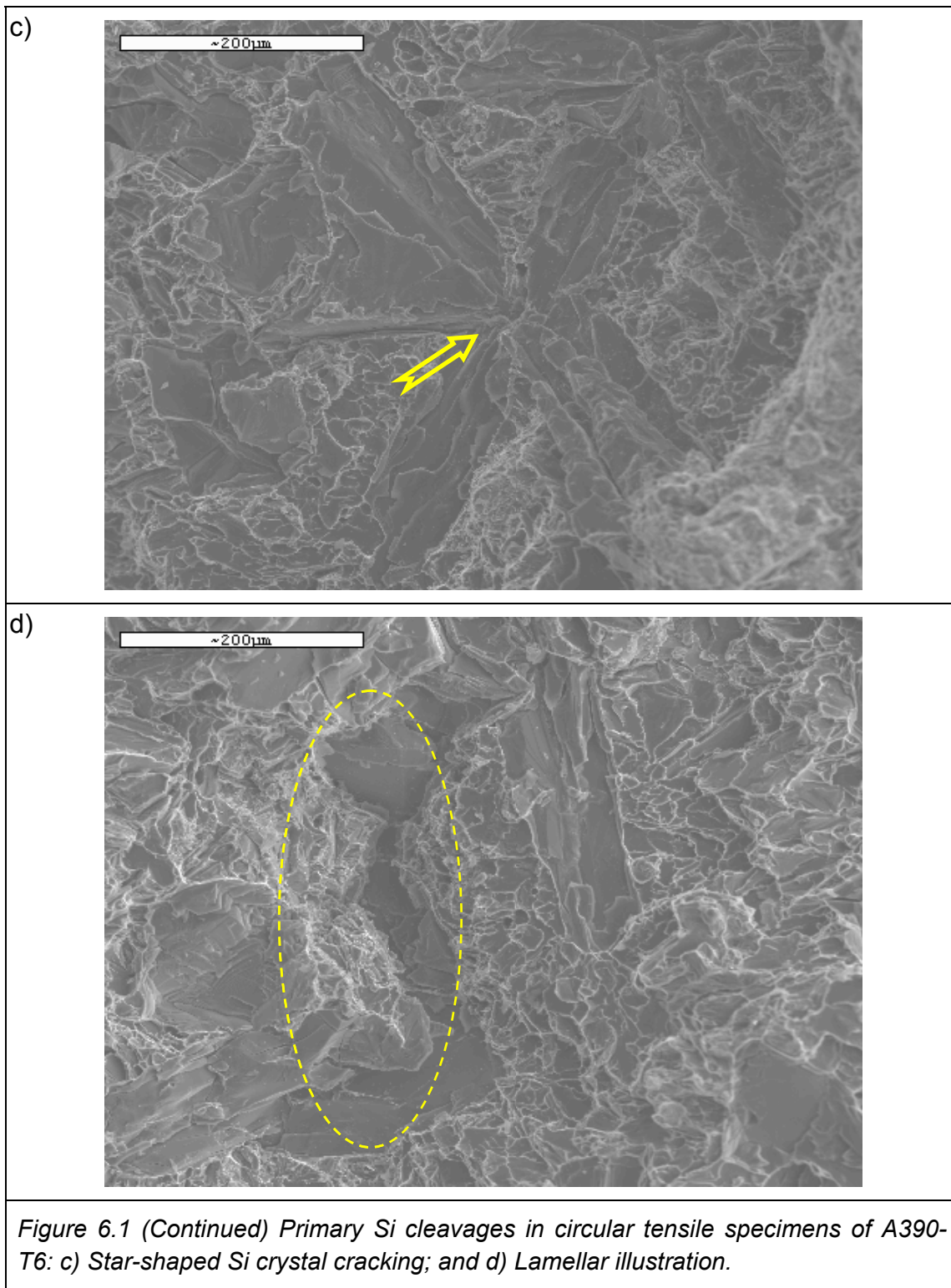
## CHAPTER 6. General discussion

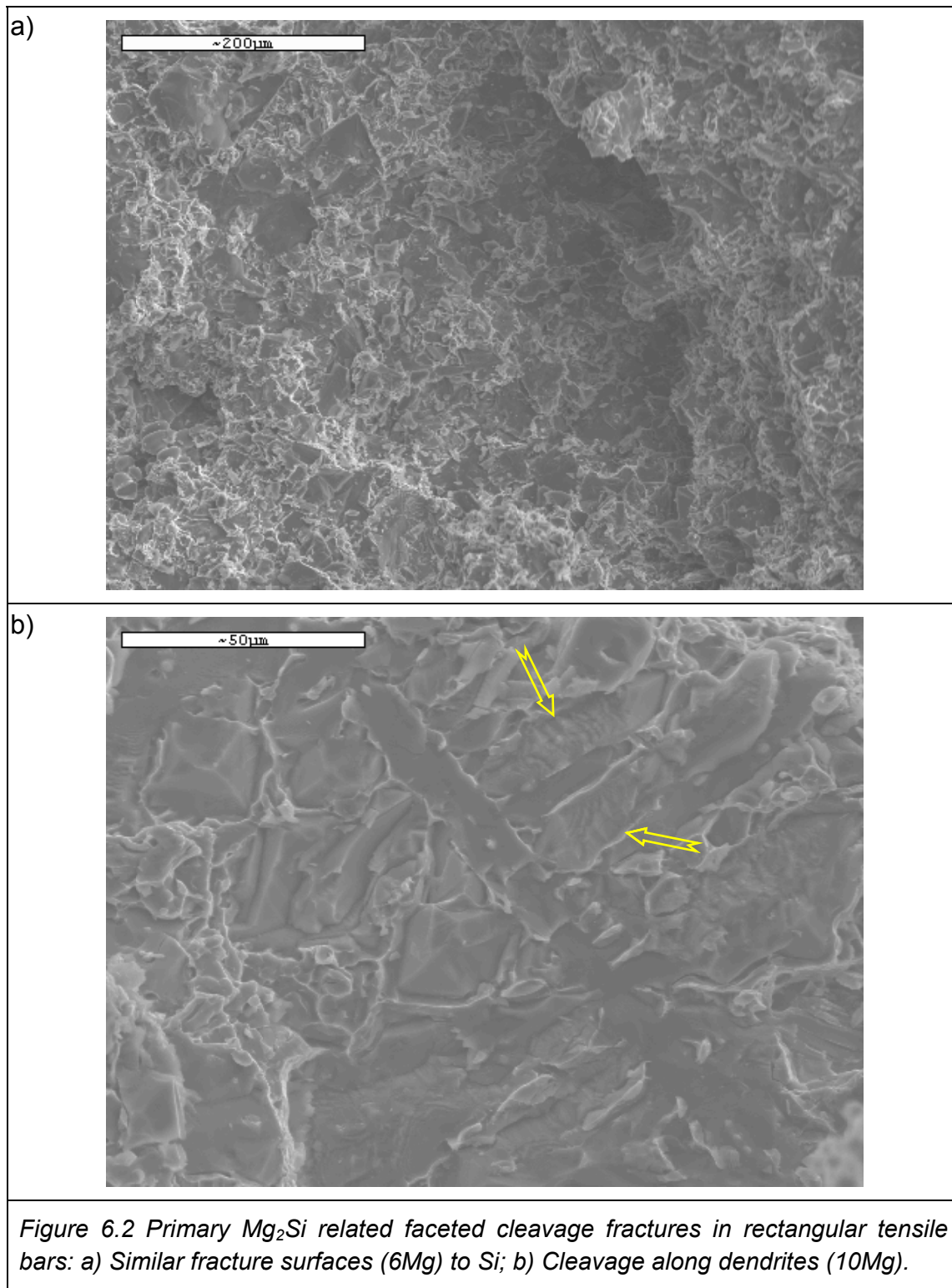
Every time a brittle fracture occurs, a set of new surfaces will be created by the release of tensile loading energy, which can also be partially transferred to plastic deformations. Cleavage facets are observed in most brittle fractures whenever the lowest initial fracture energy is reached. Although casting defects are always considered to be the principle source of crack propagation, subsequent resistance to cleavage is a measure of the material toughness. Therefore, the cleavage fracture toughness resulting from the presence of primary Si and  $\text{Mg}_2\text{Si}$  plays an important role in influencing the tensile properties of the Mg containing alloys investigated in this study. For a hypereutectic alloy matrix, fracture cleavages might occur directly in large primary Si precipitates as shown in Figure 6.1 a) while the crack origin can be traced to a Si phase precipitate as seen in the Figure 6.1 b). Also, Figure 6.1 c) has a similar crack structure illustrating a single star-shaped Si crystal.

Figure 6.1 d) shows two levels of cleavage fractures including a lamellar character on the center left. This type of fracture surface can be seen in most tensile fractures where both layers were related to the cleavages, consisting of the  $\text{Mg}_2\text{Si}$  associated cracking regions shown in the Figure 6.2 a). In addition, Figure 6.2 b) indicates the fracture at the  $\text{Mg}_2\text{Si}$  dendrites sometimes also can be found in the 10 wt% Mg alloys.

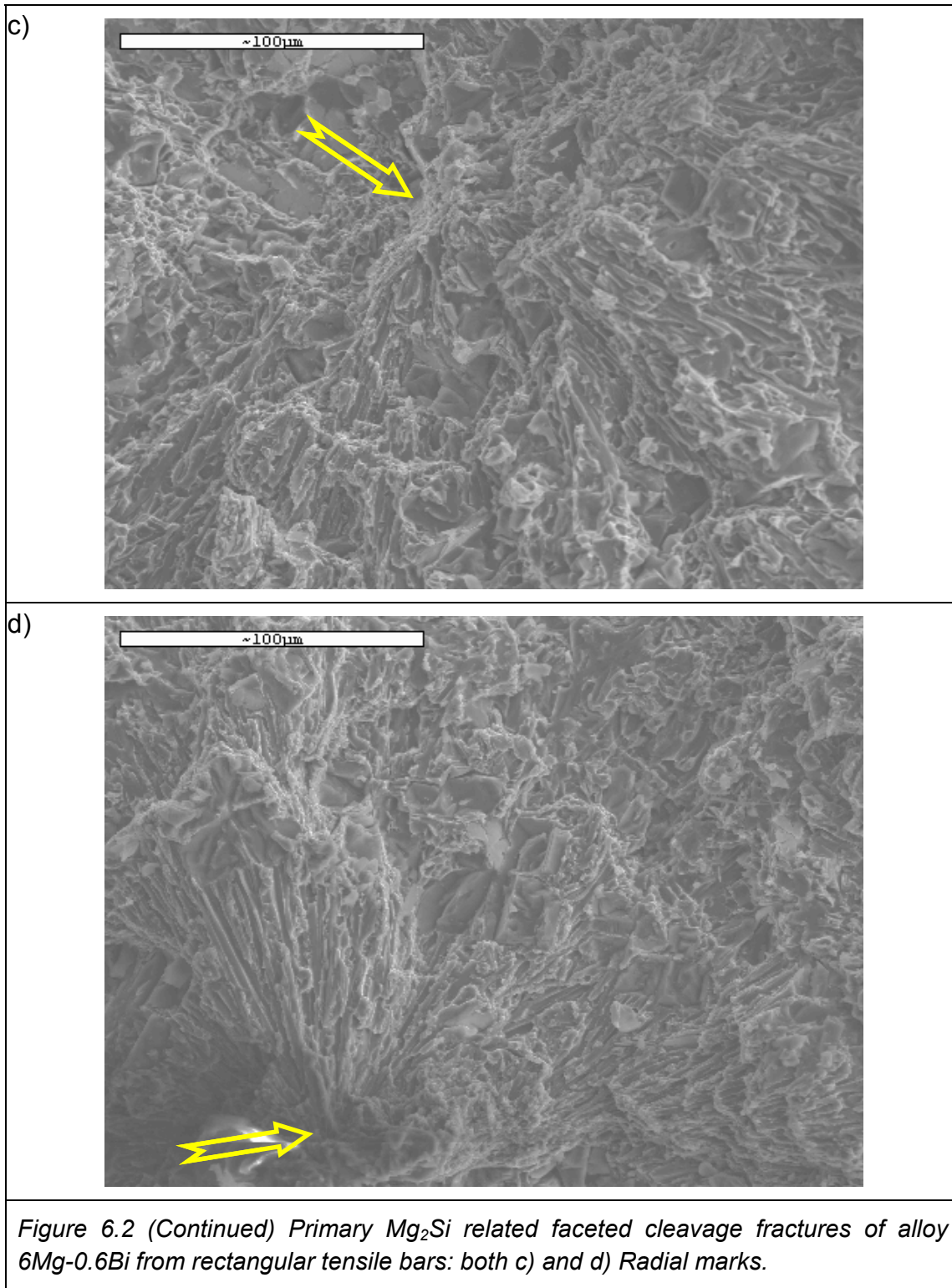


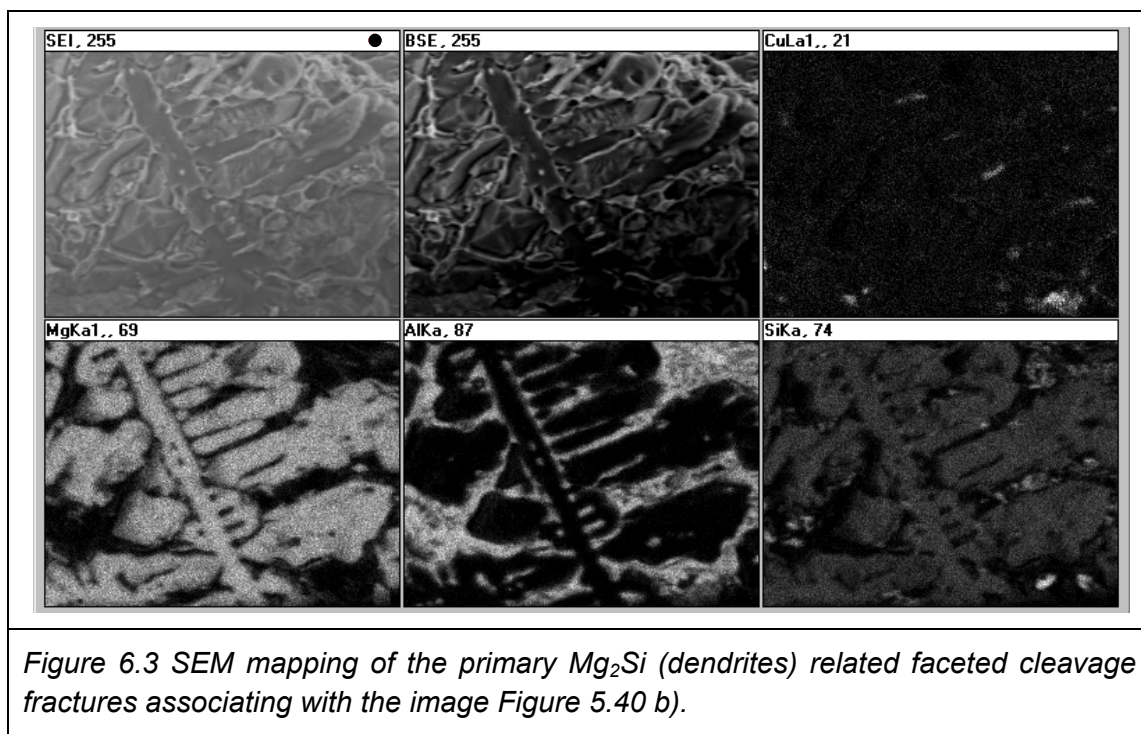












SEM mapping (Figure 6.3) has confirmed the phase compositions with a clear dendrite profile of primary  $Mg_2Si$ . It seems such cracks were caused by the large size of dendrites and the lack of the aluminum matrix that surround them. Figure 6.2 c) and d) show evidence of radial marks representing crack growth with dynamic fracture propagation along the weakest path. Crack initiation can be easily traced back to a point as illustrated with the arrows in the Figure 6.2 c) and d).

The replacement of the primary Si by primary  $Mg_2Si$  in cast conventional hypereutectic Al-Si alloys was investigated by the addition of Mg to these alloys. Although  $Mg_2Si$  has a lower density ( $1.88g/cm^3$ ) than Si ( $2.33g/cm^3$ ), its micro-

hardness at room temperature (5.3GPa) is lower than the Si (12GPa) as reported in the literature and confirmed by the Vicker's hardness measurements. The same study states that the micro-hardness at 300°C (kept for 1 hour) of the  $\text{Mg}_2\text{Si}$  (1.77GPa) is much lower and makes it thermally unstable, while the Si performs much better (8GPa). This property might limit the applications of Mg containing alloys, especially in the field where the high temperature working environments are required.

Two types of permanent mould tensile bar castings, circular and rectangular in cross sections were tested for mechanical properties to compare the values of the Mg containing alloys and A390. It seems that the Mg addition to the hypereutectic Al-Si alloys decreases their castability as observed in the two different sets of castings. This results in poor fluidity due to the lack of the silicon phase precipitation in the new alloy system, directly resulting in the significant porosities and oxidation in the cast matrix even after increasing the pouring temperature. The high latent heat of the fusion of the Si contributes to good melt fluidity of the parent alloy A390 (about 14 times higher than that of  $\text{Mg}_2\text{Si}$ ). The Mg addition also has a tendency to form a strong surface film  $\text{MgO}$  which adheres to the mould walls during the pouring, contributing to the poor fluidity. Porosities were observed in both the 6 and 10 wt% Mg alloys. A degassing procedure (Argon bubbling) was used before casting the circular tensile bar sets but it was still not possible to eliminate all the voids. Gas porosities can also be

related to the high Mg vapour in addition to the shrinkage cavities that were identified in the castings. The latter case probably indicates an increased difficulty of feeding the liquid alloy to the last freezing region as result of the poor melt fluidity. The pouring temperature for the rectangular tensile bar castings was higher than that used for the circular samples because of the more rapid cooling of the smaller rectangular castings. A superheat of  $\sim 200^{\circ}\text{C}$  was used in the 10Mg alloy for the rectangular tensile bar castings, while only  $\sim 100^{\circ}\text{C}$  was required for the same alloy for the circular castings. The higher superheat results in larger shrinkage of the final components, particularly for the Mg alloys that have low latent heat benefits. As a consequence, the oxidation products can easily form at high temperature which results in inclusions because the fast solidification rate will not facilitate their floating to the melt surface. This problem could be resolved if the castings are produced under pressure such as by the HIP (hot isostatic pressing) technique and incorporating ceramic filter. A die casting technology might be more suitable for Mg containing alloys instead of permanent mould casting because of the rapid mould filling under pressure.

The specimen hardness and tensile properties were affected by casting quality. Nevertheless, some property tendencies are still able to be deduced from the current results. First, the Mg containing alloys have increased hardness when compared to A390 for as cast condition, roughly proportional to the Mg contents. There was an exception for the 10Mg rectangular samples which showed a

lower hardness than the 6Mg alloy. This can be explained by the large amount of micro-porosities on the test surfaces, influencing the measurements. The higher  $\text{Mg}_2\text{Si}$  solid fraction might lead to this hardness increment for the new Mg alloys. Also, the as cast tensile properties showed that the Mg addition has little effect on the yield strength (~50 to 66 MPa, at 0% offset) compared to the base alloy A390 when considering the casting defects and data collecting errors. The values of Young's modulus (~72 to 82 GPa) is almost the same for all three types of alloys. However, the fracture tensile strength of the alloys with the Mg additions was found to be lower than for the alloy A390, possibly related to the casting defects. Furthermore, the T6 heat treatment shows an overall increase of both the tensile properties and hardness for all three alloys, but largest increase occurred for the A390 alloy. The same heat treatment parameters were used for each of the cast alloys, corresponding to the ASTM recommendation for A390. The conditions were not optimized for the Mg containing alloys and further investigation would be required to study their effect on the Mg alloys.

The microstructures of the fracture surfaces showed that the eutectic Si and Q phases contribute to the precipitation strengthening effect in addition to the main aging factor of the  $\theta\text{-Al}_2\text{Cu}$  in the matrix. The structure modifications were found to have positive influences on the alloy properties. Conventional A390 was also modified by phosphorus additions of ~100p.p.m.. Although the sizes of the primary Si phases were reduced, there was no tensile property enhancement



found for A390. This might also be related to the casting defects. However, the Bi additions (0.6 – 0.8%, referred to the Appendix 9.1) to the 6 wt% Mg alloy did increase the tensile strength probably as a result of the slight size reduction of the primary  $\text{Mg}_2\text{Si}$  phases. This reduction in size is probably caused by the Bi-bearing precipitates segregating on the solidifying crystals and retards their growth. These particles are distributed in the matrix and will most likely strengthen the alloys with their fine snowflake-shaped morphologies. The 10Mg alloy should have similar effects with the bismuth modifications but unfortunately, they were very difficult to cast and resulted in numerous casting defects.

The results of the tensile fracture analysis showed that brittle fractures occur in all of the Mg added alloys. The cracks seem to be initiated by casting defects such as porosities or oxidation products. The size, morphology and distribution of the primary precipitates all have an influence on the ease of the cleavage fracture taking place. It can be generally stated that the finer and more rounded structures will improve the brittle fracture strength together with a minimization of the casting defects.

## CHAPTER 7. Conclusion and future studies

### 7.1. Conclusion

- The addition of Mg to the hypereutectic Al-Si alloys changes the alloy solidification behaviour. Primary Si phase particles are gradually substituted by primary  $\text{Mg}_2\text{Si}$  crystals. A depression of the eutectic temperature is also attained resulting in a finer fibrous structure of Si. The experimental results of the observed phase transformation and temperatures agreed with the thermodynamic predictions.
- The  $\text{Mg}_2\text{Si}$  phase has a lower thermal stability than Si, indicating limited applications where the high temperature is required. Also, the CTE (Coefficient Thermal Expansion) and latent heat of the fusion of the  $\text{Mg}_2\text{Si}$  are lower than Si, further influencing the component dimensional stability and melt fluidity.
- There were significant casting defects in the Mg added alloys cast in permanent mould such as porosities and oxide formation. A high magnesium content in the alloys will produce these defects since the high vapour pressure of Mg can result in gas pore nucleation and can also create surface oxide films. To avoid these casting defects, hot isostatic pressing (HIP) or die casting technologies with melt degassing should be used to improve properties.

- The as cast Mg added alloys will increase in hardness with Mg additions as a result of the solid solution strengthening mechanism. However, the yield strength at 0% offset and the elastic modulus exhibited only slight differences compared to A390. The tensile strength of the Mg containing alloy was found to be lower.
- T6 heat treatment can greatly improve the mechanical properties of the cast alloys as long as the proper processing parameters are adopted. The improvements are due to the precipitation strengthening mechanisms of the Cu-bearing intermetallic  $\theta$ -Al<sub>2</sub>Cu phase, resulting from the modification of the eutectic Si and Q-Al<sub>5</sub>Cu<sub>2</sub>Mg<sub>8</sub>Si<sub>6</sub> constituents.
- The bismuth modification in the 6Mg alloy has resulted in a marked improvement of mechanical properties. The optimum addition of the bismuth in this alloy was found to be at around 0.6 – 0.8 wt%. The optimal value for the 10Mg alloy could not be determined because of the poor castability.
- A brittle cleavage tensile fracture mechanism occurs in all three alloy compositions, usually initiated at casting defects. Most cleavages occur in the primary phase of either Mg<sub>2</sub>Si or Si. Finer and more compact morphologies of these constituents could enhance alloy fracture strength.
- The new Mg added alloys were found to be difficult to cast using the conventional gravity permanent mould technology. Improved properties can be achieved by forming components of these alloys using a pressure die casting or liquid hot isostatic pressing.

## 7.2. Future studies

- New casting technologies such as hot isostatic pressing (HIP) or die casting need to be explored for forming these high Mg alloys in order to improve the mechanical properties of the casting.
- Optimum T6 heat treatment parameters need to be determined for the new alloy compositions.
- The amount of bismuth addition to the 10Mg alloy needs to be optimized using new casting methods other than the current gravity permanent mould casting approach. Other modifiers such as Sr, P, RE etc. and their effect on the modification of the  $\text{Mg}_2\text{Si}$  phase could also be investigated.

## References

- Ardakan, A. H. (2006). *Rheological Characteristics of Hypereutectic Al-Si(A390) in the Semi-Solid State*. Master thesis.ECOLE POLYTECHNIQUE DE MONTREAL.
- ASTM. (2006). *Aluminum and Magnesium Alloys Annual (Volume 02.02)*. ASTM standards .
- Backerud, L., Chai, G., & Tamminen, J. (1990). *Solidification Characteristics of Aluminum Alloys, Volume 2 Foundry alloys*. AFS and Skanuminum Norway.
- Becker, P. C., Chen, Y.-C., & Myers, M. (2000). *Diesel Engine Emissions Reduction Workshop*. San Diego, California: Cummins Inc.
- Brookes, C. R., & Choudhury, A. (1993). *Metallurgical failure analysis*. McGraw-Hill Inc.
- C.G. Kang, S. L.-M. (2008). A study of die design of semi-solid die casting according to gate shape and solid fraction. *Journal of materials processing technology* .
- Compbell, J. (2003). *castings*. P15: Elsevier Science Ltd.
- Cook, R. (1998). *Modification of Aluminum-Silicon Foundry Alloys*. London & Scandinavian Metallurgical Co. Limited.
- CRCT. (2009). *The Integrated Thermodynamic Databank System*. montreal: Centre for Research in Computational Thermochemistry (<http://www.crct.polymtl.ca/>).
- Davis, J. R. (1990). ASM Handbook Vol.2: properties and selection: Non-ferrous alloys and special purpose materials; 10th edition. ASTM international.
- Donahue, D. R., & Fabiyi, P. A. (2000). Manufacturing Feasibility of All- Aluminum Automotive Engines Via Application of High Silicon Aluminum Alloy. *Society of Automotive Engineers, Inc* .
- Flemings, M. (1991). Behavior of Metal Alloys in the Semi-Solid State. *Metallurgical Transactions, Vol. 22A* , 957-981.
- George F. (2004). *Metallography and Microstructures, Volume 9 of the ASM Handbook*. ASM international.
- Gruzleski, J. E., & Closset, B. M. (1990). *The treatment of liquid Al-Si alloys*. AFS inc.
- Hatch, J. E. (1984). Aluminum: Properties and Physical Metallurgy. *ASM international* , 346-347.
- Hyung Yoon, T. S. (2000). Scuffing behavior of 390 aluminum against steel under starved lubrication conditions. *Wear* 237 , 163-175.
- John Gilbert Kaufman, E. L. (2004). *Aluminum alloy castings*. ASM International.

Jorstad, J. (1996). Hypereutectic Al-Si casting alloys: 25 years, what's next? *AFS transaction* , 669-671.

Jr., C. R. (1992). Fluidity of aluminum-silicon casting alloys. *AFS Transactions* , 533-538.

Jung, H., Seo, P., & Kang, C. (2001). Microstructural characteristics and mechanical properties of hypo-eutectic and hyper-eutectic Al-Si alloys in the semi-solid forming process. *Journal of Materials Processing Technology* , 568-573.

KS Aluminum-Technologie AG. (2007). *high pressure die cast and squeeze cast cylinder blocks made of Al*. Retrieved from [http://www.kspg-ag.de/pdfdoc/kspg\\_produktsbroschueren/2007/at07\\_die\\_cast\\_squeeze\\_casting.pdf](http://www.kspg-ag.de/pdfdoc/kspg_produktsbroschueren/2007/at07_die_cast_squeeze_casting.pdf)

Lee, J. A. (2003). cast aluminum alloy for high temperature applications. *the Minerals, Metals & Materials Society (TMS)* .

Li, J. (2006). *In-situ fabrication of functionally graded Al/Mg<sub>2</sub>Si by electromagnetic separation*. ShangHai: 2nd Sino-Germany workshop on Electromagnetic processing of materials.

Liao, H., Sun, Y., & Sun, G. (2003). Restraining effect of strontium on the crystallization of Mg<sub>2</sub>Si phase during solidification in Al-Si-Mg casting alloys and mechanisms. *Material Science and Engineering A358* , 164-170.

LSM. (1998). *grain refinement of aluminum-silicon foundry alloys*. London & Scandinavian Metallurgical Co. Limited.

Lu, S.-Z., & Hellawell, A. (1995). Modificatin of Al-Si alloys: Microstructure, thermal analysis, and mechanisms. *JOM* , 38-40.

MAC, A. (2005). Retrieved from A Guide to Aluminum Casting Alloys: [http://www.mid-atlanticcasting.com/alum-casting-alloys\\_FEB05.pdf](http://www.mid-atlanticcasting.com/alum-casting-alloys_FEB05.pdf).

MAHLE. (2007). *ALBOND® - rough surface, improved fuel consumption*. Retrieved from [www.mahle.com.br/C125705E004FDAF9/vwContentByKey/W276WF8H497STULEN](http://www.mahle.com.br/C125705E004FDAF9/vwContentByKey/W276WF8H497STULEN)

MatWeb. (2009). Retrieved from [www.matweb.com](http://www.matweb.com)

Meara, T. (2008). New honing options for hypereutectic aluminum cylinder bores. *MMS online* .

MSFC. (1997). *High-strength aluminum casting alloy for high-temperature applications*. MSFC Center Director's Discretionary Fund Final Report, Project No. 97-10.

Nafisi, S., & Ghomashchi, R. (2007). Boron-based refiners: Implications in conventional casting of Al-Si alloys. *Materials Science and Engineering* , 445-453.

NTU. (2006, 12). Retrieved from Department of Material Science and Engineering of Natinal TaiWan University (NTU):

40.112.32.1/download.php?filename=140\_59624e47.ppt&dir=community\_forum/71&title=Chapter+10

Ogris, E. (2002). *Development of Al-Si-Mg Alloys for Semi-Solid Processing and Silicon Spheroidization Treatment (SST) for Al-Si Cast Alloys*.

Pekguleryuz, M. O. (2007). *Aluminum physical metallurgy*. Montreal.

Pelton, A. D. (2001). *Thermodynamics and phase diagrams of materials*.

Rearset. (n.d.). Retrieved from [rearset.blogspot.com/2008/03/yamaha-to-introduce-diasil-cylinder-in.html](http://rearset.blogspot.com/2008/03/yamaha-to-introduce-diasil-cylinder-in.html)

Rin, M. (2005). *research on porosity defects of Al-Si alloy castings made with permanent mold*.

Rockwell, K. (2007). Retrieved from <http://www.kenrockwell.com/bmw/m3/2007/engine.htm>

Ryabchikov, I. V. (2007). Characteristics of Modifiers. *Materials Science and Engineering A* , 516-521.

Sabatino, M. D. (2005). *FLUIDITY OF ALUMINIUM FOUNDRY ALLOYS*. IMT-Report 2005:76.

Sabatino, M. D., & Arnberg, L. (2005). *A review on the fluidity of Al based alloys*. Norwegian university of science and technology.

SRS. (1999). Retrieved from [http://www.srs-ltd.co.uk/support/downloads/problem\\_solving/p\\_solving\\_shrinkage\\_porosity.pdf](http://www.srs-ltd.co.uk/support/downloads/problem_solving/p_solving_shrinkage_porosity.pdf)

Stefanescu, D. (1988). *Casting, vol.15*. ASM international.

TALAT. (1994). *the liquid metal*. EAA - European Aluminium Association.

Tani, J.-i., & Kido, H. (2005). Thermoelectric properties of Bi-doped Mg<sub>2</sub>Si semiconductors. *Physica B: Condensed Matter* , 218-224.

VHS. (2009). Retrieved from the web site of the Automotive Mechanics Department of Victoria High School: [www.abbysenior.com/mechanics/short.htm](http://www.abbysenior.com/mechanics/short.htm)

Weiss, J. (1987). Primary Silicon in hypereutectic Aluminum-Silicon casting alloys. *AFS transactions* , 51-62.

wikia. (n.d.). Retrieved 2009, from [http://schools.wikia.com/wiki/Buoyancy\\_&\\_Archimedes%27\\_Principle](http://schools.wikia.com/wiki/Buoyancy_&_Archimedes%27_Principle)

WikiPedia. (2009). Retrieved from <http://en.wikipedia.org/wiki/Aluminium>

Y.G. Zhao, Q. Q. (2004). in situ Mg<sub>2</sub>Si/ Al-Si composite modified by K<sub>2</sub>TiF<sub>6</sub>. *Materials Letters* 58 , 2192-2194.

Yamaha. (2008). Retrieved from [www.yamaha-motor.co.jp/global/asean-touring/machine/technology/002/index.html](http://www.yamaha-motor.co.jp/global/asean-touring/machine/technology/002/index.html)

Ye, H. (2003). An overview of the development of Al-Si alloy based material for engine applications. *Journal of Materials Engineering and Performance* , 288-297, vol.12(3).

Yuan, G. (2001). Effects of bismuth and antimony additions on the microstructure and mechanical properties of AZ91 magnesium alloy . *Materials Science and Engineering A* , 38-44.

Zhang, J., Fan, Z., Wang, Y., & Zhou, B. (2000). microstructure development of Al-15wt% Mg2Si in situ composite with mischmetal addition. *materials science and engineering A281* , 104-112.

Zhang, R., Zhao, Z. L., Huang, T. W., & Liu, L. (n.d.). Morphology of Primary Silicon and its Growth Mechanism in Hypereutectic Al-Si Alloys during Melt Overheating Treatment. *PRICM-5 /Materials Science Forum (MSF)* , p2587.

Zhang, Y. e. (2007). Transformation of microstructure after modification of A390 alloy. *Transactions of Nonferrous metals society of China* , 413-417.

Zhao, H. (. (2006). *铸造铝硅合金熔炼与铸锭 (Melting and ingot casting of Al-Si alloys)*. China North-East University Press.

Zolotarevsky, V., Belov, N. A., & Glazoff, M. V. (2007). *Casting aluminum alloys*. Elsevier Ltd.



## Appendix: Casting chemical compositions

<i>Table 9.1 The casting chemical compositions reported by the LAB ÉLITE LTÉE.</i>							
Specimen #	Si(wt%)	Cu(wt%)	Mg(wt%)	Fe(wt%)	P(wt%)	Bi(wt%)	Al(wt%)
UQAC A390	13.83	4.33	0.62	0.21	—	—	Bal.
A390-6Mg	14.37	4.87	5.75	0.25	—	—	Bal.
A390-10Mg	15.45	4.35	11.84	0.24	—	—	Bal.
McGill A390-1	15.78	4.30	0.61	0.31	—	—	Bal.
A390-2	15.98	4.31	0.61	0.31	—	—	Bal.
A390-0.01P-10	15.45	4.57	0.63	0.32	N/A	—	Bal.
A390-0.01P-11	15.94	4.71	0.64	0.32	N/A	—	Bal.
6Mg-3	16.29	4.49	6.53	0.28	—	—	Bal.
6Mg-4	16.21	4.49	6.57	0.29	—	—	Bal.
10Mg-6	16.48	4.55	11.04	0.27	—	—	Bal.
10Mg-7	15.70	4.47	10.96	0.27	—	—	Bal.
10Mg-0.7Bi-13	15.83	4.41	10.70	0.27	—	0.32	Bal.
10Mg-0.7Bi-14	15.97	4.39	10.66	0.27	—	0.30	Bal.
10Mg-1.0Bi-15	15.60	4.47	10.52	0.28	—	0.64	Bal.
10Mg-1.0Bi-16	15.88	4.46	10.53	0.22	—	0.55	Bal.
10Mg-1.3Bi-17	14.31	4.52	10.63	0.27	—	0.86	Bal.
10Mg-1.3Bi-18	15.90	4.37	10.45	0.26	—	0.85	Bal.
6Mg-0.6Bi-19	15.53	4.56	6.63	0.29	—	0.41	Bal.
6Mg-0.6Bi-20	15.28	4.43	6.54	0.28	—	0.45	Bal.
6Mg-0.9Bi-21	15.72	4.49	6.63	0.28	—	0.69	Bal.
6Mg-0.9Bi-22	14.17	4.50	6.94	0.32	—	0.81	Bal.
6Mg-1.2Bi-24	15.97	4.44	6.49	0.26	—	0.98	Bal.
6Mg-1.2Bi-25	15.18	4.53	6.69	0.28	—	1.09	Bal.

As seen in the Table 9.1, the Si and Mg contents of the alloy A390 in the reports have a little bit different from the original data (Si: 16.81 wt%; Mg: 0.29 wt%) provided by the supplier, leading to the overall relative lower Si ( $\leq 17$  wt%) and higher Mg results. Therefore, the recovery rates of the Si and Mg should be same to the assumptions as 100% and 93~95% respectively under both the electric resistance and the induction furnaces. As well as the Cu will be perfect for 100% recovery. Nevertheless, the bismuth has been reported as a rather high melt lost, ~65 to 85% of the recovery for pouring at 800°C and ~40 to 60% of that for casting at 850°C, instead of the 95% used during the practices.